OCS Study
BOEM 2022-044

Update of the River Overflood on Sea Ice and Strudel Scour in the U.S. Beaufort Sea

US Department of the Interior
Bureau of Ocean Energy Management
Alaska OCS Region, Anchorage, AK

OCS Study
BOEM 2022-044

Update of the River Overflood on Sea Ice and Strudel Scour in the U.S. Beaufort Sea

August 2022

Authors:

Gregory Hearon
Ana Plana Casado
Christopher Scott
David Dickins

Prepared under Contract No. M0121C0001
By
Coastal Frontiers Corporation
882A Patriot Drive
Moorpark, CA 93021

and

DF Dickins Associates, LLC
306 Belladera Court
Monterey, CA 93940

Disclaimer

Study concept, oversight, and funding were provided by the U.S. Department of the Interior, Bureau of Ocean Energy Management (BOEM), Environmental Studies Program, Washington, DC, under Contract Number M0121C0001. This report has been technically reviewed by BOEM, and it has been approved for publication. The views and conclusions contained in this document are those of the authors and should not be interpreted as representing the opinions or policies of BOEM, nor does mention of trade names or commercial products constitute endorsement or recommendation for use.

Report Availability

To download a PDF file of this report, go to the U.S. Department of the Interior, Bureau of Ocean Energy Management Data and Information Systems webpage (http://www.boem.gov/Environmental-Studies-EnvData/), click on the link for the Environmental Studies Program Information System (ESPIS), and search on 2022-044. The report is also available at the National Technical Reports Library at https://ntrl.ntis.gov/NTRL/.

Citation

Hearon G, Plana Casado A, Scott C, Dickins D (Coastal Frontiers Corporation, Moorpark, CA and DF Dickins Associates, LLC, Monterey, CA). 2022. Update of the river overflood on sea ice and strudel scour in the U.S. Beaufort Sea. Anchorage (AK): U.S. Department of the Interior, Bureau of Ocean Energy Management. 98 p plus appendices. Report No.: OCS Study BOEM 2022-044. Contract No.: M0121C0001.

About the Cover

Photo of river overflood onto the sea ice at the mouth of the Sagavanirktok River on the U.S. Beaufort Sea Coast. Photo taken east of Endicott Causeway (looking northwest) on May 24, 2014.

Executive Summary

This report describes a study conducted to improve the understanding of the spatial and temporal variability in overflood processes on the North Slope of Alaska and the related pipeline and facility siting hazards. The work builds on, updates, and supersedes all products generated as part of a similar study published in 2009 in the framework of the United States (U.S.) Department of the Interior, Minerals Management Service (MMS) project *Mapping Sea Ice Overflood Using Remote Sensing: Smith Bay to Camden Bay* (the "2009 Study"; Hearon *et al.*, 2009).

A geodatabase was compiled that includes satellite imagery, interpreted overflood boundaries, isolines of probability of overflood occurrence, strudel drain and scour data, and an inventory of offshore ice roads for the 26-year study period from 1995 to 2020. The geodatabase can be used by the U.S. Department of the Interior, Bureau of Ocean Energy Management (BOEM), Bureau of Safety and Environmental Enforcement (BSEE), and the State of Alaska to assess the potential environmental hazards associated with present and future oil and gas facilities that may be located within the study area.

The principal study findings derived from the data presented in the geodatabase and summarized in this report are:

1. ***Overflood Boundary Mapping***: A total of 274 overflood boundaries were mapped over the 13-year period from 2008 through 2020. The peak overflood extents between 1995 and 2007 mapped as part of the 2009 Study were refined, as needed, based on newly available imagery. In addition, overflood boundaries missing from the 2009 Study due to lack of imagery at the time were mapped. Aside from one instance in 2019, the overflood edge was mapped for all watercourses in the study area over the 21-year Moderate Resolution Imaging Spectroradiometer dominated era (2000 through 2020).

2. ***Overflood Occurrence Probability:*** Isolines of overflood probability were developed using the overflood extents mapped during the 21-year period from 2000 through 2020. The immediate region fronting all but one of the thirteen major rivers in the study area (Topagoruk River) flooded annually (100% probability of occurrence). In the central portion of the study area, between Cape Halkett and the Staines River, the entire coast flooded 25% of the time. Elsewhere, the flooded areas were discontinuous.

3. ***Correlation of River Overflood with Environmental Variables:*** Consistent with the 2009 Study findings, no meaningful correlations were identified between the annual overflood areas of the Colville, Kuparuk, and Sagavanirktok Rivers and environmental data related to streamflow, precipitation, snowpack, and air temperature. This indicates that the extent of river overflood onto the sea ice cannot readily be predicted by any single environmental variable for which historical data currently exist. The overflood phenomenon appears to be governed by interactions between a number of environmental forces, some of which (*e.g.,* soil moisture at high elevations at the onset of snowpack thawing, ice jams in distributary channels, roughness and snow cover on the sea ice, wind events during flooding, and the density of drainage features on the sea ice) are complex, for the most part poorly understood, or lack sufficient data to evaluate their contributions to the overall overflood process. In the absence of such direct correlations, the detailed long-term mapping of overflood boundaries in this study provides a valuable probabilistic assessment of potential hazards to coastal facilities based on past events. Investigations into the complex interactions governing river overflood is a recommended area of further research.

4. ***Long-Term Trends:*** The environmental and overflood data sets exhibit considerable year-to-year variability. However, clear trends in several parameters are evident over the 26-year study period. Both the end-of-winter snow water equivalent and average air temperature generally increased over the study period, while the streamflow and precipitation data exhibited inconsistent and weak trends. The annual overflood area within the study region decreased with time (rate ≈ 18 km^2/yr) and both the start and peak of overflood occurred earlier in the year (rate ≈ 0.4 days/yr).

5. ***Facility Hazards***: River overflood on the sea ice introduces two hazards to man-made facilities in the U.S. Beaufort Sea: interdiction of access to offshore facilities by flooding, and disturbance of the sea bottom above buried subsea pipelines by strudel scouring (which can compromise the integrity of the pipeline).

   Rapid deterioration of the ice sheet can render ice roads impassable within the zone of river overflood, impacting both facilities access and oil spill response. At least some portion of every nearshore ice road mapped between 1995 and 2020 was located within the zone of river overflood and vulnerable to damage during break-up.

   Strudel scouring can constitute a significant design consideration for subsea pipelines in nearshore areas adjacent to river and stream mouths. In the event that a strudel drain is located directly above a buried subsea pipeline, a sufficiently deep strudel scour may expose the pipeline and lead to an unsupported span. A strudel scour that forms directly over a buried pipeline also can remove the backfill material that is needed to prevent damage from ice keels and prevent upheaval buckling. An additional concern is that strudel drainage provides a potential mechanism to transport spilled oil below the ice sheet.

   Strudel scour frequency and severity can be segregated into zones according to water depth. Strudel scouring typically is most common and severe in the Primary Strudel Zone, which extends offshore from the grounded landfast ice edge to approximately 6 m water depth. In the zone of grounded landfast ice (the “Secondary Strudel Zone”) and offshore of the Primary Zone (the “Tertiary Strudel Zone”), scouring tends to be more modest and occur less frequently. When the major rivers in this region were considered, the Secondary Strudel Zone accounted for the greatest portion of the overflood area in any given year. On average, this zone encompassed 62% of the total overflood area. The Primary Strudel Zone accounted for 37% of the total overflood area, while the Tertiary Zone accounted for a mere 1%. Strudel zone and overflood occurrence information should be used to assess the hazard to prospective pipeline routes posed by strudel scouring in different coastal areas.

Contents

List of Figures

List of Tables

Abbreviations and Acronyms

ALOS	Advanced Land Observing Satellite
ASF DAAC	Alaska Satellite Facility Distributed Active Archive Center
Avg.	Average
AVNIR-2	Advanced Visible and Near Infrared Radiometer type 2
AWiFS	Advanced Wide Field Sensor
BOEM	Bureau of Ocean Energy Management
BPXA	BP Exploration Alaska
CSA	Canadian Space Agency
Col.	Colville
BSEE	Bureau of Safety and Environmental Enforcement
CFC	Coastal Frontiers Corporation
DFD	DF Dickins Associates, LLC
ERS	European Remote Sensing
ESA	European Space Agency
ETM+	Enhanced Thematic Mapper
FDD	Freezing Degree Days
GIS	Geographic Information Systems
GPS	Global Positioning System
GRD	Ground Range Detected
Horiz.	Horizontal
HU8	Level 8 Hydrologic Unit
IRS	Indian Remote Sensing
ISRO	Indian Space Research Organization
JAXA	Japanese Aerospace Exploration Agency
Kad.	Kadleroshilik
Kup.	Kuparuk
LISS-3	Linear Imaging Self-Scanning Sensor 3
Max.	Maximum
Min.	Minimum
MLLW	Mean Lower Low Water

MMS	Mineral Management Service
MODIS	Moderate Resolution Imaging Spectroradiometer
MSL	Mean Sea Level
MSS	Multispectral Scanner
NAD83	North American Datum of 1983
NASA	National Aeronautics and Space Administration
NOAA	National Oceanic and Atmospheric Administration
NOS	National Ocean Service
NRCS	Natural Resources Conservation Service
PALSAR	Phased Array Type L-band Synthetic Aperture Radar
R^2	Correlation coefficient
R.	River
SAR	Synthetic Aperture Radar
Sag.	Sagavanirktok
Shav.	Shaviovik
Simp.	Simpson
Sta.	Staines
SLC	Single Look Complex
SPOT	Satellite Pour l'Observation de la Terre (France)
SWE	Snow Water Equivalent
SWIR	Shortwave Infrared
TAPS	Trans-Alaska Pipeline System
TDD	Thawing Degree Days
TM	Thematic Mapper
UAF	University of Alaska, Fairbanks
U.S.	United States
USGS	United States Geological Survey
UTM	Universal Transverse Mercator
VIIRS	Visible Infrared Imaging Radiometer Suite
VNIR	Visible and Near-Infrared
WAAS	Wide Area Augmentation System
WBD	Watershed Boundary Dataset

WERC	Water and Environmental Research Center
Wshd.	Watershed

1 Introduction

River overflood on the sea ice occurs annually in the nearshore region of the United States (U.S.) Beaufort Sea during a brief period in the spring when river break-up precedes the break-up of the landfast sea ice (sea ice that is attached to the coast for an extended period of time, typically exceeding one week). Upon arrival at the coast, the river water flows on top of the grounded (attached to the seafloor) and floating sea ice, spreading up to 10 km offshore. This brief but energetic phenomenon constitutes a potential hazard to offshore oil and gas development in that it can impede access to facilities, disperse spilled oil, and expose buried subsea pipelines through strudel scouring.

This study was designed to map the extent of peak river overflood onto the landfast ice in the nearshore region of the U.S. Beaufort Sea during the 13-year period from 2008 to 2020. The present effort builds on, updates, and supersedes all products generated as part of a similar study published in 2009 (hereafter the "2009 Study") in the framework of the U.S. Department of the Interior, Minerals Management Service (MMS) project *Mapping Sea Ice Overflood Using Remote Sensing: Smith Bay to Camden Bay* (covering the period from 1995 to 2007; Hearon *et al.*, 2009). Both studies were conducted by Coastal Frontiers Corporation (CFC) and DF Dickins Associates, LLC (DFD).

The general objective of this study is to map river overflood boundaries to improve the understanding of the spatial and temporal variability in overflood processes and related pipeline and facility siting hazards. The specific objectives are as follows:

1. Document the maximum river overflood boundaries (peak seaward extent) from Admiralty Bay to Camden Bay between 2008 and 2020 using remote sensing and historical helicopter-based surveys;

2. Update the overflood information in the 2009 Study geodatabase where applicable, based upon newly available data;

3. Develop isolines of annual overflood occurrence probability based on the expanded dataset;

4. Update the strudel scour information in the 2009 Study geodatabase by incorporating information acquired since 2007;

5. Evaluate the environmental factors that contribute to river overflood and any changes in overflood extent or timing that have occurred over the study period; and

6. Combine the 2009 Study geodatabase with the river overflood boundaries and strudel scour information derived for the present study.

The primary study product is a geodatabase that includes satellite imagery, interpreted overflood boundaries, isolines of probability of overflood occurrence, strudel drain and scour data, and an inventory of offshore ice roads for the entire 26-year study period. The findings can be used by the U.S. Department of the Interior, Bureau of Ocean Energy Management (BOEM), Bureau of Safety and Environmental Enforcement (BSEE), and the State of Alaska to assess the potential environmental hazards associated with present and future oil and gas facilities that may be located within the study area.

This report presents a detailed account of the study. **Section 2** identifies the points of contact. **Section 3** describes the study area, while **Section 4** provides an overview of the physical processes governing river overflood and strudel scour formation. **Section 5** discusses prior studies (including the 2009 Study). The source data used in this study are described in **Section 6,** with mapping methods summarized in **Section 7.** Results are provided in **Section 8,** followed by a discussion of environmental factors contributing to the overflood process and trends observed over the study period in **Section 9** and **Section 10**, respectively. The facilities hazards associated with overflood are assessed in **Section 11**. Key conclusions are summarized in **Section 12**, followed by references in **Section 13**. Figures and tables are interspersed with the text.

A summary of the satellite platforms used as part of this study is provided in **Appendix A**. The mapped overflood boundaries are illustrated in **Appendix B**. Documentation for the geodatabase is provided in **Appendix C**, and correlations between the overflood and environmental parameters are presented in **Appendix D**.

2 Points of Contact

Scientific inquiries regarding the study should be directed to:

Gregory Hearon, P.E.
Principal Investigator
Coastal Frontiers Corporation
882A Patriot Drive, Moorpark, California 93021
(818) 341-8133
ghearon@coastalfrontiers.com

Inquiries regarding data access and dissemination should be directed to:

U.S. Department of the Interior
Bureau of Ocean Energy Management, Alaska Regional Office
Environmental Sciences Management
3801 Centerpoint Drive, Mailstop AM 500, Anchorage, Alaska 99503
(907) 334-5200

3 Study Area

The study area covers a 470 km stretch of shoreline between Admiralty Bay on the west and Camden Bay on the east in the U.S. Beaufort Sea (**Figure 1**). Located at the northern extremity of the Arctic Coastal Plain province, this area is part of the North Slope of Alaska physiographic unit. The region is characterized by a gently sloping, tundra-covered plain extending from the foothills of the Brooks Range to the U.S. Beaufort Sea. The coastal plain consists of alluvial and glacial sediments overlying continuous permafrost (TAPS, 2001).

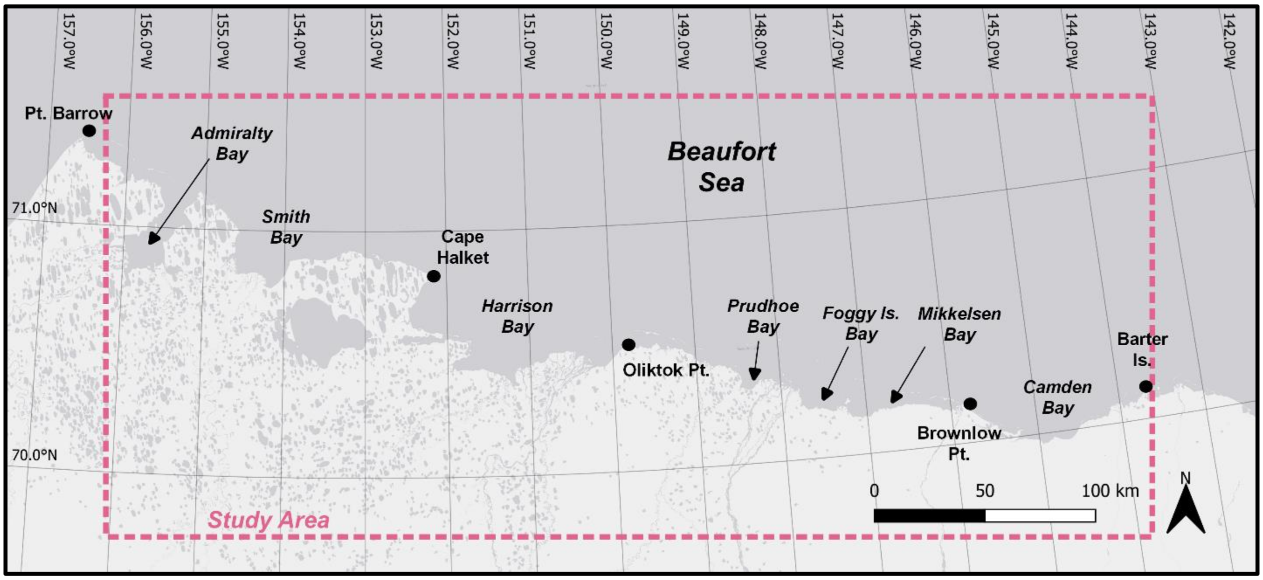

Figure 1. Study area

The U.S. Beaufort Sea Coast is predominantly low-lying tundra with numerous thaw lakes. The shoreline contains several bays and lagoons, with barrier islands prevalent between Harrison Bay and Barter Island. The shallow continental shelf extends 50–100 km off the coast (Norton and Weller, 1984).

Ice covers the U.S. Beaufort Sea for about nine months of each year. First ice in the nearshore region typically forms in early October, with complete freeze-up occurring around mid-November (CFC and Vaudrey, 2021). Typically, the ice becomes landfast (attached to the coast for an extended period of time, typically exceeding one week) in the nearshore waters of the bays and lagoons by January, and persists until break-up commences with the thawing of the upland rivers and overflooding of the nearshore sea ice in late May and early June (CFC and Vaudrey, 2022).

Within the study area, there are 13 major rivers and numerous small rivers, creeks, and streams that discharge into the U.S. Beaufort Sea. The region is segmented into nine watersheds, as defined by the United States Geological Survey (USGS) Watershed Boundary Dataset (WBD) for Arctic Alaska (USGS, 2021a). **Table 1** lists the major rivers in the study area, along with their approximate location near the coast and USGS WBD designation. The location of each river and key points of interest are shown in **Figure 2** and **Figure 3**, while the watershed boundaries are shown in **Figure 4** and **Figure 5**.

Table 1. Major rivers discharging into the U.S. Beaufort Sea

River	Latitude[1]	Longitude[1]	USGS WBD
Topagoruk River	70°45'24" N	155°55'35" W	Admiralty Bay-Dease Inlet
Ikpikpuk River	70°49'25" N	154°18'09" W	Ikpikpuk River
Colville River	70°23'02" N	150°48'24" W	Lower Colville River
Kuparuk River	70°24'42" N	148°52'38" W	Kuparuk River
Sagavanirktok River	70°16'39" N	147°59'55" W	Sagavanirktok River
Kadleroshilik River	70°12'23" N	147°37'00" W	Mikkelsen Bay[2]
Shaviovik River	70°12'21" N	147°17'42" W	Mikkelsen Bay[2]
Staines River	70°08'17" N	145°59'57" W	Canning River
Canning River	70°04'42" N	145°33'56" W	Canning River
Katakturuk River	69°58'33" N	144°59'51" W	Camden Bay
Sadlerochit River	70°01'22" N	144°26'08" W	Camden Bay
Hulahula River	70°03'54" N	144°04'57" W	Camden Bay
Okpilak River	70°04'40" N	144°03'09" W	Camden Bay

[1] Location is approximate and provided relative to North American Datum of 1983 (NAD83)

[2] USGS refers to "Mikkelsen Bay" as "Mikkelson Bay." Traditional spelling ("Mikkelsen") used herein.

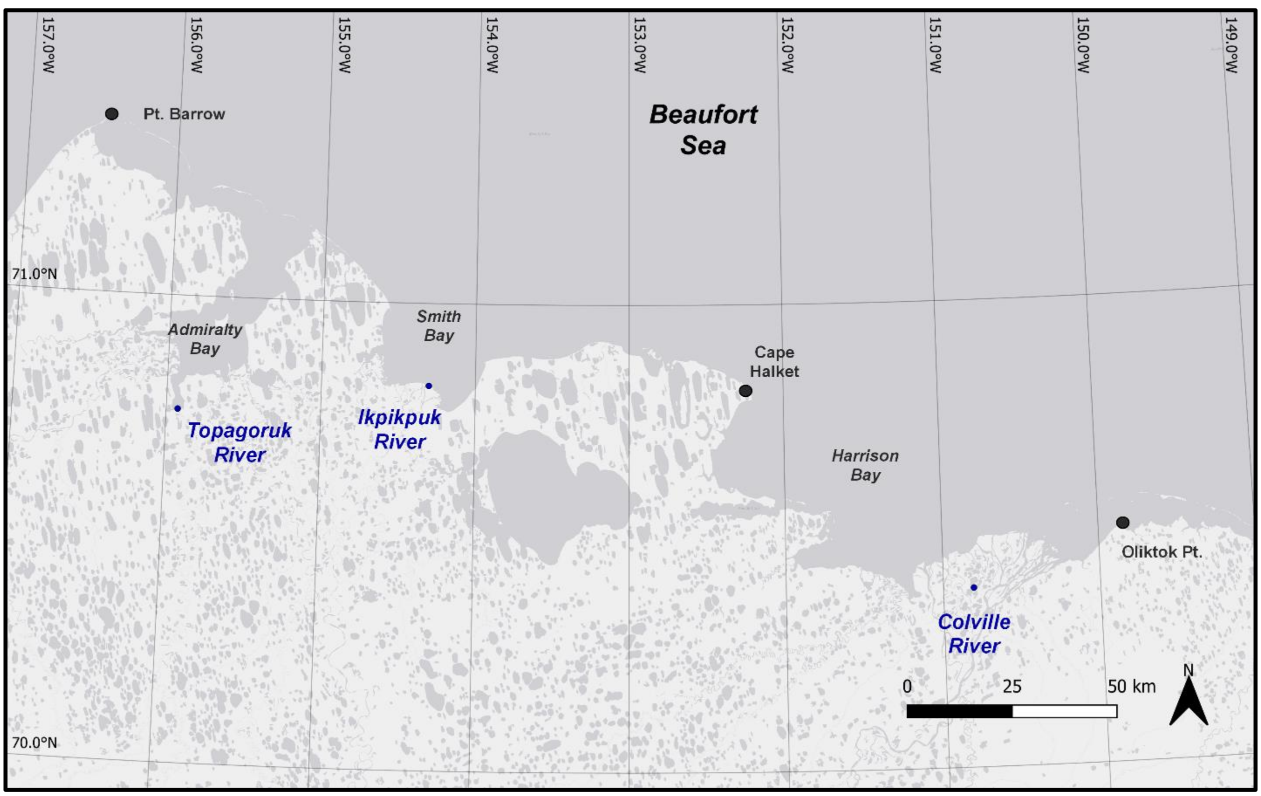

Figure 2. Major rivers discharging into the U.S. Beaufort Sea, west study region

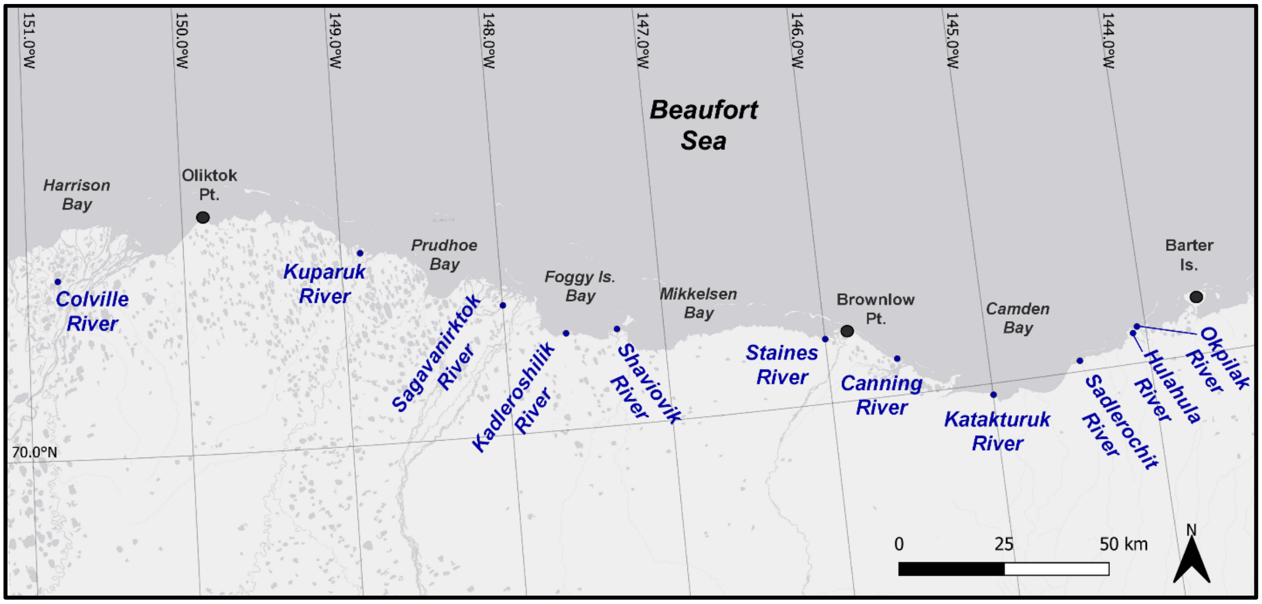

Figure 3. Major rivers discharging into the U.S. Beaufort Sea, east study region

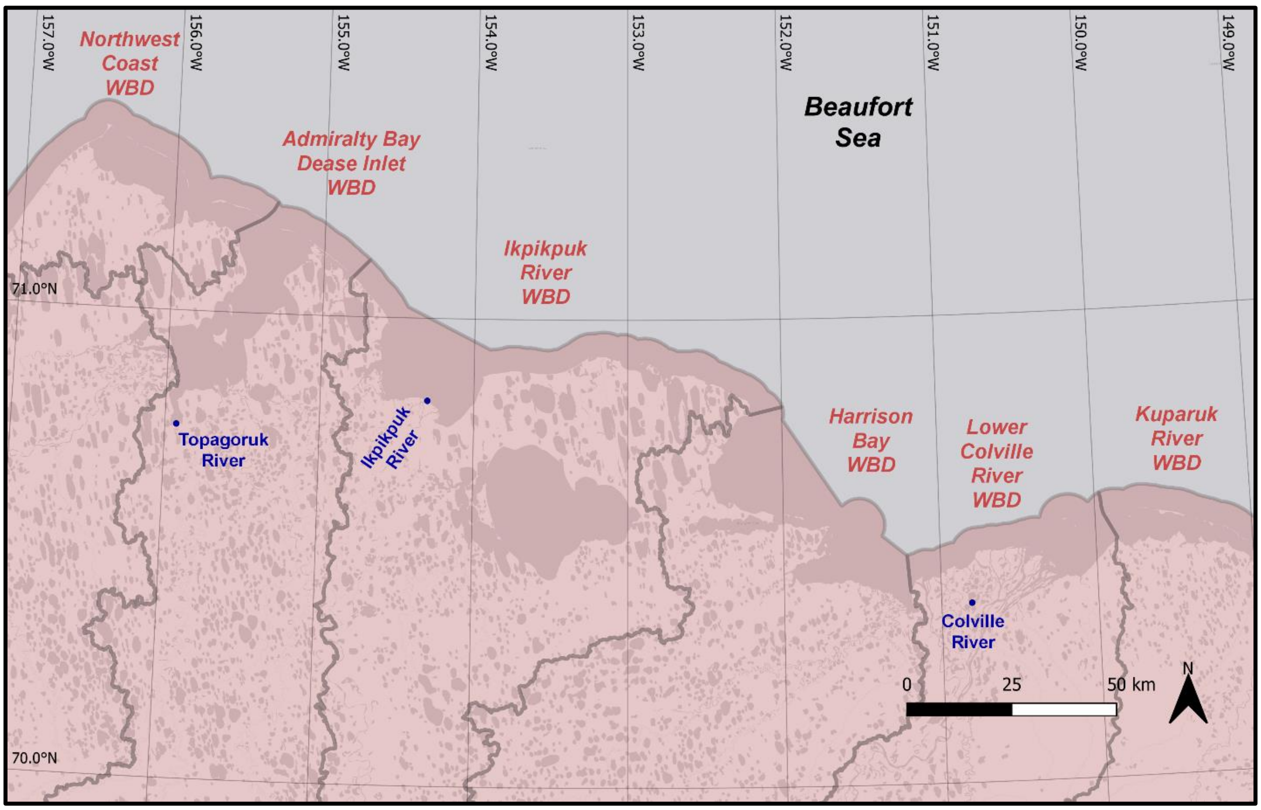

Figure 4. USGS watershed boundaries (WBD), west study region

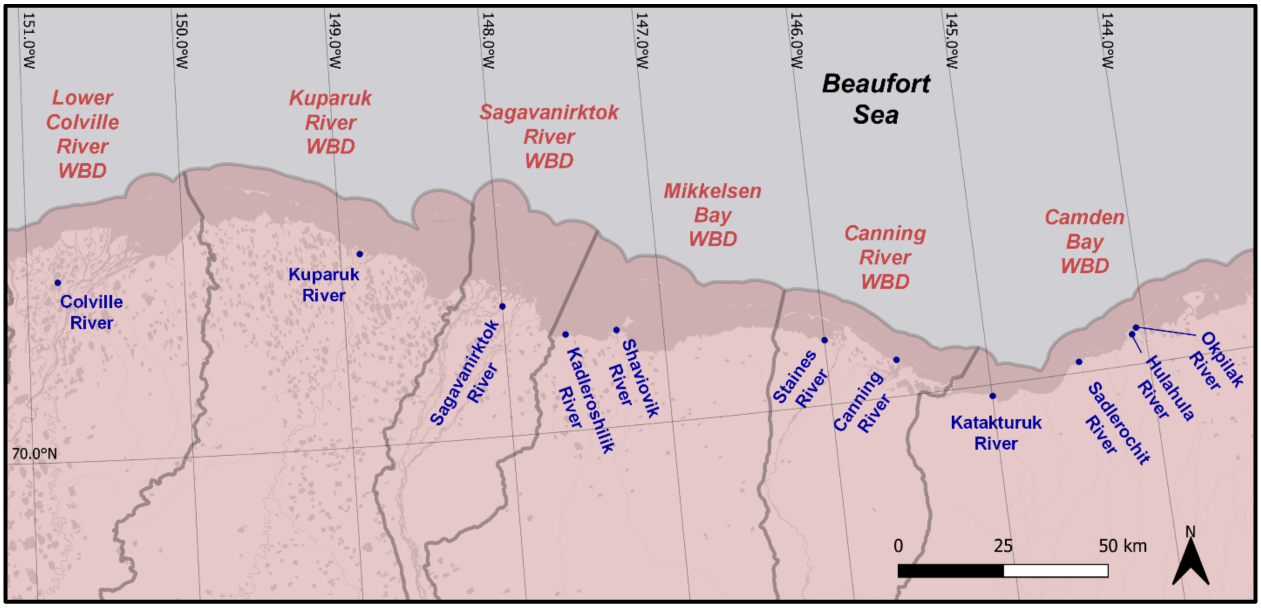

Figure 5. USGS watershed boundaries (WBD), east study region

4 Physical Processes

This section describes the physical processes that govern river overflood and strudel scour formation.

4.1 River Overflood

Overflooding of fresh water onto sea ice from rivers draining into the U.S. Beaufort Sea occurs each spring during a brief period when river break-up precedes the break-up of the sea ice. Rivers on the North Slope of Alaska are characterized by a virtual cessation of river flow during the winter, and the annual flow is concentrated during a relatively short period in the spring (typically from late May to early June; Walker, 1974). As air temperatures increase in the spring, the snow in the Brooks Range begins to melt and flow downstream. Upon arrival at the coast, the presence of landfast sea ice at the river mouth forces the flood water to flow on top of the grounded and floating landfast sea ice.

The overflood can spread up to 10 km offshore (Hearon *et al.*, 2009; Dickins *et al.*, 2011). While the depth of overflood on top of the ice can reach 1.5 m in places, depths of 0.6 to 0.9 m are considered more typical (Vaudrey, 1984, 1985, 1986). The intense flooding typically lasts for a period of days to weeks, depending on the river. **Figure 6** shows overflood water from the Sagavanirktok River on the sea ice near the Endicott Development.

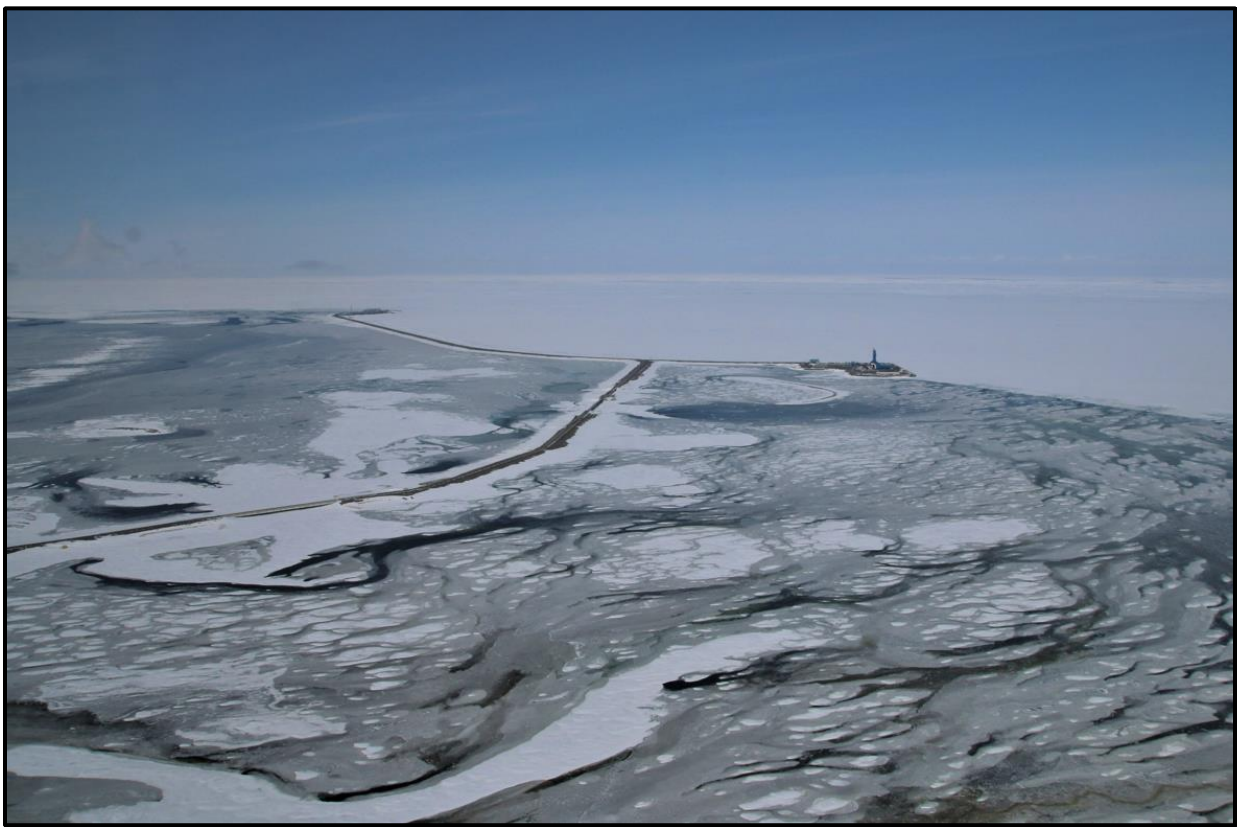

Figure 6. Overflood water from the Sagavanirktok River near the Endicott Development

While each river system has its own unique characteristics depending on the channel geometry and flow regime, the stages of overflood generally are repeated at each of the drainages along the U.S. Beaufort Sea Coast within a relatively short window of a few weeks or less.

The overflood phenomenon occurs on a large scale and is clearly visible in satellite imagery. **Figure 7** is a Resourcesat-2A Advanced Wide Field Sensor (AWiFS) image (56-m resolution) acquired on May 29, 2020 by the Indian Space Research Organization's (ISRO) Indian Remote Sensing (IRS) Resourcesat satellite platform. It shows rivers flowing onto the sea ice (dark areas) from the Colville River on the west to the Shaviovik River on the east.

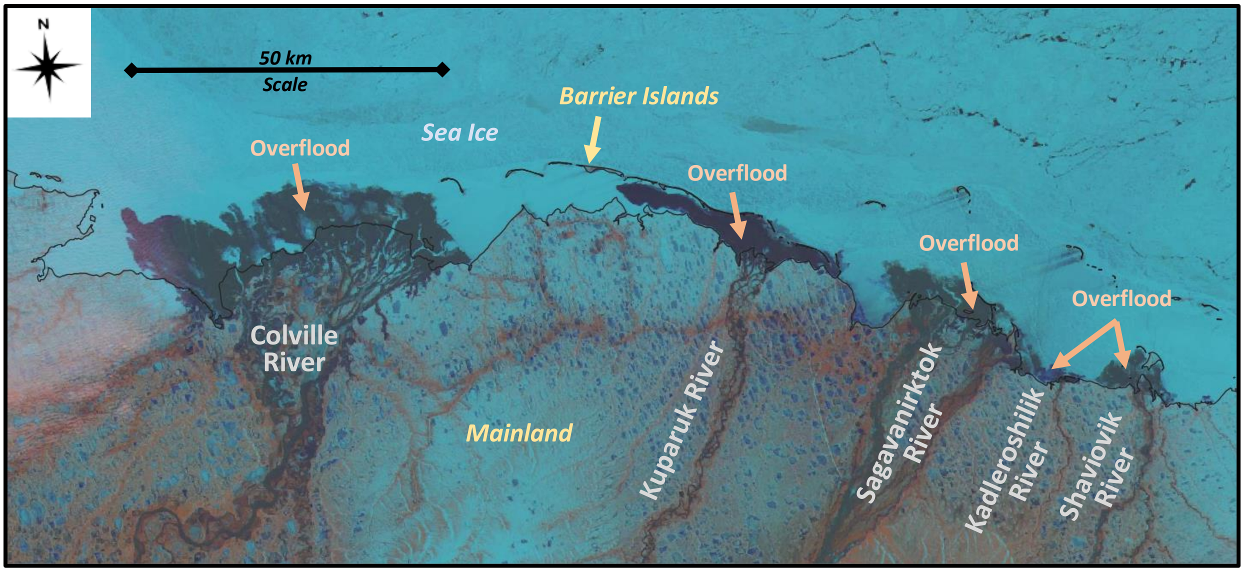

Figure 7. Resourcesat-2A AWiFS image showing river overflood on May 29, 2020

Anthropogenic features, such as causeways or ice roads, can strongly influence the progression and spatial distribution of the flood waters on the sea ice. This is illustrated in **Figure 8**, where flood waters emanating from the Colville River have been diverted by a winter ice road constructed to service an offshore facility.

Figure 8. Overflood from the Colville River impeded by an ice road

4.2 Strudel Scour

Early in the overflood period, the flood waters pass over the region of grounded landfast sea ice (typically extending to a water depth approaching 2 m; Leidersdorf *et al.,* 2007). Farther offshore, in water depths greater than about 2 m (the floating landfast ice region), the flood waters drain through holes and discontinuities in the ice sheet caused by tidal cracks, thermal cracks, stress cracks, and ice seal breathing holes. This process is termed "strudel drainage." Initially, strudel drainage is precluded in the grounded landfast ice region by the lack of a flow path through the ice sheet, even if discontinuities are present. As the overflood period progresses, the grounded landfast ice sheet breaks free and rises to the surface, allowing strudel drainage to commence (Reimnitz *et al.,* 1974).

Strudel drainage features tend to fall into one of two general categories – linear crack drains or circular drains. **Figure 9** shows an active linear crack drain in the Colville River Delta, while an active circular drain in the same area is shown in **Figure 10. Figure 11** and **Figure 12** show circular drainage features off of the Sagavanirktok and Kuparuk Rivers near the end of the overflood process, after most of the flood water has receded.

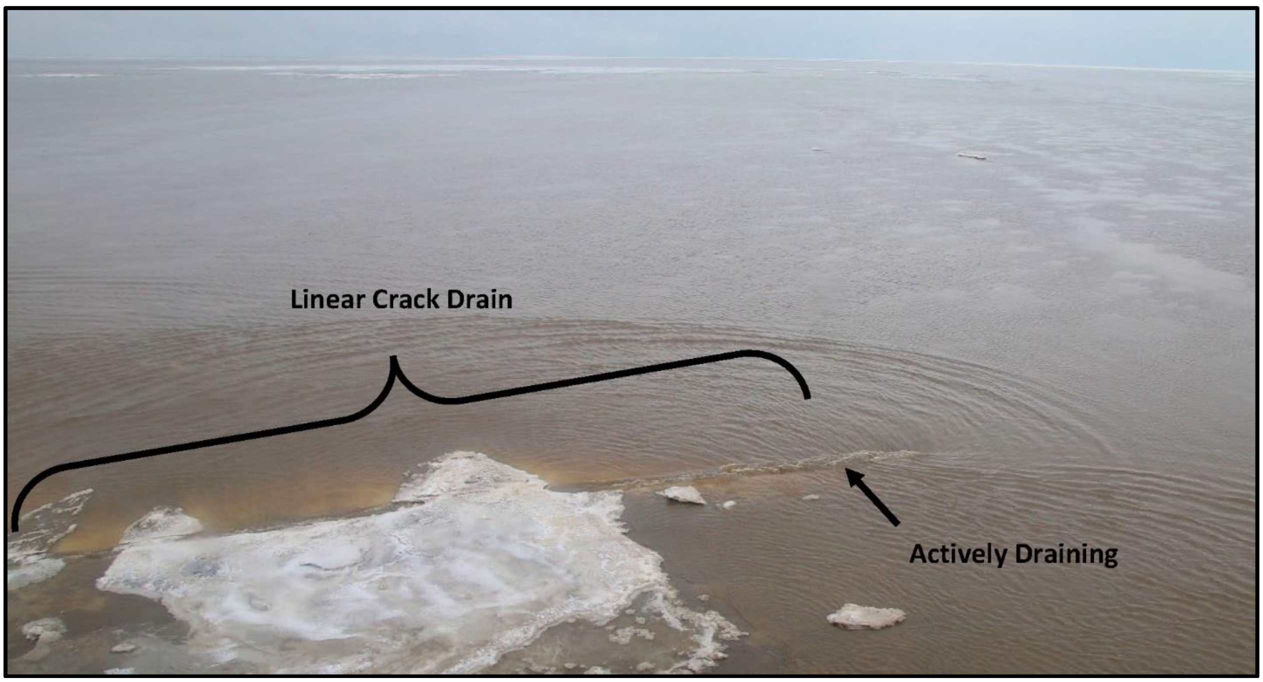

Figure 9. Active linear crack drain in the Colville River Delta

When the drainage rate is high, powerful strudel jets, or whirlpools, can develop at the drain sites and create large scour depressions on the seafloor. These seafloor depressions were documented in USGS investigations off the North Slope of Alaska in the 1970s (*e.g.*, Reimnitz *et al.*, 1974; Reimnitz and Kempema, 1982).

Strudel scours can constitute significant design considerations for subsea pipelines in cold regions (Lanan *et al.,* 2008). In the event that a strudel drain is located directly above a buried subsea pipeline, a sufficiently deep strudel scour may expose the pipeline and lead to an unsupported span (**Figure 13**). A strudel scour that forms directly over a buried pipeline also removes backfill material that is needed to help prevent upheaval buckling and protect against ice keels. An additional concern is that strudel drainage may provide a pathway to transport an oil spill below the ice sheet (Dickins and Owens, 2002).

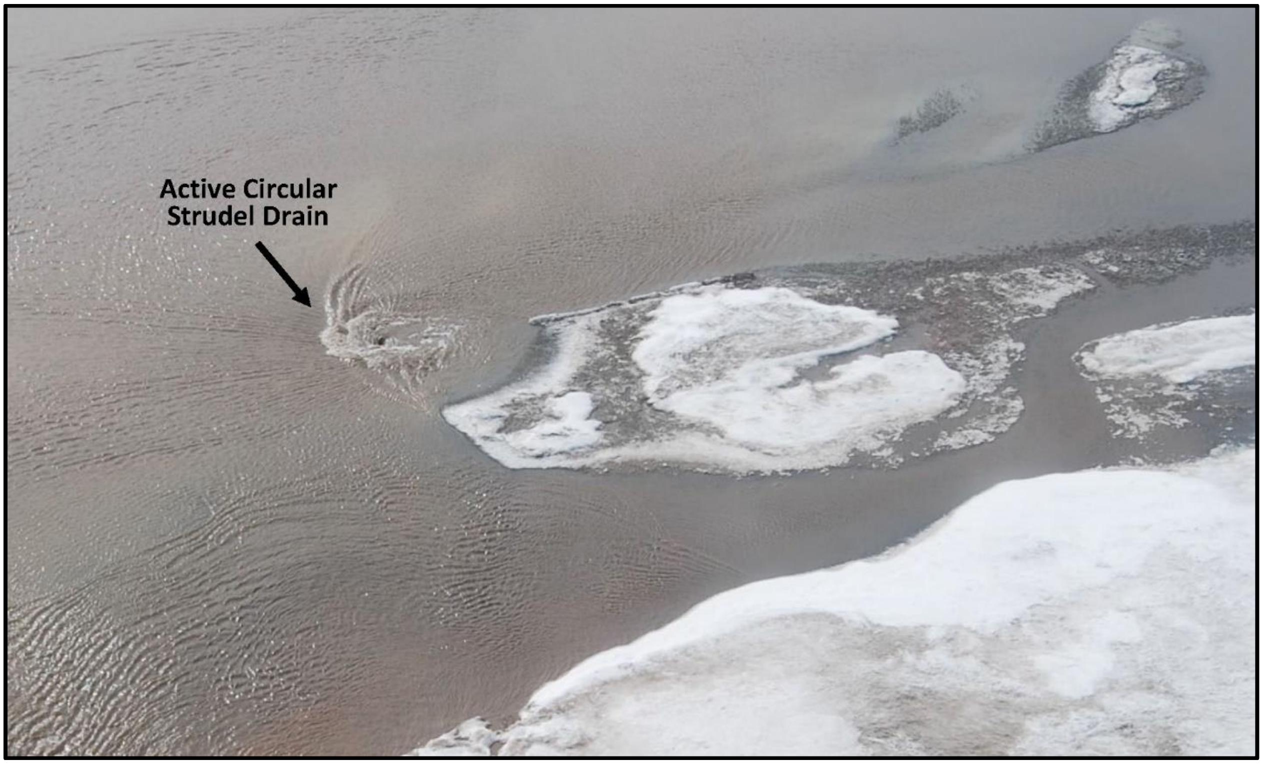

Figure 10. Active circular strudel drainage in the Colville River Delta

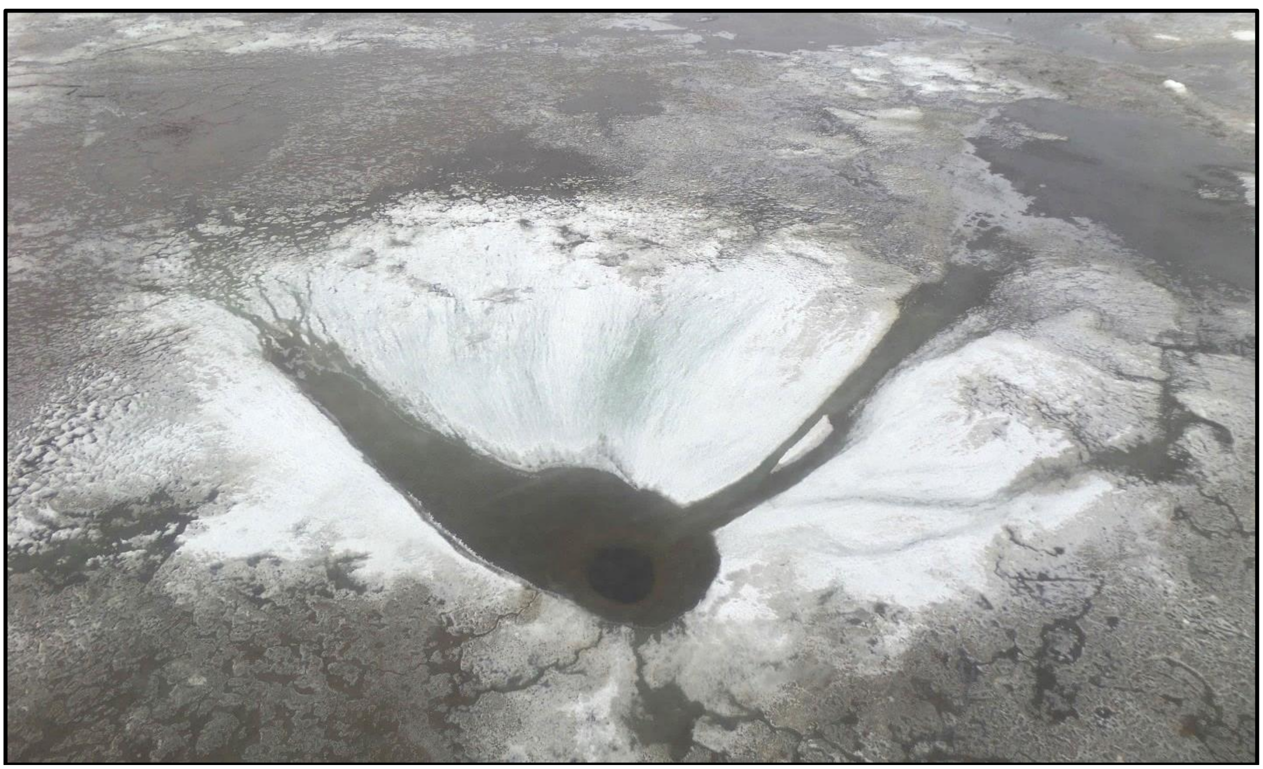

Figure 11. Circular strudel drain off the Sagavanirktok River near the end of the overflood period

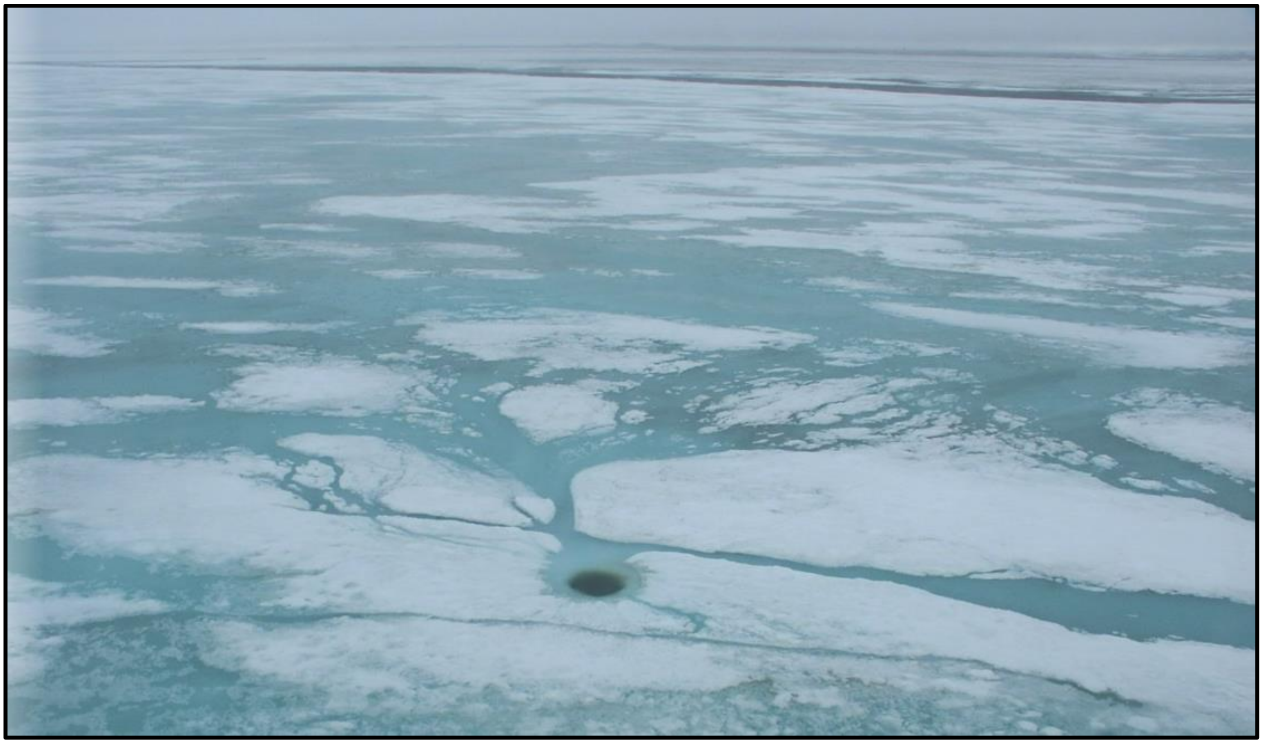

Figure 12. Circular strudel drain in the Kuparuk River Delta near the end of the overflood period

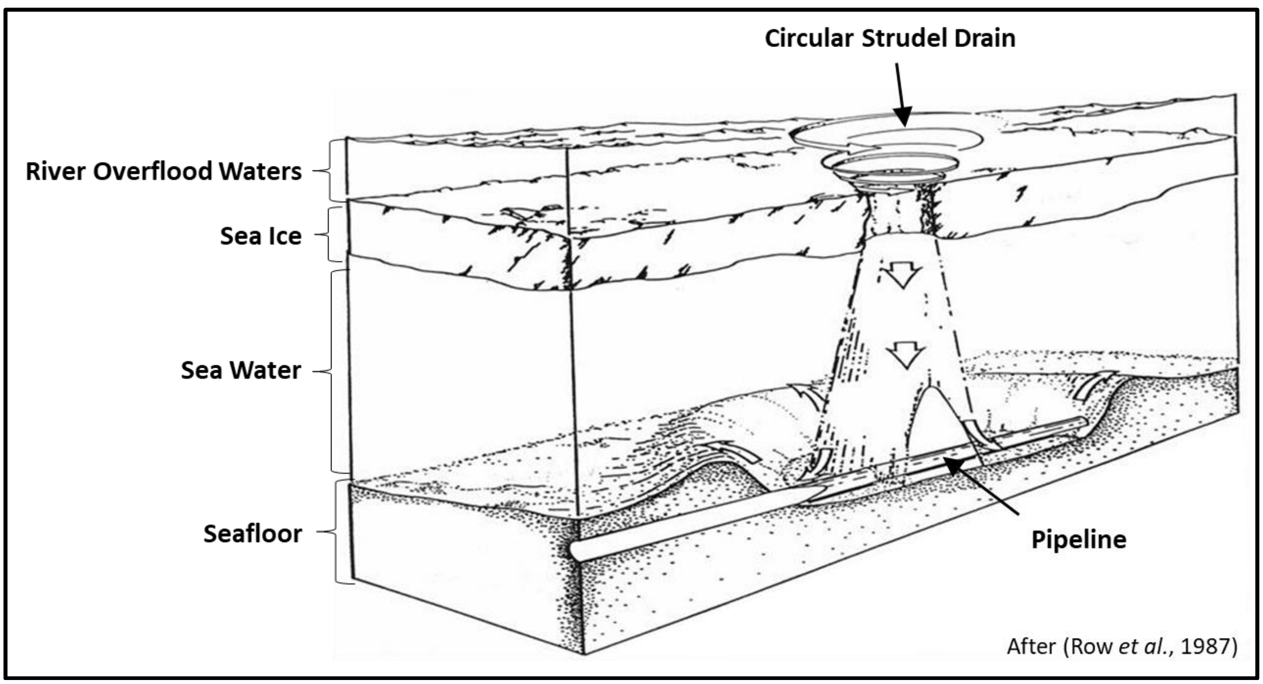

Figure 13. Schematic of strudel scour occurring over a subsea pipeline

The processes of strudel drainage and seafloor scouring tend to be more severe in the floating landfast ice zone than in the grounded landfast ice zone (Leidersdorf *et al.*, 2007). Because drainage in the grounded landfast ice zone occurs later in the overflood period after the peak river discharge has subsided, the drainage tends to be less vigorous. As a result, scouring tends to be milder than that which occurs farther offshore.

Based on the strudel formation process and an assessment of strudel scour data obtained for the Northstar Oil and Gas Development, Leidersdorf *et al.* (2007) classified the zone of grounded landfast ice as the "Secondary Strudel Zone" and the zone of floating landfast ice as the "Primary Strudel Zone." The Primary Strudel Zone is defined as the region between the 1.5-m and 6-m isobaths, while the Secondary Strudel Zone is located between the shoreline and the 1.5-m isobath. Based on the recognition that the potential for strudel scour formation diminishes in water depths beyond approximately 6 m, a third zone (the "Tertiary Strudel Zone") was defined as part of the 2009 Study as the region offshore of the Primary Strudel Zone. Strudel scour formation and zonation are illustrated in **Figure 14**.

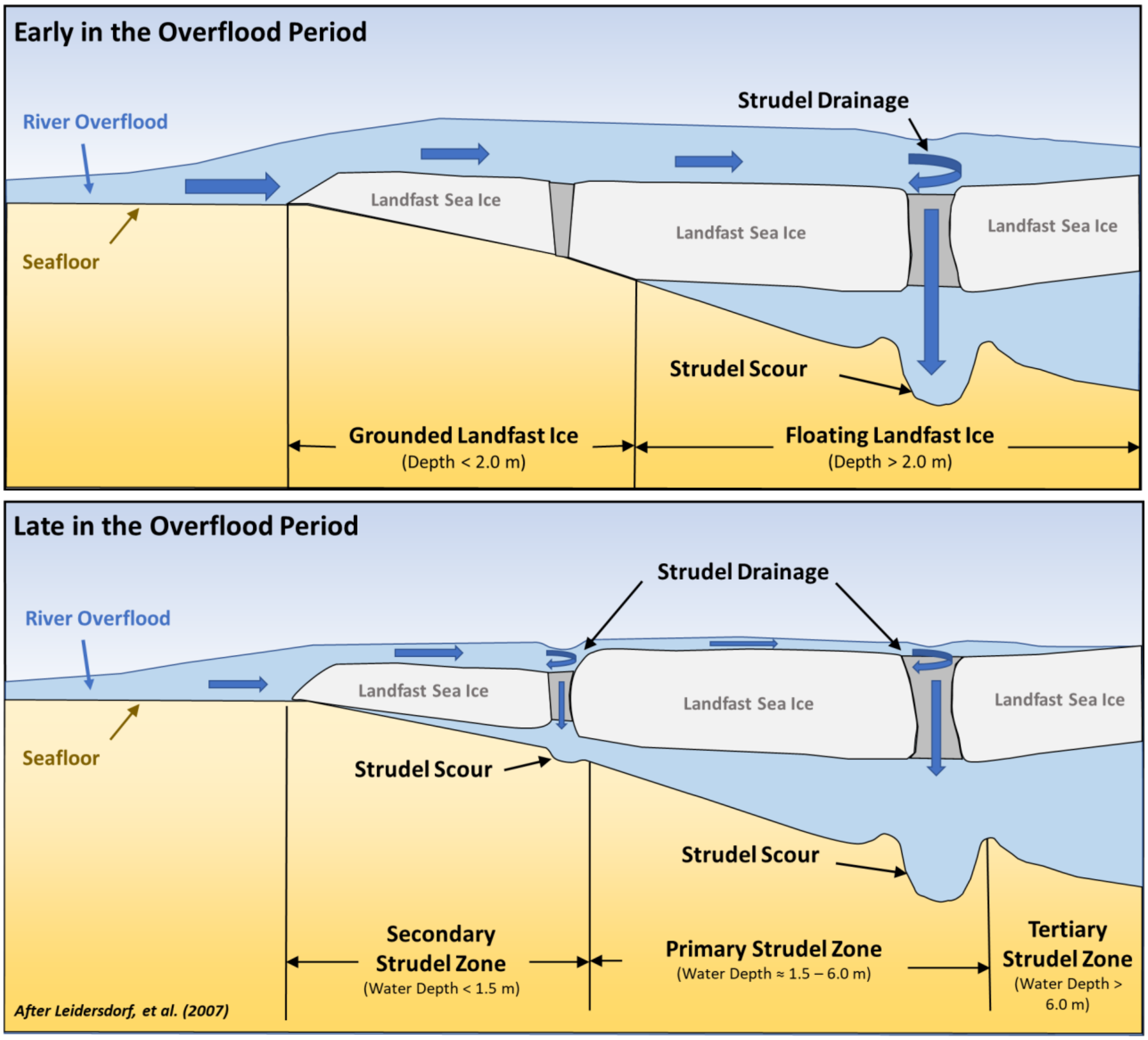

Figure 14. Schematic of strudel scour process, zonation, and types of landfast sea ice

5 Prior Studies

Studies of the overflood processes along the U.S. Beaufort Sea Coast have been undertaken since the early 1960s. While the primary motivation of early investigations was scientific inquiry, the advent of offshore oil production and subsea pipeline construction in the U.S. Beaufort Sea has led to more systematic engineering applications. The sections below summarize early scientific studies, industry-based studies, and the 2009 Study (which is the basis for the present study).

5.1 Early Scientific Studies

In one of the earliest studies of river overflood on the North Slope of Alaska, Arnborg *et al.* (1966) conducted field work to understand the hydrological characteristics of the Colville River Delta. Walker (1974) extended this work with additional field measurements in the early 1970s and published a comprehensive description of overflood processes. Around the same time, Barnes and Reimnitz (1976) combined field measurements obtained near the Kuparuk River with satellite imagery to describe the development of river overflood and associated phenomena, such as strudel scours. Scientific study of overflood processes along the U.S. Beaufort Sea Coast continued through the 1970s and into the 1980s (*e.g.*, Barry *et al.*, 1979; Carlson *et al.*, 1977; Craig *et al.*, 1985; Reimnitz and Kempema, 1982).

Much of the original documentation of river overflood in the Prudhoe Bay area was generated through field studies carried out by the U.S. Geological Survey, the University of Alaska, and the National Oceanic and Atmospheric Administration (NOAA) (LaBelle *et al.*, 1983). The first use of relatively high-resolution (100 m) Landsat imagery to document overflood boundaries occurred in the 1970s. These efforts often were hindered by cloud cover and the long repeat cycle of the satellites (16 to 18 days). Vaudrey (1984, 1985, and 1986) mapped overflood boundaries by helicopter in the 1980s as part of break-up studies conducted as joint-industry projects. **Figure 15** provides an overflood boundary and strudel drain locations mapped by Vaudrey (1984).

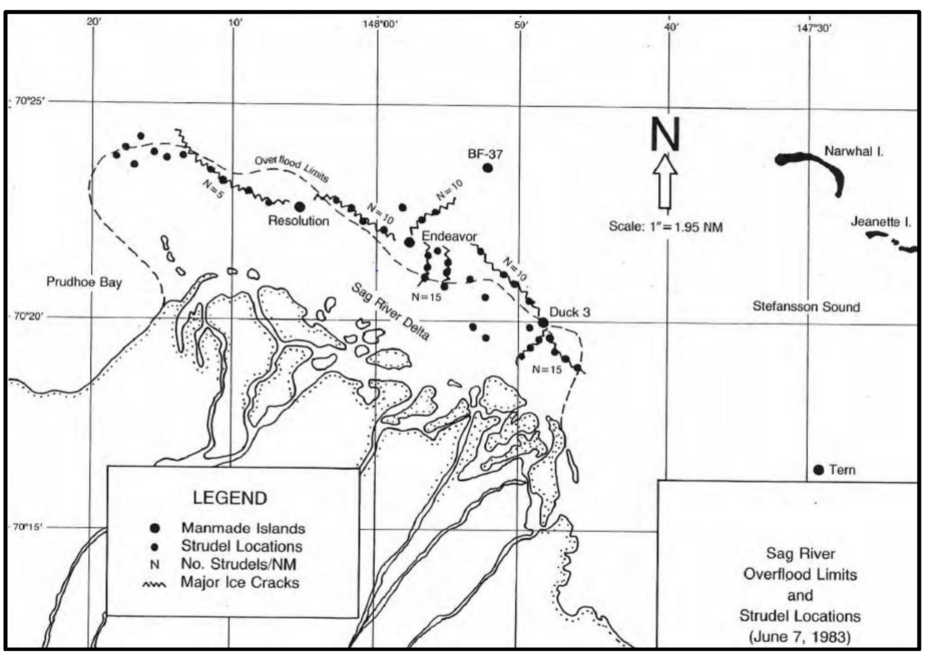

Source: Vaudrey, 1984

Figure 15. River overflood and strudel drains in Sagavanirktok River Delta, 1983

5.2 Industry-Sponsored Studies

The discovery of oil in Prudhoe Bay prompted industry interest in the engineering and operational impacts of river overflood on the North Slope of Alaska. Beginning in the 1980s, a number of industry-sponsored projects were conducted in support of the Endicott and Northstar Oil and Gas Developments and the Liberty Prospect (*e.g.*, McClelland Engineers Inc, 1982; Atwater, 1991; CFC, 1997 and 1998; DF Dickins *et al.*, 1999). These studies utilized a combination of helicopter surveys and visible satellite images to interpret and map the peak overflood extent and strudel drain locations in the Sagavanirktok River Delta, Simpson Lagoon, and Stefansson Sound. Similar studies have been conducted in Smith Bay (CFC, 2016), on the east side of the Colville River Delta (*e.g.*, CFC, 2006), and in Mikkelsen Bay (*e.g.*, CFC, 2007).

A primary objective of the industry studies was to document strudel scour characteristics in order to evaluate risk (both the probability of occurrence and the impact, or size, of the scour) and establish design criteria for subsea pipelines. In the case of the three subsea pipelines in the U.S. Beaufort Sea, these studies continued after installation in the form of monitoring programs to ensure pipeline integrity and permit compliance. The studies typically included a helicopter-based reconnaissance to map the river overflood boundary and strudel drainage features within a specified corridor, followed by a vessel-based sea bottom survey during the open-water season to map any strudel scours that formed at the drainage sites. **Table 2** provides a summary of the industry studies conducted between 1995 and 2020. A detailed description of the field methods used as part of the industry-sponsored studies is provided in **Section 6.2**.

Table 2. Industry-sponsored overflood studies, 1995 to 2020

Project	Data Provider	Years	Major Rivers	Overflood Extent	Strudel Drains	Strudel Scours
Tulimaniq Prospect	Caelus	2016	Ikpikpuk River	Yes	Yes	No
AK North Slope Development	Confidential	2005–2020	Colville River	Yes	Yes	Yes
AK North Slope Development	Confidential	2007, 2009–2020	Colville and Kuparuk Rivers	Yes	Yes	Yes
Northstar Development	BPXA / Hilcorp	1996–2020	Kuparuk River	Yes	Yes	Yes
Liberty Prospect	BPXA / Hilcorp	1997–2001, 2003, 2005, 2013–2017	Sagavanirktok, Kadleroshilik, and Shaviovik Rivers	Yes	Yes	Yes
Sivulliq Prospect	Shell	2006–2008, 2010	Canning and Staines Rivers	Yes	Yes	Yes

5.3 Minerals Management Service 2009 Study

In 2007, the MMS, Alaska Outer Continental Shelf Region commissioned a study designed to improve the knowledge of the spatial and temporal variability of overflooding along the coastline of the North

Slope of Alaska and related pipeline and facility siting concerns ("the 2009 Study"; Hearon *et al.*, 2009). The present effort builds on, updates, and supersedes all products generated as part of the 2009 Study.

As part of the work, historical overflood boundaries were mapped for the 13-year period from 1995 to 2007 using a combination of helicopter surveys and satellite imagery. Several satellite platforms were evaluated to quantify their accuracy and limitations for mapping river overflood. In addition, hazards associated with strudel scouring were assessed with databases developed for several industry projects. The study area was identical to that used in the current study. The results were incorporated into a geodatabase.

Salient findings from the 2009 Study are provided below:

1. *Field Survey Program and Satellite Image Validation*: Helicopter-based mapping techniques provide the most accurate depiction of river overflood limits. The helicopter-derived 2007 Colville River overflood boundary was compared to the boundaries mapped using images from three visible spectrum satellite platforms (Landsat 7, Satellite Pour l'Observation de la Terre (France) [SPOT], and Moderate Resolution Imaging Spectroradiometer [MODIS]) and two Synthetic Aperture Radar (SAR) satellite platforms (European Remote Sensing [ERS-2] and Radarsat) to gain an understanding of the accuracy and limitations of various image platforms. Landsat 7, MODIS, and ERS-2 performed equally well among the satellite platforms and provided the most accurate depiction of the overflood limit relative to the helicopter survey. The SPOT and Radarsat imagery provided the least accurate results. The findings suggest that satellite imagery can be used to derive overflood limits that approach the accuracy of helicopter-based results under favorable conditions. However, late in the overflood period and under unfavorable conditions, overflood boundaries derived from satellite-based imagery can differ materially from those derived from helicopter-based mapping. Because the availability of images from multiple satellite platforms in a given year is rare, however, none of the satellite platforms investigated should be excluded from consideration when mapping historical overflood limits.

2. *Historical Overflood Boundary Mapping*: River overflood boundaries were mapped for all major rivers and streams in the study area for the 13-year period between 1995 and 2007 using a combination of historical helicopter surveys and satellite images. Satellite imagery, and particularly radar satellite imagery, formed the key data source needed to develop the final mapped boundaries. To increase the probability of capturing the peak overflood, a maximum composite overflood limit was developed for each watercourse by integrating all of the mapped overflood limits for a given year. When the major river systems in the study are considered, overflood limits were mapped for 129 out of 143 possible river and year combinations, resulting in a mapping success of 90%.

3. *Correlation of River Overflood with Environmental Variables*: No meaningful correlations were identified between annual overflood areas and the corresponding values of streamflow, precipitation, and air temperature. Attempts to correlate streamflow with either precipitation or air temperature also proved to be fruitless. The most important implication of these findings is that the extent of river overflood onto the sea ice cannot be predicted by any single environmental variable for which historical data currently exist. The overflood phenomenon appears to be governed by complex interactions between a number of environmental forces, some of which, such as ice jams in distributary channels, roughness and snow cover on the sea ice, and the density of drainage features on the sea ice, have not been quantified to date.

4. *Hazards Related to River Overflood*: Strudel scouring can constitute a significant design consideration for subsea pipelines in nearshore areas adjacent to river and stream mouths. Strudel

scour concerns have resulted in the burial of the three existing subsea pipelines in the U.S. Beaufort Sea. An additional concern is that strudel drainage provides a potential mechanism to transport spilled oil below the ice sheet. Rapid deterioration of the ice sheet can render ice roads impassable within the zone of river overflood, impacting both facilities access and oil spill response.

5. *Strudel Scour Zonation*: Strudel scour frequency and severity can be segregated into zones according to water depth. Strudel scouring typically is most common and severe in the Primary Strudel Zone, which extends offshore from the grounded landfast ice edge to approximately 6 m water depth. In the zone of grounded landfast ice (the Secondary Strudel Zone) and offshore of the Primary Zone (the Tertiary Strudel Zone), scouring tends to be more modest and occur less frequently. When the major rivers in this region were considered, the Secondary Strudel Zone accounted for the greatest portion of the overflood area in any given year. On average, this zone encompassed 66% of the overflood area. The Primary Strudel Zone accounted for 32% of the total overflood area, while the Tertiary Zone accounted for a mere 2%. Strudel zone information should be used to assess the likelihood that prospective pipeline routes may be impacted by strudel scouring in different coastal areas.

6. *Strudel Scour Pipeline Encounter Frequency:* A case study of strudel scours in the vicinity of the Northstar Development suggests that the presence of the operational pipeline materially altered the scour regime and has led to a substantially higher than expected scour encounter frequency with the pipelines. This phenomenon is most prominent in the Secondary Zone and is believed to be attributable to radiant heat from the pipelines propagating through the backfill and degrading the overlying ice cover. While less pronounced, a statistical analysis of strudel occurrence also indicates an increased encounter frequency in the Primary Zone. Radiant heat from the pipelines also may explain the high encounter frequency in this zone. However, it is not known whether the impact is direct (degradation of the ice sheet), indirect (increased biological activity in the warmer water), or a combination of the two. Because scouring is more severe in the Primary Zone, the potential consequences of scour depressions forming over the pipelines are greater in this zone than in the Secondary Zone.

7. *Hazards Related to Facilities Access*: Rapid deterioration of the ice sheet can render ice roads impassable within the zone of river overflood, impacting both facilities access and oil spill response.

It is important to note that this report is intended to update that prepared as part of the 2009 Study. Where inconsistencies exist, the current study findings should be used.

6 Source Data

The overflood boundary geodatabase developed for this study was derived from a combination of satellite image mapping and historical helicopter-based surveys. Strudel drain and strudel scour data were obtained from studies conducted on behalf of the petroleum industry. Ice road locations provided in the geodatabase were derived from both industry data and the aforementioned satellite imagery. Access to the data granted by the industry sponsors is gratefully acknowledged. The source data used for each of these components are described below.

6.1 Satellite Imagery

Satellite imagery served as the primary data source for the overflood boundary geodatabase developed for the 2009 Study (Hearon *et al.*, 2009). Overflood boundaries also have been mapped using satellite imagery on numerous occasions to support oil and gas development (DF Dickins *et al.*, 1999; CFC, 2014). While visible satellite imagery has been widely used to document river overflood, SAR imagery was not used extensively prior to the 2009 Study.

The number of satellite platforms providing high-resolution open and free imagery has increased since the original 2009 Study. In addition, the retrieval of useful images has been simplified by the proliferation of browsable online archives such as the USGS Earth Explorer, European Space Agency's (ESA) Copernicus Hub, and National Aeronautics and Space Administration's (NASA) Worldview. Similarly, SAR data (which traditionally necessitated advanced post-processing) have become more user-friendly thanks to institutions such as the NASA-sponsored Alaska Satellite Facility Distributed Active Archive Center (ASF DAAC), which processes raw SAR data into analysis-ready products on demand.

Several satellite platforms active during the 2008–2020 study period were evaluated to identify imagery datasets well-suited for overflood mapping. The investigation was limited to missions providing imagery under user agreements that allow open and free access for research, commercial, and personal use. Both optical and SAR instruments were considered. Satellite platforms were evaluated based on their product specifications: product type, period of record, spatial resolution, repeat cycle, and coverage of the study area. Following a literature review, seven earth observation programs were identified as potential sources of imagery for the current study. The image platforms are summarized below, with additional details provided in **Appendix A**.

- <u>MODIS</u>: The MODIS sensor is onboard the NASA Terra and Aqua satellites, which were launched in 1999 and 2002, respectively. The sensor has a viewing swath width of 2,330 km, a maximum spatial resolution of 250 m, and a daily repeat cycle (NASA, 2021a). The optical sensor is unable to penetrate cloud cover.

- <u>Landsat</u>: Three Landsat satellites provide coverage of the study area (USGS, 2021b) during the period of this investigation: Landsat 5 (1984-2013; USGS, 2021c), Landsat 7 (1999-present; USGS, 2021d), and Landsat 8 (2013-present; USGS, 2021e). Landsat 7 and 8 carry comparable optical and thermal infrared sensors and produce a scene size of 185 km x 180 km with a typical spatial resolution of 30 m. Each satellite has a 16-day repeat cycle. Unfortunately, since June 2003 the Enhanced Thematic Mapper (ETM+) sensor onboard Landsat 7 has acquired and delivered data with gaps caused by the Scan Line Corrector failure. As a result, Landsat 7 scenes only have 78% of their pixels remaining. Landsat 5 carried the Multispectral Scanner (MSS) and the Thematic Mapper I sensors, and produced imagery products similar to those of Landsat 7 and 8 in terms of resolution, swath, overlap, and repeat cycle. The optical sensor is unable to penetrate cloud cover.

- Sentinel: The Sentinel-1 (2014-present; ASF DAAC, 2021a) and Sentinel-2 (2015-present; USGS, 2021f) missions were launched by the ESA. Sentinel-1 includes twin polar-orbiting satellites that each carry C-band SAR that is able to penetrate cloud cover and is insensitive to darkness. The combined repeat cycle of Sentinel-1 is six days. Sentinel-2 includes twin satellites with multispectral high-resolution imaging sensors, which are unable to penetrate cloud cover. The combined repeat cycle of Sentinel-2 is five days.

- Resourcesat-2A: The ISRO launched Resourcesat-2A in 2016 (USGS, 2021g). The satellite acquires imagery in four spectral bands ranging from Visible and Near-Infrared (VNIR) to Shortwave Infrared (SWIR) wavelengths. The orbital swath width of the open access products ranges from 140 to 740 km, with spatial resolutions of 24 to 56 m. The repeat cycle ranges from 5 to 24 days, depending on the sensor. The optical sensor is unable to penetrate cloud cover.

- Advanced Land Observing Satellite (ALOS): The ALOS mission was sponsored by the Japanese Aerospace Exploration Agency (JAXA) and operative between 2006 and 2011 (JAXA, 2021a). The Phased Array Type L-band Synthetic Aperture Radar (PALSAR) provides cloud-free and day-and-night land observation, and offers products with swath widths ranging from 30 to 350 km and spatial resolutions ranging from 10 to 100 m. The repeat cycle is 46 days (with a sub-cycle of two days for event monitoring).

- European Remote Sensing (ERS): The ESA provides high-resolution imagery obtained in Image Mode by the SAR instrument onboard the ERS-2 satellite for the period between 1995 and 2011 (ESA, 2021a). The three-day repeat cycle provides products with a 100 m swath width and 26 m spatial resolution. The sensor is insensitive to cloud cover or darkness.

- Visible Infrared Imaging Radiometer Suite (VIIRS): Imagery obtained by VIIRS instruments developed by NOAA has been readily available for the study area since 2016. However, this platform was excluded from further consideration due to its resemblance to MODIS imagery.

A summary of the selected imagery types and their availability during the study period is provided in **Table 3**. MODIS and Landsat 7 are the only platforms available for the entire period. As indicated above, however, the utility of Landsat 7 is hindered by the 16-day repeat cycle and the image degradation resulting from the Scan Line Corrector failure in 2003. In terms of satellite imagery availability, the study period can be divided into two eras separated by a transition period:

- 2008–2011, SAR-Dominated Era: Characterized by a paucity of high-resolution optical imagery (Landsat 5 and 7 only), but an abundance of SAR scenes (ALOS PALSAR and ERS-2).

- 2012–2016, Transition Period: Transition period between the decommissioning of the ALOS and ERS SAR missions and the launch of the new generation of high-resolution multispectral imagery platforms. Other than MODIS, only Landsat 7 and 8 imagery is available during this time.

- 2017–2020, High-Resolution Optical Era: Recent years are characterized by an abundance of high-resolution multispectral imagery (Sentinel-2, Landsat 7 and 8, Resourcesat-2A). SAR imagery is available through the Sentinel-1 mission, but the temporal resolution is less than that provided by the combination of the ALOS and ERS-2 products during the 2008–2011 period.

Table 3. Availability of selected imagery platforms, 2008–2020

Platform (imagery type)	2008	2009	2010	2011	2012	2013	2014	2015	2016	2017	2018	2019	2020
Terra MODIS (optical)	yes	yes	yes	yes	yes	yes	yes	yes	yes	yes	yes	yes	yes
Landsat 8 (optical)	no	no	no	no	no	yes	yes	yes	yes	yes	yes	yes	yes
Landsat 7 (optical)	yes	yes	yes	yes	yes	yes	yes	yes	yes	yes	yes	yes	yes
Landsat 5 (optical)	yes	yes	yes	yes	no	no	no	no	no	no	no	no	no
Sentinel-1 (SAR)	no	no	no	no	no	no	no	yes	no	yes	yes	yes	yes
Sentinel-2 (optical)	no	no	no	no	no	no	no	no	yes	yes	yes	yes	yes
Resourcesat-2A AWiFS (optical)	no	no	no	no	no	no	no	no	no	yes	yes	yes	yes
Resourcesat-2A LISS-3 (optical)	no	no	no	no	no	no	no	no	no	yes	yes	yes	yes
ALOS PALSAR (SAR)	yes	yes	yes	no	no	no	no	no	no	no	no	no	no
ERS-2 (SAR)	yes	yes	yes	yes	no	no	no	no	no	no	no	no	no
Total Number of Sources of Imagery	**5**	**5**	**5**	**4**	**2**	**3**	**3**	**4**	**4**	**7**	**7**	**7**	**7**

[1] yes = Imagery available, no = Imagery not available.

A detailed assessment was conducted to determine the relative strengths and weaknesses of each platform for mapping overflood features. The assessment was based on image resolution (higher resolution is preferred), computational requirements (smaller file size is preferred), usability (GIS-ready format is preferred), and, in the case of SAR data, processing level (Level-1 Ground Range Detected (GRD) or Single Look Complex (SLC) is preferred over raw Level-0 products). The results of the assessment are as follows:

- The most suitable product for overflood mapping is MODIS imagery. The strength of MODIS resides in the combination of its daily repeat cycle and wide acquisition swath.
- After MODIS images, the most useful products are Resourcesat-2A AWiFS images. Their main advantage over other imagery types is a large swath width (740 km), which captures the entire study area in one or two scenes.
- Resourcesat-2A Linear Imaging Self-Scanning Sensor 3 (LISS-3), Sentinel-2, and Landsat 5, 7, and 8 images were found to be essentially interchangeable in terms of suitability for this project. These images have higher resolution than Resourcesat-2A AWiFS scenes, but a considerably

smaller swath width (under 200 km). The strength of these five platforms resides in the frequency of imagery within the combined dataset.

- Landsat 7 imagery is included in the above group, but the missing data strips present in Landsat 7 products since 2003 can make interpretation challenging. Nevertheless, they do provide important information for the years prior to the deployment of the Sentinel and Resourcesat satellites.

- ALOS Advanced Visible and Near Infrared Radiometer type 2 (AVNIR-2) imagery was discarded due to the very limited number of scenes available for the study area.

- In recent years, the proliferation of high-resolution imagery in the visible spectrum has greatly reduced the need for SAR imagery to study the overflood process. If cloud cover is not total and persistent for an extended period, the overflood extent can be derived from the former with a high level of confidence. However, SAR imagery continues to play an essential role in particularly cloudy overflood seasons.

- ALOS PALSAR and ERS-2 images were found to be extremely useful by virtue of their combined repeat cycle between 2008 and 2010 (prior to the launch of new generation satellites).

- Sentinel-1 SAR products share similar characteristics with ALOS PALSAR and ERS-2 images, but do not overlap in time. As a result, their usefulness is hindered by their lower frequency.

Based on the foregoing evaluation and experience monitoring overflood processes for petroleum industry operators on the North Slope of Alaska during the last decade, MODIS was selected as the cornerstone of the current study. Notwithstanding MODIS' relatively low resolution and inability to penetrate cloud cover, the imagery is sufficient to provide either an accurate representation of peak overflood extent (in cloudless conditions) or a basic understanding of the overflood timing and magnitude (in cloudy conditions).

Supplemental imagery was used to refine the overflood boundaries derived from the MODIS scenes, map overflood boundaries in those cases when the use of MODIS imagery was precluded due to dense cloud cover, capture fine details that are not well imaged in MODIS scenes, and investigate the possible impacts of small features on the overflood process (*e.g.*, ice roads and cracks). The supplemental imagery included both optical and SAR products derived from the earth observation missions listed above. The variability in available scenes from the supplementary data sources (**Table 3**) highlights the value of MODIS imagery, which covers the entire study period and provides a consistent dataset against which other images can be interpreted.

An overview of each platform is provided in **Table 4**, along with the number of scenes downloaded for this study. The downloaded scenes generally cover the period from May 1st to June 30th. It should be noted that the geodatabase contains only those images used to map the final overflood boundaries, which represents a small subset of the imagery listed in **Table 4**.

Table 4. Selected satellite platforms and imagery types

Satellite Platform	Terra (MODIS)	Landsat 8	Landsat 7	Landsat 5
Years	2008–2020	2013–2020	2008–2020	2008–2011
Data Originator	NASA	NASA	NASA	NASA
Data Provider	NASA	USGS	USGS	USGS
Download Site	NASA Worldview Snapshots	USGS EarthExplorer	USGS EarthExplorer	USGS EarthExplorer
Type	Optical	Optical	Optical	Optical
Products	**Terra MODIS True Color Corrected Reflectance Images:** JPEG + Worldfile format 250-m spatial resolution Daily images May 1st–June 31st (61 per year, 793 in total) and **Terra MODIS 7-2-1 Corrected Reflectance Images:** JPEG + Worldfile format 250-m spatial resolution Daily images May 1st–June 31st (61 per year, 793 in total)	**LandsatLook Collection 1 Natural Color Images:** GeoTIFF format 170 km x 183 km tiles 30-m spatial resolution 2013: 58 scenes 2014: 58 scenes 2015: 59 scenes 2016: 54 scenes 2017: 47 scenes 2018: 54 scenes 2019: 94 scenes 2020: 32 scenes Total: 456 scenes	**LandsatLook Collection 1 Natural Color Images:** GeoTIFF format 170 km x 183 km tiles 30-m spatial resolution 2008: 36 scenes 2009: 69 scenes 2010: 38 scenes 2011: 48 scenes 2012: 69 scenes 2013: 47 scenes 2014: 58 scenes 2015: 43 scenes 2016: 78 scenes 2017: 0 scenes 2018: 0 scenes 2019: 0 scenes 2020: 0 scenes Total: 486 scenes	**LandsatLook Collection 1 Natural Color Images:** GeoTIFF format 170 km x 183 km tiles 30-m spatial resolution 2008: 75 scenes 2009: 83 scenes 2010: 19 scenes 2011: 42 scenes Total: 219 scenes
Notes	Worldview Snapshots allows user-defined download bounds for MODIS imagery. The downloaded scenes, which cover the entire study area, are bounded by the 69°N and 72°N parallels and the 157°W and 141°W meridians.		Due to the abundance of higher-quality imagery sources during the period 2017-2020, Landsat 7 scenes were only acquired for those years when the overflood extents could not be adequately characterized using the remaining imagery types.	-

(continued on next page)

Table 4. Selected satellite platforms and imagery types (continued)

Satellite Platform	Sentinel-2	Resourcesat-2A	Sentinel-1	ALOS	ERS-2
Years	2016-2020	2017-2020	2015, 2017-2020	2008-2010	2008-2011
Data Originator	ESA	ISRO	ESA	JAXA	ESA
Data Provider	USGS	USGS	ASF DAAC (NASA)	ASF DAAC (NASA)	ASF DAAC (NASA)
Download Site	USGS EarthExplorer	USGS EarthExplorer	ASF Vertex	ASF Vertex	ASF Vertex
Type	Optical	Optical	SAR	SAR	SAR
Products	**Level-1C Full Resolution Browse Images:** GeoTIFF format 100 km x 100 km tiles 20-m spatial resolution 2016: 29 scenes 2017: 102 scenes 2018: 99 scenes 2019: 136 scenes 2020: 51 scenes Total: 417 scenes	**AWiFS Full Resolution Browse Images:** GeoTIFF format Swath Width 740 km 56-m spatial resolution 2017: 33 scenes 2018: 26 scenes 2019: 29 scenes 2020: 25 scenes Total: 113 scenes and **LISS-3 Full Resolution Browse Images:** GeoTIFF format Swath Width 140 km 24-m spatial resolution 2017: 23 scenes 2018: 18 scenes 2019: 29 scenes 2020: 13 scenes Total: 83 scenes	**Level-1 Interferometric Wide Swath SLC/GRD Images:** GeoTIFF format Swath Width 250 km 30-m spatial resolution 2015: 3 scenes 2017: 47 scenes 2018: 43 scenes 2019: 51 scenes 2020: 39 scenes Total: 183 scenes	**PALSAR Level-1.5/RTC Images, various beam modes:** CEOS/GeoTIFF format Swath and spatial resolution depending on beam mode 2008: 51 scenes 2009: 42 scenes 2010: 23 scenes Total: 116 scenes	**Level-1 Standard Mode SAR Images:** CEOS format 100 km x 100 km tiles 12.5-m spatial resolution 2008: 31 scenes 2009: 40 scenes 2010: 34 scenes 2011: 26 scenes Total: 131 scenes
Notes	-	Resourcesat imagery exists for the period 2011-2016, but it is not publicly available. A fraction of all Resourcesat scenes hosted by the USGS had to be discarded due to inaccurate georeferencing.	Out of data storage and handling considerations, Sentinel-1 SAR imagery was not used when the maximum overflood extents could be adequately assessed using optical images.	Out of data storage and handling considerations, ALOS PALSAR SAR imagery was not used when the maximum overflood extents could be adequately assessed using optical images.	Out of data storage and handling considerations, ERS-2 SAR imagery was not used when the maximum overflood extents could be adequately assessed using optical images.

6.2 Helicopter-Mapped Overflood Boundaries

Between 1996 and 2020, CFC conducted field studies related to overflood processes for various industry sponsors operating on the North Slope of Alaska. A primary objective of these studies was to document strudel scour characteristics in order to establish design criteria for proposed subsea pipelines or to monitor the integrity of existing subsea pipelines. The maximum overflood boundary was mapped at each project site as part of these studies, along with strudel drainage feature and scour information (discussed in **Section 6.3**).

Most overflood field studies completed between 1996 and 2020 were conducted via helicopter. Helicopters provide an ideal platform from which to map the locations of the overflood boundary and strudel drains on the sea ice due to their ability to operate at a variety of altitudes safely and hover over features of interest. While the equipment used to conduct the work has improved over the past two decades, the general approach has remained the same.

The helicopter missions were conducted near the end of the overflood period, rather than at its peak, to ensure that the maximum extent of the flood was documented. Mapping was performed using a survey-grade Global Positioning System (GPS) receiver installed in an overhead window of the aircraft. Beginning in 2005, the GPS receiver was interfaced with a laptop computer and navigation software which displayed a map of the region to allow the survey crew to view the aircraft's position relative to coastal landmarks in real-time.

Prior to 2004, the surveys were conducted with the GPS operated in autonomous mode, resulting in a horizontal accuracy of approximately 100 m. In 2000, the U.S. Government discontinued Selective Availability, thereby increasing the accuracy of autonomous positions to approximately 7 m (Milbert, 2001). Commencing in 2004, differential corrections broadcast in real-time via the Wide Area Augmentation System (WAAS) were used. Position checks conducted on the North Slope of Alaska by CFC have indicated that the accuracy of WAAS-corrected horizontal positions is 1 to 3 m. The higher accuracy attainable with a kinematic solution was judged to be unwarranted due to the imprecision inherent in mapping features on the ice from a helicopter hovering overhead.

The offshore boundary of the river overflood on the sea ice was delineated by recording successive positions with the GPS receiver while flying over the observed boundary at altitudes of 30 to 200 m and a speed of approximately 60 knots. Although mapping often was conducted after the flood waters had started to drain or retreat, evidence of the seaward extent of the overflood limit typically was identifiable by sediment-laden water or discolored ice on the inshore side of the boundary. Evidence of strudel drainage also was apparent inside the overflood boundary. In contrast, the ice offshore of the overflood boundary generally was a pristine white or blue color with areas of snow cover. **Figure 16** shows a well-defined overflood boundary off the Sagavanirktok River on May 24, 2014.

In cases where the overflood limit was difficult to discern during the initial flight path, additional mapping was conducted from the opposite direction or at different altitudes. On occasions when the boundary was mapped multiple times, a single merged boundary was created based on field notes and observations (including mapping confidence and flight precision).

A summary of the available overflood boundaries is provided in **Table 5**.

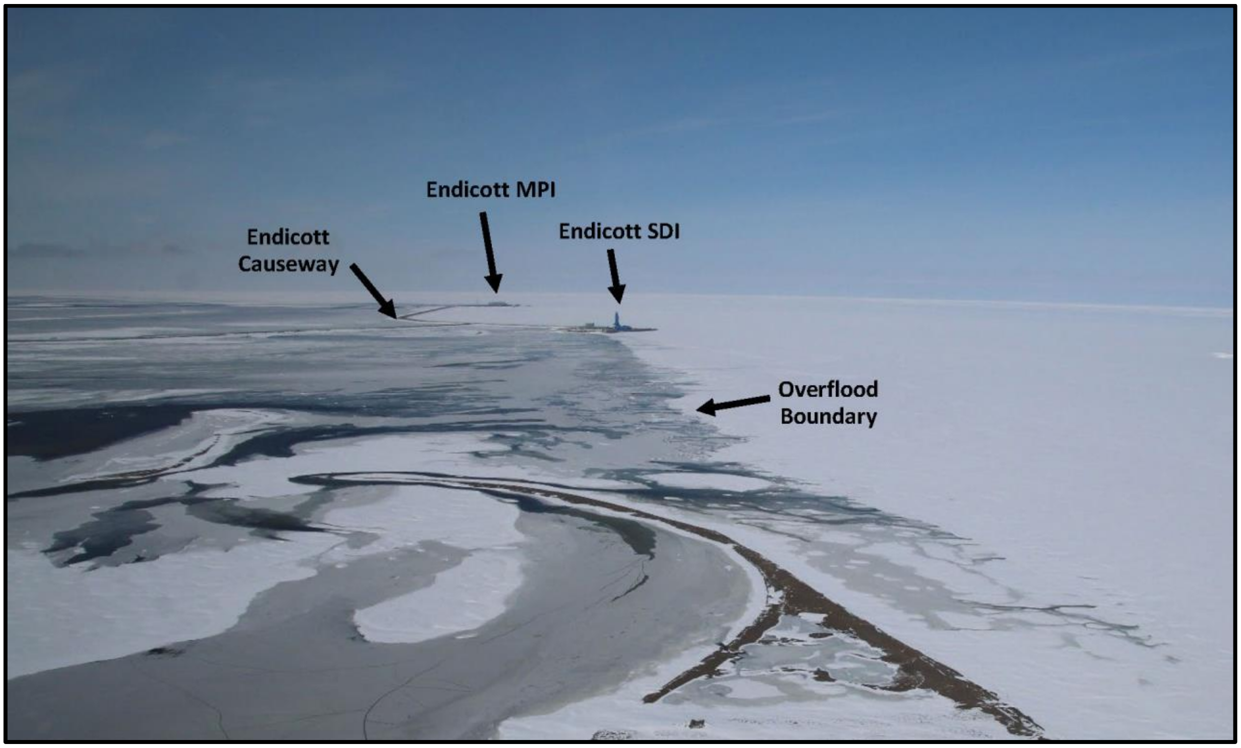

Figure 16. Overflood boundary in Sagavanirktok River Delta, 2014

6.3 Strudel Scour Data

The industry studies described in **Section 6.2** typically included mapping the location of strudel drainage features in the sea ice and determining strudel scour characteristics within pre-selected areas of interest (usually associated with a proposed or existing subsea pipeline and/or offshore facility). Strudel drains were mapped during the same helicopter-based reconnaissance mission used to document overflood boundaries (**Section 6.2**), while strudel scours were mapped during the open-water season using a sonar-equipped vessel.

The location of each strudel drain was recorded while hovering directly over the feature of interest. The type of drain (circular drain, short crack [less than 16 m long], or long crack [at least 16 m long]) and approximate size (diameter of circular drains and length of crack drains) also was recorded. In 2016 and 2017, drainage feature mapping in Simpson Lagoon was conducted via hovercraft because a helicopter was not available. The mapping methodology was similar to that used for the helicopter; however, the lower vantage point made detection of the strudel drains more difficult.

During the open-water season following the helicopter- or hovercraft-based mapping mission described above, the seabed in the vicinity of the mapped drainage features was investigated to determine if a strudel scour had formed. A strudel scour found on the seafloor at one of the drainage sites was assumed to have been formed that year. Scours also were discovered at some locations where drainage features had not been mapped during the spring reconnaissance. These scours were either relic features formed during a prior overflood event or created by a drainage feature that escaped detection during the overflight.

The characteristics of each scour were measured using a combination of multibeam sonar, single-beam sonar, and side scan sonar systems operated in concert with GPS positioning. When possible, the location, water depth, scour depth, maximum horizontal dimension, and type of feature (circular or linear) was recorded. The coordinates of the deepest point of the scour were logged as the feature location. The scour depth was measured relative to the ambient sea bottom. The maximum horizontal dimension of each circular scour refers to the largest horizontal extent measured at the elevation of the surrounding sea bottom (*i.e.*, the diameter of a perfectly circular scour or the major axis of an oblong scour), while the maximum horizontal dimension of each linear scour refers to the total length measured along the scour orientation.

The absolute accuracy of each depth measured with the multibeam and single-beam sonar system is approximately ±0.15 m. The accuracy with which the depth of a strudel scour can be determined relative to the ambient seafloor depends only on the measurement uncertainty, and is estimated to be ±0.06 m. The estimated accuracy of horizontal dimensions measured with the multibeam and single-beam sonar system is 1.0 m.

CFC requested and obtained authorization to utilize the field data obtained from 2008 to 2020 on behalf of Hilcorp Energy Company (Hilcorp), BP Exploration Alaska (BPXA), Caelus Energy (Caelus), Shell Oil Company (Shell), and one anonymous Alaska North Slope Operator. These data were incorporated into the geodatabase, along with those data included in the 2009 Study. The resulting data set encompasses the 25-year period between 1996 and 2020. A summary of the data for the 2008 to 2020 period is summarized in **Table 5,** with additional details provided in **Table 6**.

Table 5. Summary of industry-sponsored overflood and strudel scour field data, 2008–2020

Year	Ikpikpuk River	Colville River	Simpson Lagoon	Kuparuk River	Sag., Kad., and Shav. Rivers	Staines River
2008		Overflood + Scour		Overflood + Scour		Overflood + Scour
2009		Overflood + Scour		Overflood + Scour		Overflood
2010		Overflood + Scour	Overflood + Scour	Overflood + Scour		Overflood + Scour
2011		Overflood + Scour		Overflood + Scour		
2012		Overflood + Scour		Overflood + Scour		
2013		Overflood + Scour		Overflood + Scour	Overflood + Scour	
2014		Overflood + Scour	Overflood + Scour	Overflood + Scour	Overflood + Scour	
2015		Overflood + Scour		Overflood + Scour	Overflood + Scour	
2016	Overflood	Overflood + Scour	Overflood + Scour	Overflood + Scour	Overflood + Scour	
2017		Overflood + Scour	Overflood + Scour	Overflood + Scour	Overflood + Scour	
2018		Strudel Scour				
2019		Overflood + Scour	Overflood + Scour	Strudel Scour		
2020		Strudel Scour	Strudel Scour	Strudel Scour		

Notes:
1. Blank cells indicate no field study conducted.
2. “Overflood” indicates overflood extent and strudel drains were mapped.
3. “Strudel Scour” indicates strudel scours were mapped.
4. “Overflood + Scour” indicates overflood extent, strudel drains, and strudel scours were mapped.
5. Sag. = Sagavanirktok, Kad. = Kadleroshilik, Shav. = Shaviovik

Table 6. Number of features mapped as part of industry-sponsored field studies, 2008–2020

Project	Data Provider	Years	Major Rivers	Overflood Boundaries	Strudel Drains	Strudel Scours
Tulimaniq Prospect	Caelus	2016	Ikpikpuk River	1	101	n/a[1]
AK North Slope Development	Confidential	2008–2020	Colville River	11	422	251
AK North Slope Development	Confidential	2009–2020	Colville and Kuparuk Rivers	5	36	20
Northstar Development	BPXA / Hilcorp	2008–2020	Kuparuk River	10	339	224
Liberty Prospect	BPXA / Hilcorp	2013–2017	Sagavanirktok, Kadleroshilik, and Shaviovik Rivers	5	500	549
Sivulliq Prospect	Shell	2008, 2010	Canning and Staines Rivers	2	34	38

[1] Strudel Scour Data not obtained as part of Tulimaniq Field Program.

6.4 Ice Roads

As noted in **Section 4.1**, ice roads can influence the distribution of flood water on the sea ice. To aid in interpreting the overflood boundaries, the locations of offshore ice roads constructed each year within the study area were incorporated in the geodatabase. The ice road locations were derived primarily from records provided by the various industry sponsors. However, in selected cases, when the presence of an offshore ice road was clearly visible in the satellite imagery, the road was mapped and added to the geodatabase. The number of features added to the geodatabase from 2008 to 2020 is shown in **Table 7**.

Table 7. Ice road data availability, 2008–2020

Year	No. Ice Roads	Year	No. Ice Roads
2008	7	2015	4
2009	4	2016	4
2010	3	2017	3
2011	4	2018	3
2012	3	2019	4
2013	3	2020	3
2014	3	**Total**	**48**

Figure 17 and **Figure 18** illustrate the locations of the 48 ice roads cataloged between 2008 and 2020. The majority of the ice roads were constructed on the east side of the Colville River, near Oliktok Point in Simpson Lagoon, and east of the Kuparuk River.

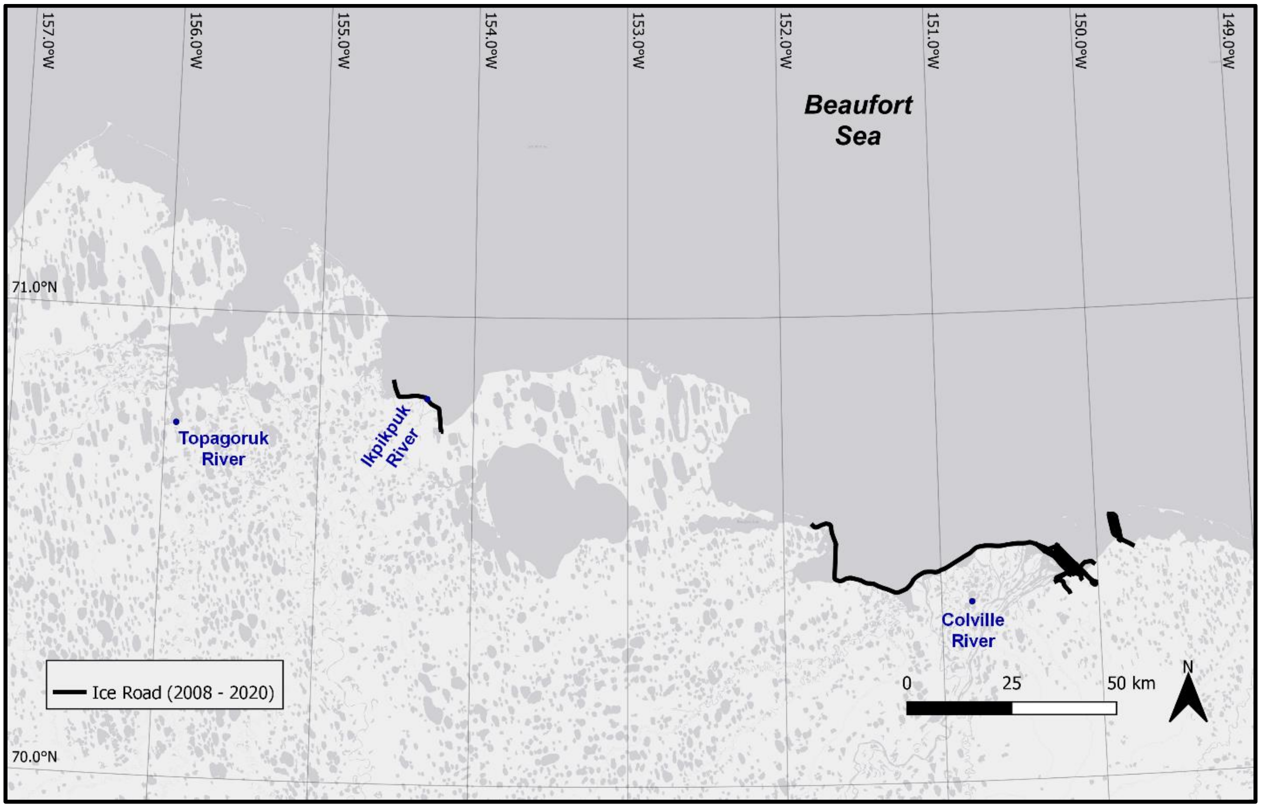

Figure 17. Ice road locations, west study region, 2008–2020

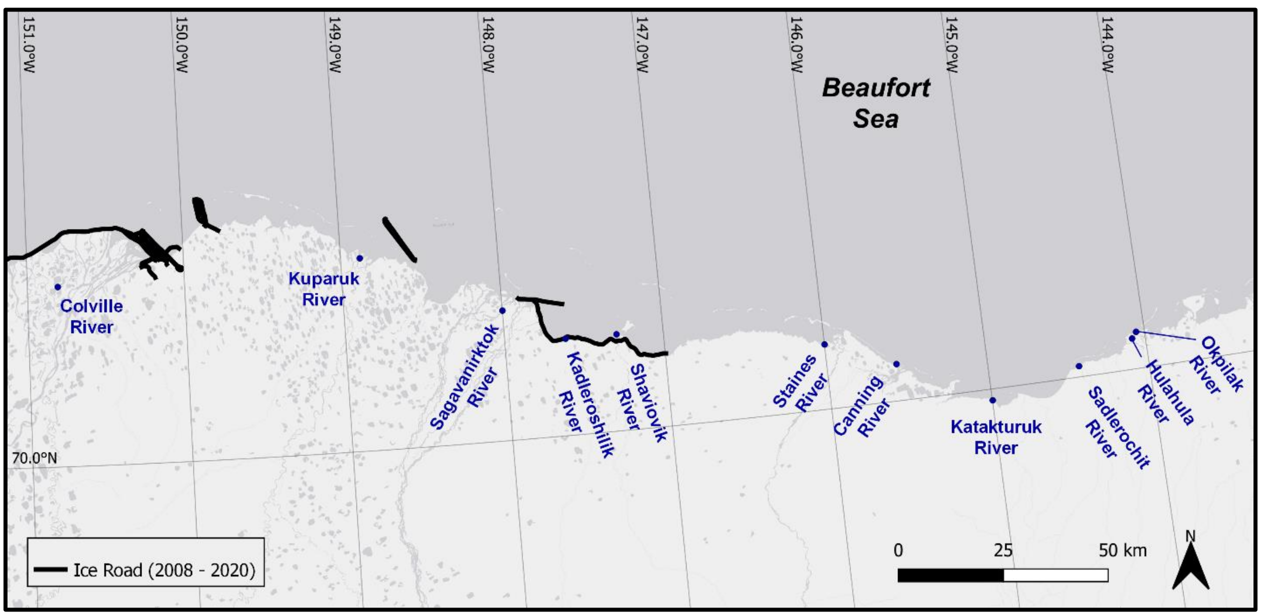

Figure 18. Ice road locations, east study region, 2008–2020

7 Overflood Mapping Methods

The source data described in **Section 6** were used to develop annual overflood boundaries for each watercourse within the study area during the 13-year period between 2008 and 2020. In addition, the boundaries mapped as part of the 2009 Study, covering the years from 1995 to 2007, were updated and/or refined based on newly available information. The sub-sections that follow describe the mapping methods used and the derivative products developed as part of this task.

7.1 Overflood Extent

For each year under consideration, a GIS project was created and all available imagery (**Table 4**) was imported along with polylines representing the helicopter-derived overflood boundary (**Table 5**). For each watercourse in the study area, the maximum offshore extent of the flood waters was mapped using the following procedure:

- MODIS imagery was screened to determine the approximate dates on which the flood waters reached the coast (start of overflood) and their maximum offshore extent (peak of overflood). This is illustrated in **Figure 19**. High-resolution imagery (*e.g.*, Resourcesat-2A AWiFS, Sentinel-2) were evaluated during this period, and adjustments were made to the start and peak overflood dates, as needed.
- Suitable imagery obtained from each satellite platform near the peak overflood date was identified and loaded into a GIS utility (QGIS).
- The maximum overflood extent was mapped on each image by tracing a polyline along the maximum overflood extent and clipping the polyline where it intersected the U.S. Beaufort Sea Coast. This is illustrated in **Figure 20A**.
- A composite polyline was generated for each year using all available satellite- and helicopter-derived overflood extents for the watercourse. Preference was given to those polylines derived from scenes acquired near the peak overflood date with high resolution and clear conditions, or those mapped from helicopter surveys. While the helicopter-derived overflood extents generally are considered to be more accurate than those derived from satellite imagery, exceptions were made in areas where fine details were not feasible to map using the aircraft, in areas noted as low confidence during the flights, or when it was known that the mission was conducted prior to or well after the peak overflood. Development of the final composite boundary is illustrated in **Figure 20B**.
- Closed polygons representing the final composite maximum overflood extent for each watercourse and year were saved in the geodatabase under feature class "*overflood_extent_1995_thru_2020*". The polygons are bound by the composite polylines described above and a polyline representing the U.S. Beaufort Sea Coast. Metadata associated with each feature includes:
    - ***River:*** Name of the river, stream, or creek from which the flood waters originated. When the flood waters from multiple streams merged offshore and could not be accurately assigned to an individual river, all the contributing bodies of water were included. When flood waters of a stream reached an area previously occupied by another stream for which the overflood extent was accurately documented, the overlapping area was assigned to the first stream. The only exception being the Colville, Kuparuk, or Sagavanirktok Rivers, which always took precedence.

- ***Hydrologic Unit:*** Name of the level 8 hydrologic unit (HU8) containing the river, stream, or creek from which the overflood originated. HU8 are those defined by the USGS Watershed Boundary Dataset (USGS, 2021a).
- ***Start Date:*** Overflood start date. Corresponds to the day when river discharge was first detected on the sea ice adjacent to a river mouth. Overflood start dates were only documented when they could be determined with an accuracy of ±2 days (or ±1 day for the Colville, Kuparuk, and Sagavanirktok Rivers).
- ***Peak Date:*** Overflood peak date. Corresponds to the day when the maximum overflood extent was registered. Note that the overflood of major rivers progresses heterogeneously in different directions. As a result, on a given day, the flood water boundary can advance in one region while retreating in another. In these cases, the peak date is defined as the last day during which flood waters advanced anywhere in the region. The overflood peak dates were only documented when they could be determined with an accuracy of ±2 days (or ±1 day for the Colville, Kuparuk, and Sagavanirktok Rivers).
- ***Area:*** Area, in square kilometers, covered by the flood waters when the maximum overflood extent occurred. The area was computed for each item in feature class *overflood_extent_1995_thru_2020* using QGIS. The projection used for the area calculation is Universal Transverse Mercator (UTM) Zone 5N, relative to NAD83, with units of meters (EPSG code 26905). The area is ellipsoidal relative to the GRS 1980 ellipsoid and rounded to the nearest square kilometer. Areas less than 0.5 square kilometers are assigned a value of 0.
- ***Confidence:*** Level of confidence attributed to the geometry of the overflood extent. This is a qualitative assessment to describe how well the mapped overflood extent matches the true maximum overflood that occurred for the river, stream, or creek under consideration. The confidence levels are defined as follows:
    - **High:** Clear and abundant satellite imagery or survey data available. High degree of confidence that the derived geometry accurately matches the true maximum overflood extent.
    - **Medium-High:** Mostly clear and abundant satellite imagery or survey data available. High degree of confidence that the derived geometry accurately matches the true overflood extent in most of the region. Uncertainties exist in isolated locations, and/or the overflood edge is diffuse due to light cloud cover.
    - **Medium:** The available satellite imagery and survey data are sufficient to derive a meaningful overflood extent, but in certain areas the linework relies on the interpretation of scarce/flawed data. This is generally the case when cloud cover is present intermittently during the overflood season and limited SAR images are available.
    - **Medium-Low:** The available satellite imagery and survey data are sufficient to derive a meaningful overflood extent, but the linework heavily relies on the interpretation of scarce/flawed data. This is generally the case when abundant cloud cover is present throughout the overflood season and no SAR images are available, or when the overflood extent is very small.
    - **Low (1995-99):** Confidence level reserved for overflood extents from the pre-MODIS era (pre-2000). It reflects the lack of daily data covering the entire study area, which could have resulted in a general underestimation of overflood areas

relative to the MODIS era. Caution must be used when including these data in numerical analysis.

- ***Source:*** Source of the overflood extent data (satellite imagery and/or helicopter surveys).
- ***Imagery:*** List of satellite images used to trace the final overflood extent.

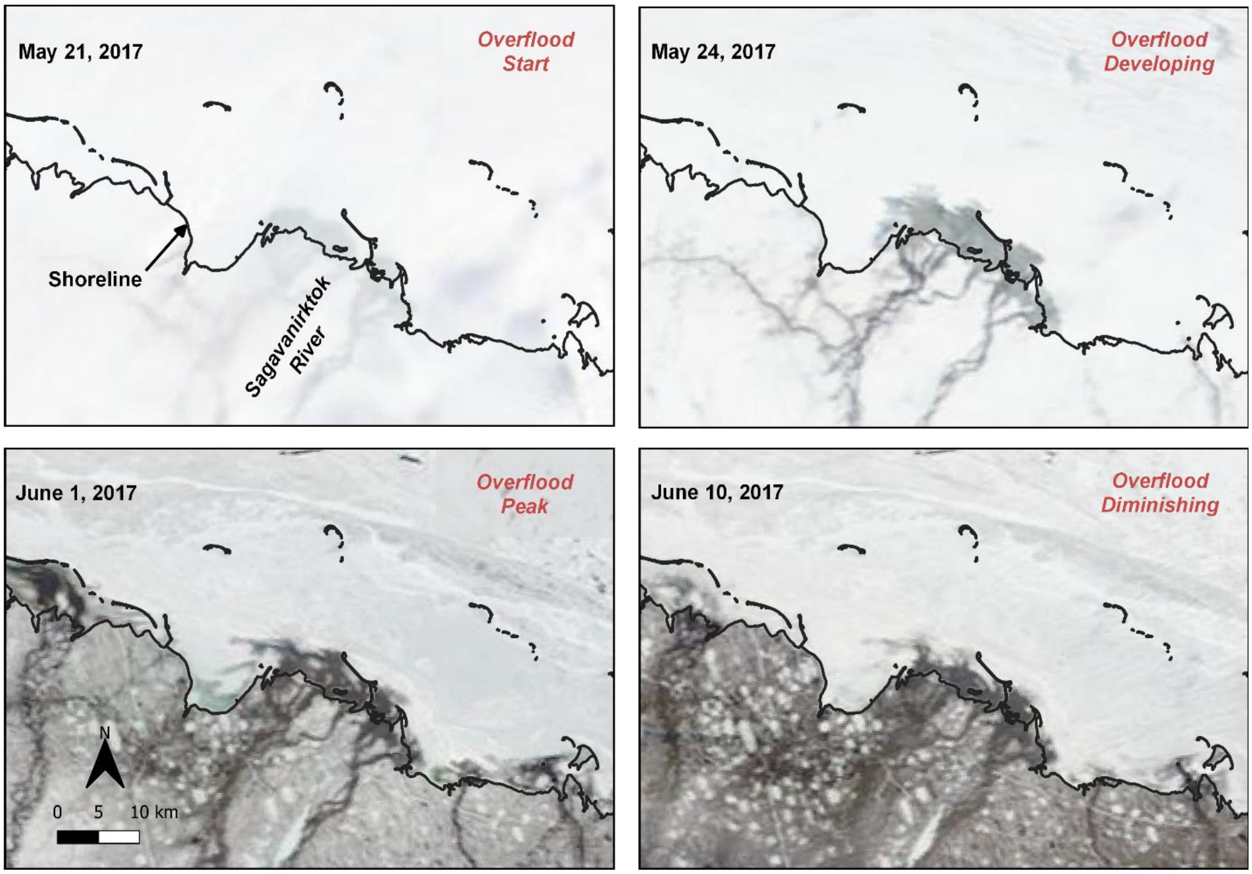

Figure 19. Selection of approximate overflood start and peak dates using MODIS imagery

Once overflood boundaries were mapped for all watercourses in the study area, a single polygon was created representing the maximum overflood extent within the entire study area for each year under consideration using the QGIS "dissolve" command. These polygons were stored in the geodatabase under feature class "*overflood_extent_yearly_envelope_1995_thru_2020*." Attributes associated with this feature class were limited to the feature type ("overflood extent"), year, and area within the polygon.

Finally, a single polygon encompassing all the overflood boundaries mapped between 1995 and 2020 was created using the QGIS "dissolve" command and stored in the geodatabase under feature class "*overflood_extent_maximum_envelope_1995_thru_2020*."

For archival purposes, the geodatabase also contains all helicopter-derived overflood limits (feature class "*overflood_extent_from_field_surveys_1995_thru_2020*" obtained between 1995 and 2020, and the peak overflood extent for various rivers in the study area during overflood seasons pre-dating 1995 (feature class "*overflood_extent_pre_1995*").

(A) Maximum Extent from Satellite Imagery and Helicopter Survey

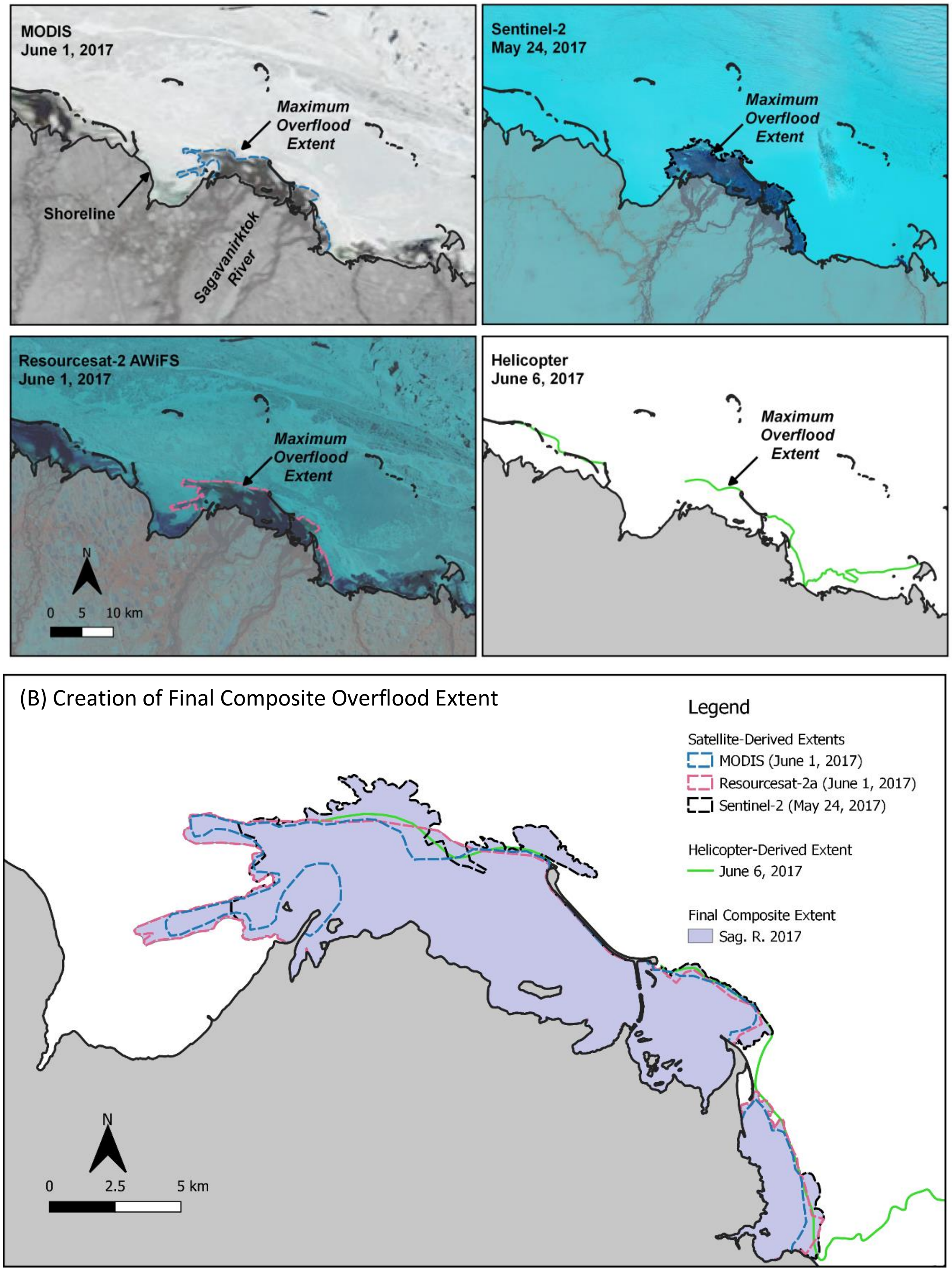

(A) Overflood extent mapped from three satellite platforms and one helicopter survey.
(B) Creation of final composite overflood extent. Final extent encompasses all mapped boundaries, except for two areas on the east side where the helicopter boundary was excluded in the vicinity of the shoreline. Fine details in this vicinity were not feasible to map via helicopter.

Figure 20. Derivation of composite overflood extent from satellite imagery and helicopter survey

7.2 Annual Overflood Occurrence Probability

Isolines of overflood probability were developed using the 21 annual composite overflood extents between 2000 and 2020. The overflood extents from 1995 to 1999 (the pre-MODIS era) were not included, given the paucity of available imagery and uncertainty associated with the overflood edges mapped during this period.

The 21 polygons representing the annual composite overflood extents were converted to raster images with 100 m square cells, all aligned on the same grid. Flooded cells were assigned a value of 1, and dry cells were assigned a value of 0. The raster images were summed, resulting in a single grid where the value of each cell corresponded to the number of years the cell was flooded.

The probability of occurrence was computed by dividing the grid cells by the number of years in the record (21 years, 2000 to 2020) and contours of probability were generated at an interval of 4.76% (1/21). These contours were used to create a second smoothed raster surface, from which probability intervals of 10%, 25%, 50%, 75%, and 90% were developed to provide a representative range of probabilities to the end-user. The 0% contour was taken to be the maximum overflood extent over the period of record (2000 to 2020). Similarly, the 100% contour was taken to be the minimum overflood extent over the same period. **Figure 21** illustrates the contours of overflood probability in the vicinity of Gwydyr Bay.

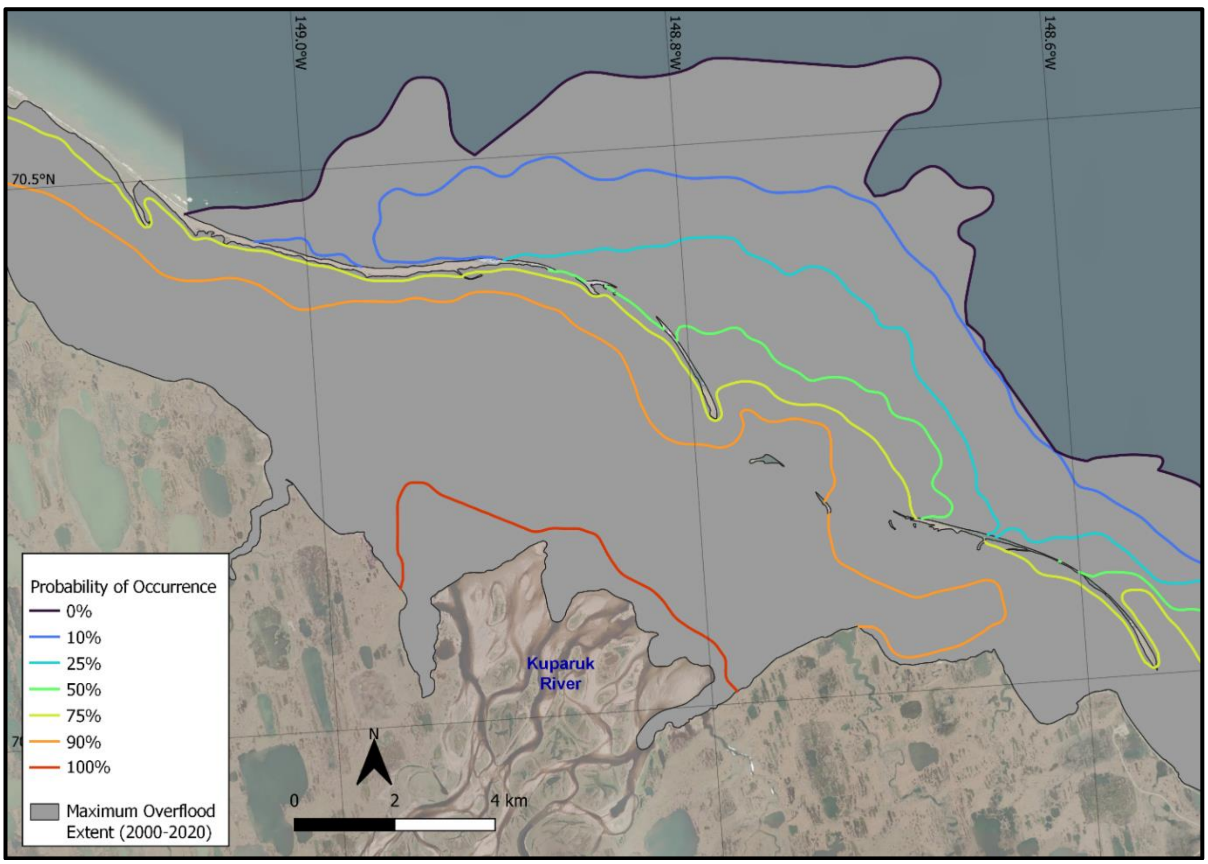

Figure 21. Probability of overflood occurrence, Gwydyr Bay

As discussed in **Section 8**, in 2019 overflood was detected in Admiralty Bay, but not mapped. In this case, the number of years used to compute the probability of occurrence was 20 years, as opposed to 21.

8 Results

8.1 Overflood Boundaries

A total of 274 overflood boundaries were mapped over the 13-year period from 2008 through 2020. In only one case was flood water detected in the available imagery but not mapped. This occurred in 2019 in Admiralty Bay, where the start of overflood was identified, but the available imagery was not sufficient to map the peak overflood extent. To mark this unique case, a feature with no geometry is included in the geodatabase. In all other cases, the absence of an overflood edge during the period between 2008 and 2020 indicates that flood water did not reach the coast at that location.

The peak overflood extents from 1995 to 2007 mapped as part of the 2009 Study were refined, as needed, based on newly available imagery. In addition, overflood boundaries missing from the 2009 Study due to lack of imagery at the time were mapped. **Appendix B** contains 52 figures showing the composite overflood edge for each year in the study period in the eastern and western portions of the study region. Aside from the one instance in 2019 noted above, the overflood edge was mapped for all watercourses in the study area over the 21-year MODIS era (2000 through 2020). Given the paucity of imagery available during the pre-MODIS era (1995 through 1999), it is possible that flood waters were undetected or that the mapped boundaries do not represent the peak overflood extent.

Figure 22 and **Figure 23** show the combined composite overflood boundaries for the west and east portions of the study region, respectively, from 1995 through 2020. The region from Harrison Bay to Brownlow Point is the largest continuous overflood area and encompasses all offshore oil and gas facilities currently operating on the North Slope of Alaska.

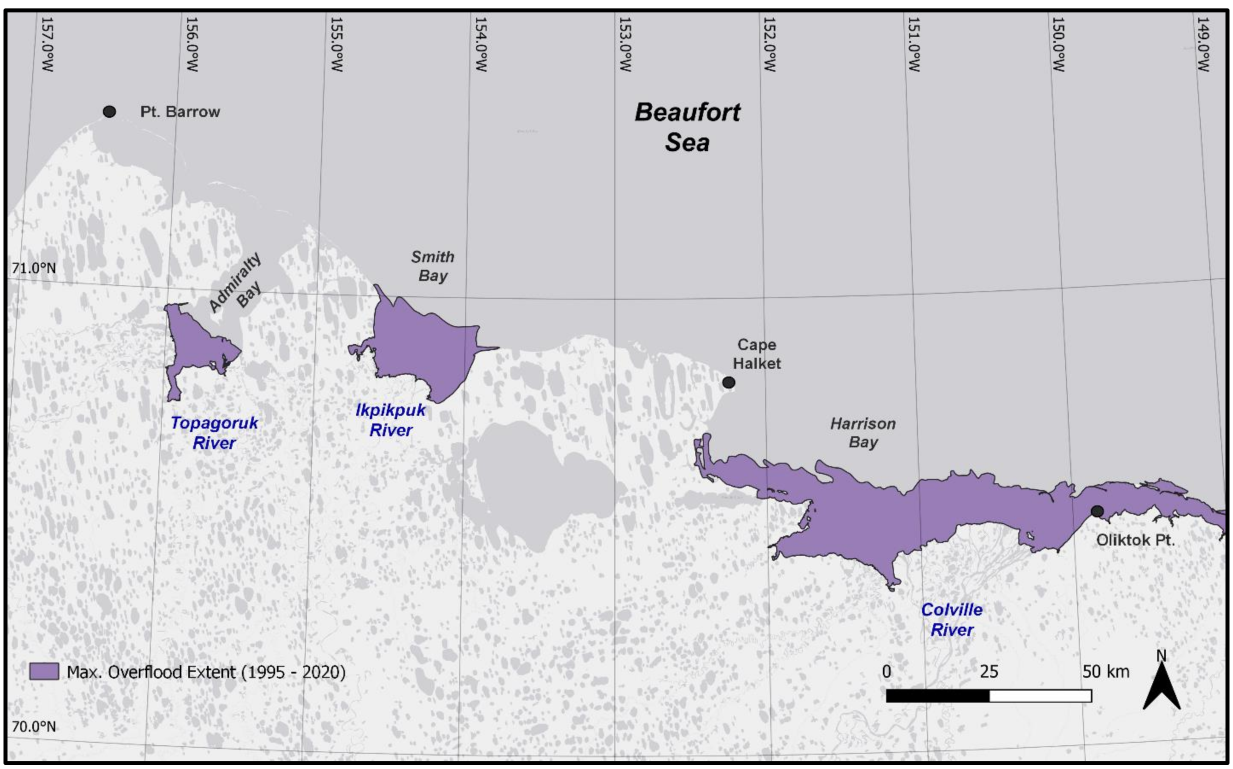

Figure 22. Maximum overflood extent, west study region

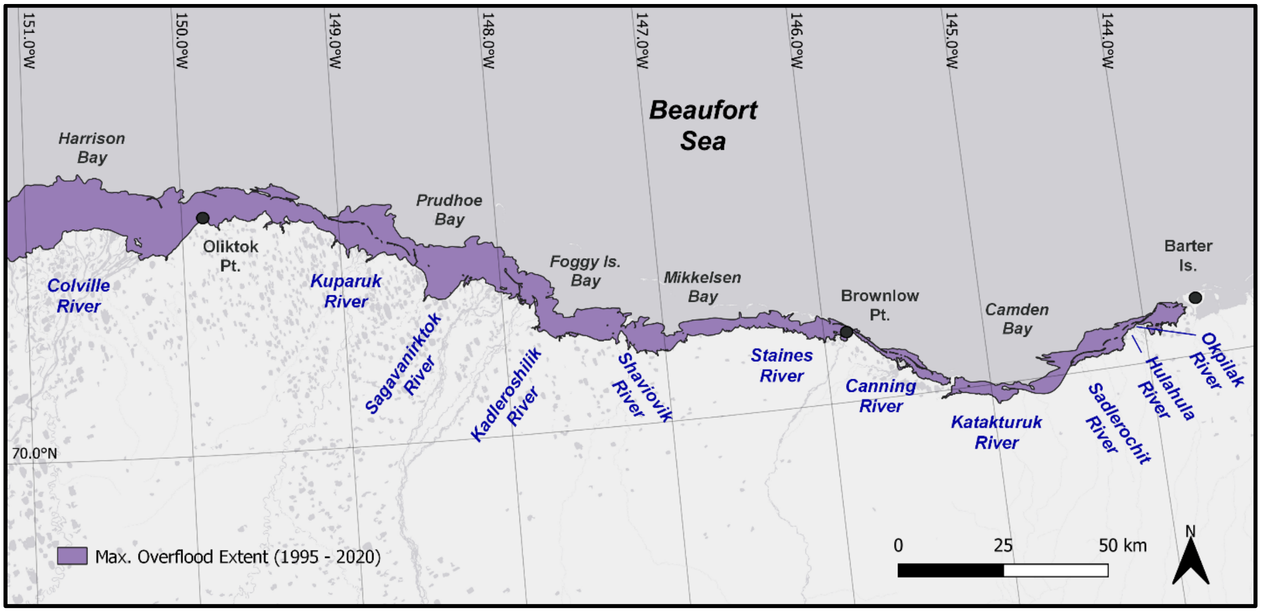

Figure 23. Maximum overflood extent, east study region

Figure 24 and **Figure 25** show the combined composite overflood boundaries segregated by the three strudel scour zones (secondary, primary, and tertiary) discussed in **Section 4.2**. The zones were delineated using bathymetric contours included in the 2009 Study and updated as needed.

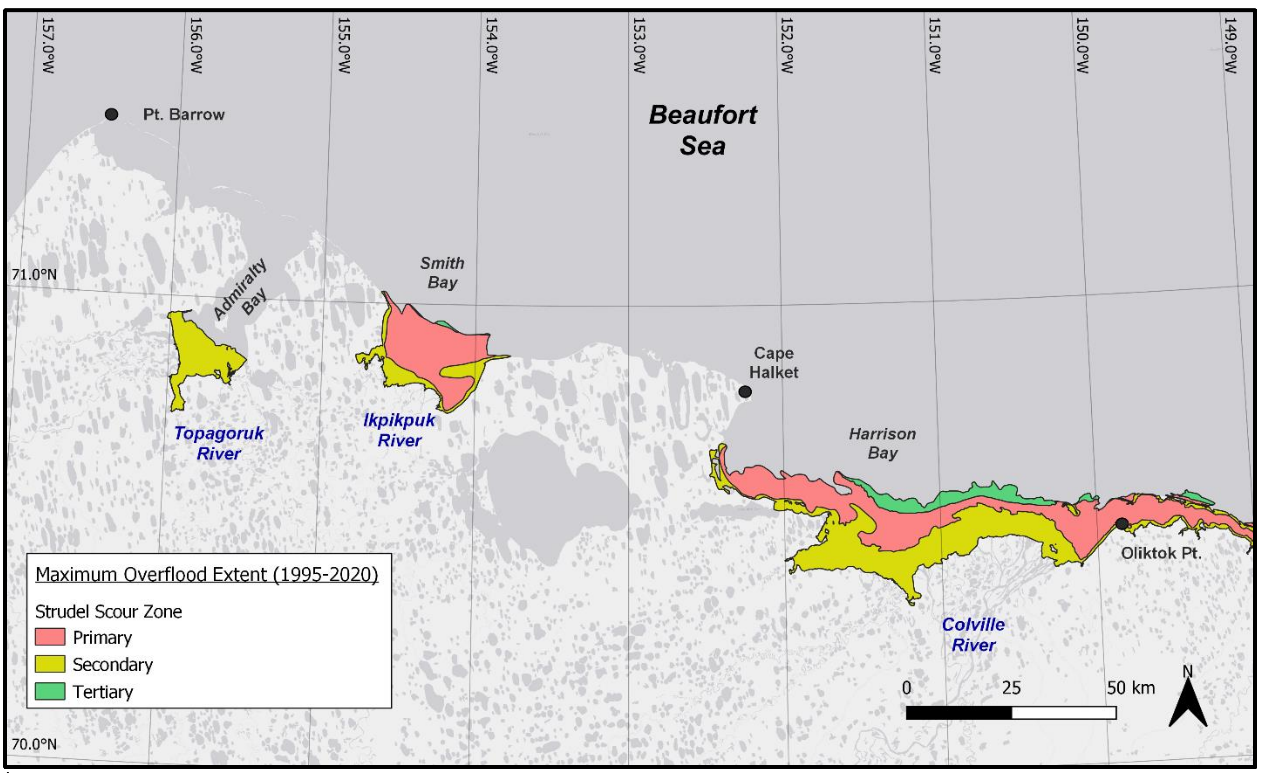

[1] The flooded area of Admiralty Bay is shallower than 1.5 m, resulting in only a secondary strudel zone near the Topagoruk River.

Figure 24. Maximum overflood extent, segregated by strudel scour zone, west study region

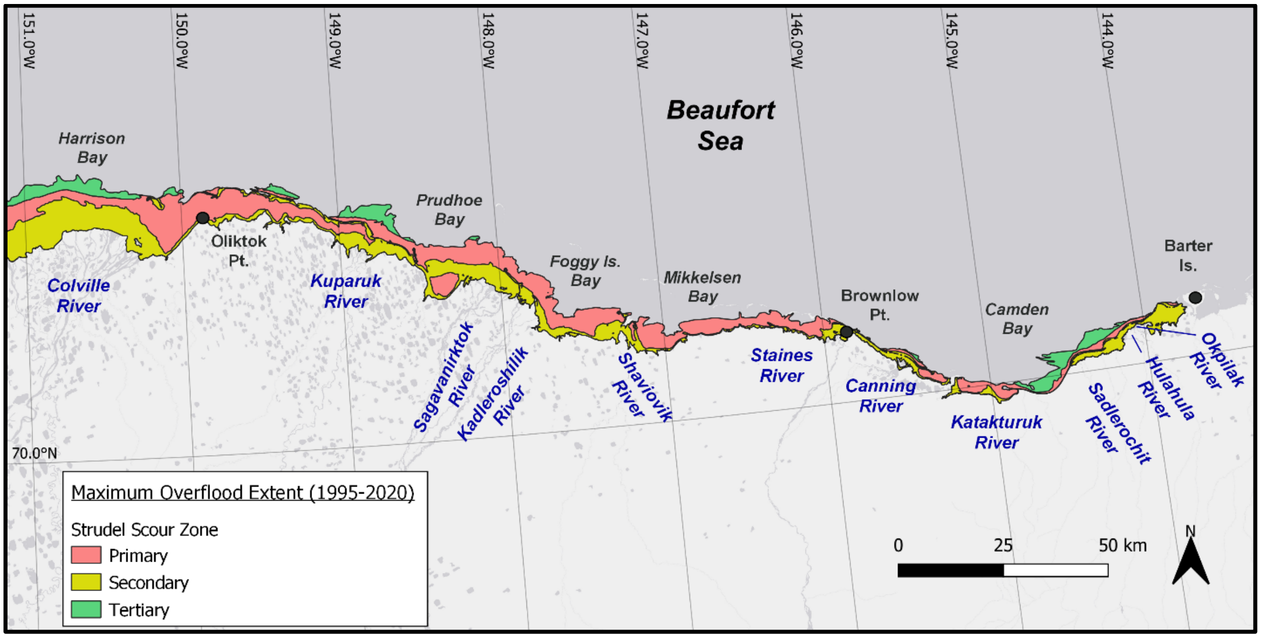

Figure 25. Maximum overflood extent, segregated by strudel scour zone, east study region

8.2 Overflood Area

Figure 26 shows the annual overflood area for each of the 13 major rivers in the study area. In each case, the river designation (**Table 8**) corresponds to the watercourse from which the flood originated. If flood waters originating from a given river reached an area previously occupied by another river, the overlapping area was assigned to the first river. The only exception being that the Colville, Kuparuk, and Sag. Rivers always took precedence (see attribute "River" in feature *overflood_extent_1995_thru_2020*).

The flood area generated by the Colville River is several times larger than any other watercourse in the study area and accounts for 30 to 80% of the total overflood area from all major rivers in a given year. The Kuparuk, Ikpikpuk, and Sagavanirktok Rivers are the next largest contributors; however, the combined contribution from all three of these rivers is typically less than that from the Colville. This is illustrated in **Figure 26**, which shows the relative contribution of each major river in a given year.

Table 9 and **Figure 27** summarize the overflood area associated with each of the USGS WBD within the study area (see attribute "Hydrologic Unit" in feature *overflood_extent_1995_thru_2020*). Similar to that noted above, the largest overflood area is associated with the Lower Colville River WBD. The relatively small increase in overflood areas shown in **Figure 27** reflects the contributions of secondary rivers and minor creeks/streams that are not included when only the major rivers are considered.

8.3 Overflood Timing

The start and peak of overflood are delineated in **Table 10** and **Table 11**, respectively, for each of the thirteen major rivers in the study area. On average, the start of overflood occurred between May 16 (Sag., Sadlerochit, Hulahula, and Okpilak R.) and May 29 (Topagoruk R.). The earliest start occurred on April 23, 2019 at the Sag., Staines, and Canning Rivers, while the latest occurred on June 11, 2000 at the Kadleroshilik and Staines Rivers. On average, the overflood peak occurred between May 25 (Sadlerochit R.) and June 5 (Hulahula and Okpilak R.). The earliest peak occurred on May 16, 2015 and 2016 at the Sadlerochit River. The latest peak occurred on June 20, 2006 at the Hulahula and Okpilak Rivers.

Table 8. Annual overflood area (km^2) for each major river, 1995–2020

Year	Topagoruk River	Ikpikpuk River	Colville River	Kuparuk River	Sag. River	Kad. River	Shaviovik River	Staines River	Canning River	Katakturuk River	Sadlerochit River	Hulahula & Okpilak R.	Total
1995[1]	-	-	738	173	192	-	-	-	29	13	9	-	1,154
1996[1]	-	-	593	90	-	4	26	13	26	-	5	-	757
1997[1]	-	-	485	100	129	10	57	17	30	12	18	41	899
1998[1]	-	4	813	153	155	17	51	34	16	2	5	14	1,264
1999[1]	-	-	483	70	122	12	48	17	16	4	6	23	801
2000	160	295	916	245	153	25	66	25	24	14	9	52	1,984
2001	2	209	869	229	172	21	68	29	30	15	11	44	1,699
2002	No Flood[2]	320	843	237	223	21	66	21	41	27	10	47	1,856
2003	No Flood[2]	113	550	263	129	20	63	10	27	7	12	42	1,236
2004	3	224	1,010	256	227	16	60	27	28	12	10	20	1,893
2005	145	151	767	205	166	13	58	8	34	7	4	16	1,574
2006	119	174	657	237	113	19	53	14	19	6	11	32	1,454
2007	29	134	553	76	127	17	50	43	10	10	15	25	1,089
2008	41	133	717	8	131	25	63	36	26	8	9	13	1,210
2009	7	159	606	233	142	14	60	24	24	15	14	41	1,339
2010	55	187	858	304	161	13	58	12	28	8	11	34	1,729
2011	49	266	592	238	180	11	55	21	31	11	16	58	1,528
2012	121	106	712	137	122	13	56	19	13	7	8	31	1,345
2013	69	117	734	266	180	23	61	35	28	5	11	56	1,585
2014	4	231	314	144	93	32	76	10	20	15	12	48	999
2015	No Flood[2]	413	749	295	172	15	62	12	28	11	13	52	1,822
2016	7	253	730	130	187	21	106	16	35	20	12	33	1,550
2017	5	147	562	120	111	20	54	17	29	12	17	21	1,115
2018	No Flood[2]	240	517	54	144	13	37	13	10	6	26	-[4]	1,060
2019	-[3]	193	621	278	135	11	60	16	27	31	103	-[4]	1,475
2020	90	258	726	342	139	15	48	18	29	7	13	46	1,731

[1] Not all watercourses mapped during pre-MODIS era (1995–1999).

[2] Flood waters from the Topagoruk River did not reach the coast.

[3] Flood boundary not mapped due to insufficient imagery.

[4] In 2018 and 2019 the overflood extents for the Sadlerochit, Hulahula, and Okpilak R. were combined. The overflood area is shown only in the Sadlerochit R. column.

Table 9. Annual overflood area (km^2) for each watershed boundary, 1995–2020

Year	Admiralty Bay - Dease Inlet	Ikpikpuk River	Harrison Bay	Lower Colville River	Kuparuk River	Sagavanirktok River	Mikkelsen Bay	Canning River	Camden Bay	Total
1995[1]	-	-	-	738	173	192	-	29	27	1,159
1996[1]	-	-	-	593	99	-	30	43	5	770
1997[1]	-	-	-	485	100	129	67	47	71	899
1998[1]	-	4	-	813	153	155	122	57	21	1,325
1999[1]	-	-	-	483	70	122	60	33	33	801
2000	160	295	15	916	285	153	127	52	99	2,102
2001	58	209	26	869	259	172	130	63	77	1,863
2002	80	320	31	843	307	223	158	70	100	2,132
2003	No Flood[2]	113	48	550	291	129	125	37	69	1,362
2004	53	224	-[4]	1010	256	227	117	63	53	2,003
2005	145	151	-[4]	770	229	166	71	42	43	1,617
2006	119	174	37	657	253	113	102	46	52	1,553
2007	36	134	14	553	137	127	150	63	55	1,269
2008	66	133	-[4]	717	102	131	123	62	45	1,379
2009	56	176	63	613	262	142	100	52	80	1,544
2010	93	187	-[4]	858	326	161	126	40	59	1,850
2011	73	266	42	592	279	180	92	58	101	1,683
2012	121	106	25	712	158	122	98	32	51	1,425
2013	78	117	-[4]	738	288	180	121	77	82	1,681
2014	11	231	94	331	239	93	136	31	79	1,245
2015	No Flood[2]	413	14	749	356	172	107	56	93	1,960
2016	75	253	-[4]	738	174	187	145	54	70	1,696
2017	19	147	97	587	193	111	113	54	67	1,388
2018	10	240	-[4]	517	55	144	50	23	32	1,071
2019	-[3]	197	7	637	296	135	82	46	138	1,538
2020	90	258	-[4]	726	359	139	90	53	103	1,818

[1] Not all watercourses mapped during pre-MODIS era (1995–1999).

[2] Flood waters did not reach the coast.

[3] Flood boundary not mapped due to insufficient imagery.

[4] Flood area for Harrison Bay WBD included in the total for the Lower Colville River WBD.

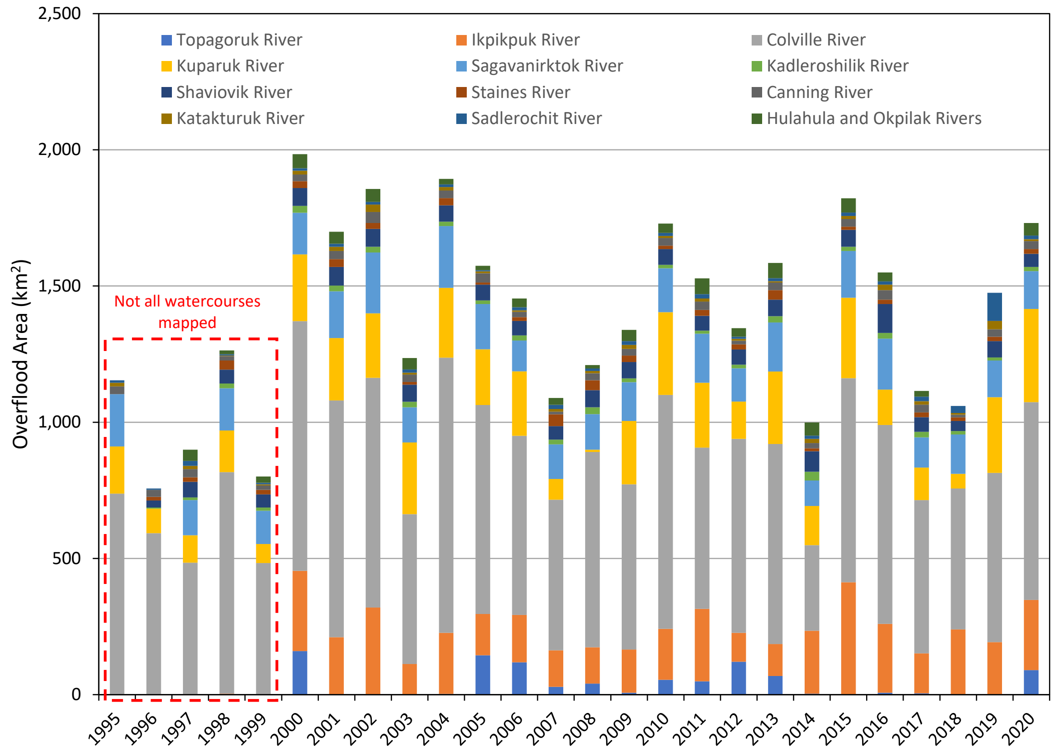

Figure 26. Overflood area for all major rivers, 1995–2020

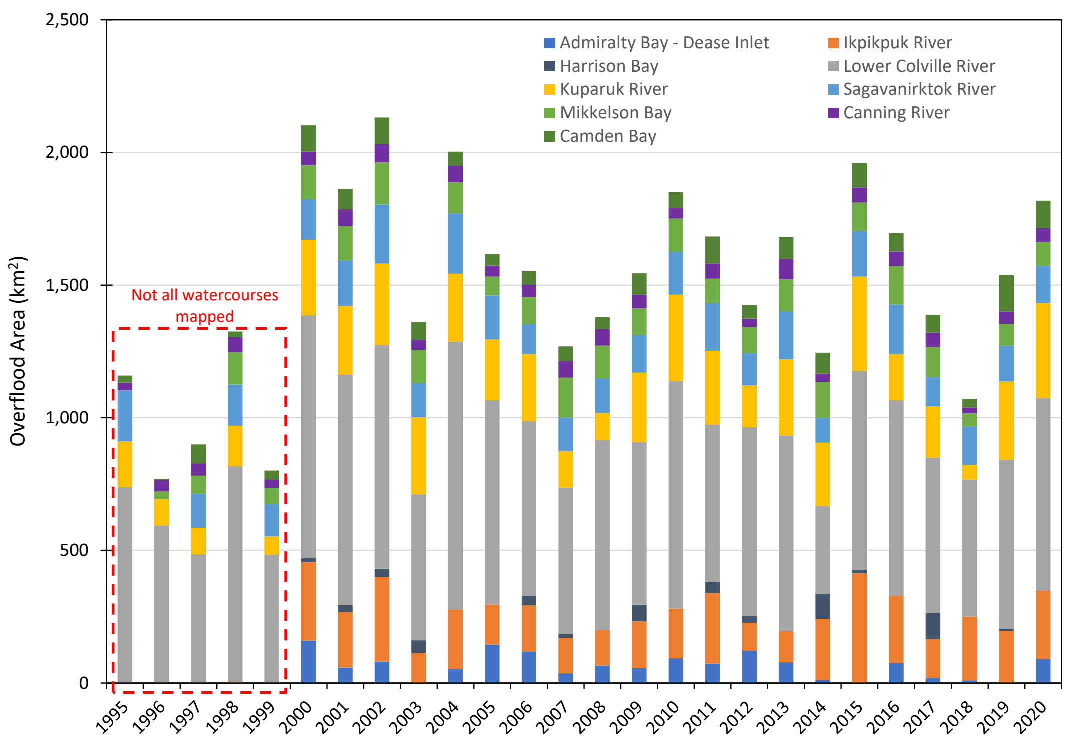

Figure 27. Overflood area for all watershed boundaries, 1995–2020

Table 10. Start of overflood (month and day) for each major river, 2000–2020

Year[1]	Topagoruk River	Ikpikpuk River	Colville River	Kuparuk River	Sag. River	Kad. River	Shaviovik River	Staines River	Canning River	Katakturuk River	Sadlerochit River	Hulahula & Okpilak R.
2000	6/8	6/6	6/7	6/10	5/27	6/11	6/8	6/11	6/4	6/8	6/4	6/3
2001	-[2]	6/9	6/6	6/7	6/1	6/9	6/9	6/6	6/7	6/2	6/4	6/2
2002	No Flood[3]	5/15	5/17	5/23	5/12	5/24	5/22	-[2]	5/20	5/19	5/15	5/15
2003	No Flood[3]	6/1	-[2]	6/2	5/16	6/5	6/1	-[2]	-[2]	-[2]	5/27	-[2]
2004	-[2]	5/25	5/21	5/22	5/18	5/26	5/21	5/18	5/19	5/19	5/19	5/19
2005	-[2]	6/6	5/17	5/25	5/12	6/4	5/28	6/2	5/22	5/24	5/12	5/12
2006	5/28	5/29	5/24	5/27	5/19	5/27	5/22	-[2]	5/13	5/18	5/16	5/12
2007	6/2	5/29	5/28	5/31	5/31	5/24	5/24	5/29	5/28	5/26	5/23	5/25
2008	5/29	5/30	5/26	5/29	5/20	5/28	5/26	5/16	5/16	5/24	5/17	5/17
2009	5/22	5/24	5/5	5/15	5/3	5/25	5/17	5/25	5/1	5/19	5/1	4/30
2010	6/5	6/4	5/26	5/29	5/20	6/2	5/27	5/31	5/28	5/24	5/23	5/22
2011	5/31	5/31	5/25	5/26	5/22	5/28	5/23	5/26	5/22	5/22	5/21	5/21
2012	5/28	5/27	5/25	5/27	5/20	5/27	5/22	6/5	5/22	5/21	5/19	5/19
2013	-[2]	5/31	5/30	6/2	5/26	6/5	5/30	6/1	5/29	5/29	5/23	5/25
2014	5/19	5/19	5/16	5/18	5/10	5/18	5/18	5/19	5/19	5/19	5/6	5/6
2015	No Flood[3]	5/21	5/18	5/19	5/3	5/20	5/17	5/17	5/13	5/15	5/5	5/11
2016	5/21	5/21	5/16	5/17	5/9	5/17	5/14	5/6	5/13	5/15	5/9	5/14
2017	6/1	6/1	5/23	5/28	5/21	5/31	5/24	5/23	5/20	5/21	5/16	5/17
2018	No Flood[3]	6/5	5/20	5/31	5/18	6/6	5/24	5/9	5/28	5/18	5/18	5/18
2019	-[4]	5/26	5/21	5/22	4/23	5/21	5/14	4/23	4/23	5/14	4/24	4/24
2020	5/30	5/29	5/22	5/27	5/13	5/29	5/24	5/26	5/18	5/21	5/8	5/12
Avg.	**5/29**	**5/28**	**5/22**	**5/26**	**5/16**	**5/28**	**5/24**	**5/23**	**5/19**	**5/22**	**5/16**	**5/16**
Max.	**6/8**	**6/9**	**6/7**	**6/10**	**6/1**	**6/11**	**6/9**	**6/11**	**6/7**	**6/8**	**6/4**	**6/3**
Min.	**5/19**	**5/15**	**5/5**	**5/15**	**4/23**	**5/17**	**5/14**	**4/23**	**4/23**	**5/14**	**4/24**	**4/24**

[1] Start of overflood not detected during pre-MODIS era (1995-1999).

[2] Start of overflood could not be determined within ±2 days (±1 day for the Colville, Kuparuk, and Sagavanirktok Rivers).

[3] Flood waters did not reach the coast.

[4] Flood boundary not mapped due to insufficient imagery.

Table 11. Peak of overflood (month and day) for each major river, 2000–2020

Year[1]	Topagoruk River	Ikpikpuk River	Colville River	Kuparuk River	Sag. River	Kad. River	Shaviovik River	Staines River	Canning River	Katakturuk River	Sadlerochit River	Hulahula & Okpilak R.
2000	6/12	6/14	6/12	6/14	6/14	6/12	6/11	6/13	6/11	6/9	6/8	6/12
2001	6/11	6/12	6/11	6/11	6/8	6/10	6/10	6/10	6/9	6/4	6/8	6/9
2002	No Flood[3]	5/31	5/25	5/25	5/25	5/25	5/25	5/25	5/23	5/22	5/23	5/25
2003	No Flood[3]	6/7	6/8	6/8	6/1	6/5	6/5	-[2]	-[2]	-[2]	-[2]	-[2]
2004	-[2]	6/1	6/1	5/29	6/2	5/28	5/28	5/21	-[2]	5/31	5/21	-[2]
2005	-[2]	6/12	6/7	6/4	5/30	6/6	6/1	6/3	6/2	5/31	-[2]	6/3
2006	-[2]	6/4	6/5	6/3	5/27	5/28	5/27	5/27	5/27	5/20	5/19	6/20
2007	6/6	6/7	6/4	6/5	6/5	6/6	6/6	6/5	6/2	6/4	6/2	6/2
2008	-[2]	6/4	6/3	6/2	5/29	5/31	5/29	-[2]	5/26	5/26	5/24	5/25
2009	5/24	5/28	5/28	5/31	5/25	5/28	5/25	5/31	5/25	5/25	5/28	5/28
2010	6/9	6/11	6/8	6/7	6/6	6/5	6/5	6/5	5/31	5/26	5/27	5/31
2011	6/3	6/4	5/31	6/1	5/25	5/30	5/26	5/28	5/25	5/28	5/24	5/27
2012	6/4	6/6	6/3	5/31	5/24	5/28	5/28	6/7	5/29	5/29	5/21	5/31
2013	6/2	6/4	6/8	6/6	6/2	6/6	6/6	6/8	6/6	5/31	5/30	6/1
2014	5/19	5/25	5/23	5/24	5/28	5/20	5/20	5/20	5/19	5/20	5/20	5/20
2015	No Flood[3]	5/26	5/26	-[2]	5/22	5/21	5/20	5/18	5/19	5/18	5/16	5/20
2016	5/23	5/28	5/20	5/21	5/21	5/19	5/18	5/20	5/18	5/19	5/16	5/19
2017	6/2	6/11	6/6	6/3	6/1	6/3	5/31	5/28	5/28	5/27	5/21	5/23
2018	No Flood[3]	6/19	6/5	6/5	5/27	6/7	6/2	6/6	6/5	5/28	6/2	6/2
2019	-[4]	6/2	6/5	5/28	6/2	5/24	5/23	5/17	5/21	5/21	5/21	5/21
2020	6/3	6/8	6/4	6/4	6/4	5/30	6/1	5/31	5/27	5/27	5/27	5/29
Avg.	**6/2**	**6/5**	**6/2**	**6/2**	**5/30**	**5/31**	**5/29**	**5/30**	**5/28**	**5/26**	**5/25**	**5/29**
Max.	**6/12**	**6/19**	**6/12**	**6/14**	**6/14**	**6/12**	**6/11**	**6/13**	**6/11**	**6/9**	**6/8**	**6/20**
Min.	**5/19**	**5/25**	**5/20**	**5/21**	**5/21**	**5/19**	**5/18**	**5/17**	**5/18**	**5/18**	**5/16**	**5/19**

[1] Peak of overflood not detected during pre-MODIS era (1995-1999).

[2] Peak of overflood could not be determined within ±2 days (±1 day for the Colville, Kuparuk, and Sagavanirktok Rivers).

[3] Flood waters did not reach the coast.

[4] Flood boundary not mapped due to insufficient imagery.

8.4 Occurrence Probability

Figure 28 and **Figure 29** illustrate isolines of overflood probability for the west and east portions of the study region, respectively. As noted above, the probabilities were developed using the overflood extents mapped during the 21-year period from 2000 through 2020.

The immediate region fronting all but one of the thirteen major rivers in the study area (Topagoruk River) flooded annually (100% probability of occurrence). Between Cape Halkett and the Staines River, the entire coast flooded 25% of the time. Elsewhere, the flooded areas were discontinuous.

8.5 Geodatabase

The final geodatabase consists of two volumes. OVERFLOOD_DATA.GDB includes the river overflood and auxiliary data compiled as part of this project, while IMAGERY_BANK.GDB includes the raw satellite imagery used to derive the overflood extents for the period 1995–2020. Details regarding each volume are provided in **Appendix C** and brief summaries are provided below.

8.5.1 River Overflood Data

OVERFLOOD_DATA.GDB: Primary geodatabase containing the river overflood data and auxiliary information compiled for the project. The geodatabase is composed of three distinct feature datasets and one table. The geodatabase structure is listed in **Table 12**.

8.5.2 Imagery Bank

IMAGERY_BANK.GDB: Supporting geodatabase containing the 344 raw satellite images used to derive the overflood extents for the period 1995–2020. Scenes are categorized by image type and are provided as is. The only modification to the file was to append a project-specific file name to the image name. The imagery collections are listed in **Table 13**.

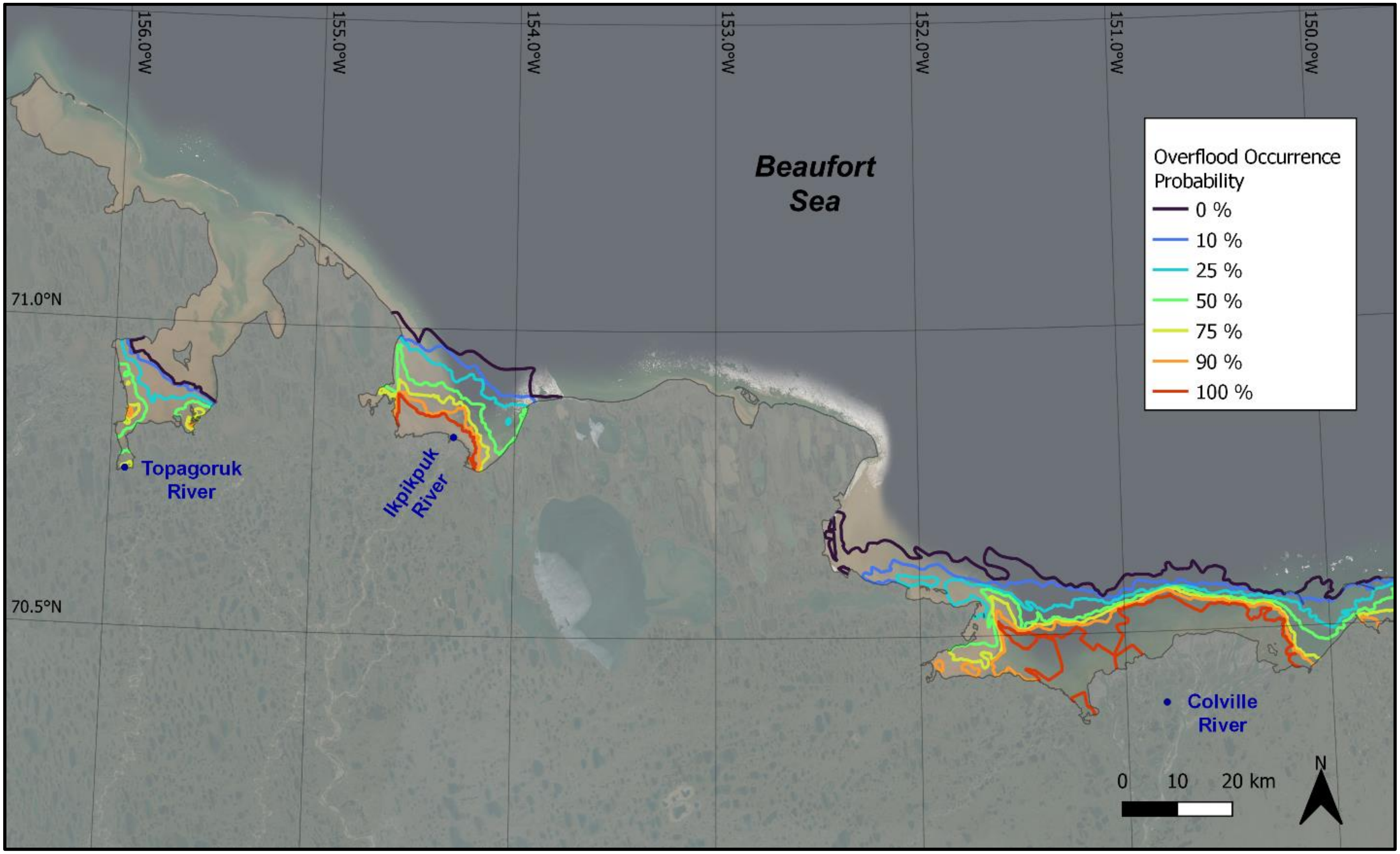

Figure 28. Isolines of overflood probability, west study region

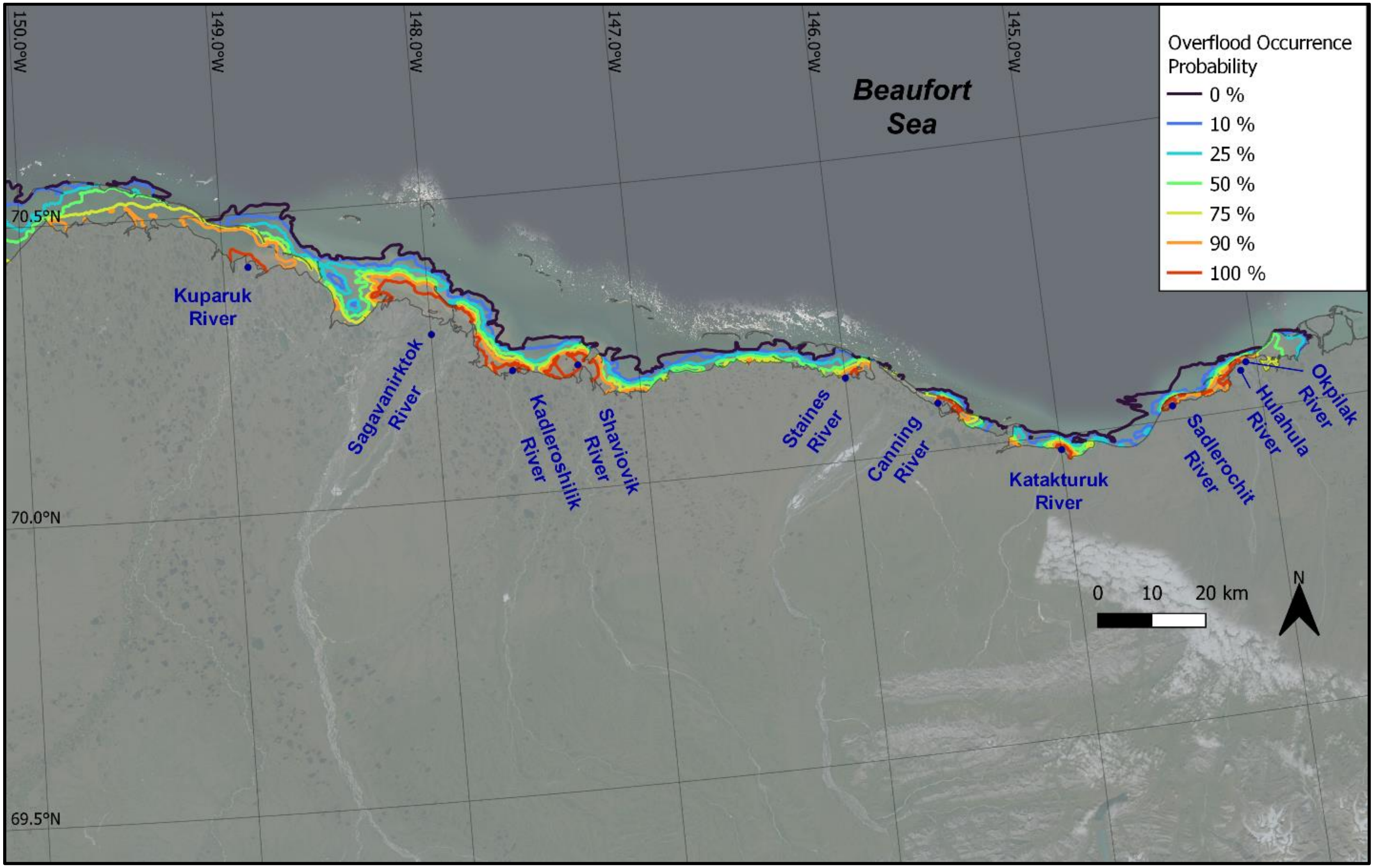

Figure 29. Isolines of overflood probability, east study region

Table 12. Contents of OVERFLOOD_DATA.GDB

Feature Dataset	Feature Class	Name
1	**-**	**Overflood_Extent_Data**
	1.1	overflood_extent_1995_thru_2020
	1.2	overflood_extent_yearly_envelope_1995_thru_2020
	1.3	overflood_extent_maximum_envelope_1995_thru_2020
	1.4	overflood_extent_from_field_surveys_1995_thru_2020
	1.5	overflood_extent_pre_1995
	1.6	overflood_extent_probability_contours_2000_thru_2020
2	**-**	**Drain_and_Strudel_Scour_Data**
	2.1	circular_drains_and_short_crack_drains_1995_thru_2020
	2.2	long_crack_drains_1995_thru_2020
	2.3	circular_strudel_scours_1995_thru_2020
	2.4	linear_strudel_scours_1995_thru_2020
	2.5	drain_and_strudel_search_areas_1995_thru_2020
	2.6	strudel_zones
	2.7	strudel_zones_with_overflood_extent_yearly_envelope_1995_thru_2020
3	**-**	**Auxiliary_Data**
	3.1	alaska_north_slope_coast
	3.2	alaska_north_slope_bathymetry
	3.3	environmental_data_stations
	3.4	WBDHU8 (hydrologic_units)
	3.5	ice_roads
Table	**-**	**image_catalog**

Table 13. Contents of IMAGERY_BANK.GDB

Collection	Imagery Source	Number of Scenes
1	ERS-2 image (European Space Agency, ESA)	20
2	Landsat 5 image (USGS/National Aeronautics and Space Administration, NASA)	15
3	Landsat 7 image (USGS/NASA)	45
4	Landsat 8 image (USGS/NASA)	42
5	Moderate Resolution Imaging Spectroradiometer (MODIS) image (NASA)	143
6	ALOS PALSAR image (Japanese Aerospace Exploration Agency, JAXA)	7
7	Resourcesat-2A Advanced Wide Field Sensor (AWiFS) image (Indian Space Research Organization, ISRO)	15
8	Resourcesat-2A Linear Imaging Self Scanning Sensor (LISS-3) image (ISRO)	5
9	Sentinel-1 image (ESA)	10
10	Sentinel-2 image (ESA)	27
11	Radarsat (Canadian Space Agency, CSA)	15

9 Environmental Correlations

River overflood on the sea ice is a complex phenomenon that likely is affected by the interaction of many environmental parameters such as streamflow, precipitation, snowpack, air temperature, river and sea ice conditions, and wind. This section presents an analysis undertaken to search for correlations between selected environmental driving forces and overflood parameters (area and timing) to provide a means of predicting the severity and onset of future overflood events.

The environmental parameters considered as part of this analysis include streamflow, precipitation, snow water equivalent (SWE), and air temperature. Correlations between overflood area and three of these parameters (streamflow, precipitation, and air temperature) were investigated as part of the 2009 Study. While no meaningful correlation was discovered as part of that work, these parameters were revisited to determine if the expanded data set improved the association.

9.1 Environmental Data

Figure 30 illustrates the location of the 25 environmental monitoring stations used in this investigation. These stations were selected primarily on the basis of location, period of record, and availability of non-proprietary data.

It should be noted that data gaps exist in nearly all of the monitoring station records. Detailed descriptions of the primary parameters of interest (streamflow, precipitation, SWE, and air temperature) are provided below.

9.1.1 Streamflow

Streamflow measurements provide an indication of the timing and relative intensity of river discharge during the break-up period. Mean daily discharge data for the three rivers of interest (Colville, Kuparuk, and Sagavanirktok) were obtained from the USGS (2021h). Metadata for each source are provided in **Table 14,** and their locations are illustrated in **Figure 30**. The Colville and Sagavanirktok stations are located approximately 150 km inland, while the Kuparuk station is located about 15 km from the coast.

Table 14. Streamflow measurement sites

Name	Station ID	Location	Latitude[1]	Longitude[1]	Elevation[1]	Period[2]
Colville River	15875000	Umiat	69.361°N	152.123°W	80 m	2002[3]–2020
Kuparuk River	15896000	Deadhorse	70.280°N	148.960°W	not specified	1971–2020
Sagavanirktok R.	15908000	Pump Station 3	69.016°N	148.818°W	340 m	1982–2020

[1] Horizontal datum is NAD83. Vertical datum is assumed to be Mean Sea Level (MSL). Elevation is approximate.

[2] Data gaps exist.

[3] Gauge installed after river overflood (August 2002).

[4] Source: USGS (2021h).

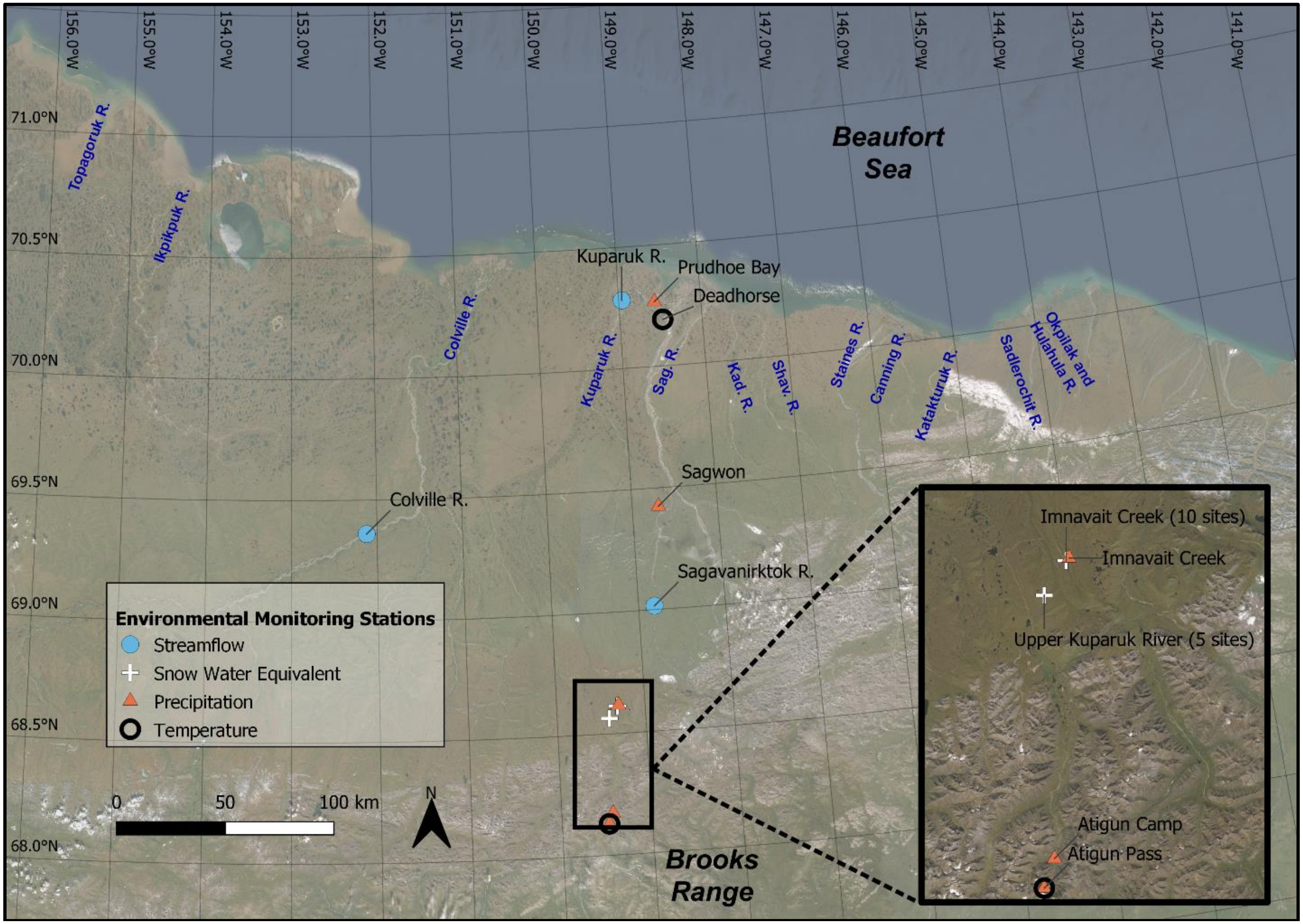

Figure 30. Environmental data stations

Annual streamflow hydrographs encompassing the typical overflood period (May through June) were generated for each of the three gauges. A flood threshold was selected to define the "break-up period" at each site. The break-up period begins on the first day prior to the daily average discharge rising above the threshold and ends on the first day after the discharge drops below the threshold. Thresholds of 600 m^3/s, 225 m^3/s, and 150 m^3/s were chosen for the Colville, Kuparuk, and Sagavanirktok Rivers, respectively, and are the same thresholds used as part of the 2009 Study.

Four streamflow parameters were derived for each river and are illustrated in **Figure 31**. The peak discharge was defined as the highest mean daily discharge value measured during the break-up period. The average discharge was calculated as the mean of the daily discharge values measured during the break-up period. The total discharge volume, or "flood volume," was determined by computing the area under the hydrograph during the break-up period. Finally, the flood intensity (the rate at which the flood developed) was computed as the slope of the rising limb of the hydrograph.

The streamflow characteristics measured during the break-up period at the Colville, Kuparuk, and Sagavanirktok Rivers are summarized in **Table 15**, **Table 16**, and **Table 17**, respectively. Generally, the magnitudes were highest on the Colville River and lowest on the Kuparuk River.

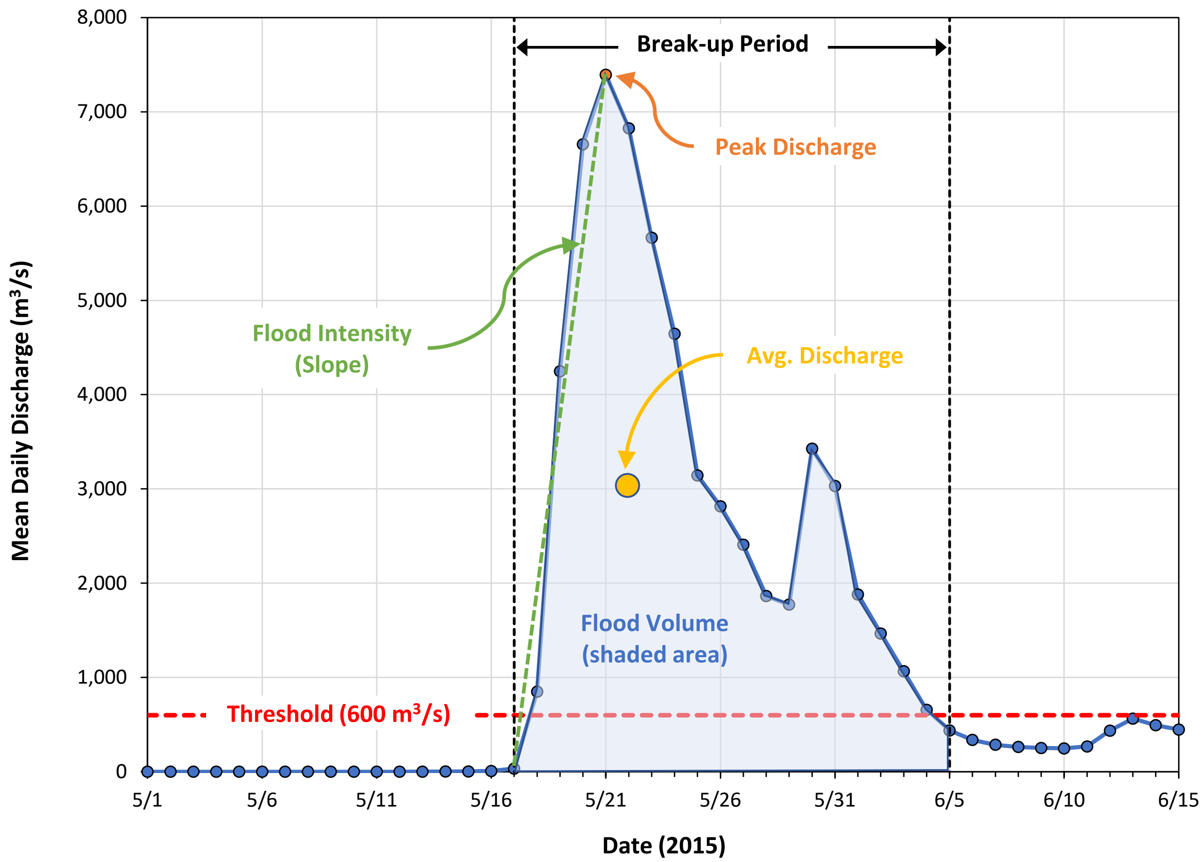

Figure 31. Streamflow parameters (Colville River, 2015)

Table 15. Colville River streamflow characteristics during break-up period

Year	Peak Discharge (m^3/s)	Average Discharge (m^3/s)	Flood Volume (m^3)	Flood Intensity ($m^3/s/day$)
1995	-	-	-	-
1996	-	-	-	-
1997	-	-	-	-
1998	-	-	-	-
1999	-	-	-	-
2000	-	-	-	-
2001	-	-	-	-
2002	-	-	-	-
2003	5,777	2,529	4,370,070,528	595
2004	5,834	2,336	4,439,561,011	1,317
2005	4,333	2,181	6,029,278,157	237
2006	4,503	2,100	2,358,272,102	694
2007	5,098	2,276	2,949,675,264	566
2008	2,775	1,435	4,712,139,878	470
2009	3,823	1,798	5,593,005,158	155
2010	5,268	2,192	4,356,123,494	673
2011	6,004	2,545	4,398,209,280	930
2012	4,644	1,996	3,966,095,923	371
2013	6,768	2,451	*6,565,871,923*	906
2014	4,531	1,904	1,315,914,854	1,369
2015	*7,392*	*3,014*	5,208,115,968	*1,472*
2016	1,982	879	607,307,674	659
2017	2,087	1,159	2,403,049,421	166
2018	3,059	1,832	2,848,375,757	365
2019	3,597	1,999	3,281,957,222	622
2020	4,106	1,719	2,821,460,429	918
Avg.	**4,532**	**2,019**	**3,790,249,114**	**694**
Max.	**7,392**	**3,014**	**6,565,871,923**	**1,472**
Min.	**1,982**	**879**	**607,307,674**	**155**

[1] Values computed using daily streamflow data exceeding threshold (600 m^3/s) during break-up period (**Figure 31**).

[2] Data not available from 1995–2002.

[3] Maximum values highlighted.

Table 16. Kuparuk River streamflow characteristics during break-up period

Year	Peak Discharge (m^3/s)	Average Discharge (m^3/s)	Flood Volume (m^3)	Flood Intensity ($m^3/s/day$)
1995	566	382	692,213,299	89
1996	1,529	673	930,120,330	283
1997	1,631	614	1,060,463,923	135
1998	1,272	546	566,151,690	157
1999	564	350	393,477,627	113
2000	2,209	784	1,015,833,416	363
2001	1,558	607	629,745,270	361
2002	1,416	699	483,228,012	425
2003	1,218	545	517,850,911	221
2004	850	524	814,506,762	71
2005	949	468	808,609,859	68
2006	850	401	623,603,681	159
2007	1,747	759	524,848,896	310
2008	850	477	411,706,644	245
2009	1,073	522	1,037,267,804	78
2010	1,133	646	893,711,232	102
2011	1,388	586	860,028,503	190
2012	850	444	690,206,884	89
2013	*2,549*	*922*	*1,513,302,083*	615
2014	1,699	776	1,408,797,204	306
2015	*2,549*	838	1,303,386,993	*627*
2016	1,076	552	572,073,062	176
2017	818	418	433,532,529	232
2018	1,623	583	1,259,833,098	300
2019	1,490	624	593,482,982	336
2020	1,815	662	743,132,206	357
Avg.	**1,357**	**592**	**799,273,650**	**246**
Max.	**2,549**	**922**	**1,513,302,083**	**627**
Min.	**564**	**350**	**393,477,627**	**68**

[1] Values computed using daily streamflow data exceeding threshold (225 m^3/s) during break-up period (**Figure 31**).

[2] Maximum values highlighted.

Table 17. Sagavanirktok River streamflow characteristics during break-up period

Year	Peak Discharge (m^3/s)	Average Discharge (m^3/s)	Flood Volume (m^3)	Flood Intensity ($m^3/s/day$)
1995	286	197	119,161,498	63
1996	391	249	193,814,830	37
1997	351	225	389,440,328	49
1998	419	229	197,436,165	72
1999	221	179	138,980,966	16
2000	*708*	*323*	586,313,718	*149*
2001	309	206	195,429,750	35
2002	227	160	69,001,114	78
2003	396	255	462,576,614	50
2004	396	255	395,802,132	28
2005	229	181	125,400,960	14
2006	283	188	97,384,550	59
2007	283	191	148,499,205	24
2008	199	162	69,784,105	26
2009	255	194	134,331,955	27
2010	354	228	295,089,869	53
2011	467	287	273,068,237	81
2012	357	224	251,707,254	20
2013	566	291	201,130,906	106
2014	459	253	*744,404,567*	22
2015	467	276	476,132,152	22
2016	153	139	35,968,666	14
2017	201	161	69,563,889	21
2018	343	230	377,401,836	16
2019	255	192	132,741,504	20
2020	317	230	238,665,554	58
Avg.	**342**	**219**	**246,893,551**	**45**
Max.	**708**	**323**	**744,404,567**	**149**
Min.	**153**	**139**	**35,968,666**	**14**

[1] Values computed using daily streamflow data exceeding threshold (150 m^3/s) during break-up period (**Figure 31**).

[2] Maximum values highlighted.

9.1.2 Precipitation

The volume of water available to contribute to river discharge was estimated using two parameters: precipitation and SWE. While interrelated, the two metrics differ as a result of multiple factors, such as measurement technique and accuracy (Stuefer *et al.*, 2020).

Monthly accumulated precipitation data were acquired from the Natural Resources Conservation Service (NRCS, 2021) at the five stations shown in **Table 18**. The stations encompass the region from the Brooks Range (Atigun Pass) to the U.S. Beaufort Sea Coast (Prudhoe Bay), as shown in **Figure 30**. While these stations are believed to represent the best available precipitation indicators in the study area, they provide neither comprehensive nor evenly-spaced coverage of the area of interest.

Table 18. Precipitation measurement sites

Name	Station ID	Latitude[1]	Longitude[1]	Elevation[1]	Period[2]	USGS WBD[3]
Atigun Pass	957	68.130°N	149.478°W	1,460 m	1983-2020	Sagavanirktok R.
Atigun Camp	X494	68.173°N	149.430°W	1,040 m	1983-2020	Sagavanirktok R.
Imnavait Creek[4]	968	68.617°N	149.300°W	940 m	1982-2020	Kuparuk River
Sagwon	1183	69.424°N	148.693°W	300 m	1983-2020	Kuparuk River
Prudhoe Bay	1177	70.267°N	148.567°W	10 m	1979-2020	Kuparuk River

[1] Horizontal datum is NAD83. Vertical datum is assumed to be Mean Sea Level (MSL). Elevation is approximate.

[2] Data gaps exist.

[3] USGS WBD containing the measurement site.

[4] Also referred to as “Imnaviat Creek.”

[5] Source: NRCS (2021).

Accumulated precipitation was tabulated at each station for the period from October 1 through May 31. October 1 was selected to approximate the start of the winter snow season, while May 31 was selected to approximate the start of the break-up period. The results are provided in **Table 19** and illustrated in **Figure 32**. The highest average precipitation occurred at Atigun Pass (21.1 cm), while the lowest occurred at Sagwon (9.4 cm).

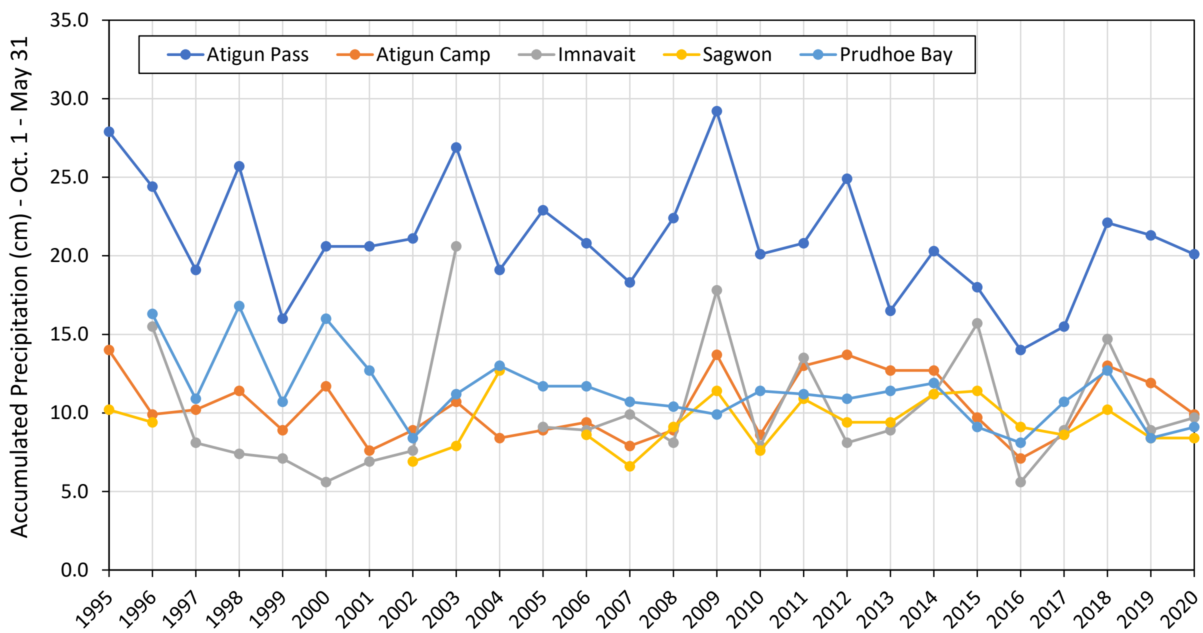

Figure 32. Accumulated precipitation at North Slope of Alaska monitoring stations, Oct. 1–May 31

Table 19. Accumulated precipitation, October 1–May 31

Year[1]	Atigun Pass Precipitation (cm)	Atigun Camp Precipitation (cm)	Imnavait Precipitation (cm)	Sagwon Precipitation (cm)	Prudhoe Bay Precipitation (cm)
1995	27.9	14.0	-[2]	10.2	-[2]
1996	24.4	9.9	15.5	9.4	16.3
1997	19.1	10.2	8.1	-[2]	10.9
1998	25.7	11.4	7.4	-[2]	16.8
1999	16.0	8.9	7.1	-[2]	10.7
2000	20.6	11.7	5.6	-[2]	16.0
2001	20.6	7.6	6.9	-[2]	12.7
2002	21.1	8.9	7.6	6.9	8.4
2003	26.9	10.7	20.6	7.9	11.2
2004	19.1	8.4	-[2]	12.7	13.0
2005	22.9	8.9	9.1	-[2]	11.7
2006	20.8	9.4	8.9	8.6	11.7
2007	18.3	7.9	9.9	6.6	10.7
2008	22.4	8.9	8.1	9.1	10.4
2009	29.2	13.7	17.8	11.4	9.9
2010	20.1	8.6	7.9	7.6	11.4
2011	20.8	13.0	13.5	10.9	11.2
2012	24.9	13.7	8.1	9.4	10.9
2013	16.5	12.7	8.9	9.4	11.4
2014	20.3	12.7	11.2	11.2	11.9
2015	18.0	9.7	15.7	11.4	9.1
2016	14.0	7.1	5.6	9.1	8.1
2017	15.5	8.6	8.9	8.6	10.7
2018	22.1	13.0	14.7	10.2	12.7
2019	21.3	11.9	8.9	8.4	8.4
2020	20.1	9.9	9.7	**8.4**	9.1
Avg.	**21.1**	**10.4**	**10.2**	**9.4**	**11.4**
Max.	**29.2**	**14.0**	**20.6**	**12.7**	**16.8**
Min.	**14.0**	**7.1**	**5.6**	**6.6**	**8.1**

[1] "Year" corresponds to the break-up period. For example, 2020 is the period from October 1, 2019 to May 31, 2020.

[2] Incomplete record.

9.1.3 Snowpack (Snow Water Equivalent)

Stuefer *et al.* (2020) describe a long-term monitoring program conducted by the Water and Environmental Research Center (WERC) at the University of Alaska, Fairbanks (UAF). As part of this program, snow water equivalent (SWE) measurements were obtained in the Upper Kuparuk River Watershed from 1997 through 2017. Similarly, SWE measurements were obtained in the Imnavait Creek Watershed from 1985 through 2017. Both the Upper Kuparuk River Watershed and the Imnavait Creek Watershed are part of the larger "Kuparuk River WBD" shown in **Figure 5**. Unfortunately, no equivalent long-term snowpack records exist for any other watershed or river system on the North Slope of Alaska.

Stuefer *et al.* (2020) distilled these measurements down to average annual end-of-winter (late-April) values for each of the two watersheds (**Table 20**). These values represent the potential water content in the snowpack just prior to the onset of significant thawing and runoff. Given that the average value obtained from multiple monitoring sites is reported herein, the precise sampling locations are not critical. However, the general locations of the two SWE measurement areas are shown in **Figure 30**.

Table 20. Average end-of-winter snow water equivalent

Year	SWE (cm) Upper Kuparuk River Watershed	SWE (cm) Imnavait Creek Watershed
1997	9.7	14.0
1998	7.5	9.6
1999	no data	8.8
2000	9.6	11.2
2001	10.7	12.7
2002	8.0	8.9
2003	11.0	13.7
2004	9.6	11.6
2005	11.0	12.3
2006	7.0	9.6
2007	7.7	11.5
2008	5.1	7.5
2009	11.1	15.5
2010	7.2	12.1
2011	11.3	17.4
2012	11.0	15.0
2013	12.9	16.1
2014	no data	no data
2015	16.9	20.7
2016	11.2	13.8
2017	15.9	17.6

[1] Measurements obtained in late April.

[2] Source: Stuefer *et al.,* 2020.

9.1.4 Air Temperature

Air temperatures play a key role in melting the snowpack prior to river break-up. Daily air temperature records were analyzed at two locations: Atigun Pass in the Brooks Range (NRCS, 2021) and Deadhorse near the coast (NOAA, 2022a). While air temperature data are available at other locations in the study area, these sites were selected based on the length of the data record and to bracket the geographic and climatological range of the region. The Kuparuk station used in the 2009 Study discontinued daily air temperature readings in 2017 and was excluded from consideration. The locations of both sites are shown in **Figure 30**, and the site details are provided in **Table 21**.

Table 21. Air temperature measurement sites

Name	Station ID	Latitude[1]	Longitude[1]	Elevation[1]	Period[2]
Deadhorse[3]	27406	70.191°N	148.480°W	20 m	1973-2020
Atigun Pass[4]	957	68.130°N	149.478°W	1,460 m	1983-2020

[1] Horizontal datum is NAD83. Vertical datum is assumed to be Mean Sea Level (MSL). Elevation is approximate.

[2] Data gaps exist.

[3] Source: NOAA (2022a).

[4] Source: NRCS (2021).

"Thawing Degree Days" (TDD) at each site were computed as an indicator of the thermal impetus to river break-up. The calculation was performed in the following manner: (1) if the daily average air temperature was less than or equal to 32°F (the melting point of snow and freshwater ice), that day was excluded from further consideration; (2) if the daily average air temperature exceeded 32°F, the difference between 32°F and the daily average air temperature was recorded as the number of TDD for that day.

TDD were accumulated for the period commencing on April 15 and ending on May 31. This period was selected as representative of the air temperature changes during river break-up. The results, displayed in **Table 22** and **Figure 33**, ranged from 0 to 207 TDD at Atigun Pass, and 0 to 105 TDD at Deadhorse, with average values of 82 and 22 TDD, respectively.

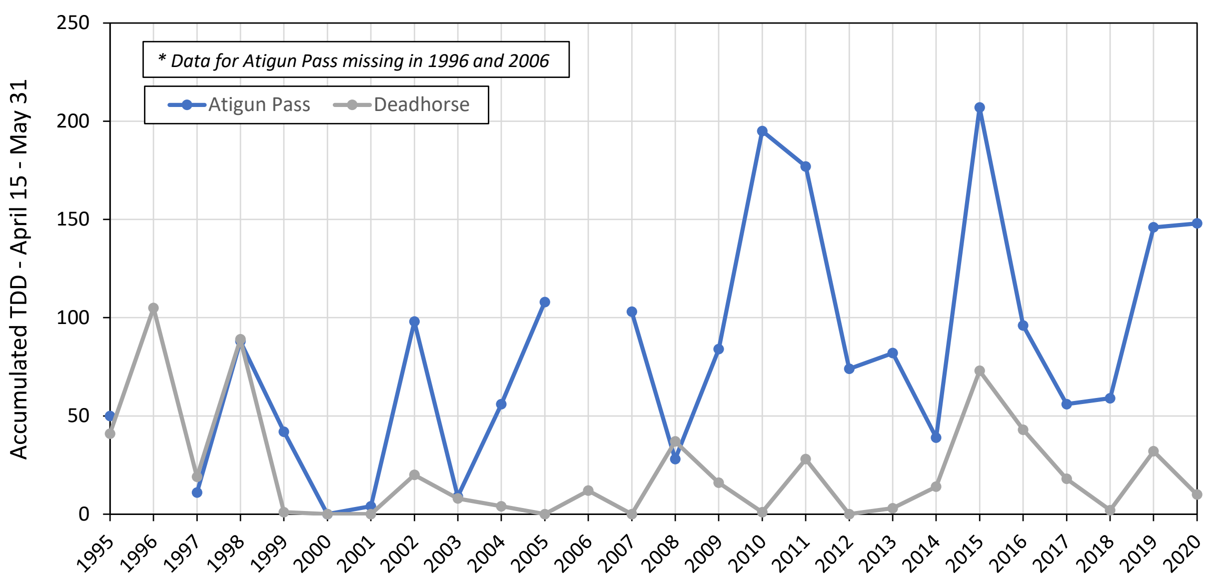

Figure 33. Accumulated thawing degree days (TDD), April 15 through May 31

Table 22. Accumulated thawing degree days (TDD), April 15 through May 31

Year	Atigun Pass TDD	Deadhorse TDD
1995	50	41
1996	-[3]	105
1997	11	19
1998	88	89
1999	42	1
2000	0	0
2001	4	0
2002	98	20
2003	9	8
2004	56	4
2005	108	0
2006	-[3]	12
2007	103	0
2008	28	37
2009	84	16
2010	195	1
2011	177	28
2012	74	0
2013	82	3
2014	39	14
2015	207	73
2016	96	43
2017	56	18
2018	59	2
2019	146	32
2020	148	10
Avg.	**82**	**22**
Max.	**207**	**105**
Min.	**0**	**0**

[1] TDD computed as difference from 32°F.

[2] TDD accumulated from April 15 through May 31.

[3] Majority of the data from April 15–May 31 missing.

The dates (month and day) in the spring when the accumulated winter season "Freezing Degree Days" (FDD) reached the annual maximum value were tabulated for both the Atigun Pass and Deadhorse stations (**Table 23**) and used to approximate the start of snow melt (note: depending on the levels of solar radiation, snowpack can undergo significant loss even on days when average air temperatures are still slightly below freezing). FDD are defined here as the difference between 32°F and the daily average air temperature. If the daily average air temperature was below 32°F, the number of FDD was positive, while if the daily average air temperature was greater than or equal to 32°F, the number of FDD was negative.

Table 23. Date (month/day) of maximum accumulated freezing degree days (FDD)

Year	Atigun Pass Max FDD Date	Deadhorse Max FDD Date
1995	-	5/24
1996	-	5/9
1997	6/3	6/3
1998	5/17	5/15
1999	5/18	6/8
2000	6/3	6/6
2001	5/26	6/9
2002	5/18	5/30
2003	5/29	6/3
2004	5/14	6/5
2005	5/20	6/6
2006	6/8	5/23
2007	5/17	6/3
2008	6/1	5/22
2009	5/18	5/29
2010	5/11	5/31
2011	5/16	5/18
2012	5/17	5/31
2013	5/21	5/28
2014	5/26	6/1
2015	5/8	5/15
2016	5/19	5/10
2017	5/11	5/23
2018	5/19	6/8
2019	5/13	5/12
2020	5/20	5/22
Avg.	**5/20**	**5/27**
Max.	**6/8**	**6/9**
Min.	**5/8**	**5/9**

[1] FDD computed as difference from 32°F.

[2] FDD accumulated beginning on September 1.

9.2 Correlation between Environmental Parameters

The foregoing environmental variables (streamflow, precipitation, SWE, and air temperature) were analyzed to determine if any positive correlation exists such that one parameter can be used as a proxy for others, or if two or more parameters can be used interchangeably. A similar analysis performed as part of the 2009 Study revealed no correlation; however, this task has been revisited herein as the input dataset has been extended from 2007 to 2020.

The degree of correlation between parameters was assessed using the square of the Pearson product-moment correlation coefficient (R^2), which is a statistical measure of the ability of one variable to predict the other. Values of R^2 range from 0.0 (no correlation) to 1.0 (perfect correlation).

A correlation matrix was generated for each of the three rivers under consideration (Colville, Kuparuk, and Sagavanirktok). The matrices, presented in **Table 24**, **Table 25**, and **Table 26**, summarize the degree of correlation between the four streamflow parameters (peak discharge, average discharge, flood volume, and flood intensity) and the computed precipitation, snowpack, and air temperature variables. The R^2 values ranged between 0.00 and 0.33, revealing no strong correlation between streamflow and the remaining environmental parameters. Figures illustrating the correlation between each of the paired variables are provided in **Appendix D**.

Additional analyses were conducted to determine if a correlation exists between accumulated precipitation and snowpack. The two SWE sites are closest geographically to the Imnavait Creek precipitation station (**Figure 30**). While the largest correlation coefficient was generated between the Imnavait Creek precipitation site and the Imnavait Creek Watershed SWE site, the relatively low value (0.24) indicates that the correlation is weak, at best (**Table 27**).

Table 24. Correlation coefficient (R^2), Colville River streamflow

Parameter	Location	Peak Discharge	Average Discharge	Flood Volume	Flood Intensity
Accumulated Precipitation (Oct 1–May 31)	Atigun Pass	0.00	0.04	0.15	0.14
	Atigun Camp	0.04	0.06	0.06	0.00
	Imnavait Creek	0.15	0.24	0.10	0.01
	Sagwon	0.06	0.04	0.05	0.22
	Prudhoe Bay	0.07	0.09	0.04	0.00
	Avg.	**0.06**	**0.09**	**0.08**	**0.07**
	Max.	**0.15**	**0.24**	**0.15**	**0.22**
	Min.	**0.00**	**0.04**	**0.04**	**0.00**
End-of-Winter SWE (late April)	Upper Kuparuk R. Wshd.	0.04	0.02	0.02	0.04
	Imnavait Creek Wshd.	0.12	0.08	0.03	0.06
	Avg.	**0.08**	**0.05**	**0.03**	**0.05**
	Max.	**0.12**	**0.08**	**0.03**	**0.06**
	Min.	**0.04**	**0.02**	**0.02**	**0.04**
TDD (April 15–May 31)	Atigun Pass	0.13	0.14	0.02	0.08
	Deadhorse	0.00	0.00	0.01	0.13
	Avg.	**0.07**	**0.07**	**0.02**	**0.11**
	Max.	**0.13**	**0.14**	**0.02**	**0.13**
	Min.	**0.00**	**0.00**	**0.01**	**0.08**

Table 25. Correlation coefficient (R^2), Kuparuk River streamflow

Parameter	Location	Peak Discharge	Average Discharge	Flood Volume	Flood Intensity
Accumulated Precipitation (Oct 1–May 31)	Atigun Pass	0.07	0.07	0.00	0.12
	Atigun Camp	0.02	0.00	0.22	0.00
	Imnavait Creek	0.02	0.01	0.09	0.01
	Sagwon	0.00	0.00	0.32	0.02
	Prudhoe Bay	0.01	0.00	0.03	0.02
	Avg.	**0.02**	**0.02**	**0.13**	**0.03**
	Max.	**0.07**	**0.07**	**0.32**	**0.12**
	Min.	**0.00**	**0.00**	**0.00**	**0.00**
End-of-Winter SWE (late April)	Upper Kuparuk R. Wshd.	0.13	0.04	0.19	0.15
	Imnavait Creek Wshd.	0.18	0.10	0.33	0.10
	Avg.	**0.16**	**0.07**	**0.26**	**0.13**
	Max.	**0.18**	**0.10**	**0.33**	**0.15**
	Min.	**0.13**	**0.04**	**0.19**	**0.10**
TDD (April 15–May 31)	Atigun Pass	0.05	0.07	0.02	0.04
	Deadhorse	0.01	0.01	0.00	0.02
	Avg.	**0.03**	**0.04**	**0.01**	**0.03**
	Max.	**0.05**	**0.07**	**0.02**	**0.04**
	Min.	**0.01**	**0.01**	**0.00**	**0.02**

Table 26. Correlation coefficient (R^2), Sagavanirktok River streamflow

Parameter	Location	Peak Discharge	Average Discharge	Flood Volume	Flood Intensity
Accumulated Precipitation (Oct 1–May 31)	Atigun Pass	0.00	0.01	0.00	0.00
	Atigun Camp	0.18	0.20	0.09	0.08
	Imnavait Creek	0.02	0.10	0.09	0.04
	Sagwon	0.17	0.21	0.21	0.03
	Prudhoe Bay	0.31	0.24	0.10	0.15
	Avg.	**0.14**	**0.15**	**0.10**	**0.06**
	Max.	**0.31**	**0.24**	**0.21**	**0.15**
	Min.	**0.00**	**0.01**	**0.00**	**0.00**
End-of-Winter SWE (late April)	Upper Kuparuk R. Wshd.	0.03	0.06	0.05	0.03
	Imnavait Creek Wshd.	0.07	0.14	0.09	0.01
	Avg.	**0.05**	**0.10**	**0.07**	**0.02**
	Max.	**0.07**	**0.14**	**0.09**	**0.03**
	Min.	**0.03**	**0.06**	**0.05**	**0.01**
TDD (April 15–May 31)	Atigun Pass	0.00	0.00	0.02	0.01
	Deadhorse	0.00	0.00	0.02	0.00
	Avg.	**0.00**	**0.00**	**0.02**	**0.01**
	Max.	**0.00**	**0.00**	**0.02**	**0.01**
	Min.	**0.00**	**0.00**	**0.02**	**0.00**

Table 27. Correlation coefficient (R^2), accumulated precipitation

Parameter	Location	Atigun Pass	Atigun Camp	Imnavait Creek	Sagwon	Prudhoe Bay
End-of-Winter SWE (late April)	Upper Kuparuk R. Watershed	0.09	0.03	0.13	0.16	0.07
	Imnavait Creek Watershed	0.02	0.12	0.24	0.20	0.08
	Avg.	**0.06**	**0.08**	**0.19**	**0.18**	**0.08**
	Max.	**0.09**	**0.12**	**0.24**	**0.20**	**0.08**
	Min.	**0.02**	**0.03**	**0.13**	**0.16**	**0.07**

9.3 Correlation with River Overflood Area

The foregoing environmental variables (streamflow, precipitation, snowpack, and air temperature) were compared with the annual overflood areas from the Colville, Kuparuk, and Sagavanirktok Rivers for the 21-year period between 2000 and 2020 (**Table 8**). The objective was to determine if any of the environmental parameters could be used to predict the severity of future overflood seasons. The pre-MODIS era (1995–1999) was not included in this portion of the analysis, given that the paucity of available imagery resulted in cases where the entire overflood area was not mapped.

The environmental parameters described above were compared to three metrics:

- The overflood area classified by river;
- The overflood area classified by watershed boundary (WBD); and
- The total overflood area within the study region.

The rivers and watershed boundaries considered as part of the analysis correspond to those with streamflow measurements: the Colville, Kuparuk, and Sagavanirktok Rivers, and the Lower Colville River, Kuparuk River, and Sagavanirktok River Watershed Boundaries.

Table 28 delineates the correlation coefficients between each environmental parameter and the corresponding overflood area for the three rivers under consideration. The R^2 values ranged from 0.00 to 0.27, indicating that none of the selected environmental parameters can be used to predict the relative magnitude of the overflood area associated with a given river. For example, **Figure 34** illustrates the agreement between the four streamflow parameters and the annual overflood area for the Colville River. The remaining figures are provided in **Appendix D**.

Similarly, little to no correlation was found when comparing the environmental parameters to the overflood areas originating from the three watershed boundaries. The R^2 values, shown in **Table 29**, ranged from 0.00 to 0.28, with the strongest correlation found between overflood area and precipitation.

Finally, the correlation between the environmental parameters and the total overflood area was investigated. Little to no correlation was identified with either the streamflow parameters (**Table 30**) or the precipitation, SWE, and TDD values (**Table 31**).

While it is likely that the selected environmental parameters influence river overflood processes, the absence of a direct correlation between any one variable and the overflood area illustrates the complexity of the processes under consideration.

Table 28. Correlation coefficient (R^2), river overflood area

Parameter	Value/Location	Colville River	Kuparuk River	Sagavanirktok River
Streamflow[1]	Peak Discharge	0.06	0.10	0.00
	Avg. Discharge	0.02	0.09	0.01
	Flood Volume	0.18	0.04	0.02
	Flood Intensity	0.02	0.04	0.06
	Avg.	**0.07**	**0.07**	**0.02**
	Max.	**0.18**	**0.10**	**0.06**
	Min.	**0.02**	**0.04**	**0.00**
Accumulated Precipitation (Oct 1–May 31)	Atigun Pass	0.02	0.00	0.06
	Atigun Camp	0.18	0.00	0.09
	Imnavait Creek	0.27	0.02	0.03
	Sagwon	0.00	0.00	0.03
	Prudhoe Bay	0.04	0.00	0.00
	Avg.	**0.10**	**0.00**	**0.04**
	Max.	**0.27**	**0.02**	**0.09**
	Min.	**0.00**	**0.00**	**0.00**
End-of-Winter SWE (late April)	Upper Kuparuk R. Wshd.	0.04	0.07	0.00
	Imnavait Creek Wshd.	0.11	0.09	0.00
	Avg.	**0.08**	**0.08**	**0.00**
	Max.	**0.11**	**0.09**	**0.00**
	Min.	**0.04**	**0.07**	**0.00**
TDD (April 15–May 31)	Atigun Pass	0.00	0.18	0.05
	Deadhorse	0.01	0.00	0.01
	Avg.	**0.01**	**0.09**	**0.03**
	Max.	**0.01**	**0.18**	**0.05**
	Min.	**0.00**	**0.00**	**0.01**

[1] Streamflow gauge corresponds to river used for overflood area
(*e.g.*, Colville streamflow gauge compared to overflood area from Colville River).

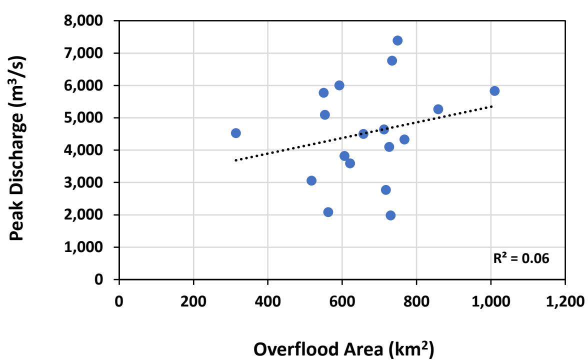

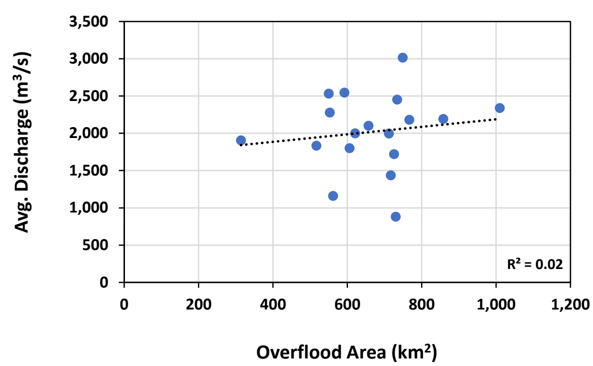

(continued on next page)

Figure 34. Correlation between streamflow and Colville River overflood area

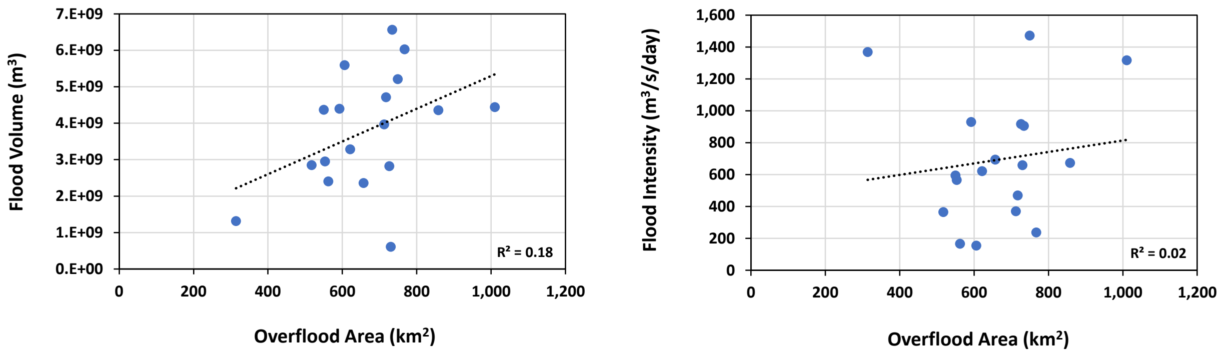

Figure 34. Correlation between streamflow and Colville River overflood area (cont.)

Table 29. Correlation coefficient (R^2), watershed boundary overflood area

Parameter	Value/Location	Lower Colville River WBD	Kuparuk R. WBD	Sagavanirktok River WBD
Streamflow[1]	Peak Discharge	0.05	0.14	0.00
	Avg. Discharge	0.02	0.15	0.01
	Flood Volume	0.17	0.03	0.02
	Flood Intensity	0.02	0.09	0.06
	Avg.	**0.07**	**0.10**	**0.02**
	Max.	**0.17**	**0.15**	**0.06**
	Min.	**0.02**	**0.03**	**0.00**
Accumulated Precipitation (Oct 1–May 31)	Atigun Pass	0.03	0.00	0.06
	Atigun Camp	0.19	0.00	0.09
	Imnavait Creek	0.28	0.01	0.03
	Sagwon	0.00	0.00	0.03
	Prudhoe Bay	0.04	0.02	0.00
	Avg.	**0.11**	**0.01**	**0.04**
	Max.	**0.28**	**0.02**	**0.09**
	Min.	**0.00**	**0.00**	**0.00**
End-of-Winter SWE (late April)	Upper Kuparuk R. Wshd.	0.03	0.10	0.00
	Imnavait Creek Wshd.	0.10	0.11	0.00
	Avg.	**0.07**	**0.11**	**0.00**
	Max.	**0.10**	**0.11**	**0.00**
	Min.	**0.03**	**0.10**	**0.00**
TDD (April 15–May 31)	Atigun Pass	0.00	0.18	0.05
	Deadhorse	0.01	0.03	0.01
	Avg.	**0.01**	**0.11**	**0.03**
	Max.	**0.01**	**0.18**	**0.05**
	Min.	**0.00**	**0.03**	**0.01**

[1] Streamflow gauge corresponds to WBD used for overflood area (*e.g.*, Colville streamflow gauge compared to Lower Colville River WBD overflood area).

Table 30. Correlation coefficient (R^2), total overflood area and streamflow

Parameter	Value	Total Overflood Area		
		Colville River	Kuparuk River	Sagavanirktok R.
Streamflow[1]	Peak Discharge	0.21	0.06	0.08
	Avg. Discharge	0.10	0.09	0.06
	Flood Volume	0.11	0.00	0.00
	Flood Intensity	0.25	0.05	0.27
	Avg.	**0.17**	**0.05**	**0.10**
	Max.	**0.25**	**0.09**	**0.27**
	Min.	**0.10**	**0.00**	**0.00**

[1] Streamflow gauge corresponds to river named in column heading

Table 31. Correlation coefficient (R^2), total overflood area and precipitation, SWE and TDD

Parameter	Location	Total Overflood Area
Accumulated Precipitation (Oct 1–May 31)	Atigun Pass	0.05
	Atigun Camp	0.09
	Imnavait Creek	0.13
	Sagwon	0.00
	Prudhoe Bay	0.00
	Avg.	**0.05**
	Max.	**0.13**
	Min.	**0.00**
End-of-Winter SWE (late April)	Upper Kuparuk R. Wshd.	0.00
	Imnavait Creek Wshd.	0.00
	Avg.	**0.00**
	Max.	**0.00**
	Min.	**0.00**
TDD (April 15–May 31)	Atigun Pass	0.06
	Deadhorse	0.02
	Avg.	**0.04**
	Max.	**0.06**
	Min.	**0.02**

9.4 Correlation with River Overflood Timing

Finally, the air temperature data were examined to determine if TDD could be used to predict the start of overflood. The accumulated TDD between April 15 and the start of overflood (for each of the three major rivers) was tabulated using data measured at the two air temperature stations (Atigun Pass and Deadhorse, **Section 9.1.4**). The results, presented in **Figure 35**, varied significantly, indicating that a TDD threshold above which overflood is likely to commence does not exist.

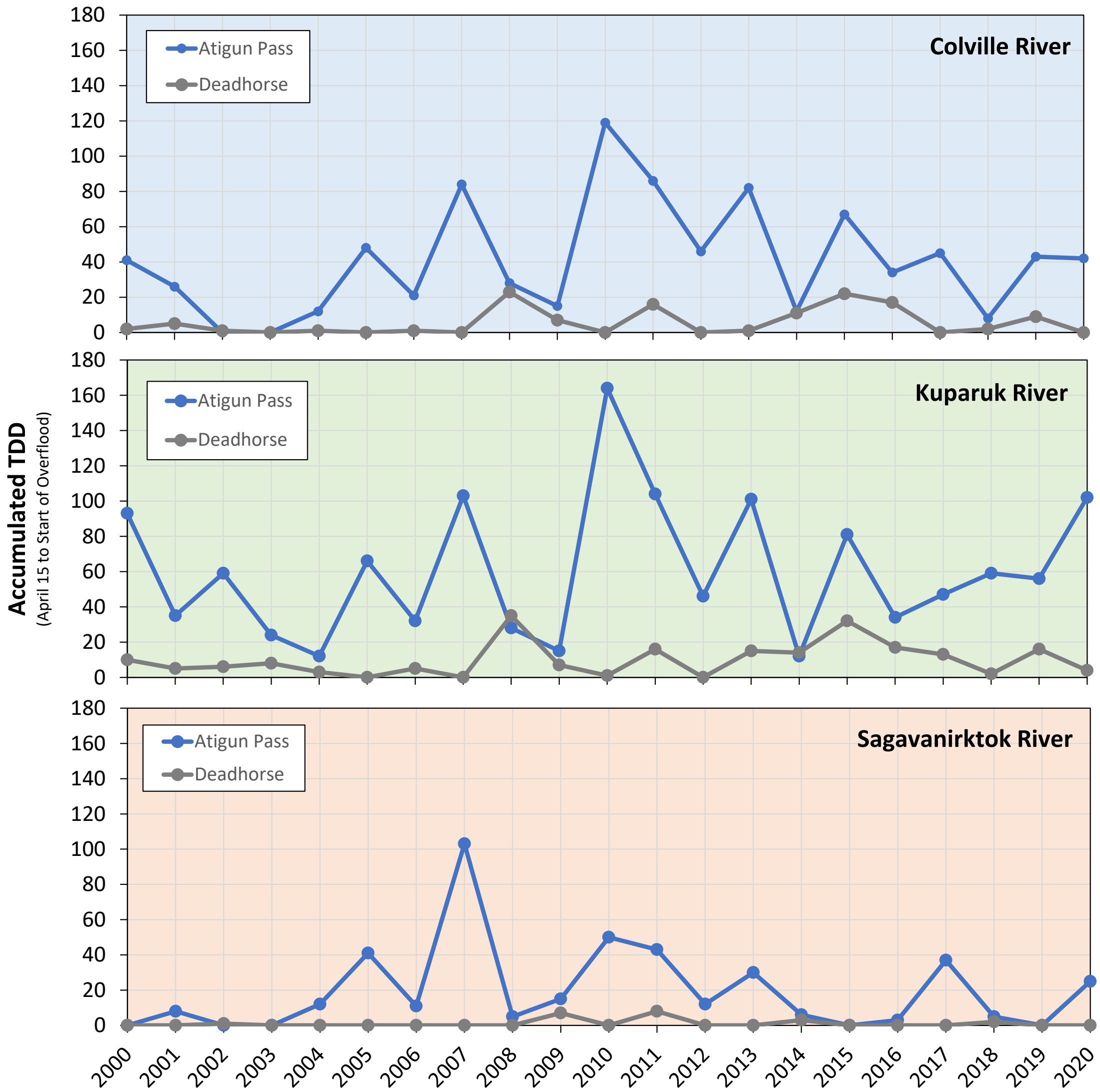

Figure 35. Accumulated thawing degree days (TDD), April 15 to start of overflood

9.5 Multivariate Correlation

Recognizing the complexity of the overflood process and the lack of evidence of any meaningful correlations between discrete variables (**Sections 9.2** to **9.4**), an effort was made to search for correlations across a broad range of potentially dependent variables. The selected variables are summarized in **Table 32**. The Kuparuk River WBD was chosen for this task, as it was the only WBD for which end-of-winter SWE data were available.

Two additional environmental parameters were included in the multivariate analysis: the maximum estimated thickness of the undeformed first-year sea ice at the end of the season and the average air temperature for the entire North Slope Borough, Alaska during the month of May. The maximum undeformed fist-year sea ice thickness was estimated using the relationship of Lebedev (Bilello, 1960). The FDD used for the sea ice computations were derived from the Deadhorse air temperature site relative to a reference air temperature of 29°F, the approximate freezing point of seawater. The average May air temperature for the North Slope Borough, the county containing the entire study area, was obtained from the U.S. Climate Divisional Database (NOAA, 2022b). This data was used in lieu of the Deadhorse or Atigun Pass air temperature sites to provide a region-wide assessment of the average May air temperatures.

Table 32. Variables used to test for multivariate correlations

Category	Location[1]	Value
Streamflow	Kuparuk River Streamflow Gauge	Peak Discharge
		Avg. Discharge
		Flood Volume
		Flood Intensity
		Start of Break-up
		Duration of Break-up
Snowpack	Imnavait Creek Watershed	End-of-Winter SWE
Air Temperature	Deadhorse Air Temperature Site	Date of Maximum FDD Accumulation (onset of thawing)
		Calculated Max. Annual Sea Ice Thickness
	North Slope Borough, Alaska[2]	Average air temperature in May
Satellite Imagery	Kuparuk River	Start of Overflood
		Overflood Area

[1] Locations shown in **Figure 30**. North Slope Borough, Alaska not shown.

[2] Source: U.S. Climate Divisional Database (NOAA, 2022b), North Slope Borough, Alaska.

The available annual values during the study period (1995–2020) were categorized by color as below-average, average, above-average, and extreme (**Table 33**). The categories then were investigated to determine if any patterns emerged among the selected parameters. While some years appeared to show a pattern, just as many others showed a completely random connection between variables.

For example, the overflood area in 2015 was close to the maximum documented for the Kuparuk River WBD (1995–2020) and accompanied by:

- Extremely high average May air temperature,
- Extremely high end-of-winter SWE,
- Extremely high river discharge (peak and average), flood volume, and flood intensity,
- Earliest recorded start of river break-up,
- Extremely low calculated sea ice thickness,
- Earlier than average onset of thawing (cessation of freezing) at the coast, and
- Much earlier start of river overflood.

At first glance, this pattern is consistent with that expected to result in a large overflood area. However, this is not always the case. In 2010, the Kuparuk River WBD overflood area was similar to that observed in 2015 (well above-average), yet this year was characterized by mostly average environmental conditions, including:

- Average May air temperature,

- Average end-of-winter SWE,
- Average flood volume and average discharge,
- Average start of river break-up,
- Average calculated sea ice thickness,
- Average onset of thawing (cessation of freezing) at the coast, and
- Average start of river overflood.

By contrast, in 2008 the overflood area was extremely low and was accompanied by:

- Average May air temperature,
- Extremely low end-of-winter SWE,
- Extremely low peak discharge and flood volume,
- Average flood intensity,
- Average start of river break-up,
- Above average sea ice thickness,
- Below average onset of thawing (cessation of freezing) at the coast, and
- Average start of river overflood.

In 2001, the average May air temperature was extremely low (11°F below the average for the 1995–2020 study period). While the other key parameters appear to fit that expected following a very cold spring (listed below), the eventual overflood area was slightly above average.

- Extremely low average May air temperature,
- Average end-of-winter SWE,
- Above average peak discharge,
- Below average flood volume,
- Above average flood intensity,
- Much later start of river break-up,
- Shorter duration of river break-up,
- Much later onset of thawing (cessation of freezing) at the coast, and
- Much later start of river overflood.

These examples illustrate the difficulty in predicting the relative magnitude of the river overflood area using the selected environmental parameters. The interactions among environmental forcing parameters appear to be sufficiently complex such that no clear correlations exist.

Table 33. Values used to test for multivariate correlations, Kuparuk River

Year	Peak Discharge (m^3/s)	Avg. Discharge (m^3/s)	Flood Volume (m^3 x10^6)	Flood Intensity (m^3/s/d)	Start of Break-up	Duration of Break-up (days)	End-of-Winter SWE[1] (mm)	Max Calc. Sea Ice Thickness (cm)	Date of Max FDD[2]	Avg. May Temp.[3] (°F)	WBD Start of Overflood	WBD Overflood Area (km^2)
1995	566	382	692	89	5/27	21	152	168	5/24	32.7	-[4]	173
1996	1,529	673	930	283	5/24	16	136	157	5/9	30.2	-[4]	99
1997	1,631	614	1,060	135	5/28	20	140	170	6/3	28.1	-[4]	100
1998	1,272	546	566	157	5/23	12	96	150	5/15	29.5	-[4]	153
1999	564	350	393	113	6/2	13	88	165	6/8	28.3	-[4]	70
2000	2,209	784	1,016	363	6/8	15	112	168	6/6	21.1	6/8	285
2001	1,558	607	630	361	6/7	12	127	165	6/9	17.4	6/7	259
2002	1,416	699	483	425	5/22	8	89	163	5/30	31.4	5/21	307
2003	1,218	545	518	221	6/3	11	137	152	6/3	27.5	6/2	291
2004	850	524	815	71	5/25	18	116	163	6/5	30.7	5/22	256
2005	949	468	809	68	5/30	20	123	163	6/6	31.0	5/25	229
2006	850	401	624	159	5/26	18	96	173	5/23	28.9	5/27	253
2007	1,747	759	525	310	6/3	8	115	165	6/3	24.4	5/31	137

[1] Location: Imnavait Creek Watershed (**Table 21**)

[2] Location: Deadhorse (**Table 21**)

[3] Location: North Slope Borough, Alaska

[4] Start of overflood not detected during pre-MODIS era (1995–1999).

(Table continued on next page)

Color Code

Magnitude	Timing	Duration
Extremely High	Much Later	Much Longer
Above-Average	Later	Longer
Average	Average	Average
Below-Average	Earlier	Shorter
Extremely Low	Much Earlier	Much Shorter

Table 33. Values used to test for multivariate correlations, Kuparuk River (continued)

Year	Peak Discharge (m^3/s)	Avg. Discharge (m^3/s)	Flood Volume (m^3 x10^6)	Flood Intensity ($m^3/s/d$)	Start of Break-up	Duration of Break-up (days)	End-of-Winter SWE[1] (mm)	Max Calc. Sea Ice Thickness (cm)	Date of Max FDD[2]	Avg. May Temp.[3] (°F)	WBD Start of Overflood	WBD Overflood Area (km^2)
2008	850	477	412	245	5/29	10	75	165	5/22	28.7	5/26	102
2009	1,073	522	1,037	78	5/23	23	155	165	5/29	29.9	5/15	262
2010	1,133	646	894	102	5/29	16	121	160	5/31	27.2	5/29	326
2011	1,388	586	860	190	5/25	17	174	160	5/18	27.1	5/24	279
2012	850	444	690	89	5/26	18	150	178	5/31	25.8	5/27	158
2013	2,549	*922*	1,513	615	6/1	19	161	170	5/28	23.5	5/30	288
2014	1,699	776	1,409	306	5/28	21	-	152	6/1	30.5	5/16	239
2015	2,549	838	1,303	627	5/18	18	207	147	5/15	34.4	5/18	356
2016	1,076	552	572	176	5/20	12	138	147	5/10	33.9	5/17	174
2017	818	418	434	232	5/31	12	176	147	5/23	29.8	5/27	193
2018	1,623	583	1,260	300	6/2	25	-	135	6/8	27.1	5/31	55
2019	1,490	624	593	336	5/23	11	-	137	5/12	32.5	5/21	296
2020	1,815	662	743	357	5/27	13	-	163	5/22	28.9	5/27	359
Avg.	**1,357**	**592**	**799**	**246**	**5/28**	**16**	**131**	**160**	**5/27**	**28.5**	**5/26**	**219**
Max.	**2,549**	**922**	**1,513**	**627**	**6/8**	**25**	**207**	**178**	**6/9**	**34.4**	**6/8**	**359**
Min.	**564**	**350**	**393**	**68**	**5/18**	**8**	**75**	**135**	**5/9**	**17.4**	**5/15**	**55**

[1] Location: Imnavait Creek Watershed (**Table 21**)

[2] Location: Deadhorse (**Table 21**)

[3] Location: North Slope Borough, Alaska

Color Code

Magnitude	Timing	Duration
Extremely High	Much Later	Much Longer
Above-Average	Later	Longer
Average	Average	Average
Below-Average	Earlier	Shorter
Extremely Low	Much Earlier	Much Shorter

9.6 Environmental Data Summary

Despite the use of what was judged to represent the best available environmental data, no meaningful correlations were identified between the annual overflood areas of the Colville, Kuparuk, and Sagavanirktok Rivers and the corresponding values of streamflow, precipitation, snowpack, and air temperature. This is consistent with the results of the 2009 Study.

The most important implication of these findings is that the extent of river overflood onto the sea ice cannot readily be predicted by any single environmental variable for which historical data currently exist. The overflood phenomenon appears to be governed by interactions between a number of environmental forces, some of which (*e.g.,* soil moisture at high elevations at the onset of snowpack thawing, ice jams in distributary channels, roughness and snow cover on the sea ice, wind events during flooding, and the density of drainage features on the sea ice) are complex, for the most part poorly understood, or lack sufficient data to evaluate their contributions to the overall overflood process.

Unfortunately, there appears to be little scientific basis to construct a quantitative model that could utilize the suite of environmental variables analyzed in this study to predict the overflood area and the potential hazard to specific offshore locations in a given year. In the absence of such a model, the detailed long-term mapping of overflood boundaries in this study provides a valuable probabilistic assessment of the potential hazard based on past events.

10 Long-Term Trends

The environmental and overflood data were investigated for evidence of long-term trends. While both data sets exhibit considerable year-to-year variability, clear trends in several parameters are evident over the 26-year study period. It should be noted that the data set used herein is relatively short compared to those typically used in modern climate science. As a result, caution is advised when using the rates of change presented herein to predict future conditions.

10.1 Environmental Data

Each of the four environmental forcing mechanisms (streamflow, precipitation, snowpack, and air temperature) was analyzed to determine if trends are evident over the 26-year study period. **Figure 36** illustrates timeseries of accumulated precipitation (October 1 through May 31) at each of the five measurement stations. Trends identified at the five stations vary considerably. For example, the annual accumulated precipitation values increased slightly over the 26-year study period at the Atigun Camp and Imnavait Creek stations, were essentially unchanged at the Sagwon station, and decreased at the Atigun Pass and Prudhoe Bay stations.

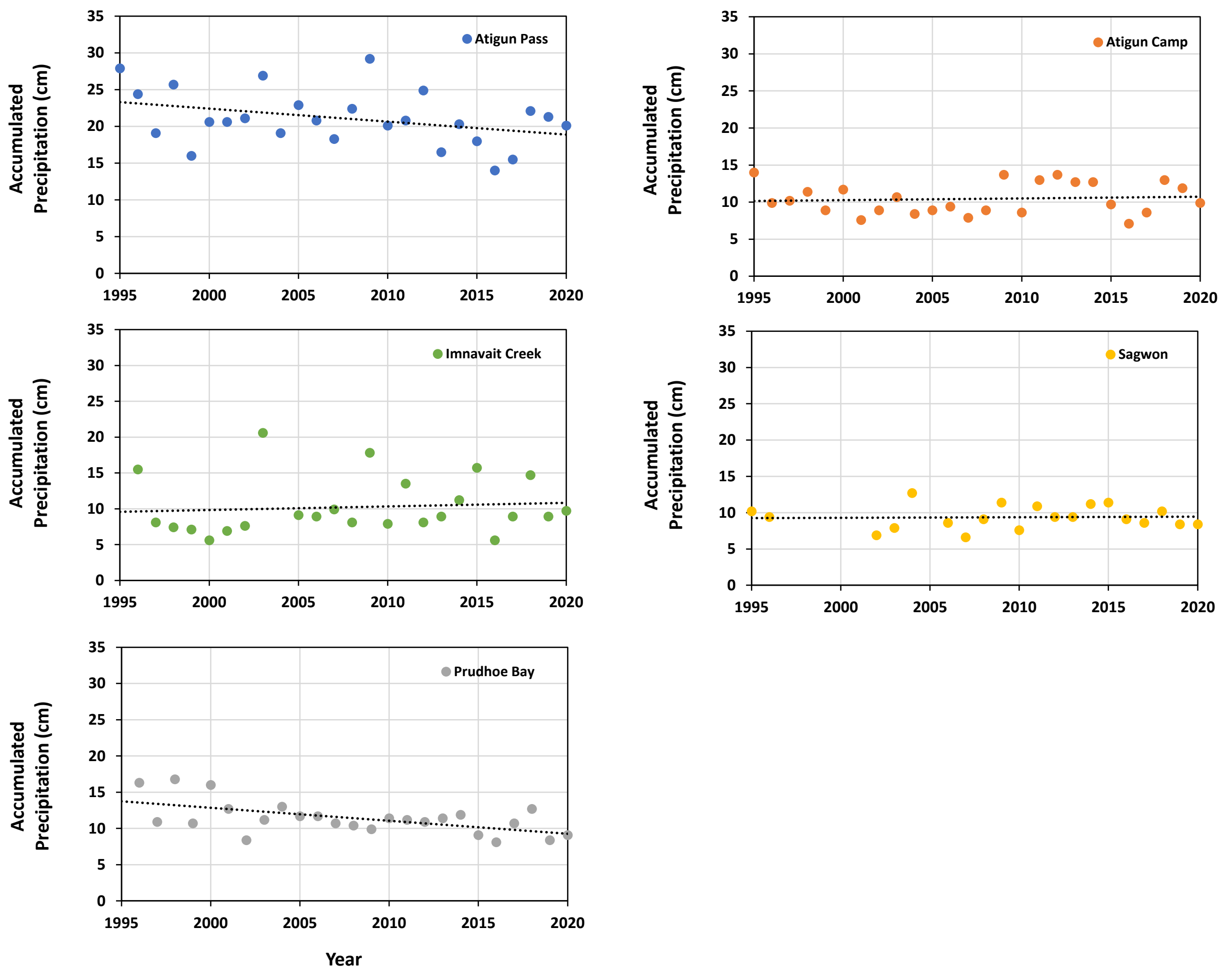

Figure 36. Timeseries of accumulated precipitation

The end-of-winter snowpack measurements clearly increase over the study period at both the Upper Kuparuk River Watershed and Imnavait Creek Watershed SWE sites (**Figure 37**). The average rate of increase is approximately 0.3 cm per year.

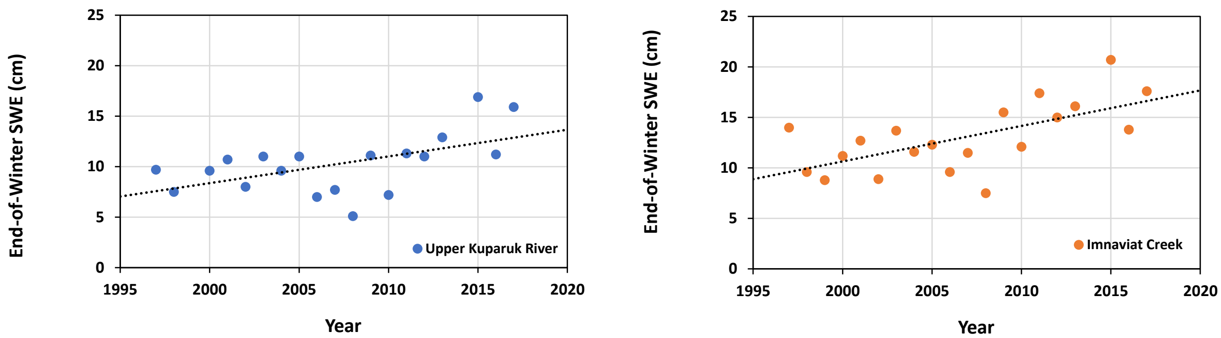

Figure 37. Timeseries of snow-water-equivalent

The average air temperature measured at the Atigun Pass and Deadhorse stations between April 15 and May 31 (the approximate pre-break-up period) is illustrated in **Figure 38**. While there is considerable year-to-year variability in the data, the average air temperature at both stations generally increased over the 26-year period of record. The rate of increase was 0.2°F per year at the Atigun Pass station and 0.1°F per year at the Deadhorse station.

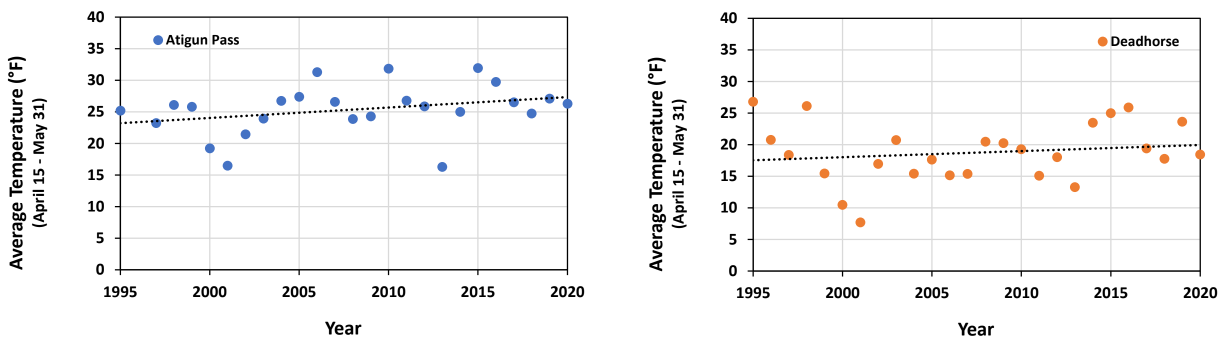

Figure 38. Timeseries of average air temperature, April 15–May 31

Timeseries of the peak and average discharge measured during overflood at the three major rivers under consideration (Colville, Kuparuk, and Sagavanirktok Rivers) are shown in **Figure 39**. Trends in the data are not particularly strong or consistent, with the peak and average discharge decreasing over the 26-year study period on the Colville and Sagavanirktok Rivers, and increasing on the Kuparuk River. Similarly, inconsistent and weak trends were identified in flood volume and flood intensity, as shown in **Figure 40**.

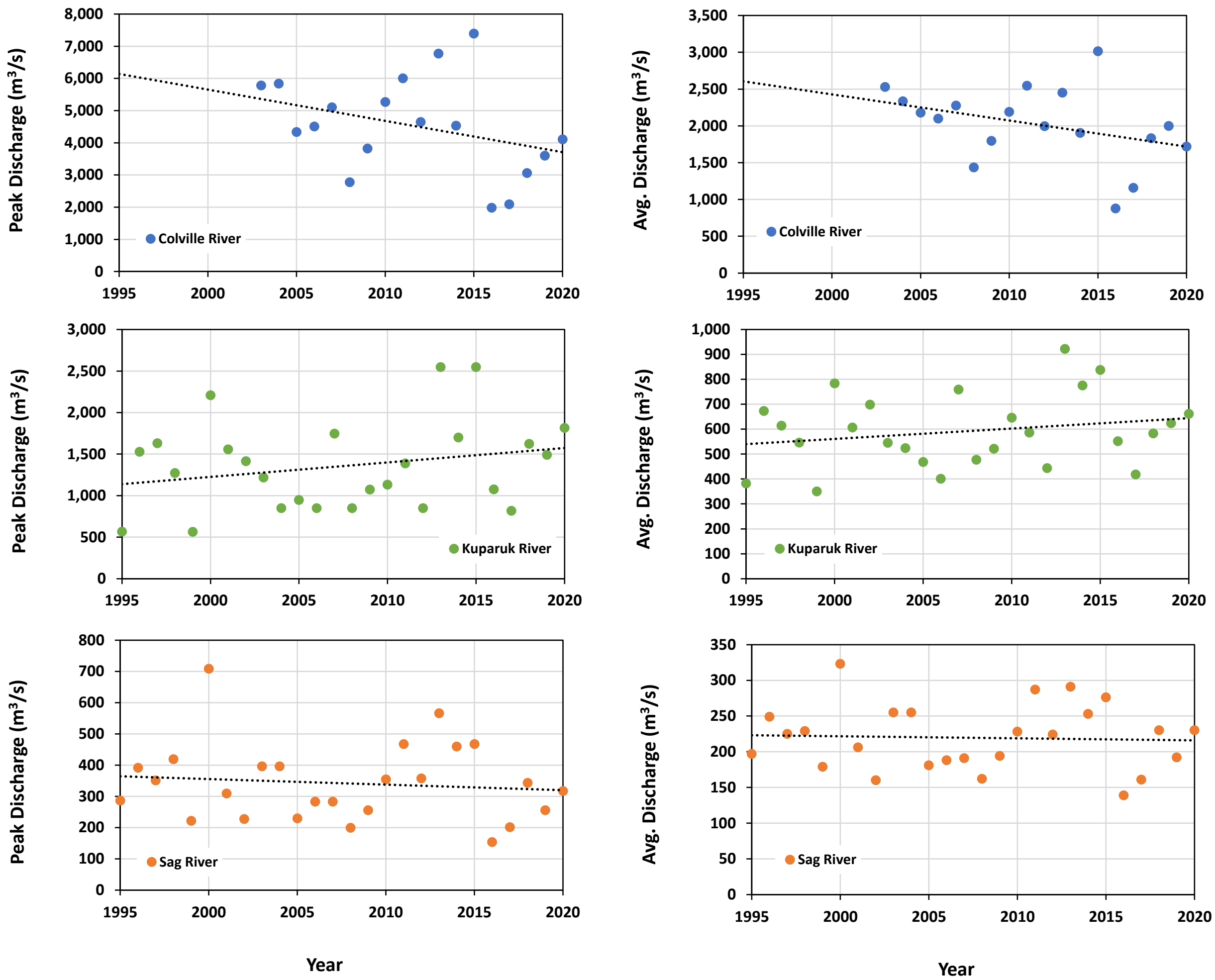

Figure 39. Timeseries of annual peak discharge and average discharge during overflood period

10.2 Overflood Parameters

Trends in overflood area and timing were evaluated using data derived from the MODIS era (2000-2020). The pre-MODIS era was excluded on the basis that the overflood edges mapped may not necessarily represent the peak extent for all rivers in the study area.

Timeseries of the overflood area associated with the Colville, Kuparuk, and Sagavanirktok Rivers are shown in **Figure 41**. A trend of decreasing area is evident over the 21-year period at all three rivers. The rate of decline is greatest at the Colville River and least at the Kuparuk River. When the overflood area associated with the watershed boundaries (rather than the individual rivers) is considered, similar trends emerge.

Figure 42 provides a timeseries of the peak overflood area within the entire study region. Notwithstanding considerable year-to-year variability, the overflood area clearly decreased with time (approximately 18 km^2 per year). It is likely that this decrease resulted from complex interactions between multiple factors, such as a decline in precipitation in parts of the watershed (**Figure 36**), an increase in snowfall on the ice (**Figure 37**), and warmer air temperatures resulting in thinner sea ice.

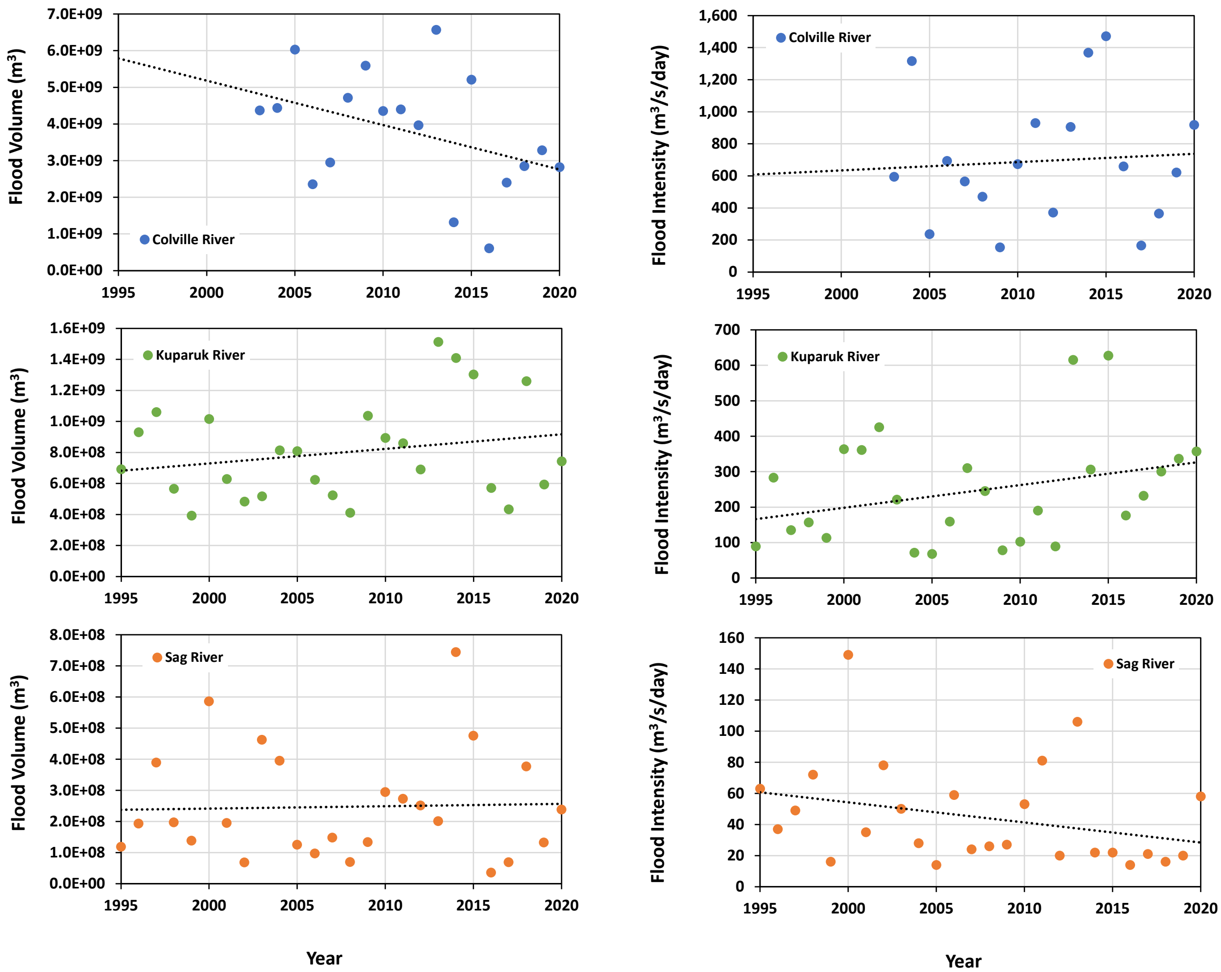

Figure 40. Timeseries of annual flood volume and flood intensity during overflood period

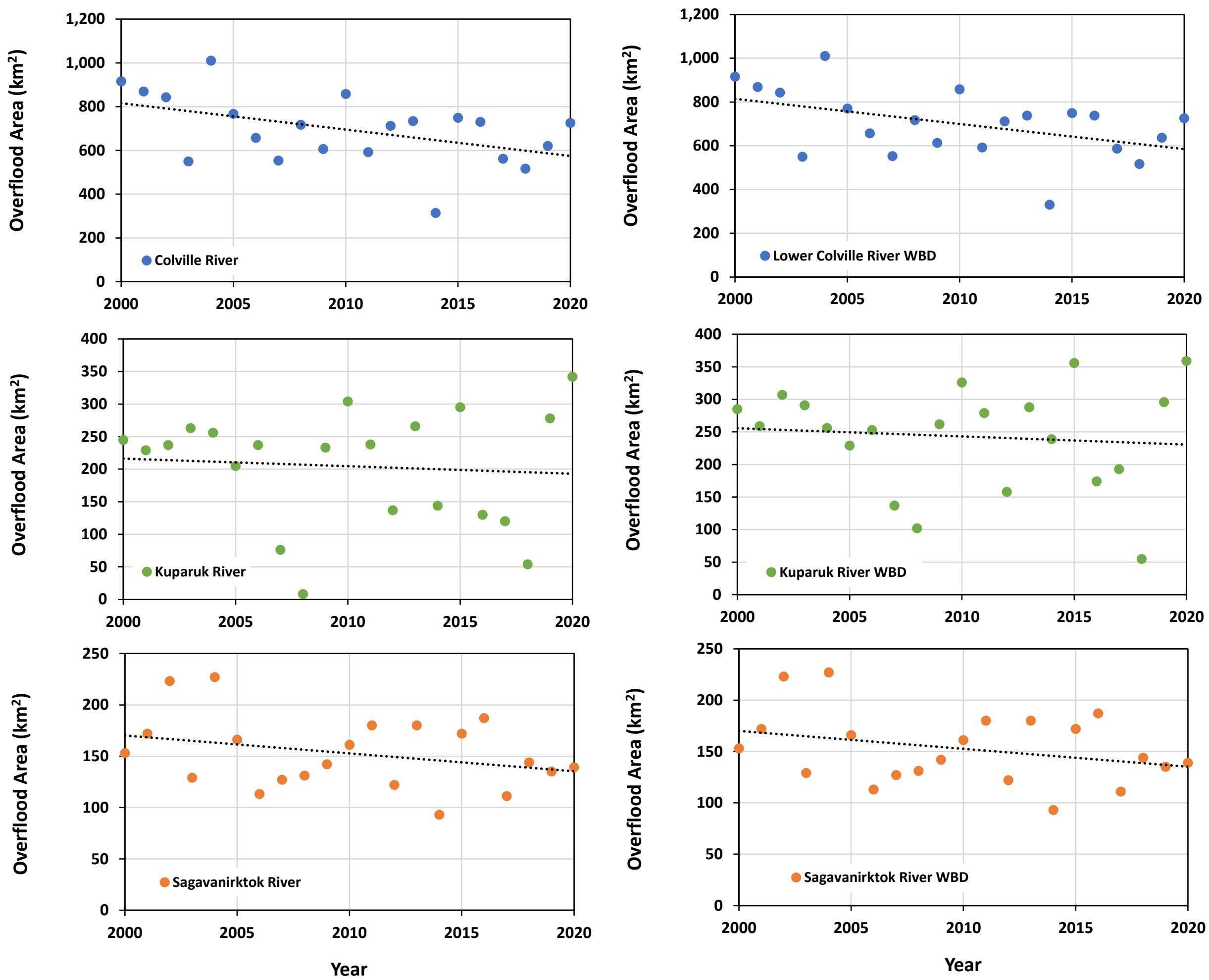

Figure 41. Timeseries of overflood area by river and watershed

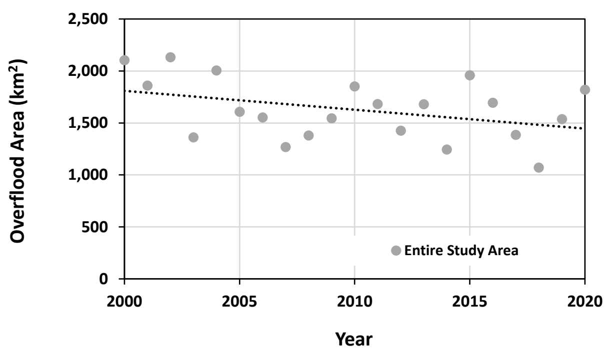

Figure 42. Timeseries of overflood area within study region

Changes in the onset and peak of overflood for each of the three major rivers and three major watershed boundaries in the study area are shown in **Figure 43**. Trends apparent in the figures indicate that the onset and peak of overflood are occurring earlier. **Table 34** summarizes the range of values for each river along with the linear rate of change. While there is some variability in the data, the start and peak of overflood are occurring about 0.4 days per year earlier.

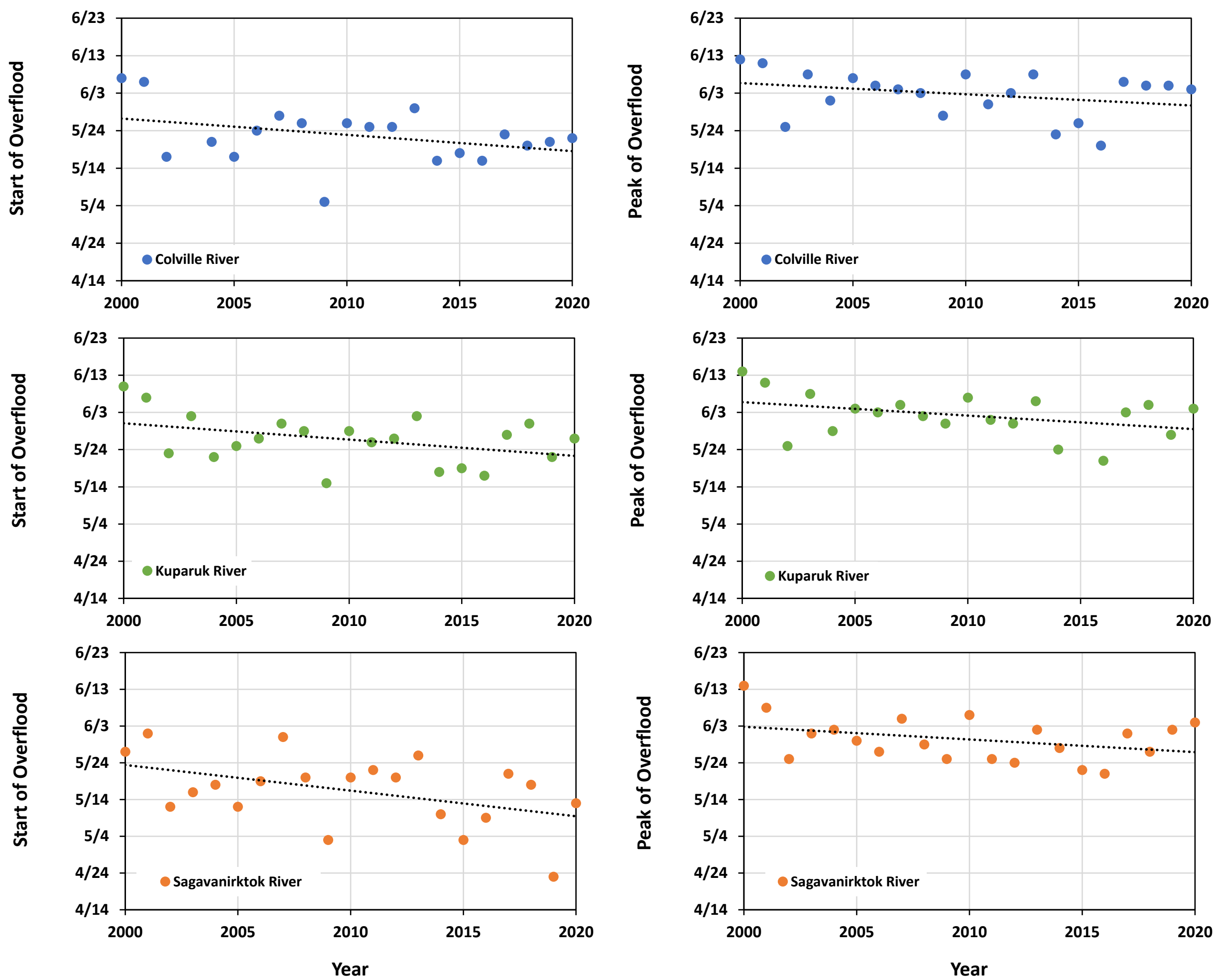

Figure 43. Timeseries of month and day for the onset and peak of river overflood.

Table 34. Trend in start and peak of overflood for primary rivers, 2000–2020

River	Overflood Date	Avg.	Min.	Max.	Trend (days/yr)
Colville River	Start	5/22	5/5	6/7	-0.4
	Peak	6/2	5/20	6/12	-0.3
Kuparuk River	Start	5/26	5/15	6/10	-0.4
	Peak	6/2	5/21	6/14	-0.4
Sagavanirktok River	Start	5/16	4/23	6/1	-0.7
	Peak	5/30	5/21	6/14	-0.3

11 Facility Hazards

This section discusses two potential hazards that river overflood on the sea ice poses to man-made facilities in the U.S. Beaufort Sea: interdiction of access to offshore facilities by flooding, and disturbance of the sea bottom above buried subsea pipelines by strudel scouring (which can compromise the integrity of the pipeline). Both processes were described in detail in **Section 4**. The following sub-sections provide assessments of each hazard based on the data sets described in **Section 6**.

11.1 Flooding

River overflood on the sea ice impacts seasonal ice roads built to support construction, drilling, and resupply operations at offshore sites. Ice roads located within the zone of river overflood can be rendered impassable due to rapid deterioration of the ice sheet (**Figure 44**). While portions of ice roads located beyond the overflood boundary typically are capable of supporting substantial vehicle and equipment loads into June (CFC, 2001), premature ice road closure can be precipitated by the impacts of flooding.

Figure 44. Damage to nearshore ice road due to flooding near the Colville River

Figure 45 and **Figure 46** illustrate the locations of the known ice roads constructed between 1995 and 2020, along with the maximum extent of river overflood for the study period (1995–2020). The ice road data were derived from the 2009 Study, as well as the sources listed in **Section 6.4.** As is illustrated in the figure, at least some portion of each ice road was located within the zone of river overflood and vulnerable to potential damage during break-up. The start date of river overflood documented in the geodatabase provides planners with a useful tool to estimate the anticipated longevity of ice roads constructed in this region.

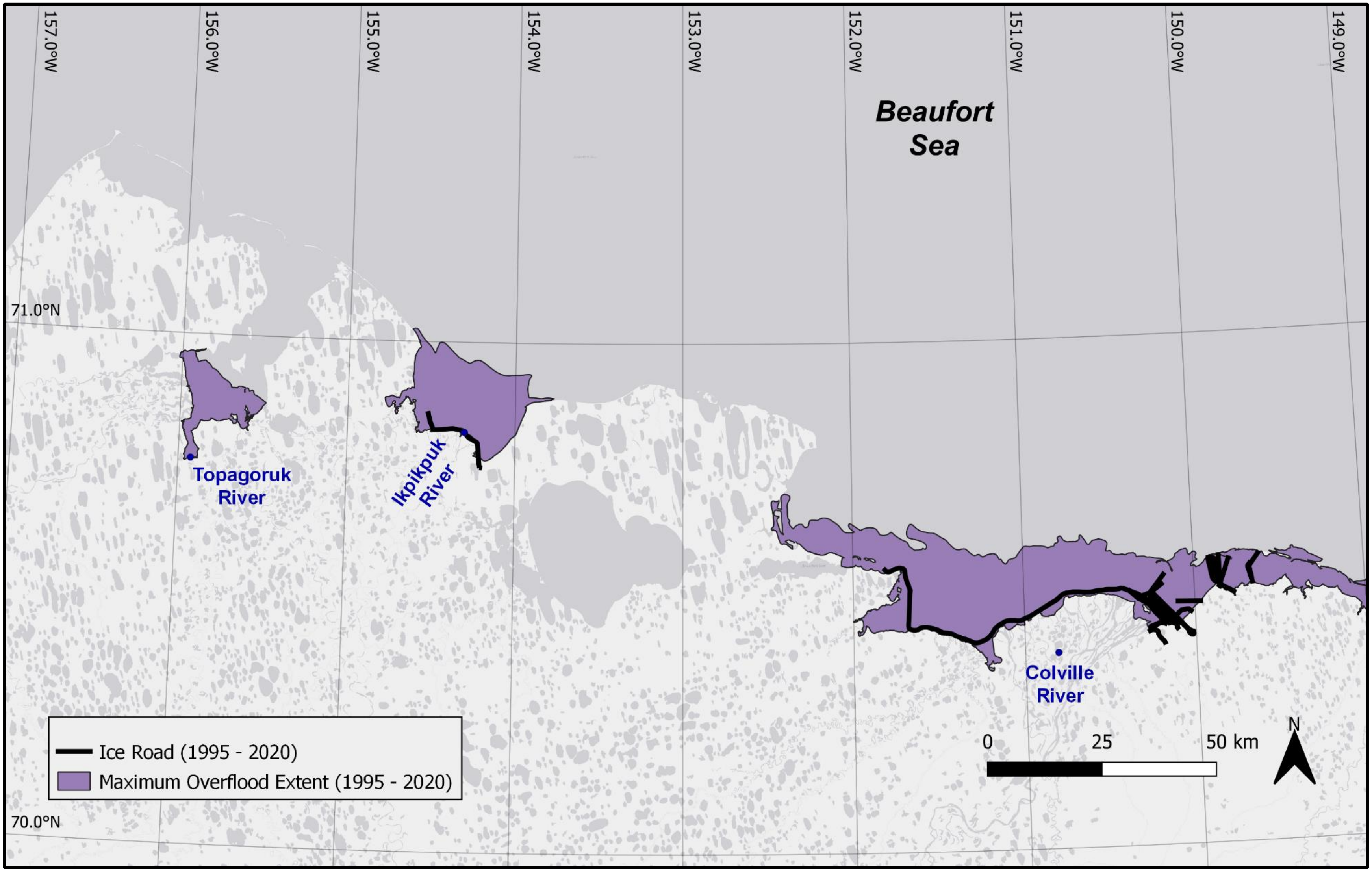

Figure 45. Ice road locations relative to maximum overflood extent, west study region, 1995–2020

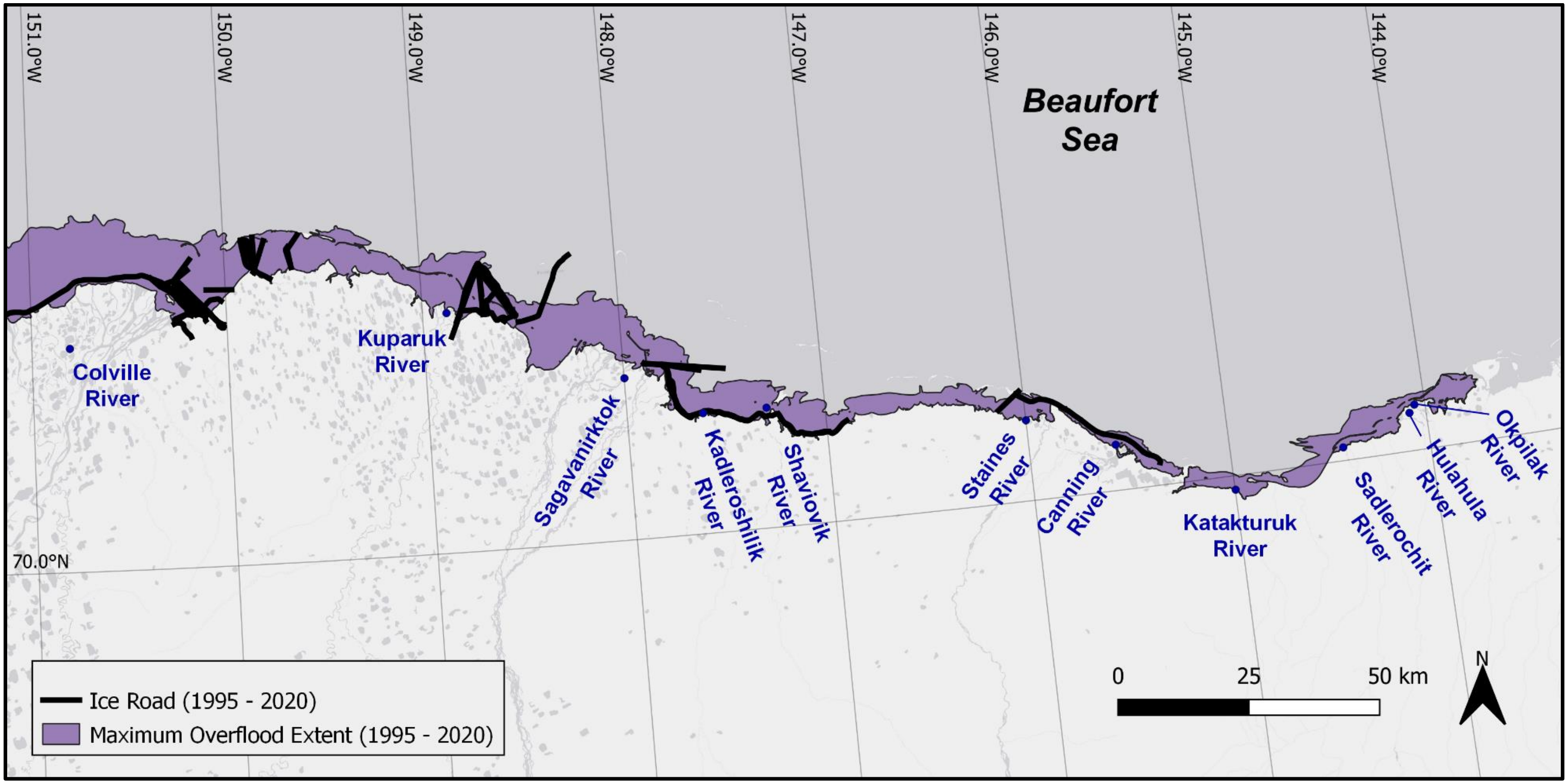

Figure 46. Ice road locations relative to maximum overflood extent, east study area, 1995–2020

11.2 Strudel Scour

As noted in **Section 4.2**, strudel scouring can constitute significant design considerations for subsea pipelines (Lanan *et al.*, 2008) in nearshore areas adjacent to river and stream mouths. In the event that a strudel drain is located directly above a buried subsea pipeline, a sufficiently deep strudel scour may expose the pipeline and lead to an unsupported span. Strudel scours that form directly over buried pipelines also can remove the backfill material that is needed to prevent damage from ice keels and prevent upheaval buckling. In addition, strudel drainage provides a mechanism to transport spilled oil below the ice sheet.

As a point of beginning, the potential for strudel scour formation was assessed using the overflood areas presented in **Section 8.1** segregated by the three zones of strudel formation discussed in **Section 4.2**. The results, presented in **Figure 47**, show that the majority of the overflood area falls within the Secondary Strudel Zone (62%), followed by the Primary (37%) and Tertiary Zones (1%).

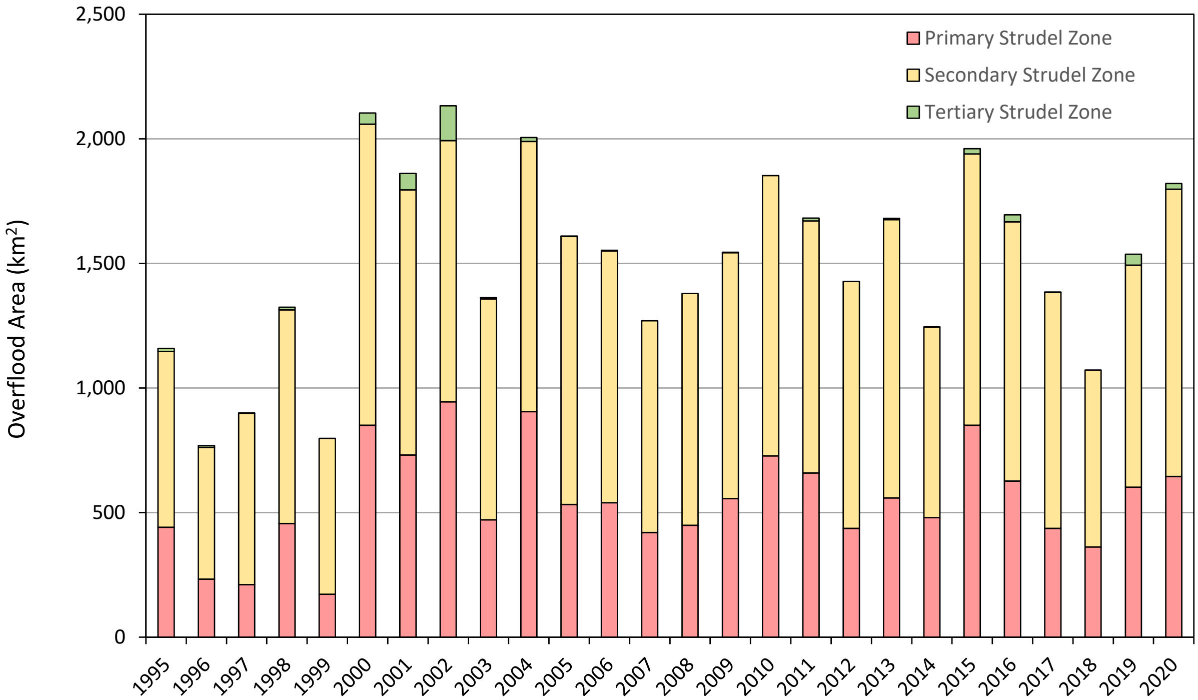

Figure 47. Overflood area segregated by strudel zone

Figure 48 through **Figure 58** illustrate the strudel drains and strudel scours mapped as part of the industry-sponsored studies described in **Section 6.3**. The scours are colored relative to the zonation described in **Section 4.2**. The distribution of the measured strudel scours in each study area is shown in **Figure 59**. As expected, the largest number of scours occurred in the Primary Strudel Zone (1,872 scours), followed by the Secondary (451 scours) and Tertiary Zones (2 scours).

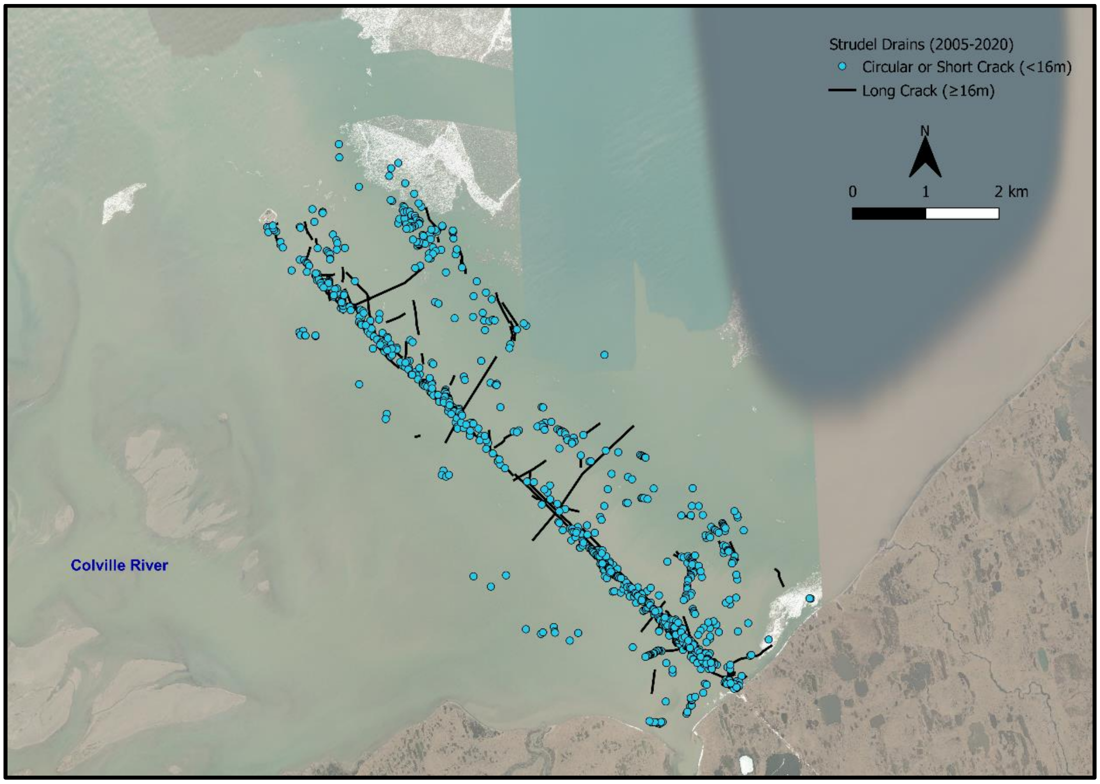

Figure 48. Strudel drains mapped near the Colville River

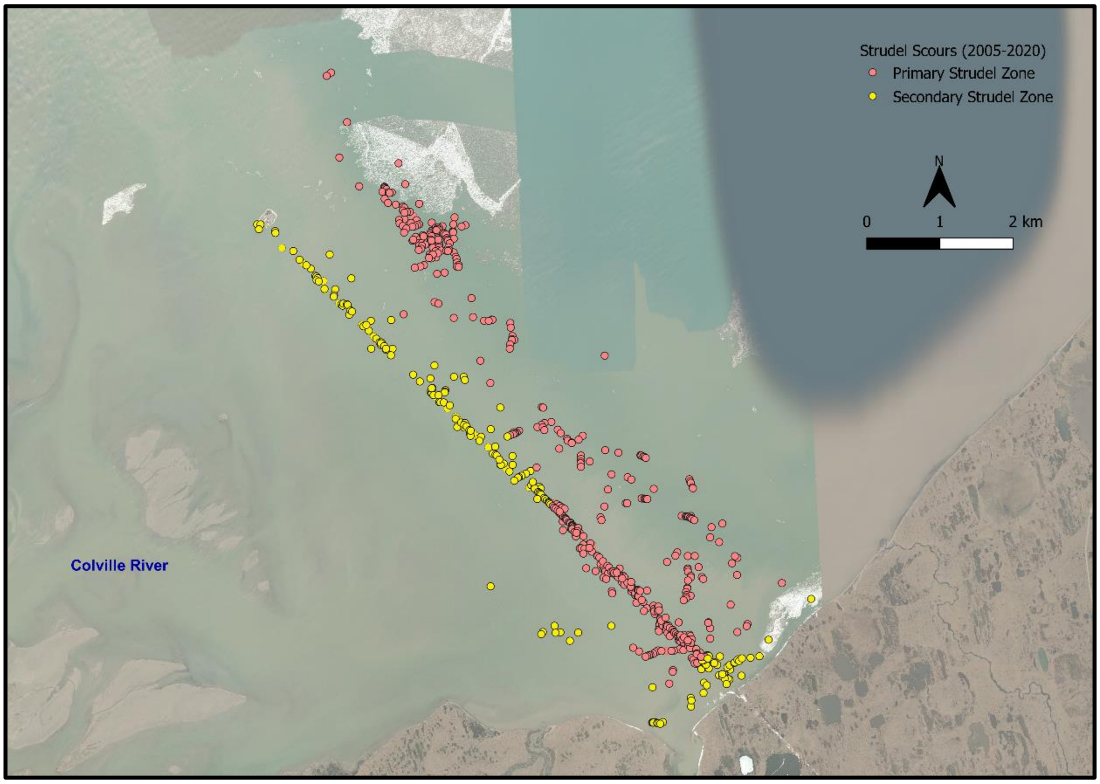

Figure 49. Strudel scours mapped near the Colville River

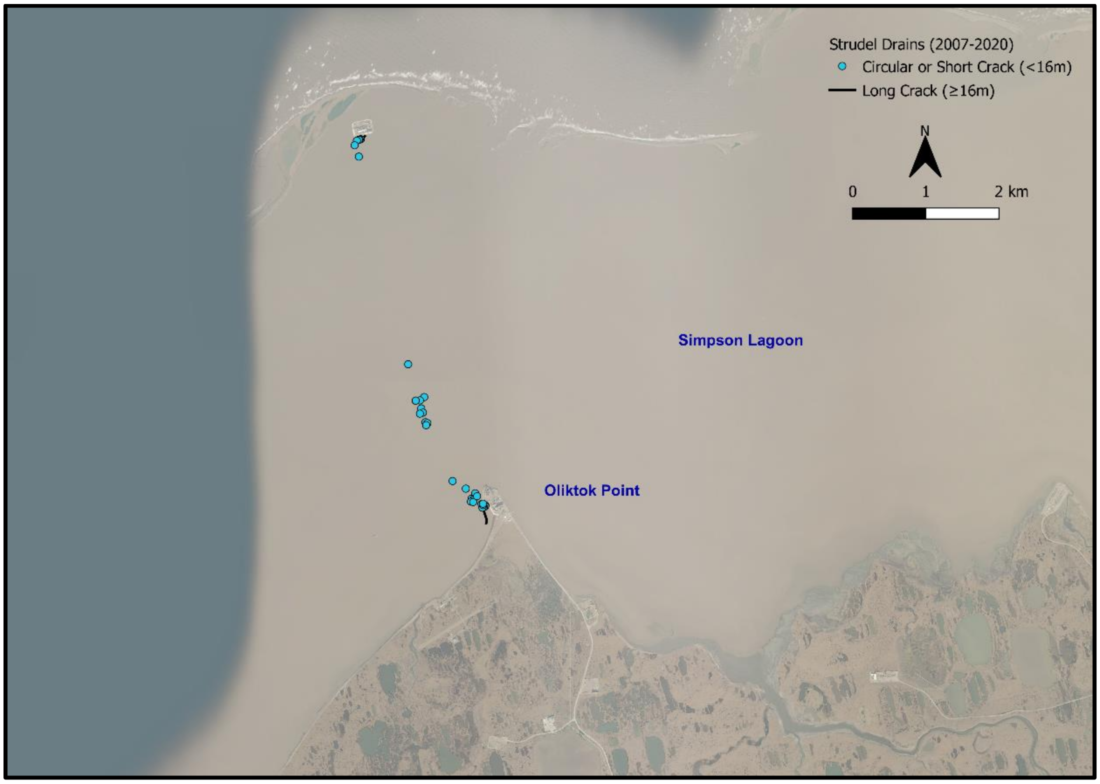

Figure 50. Strudel drains mapped near Simpson Lagoon

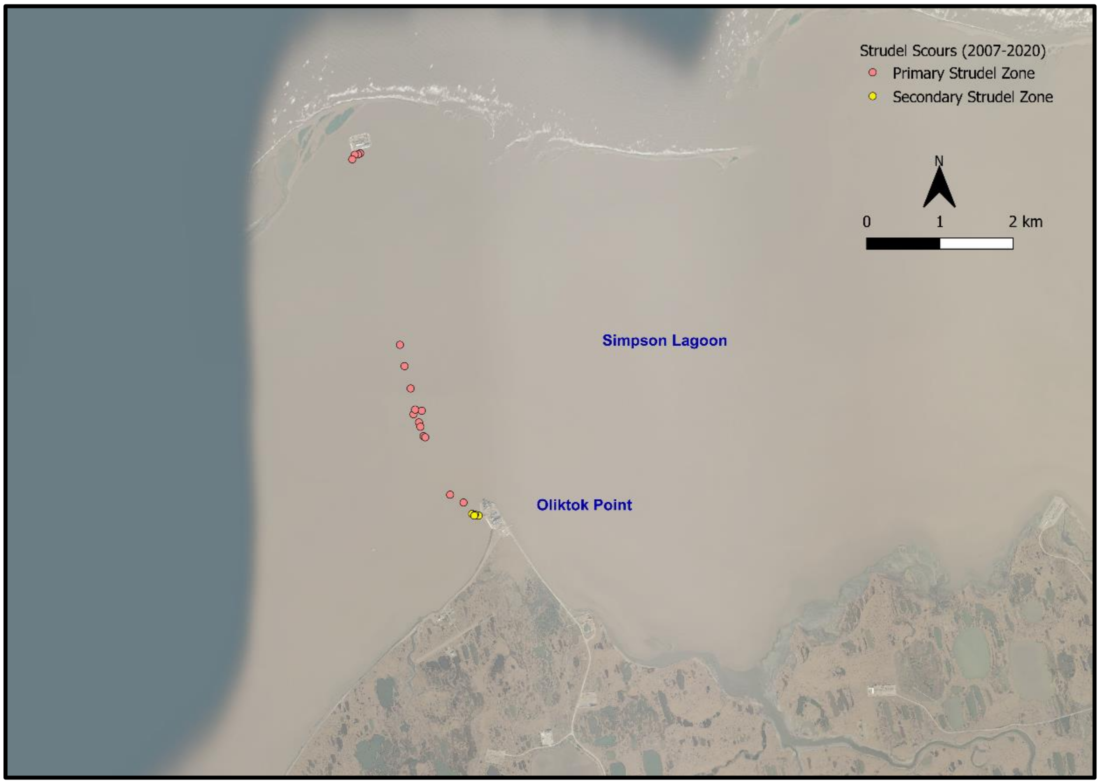

Figure 51. Strudel scours mapped near Simpson Lagoon

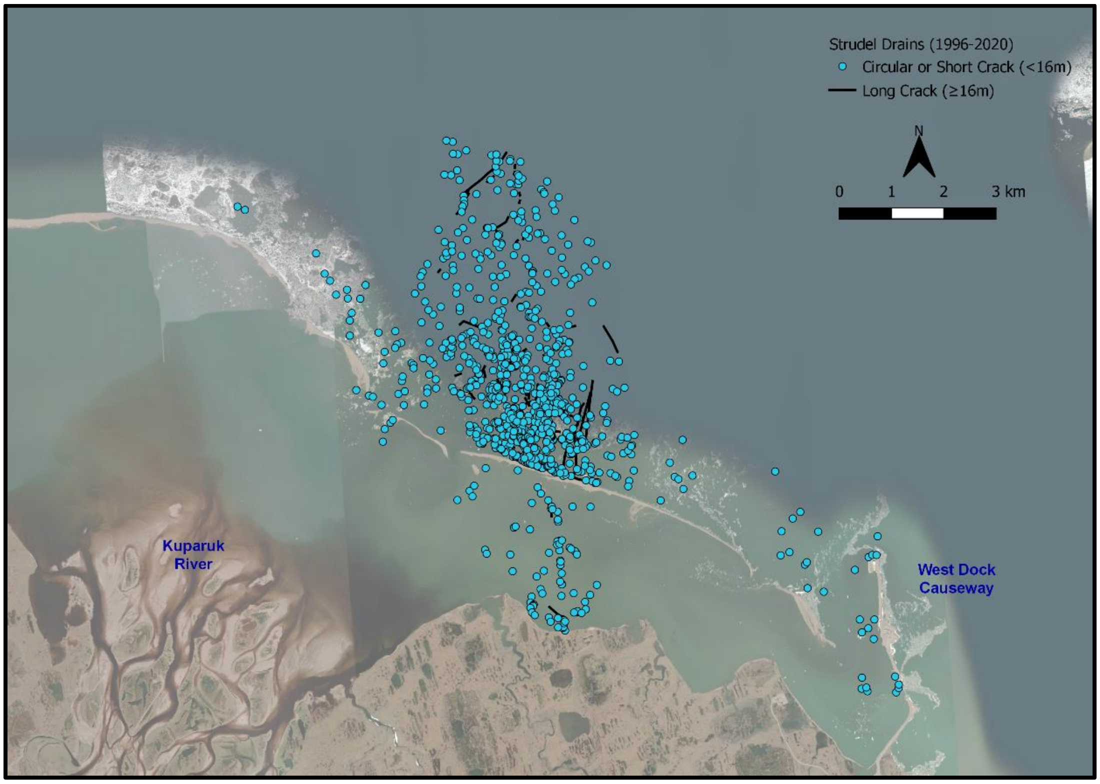

Figure 52. Strudel drains mapped near the Kuparuk River

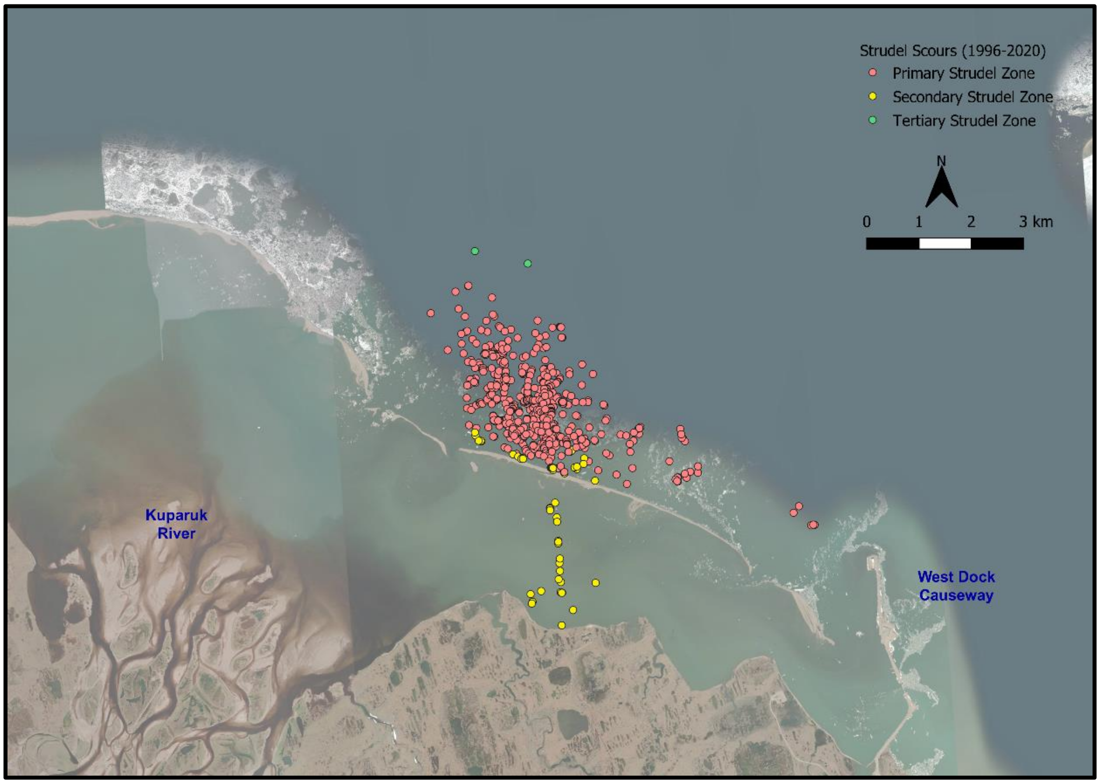

Figure 53. Strudel scours mapped near the Kuparuk River

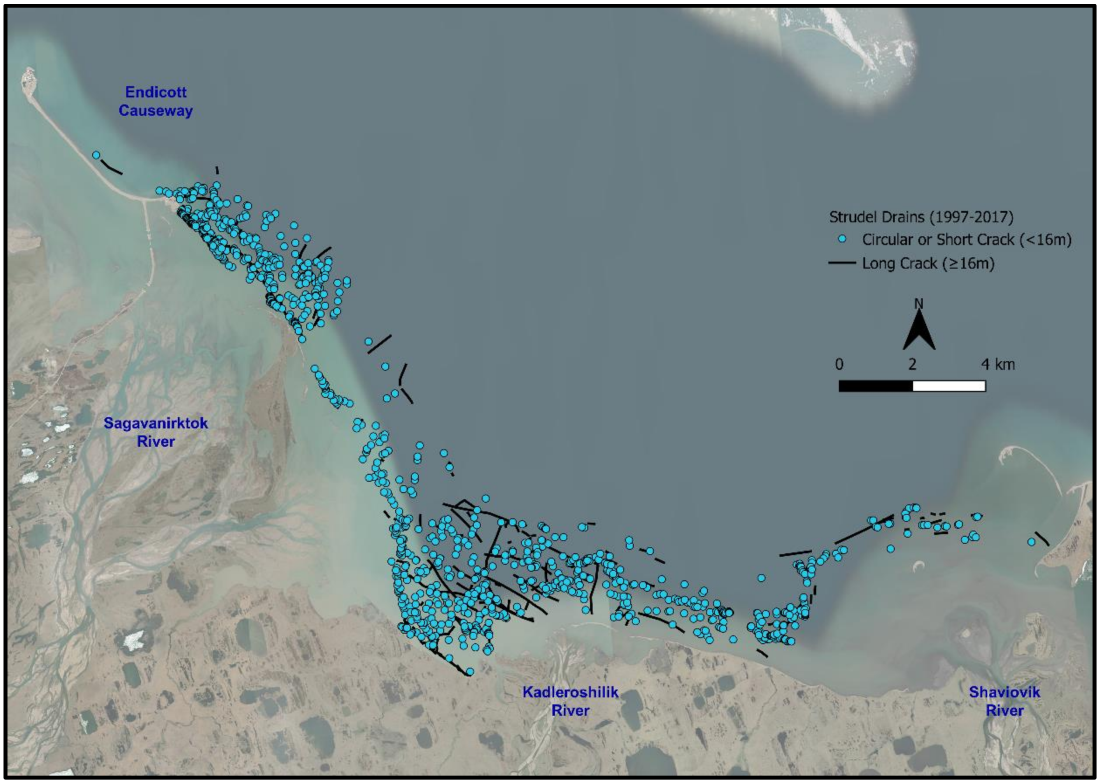

Figure 54. Strudel drains mapped near the Sagavanirktok, Kadleroshilik, and Shaviovik Rivers

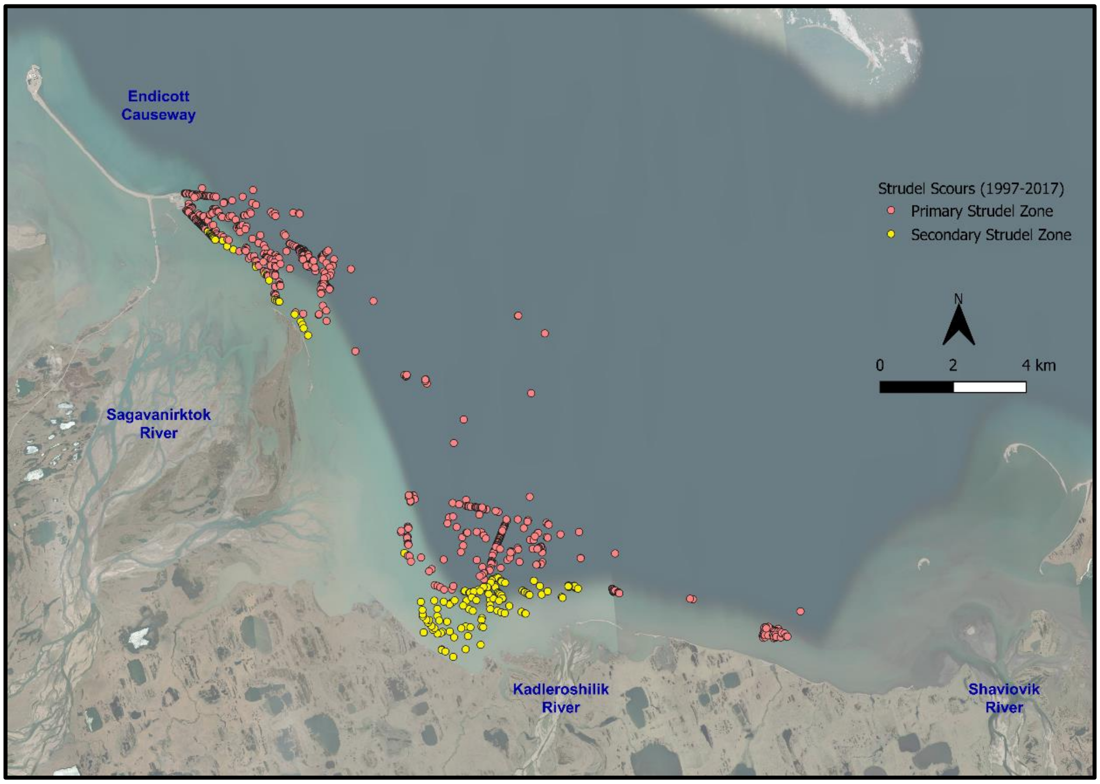

Figure 55. Strudel scours mapped near the Sagavanirktok, Kadleroshilik, and Shaviovik Rivers

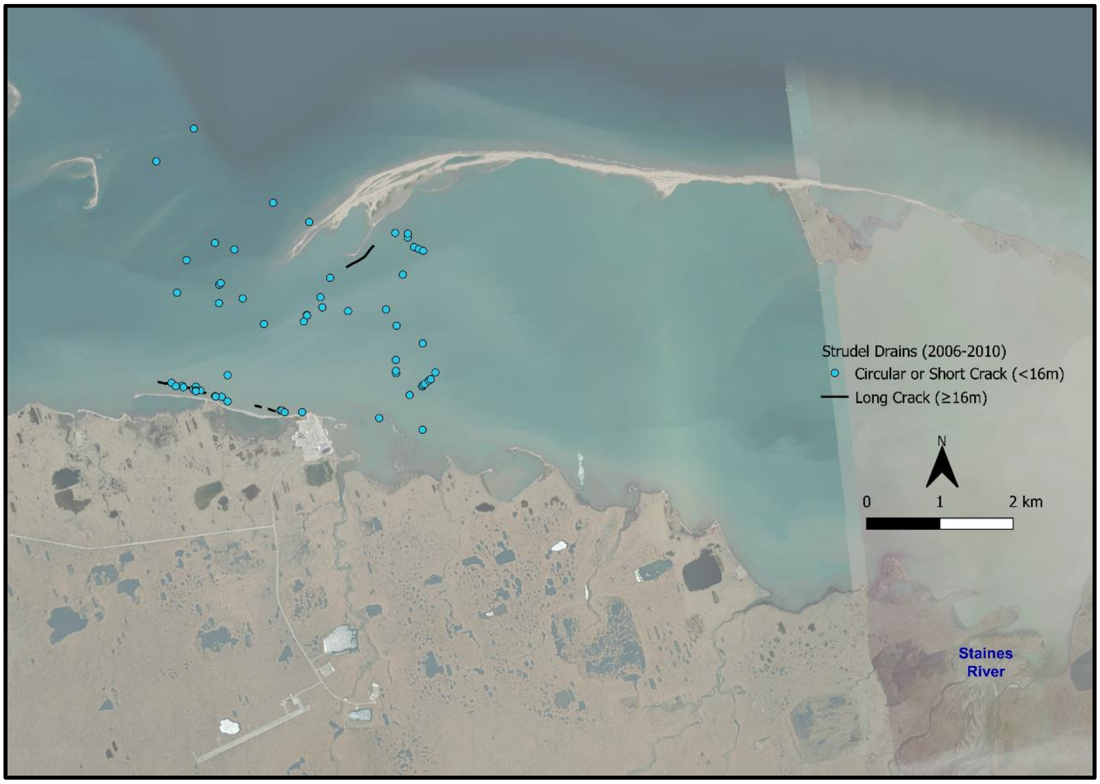

Figure 56. Strudel drains mapped near the Staines River

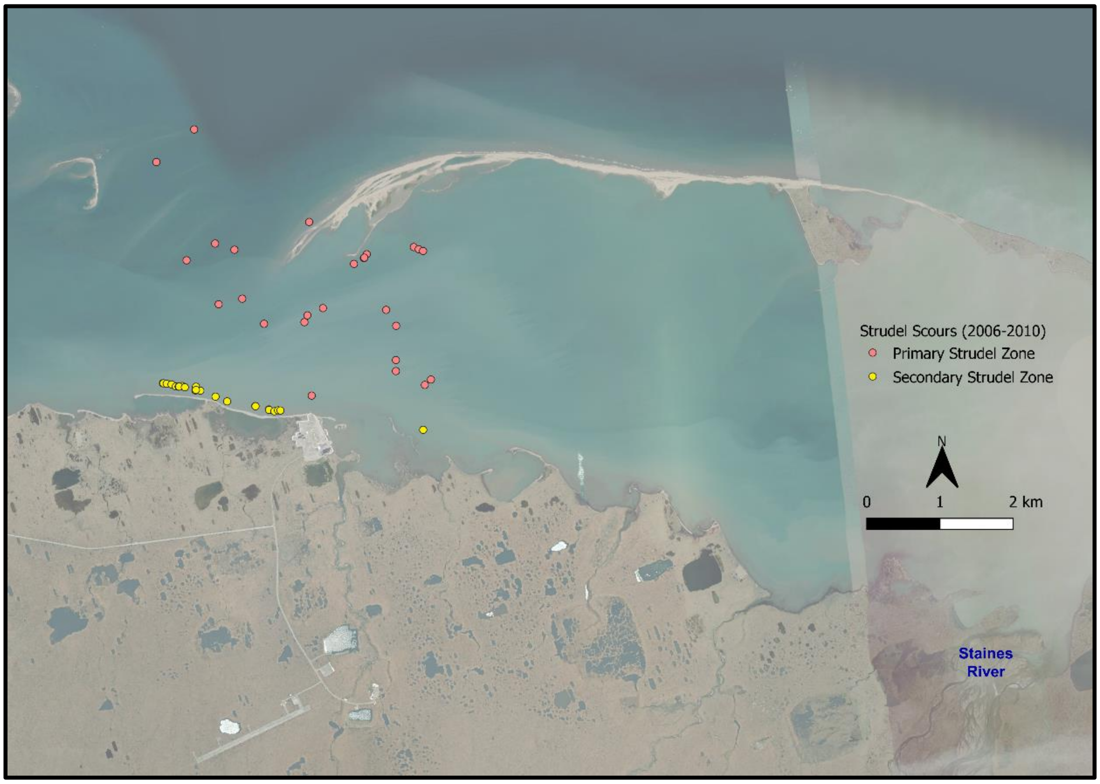

Figure 57. Strudel scours mapped near the Staines River

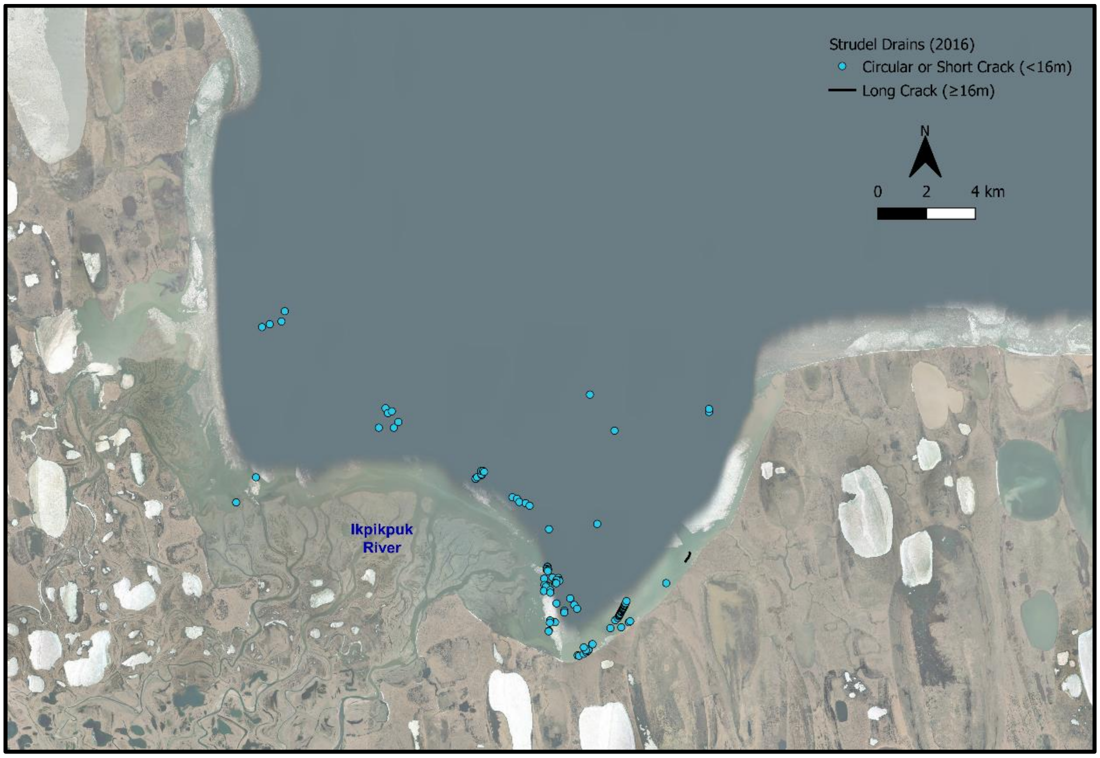

Note: Strudel scours not mapped in the vicinity of the Ikpikpuk River (**Table 5**).

Figure 58. Strudel drains mapped near the Ikpikpuk River

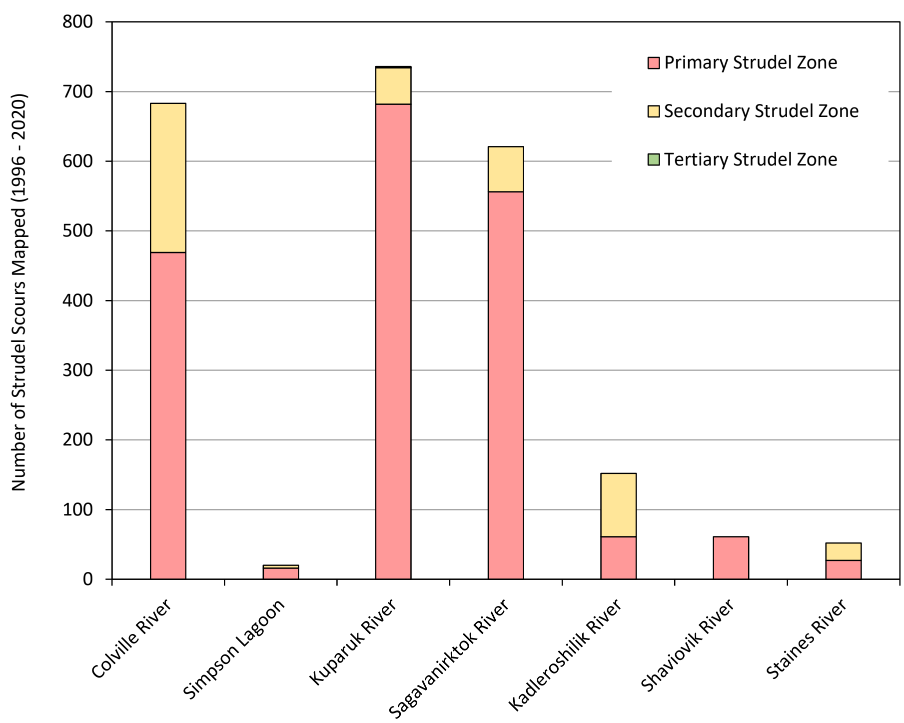

Figure 59. Number of strudel scours mapped as part of industry-sponsored studies (segregated by river and strudel zone), 1996–2020.

Table 35 through **Table 39** summarize the strudel scour characteristics measured during the industry-sponsored studies, and **Table 40** summarizes the maximum dimensions. The scour populations are segregated by zone (Secondary, Primary, and Tertiary). Because the characteristics of circular and linear scours are distinctly different, statistics are provided according to scour type. In the case of circular scours, the term “maximum horizontal dimension” refers to the largest horizontal extent measured at the elevation of the surrounding sea bottom (*i.e.*, the diameter of a perfectly circular scour or the major axis of an oblong scour). In the case of linear scours, the “maximum horizontal dimension” represents the length measured parallel to the scour orientation. The “scour depth” is the vertical distance from the surrounding sea bottom to the deepest point in the scour depression. As indicated previously, the characteristics of each individual scour are provided in the geodatabase.

The frequency of strudel scouring tends to be highest in the Primary Zone, followed by the Secondary and Tertiary Zones. Of the 1,953 features with measured scour depths, 77% (1,509 scours) were located within the Primary Strudel Zone, 23% (442 scours) were located in the Secondary Zone, and less than 1% (2 scours) were located within the Tertiary Zone. The severity (depth) of scouring also tends to be greatest in the Primary Zone. The maximum measured scour depth in the Primary, Secondary, and Tertiary Zones was 7.59, 4.45, and 0.40 m, respectively.

Scatter plots of scour depth versus water depth, scour maximum horizontal dimension versus water depth, and scour maximum horizontal dimension versus scour depth are presented for the circular scours mapped in each study area in **Figure 60**, **Figure 61**, and **Figure 62**. Because of their distinctly different nature, linear scours are excluded. **Figure 60** indicates that the greatest scour depths tend to occur in water depths of 1 to 4 m. The envelope of maximum horizontal dimensions also peaks in this range of water depths before tailing off gradually with increasing depth (**Figure 61**). Despite significant scatter, the strudel scour maximum horizontal dimensions appear to increase with scour depth (**Figure 62**).

Table 35. Summary of strudel scour characteristics measured near the Colville River, 2005–2020

Scour Type	Characteristic	Secondary Zone			Primary Zone			Tertiary Zone		
		Data Pts.	Mean (m)	Range (m)	Data Pts.	Mean (m)	Range (m)	Data Pts.	Mean (m)	Range (m)
Circular	Scour Depth (m)	188	0.59	0.09–4.45	454	0.35	0.09–3.75	0	-	-
	Max. Horiz. Dim. (m)	188	16.1	1.8–57.6	454	16.8	2.4–70.4	0	-	-
	Water Depth (m) [1]	188	1.47	0.74–2.07	454	2.04	1.37–2.57	0	-	-
Linear	Scour Depth (m)	26	0.60	0.21–2.65	15	0.40	0.15–0.91	0	-	-
	Max. Horiz. Dim. (m)	26	98.2	17.7–1,252.1	15	24.6	7.9–66.8	0	-	-
	Water Depth (m) [1]	26	1.56	1.19–1.74	15	1.93	1.58–2.48	0	-	-

[1] Depth relative to MLLW

Table 36. Summary of strudel scour characteristics measured in Simpson Lagoon, 2007–2020

Scour Type	Characteristic	Secondary Zone			Primary Zone			Tertiary Zone		
		Data Pts.	Mean (m)	Range (m)	Data Pts.	Mean (m)	Range (m)	Data Pts.	Mean (m)	Range (m)
Circular	Scour Depth (m)	4	0.36	0.12–0.88	16	0.45	0.12–0.85	0	-	-
	Max. Horiz. Dim. (m)	4	3.0	1.5–5.8	16	6.2	1.2–13.4	0	-	-
	Water Depth (m) [1]	4	1.21	1.13–1.31	16	2.30	1.92–2.59	0	-	-
Linear	Scour Depth (m)	0	-	-	0	-	-	0	-	-
	Max. Horiz. Dim. (m)	0	-	-	0	-	-	0	-	-
	Water Depth (m) [1]	0	-	-	0	-	-	0	-	-

[1] Depth relative to MLLW

Table 37. Summary of strudel scour characteristics measured near the Kuparuk River, 1996–2020

Scour Type	Characteristic	Secondary Zone			Primary Zone			Tertiary Zone		
		Data Pts.	Mean (m)	Range (m)	Data Pts.	Mean (m)	Range (m)	Data Pts.	Mean (m)	Range (m)
Circular	Scour Depth (m)	51	0.48	0.09–1.71	499	0.56	0.09–4.27	2	0.39	0.37–0.40
	Max. Horiz. Dim. (m)	52	7.2	1.5–20.1	636	9.1	1.5–48.8	2	5.2	4.0–6.4
	Water Depth (m) [1]	52	1.51	0.61–3.41	636	3.67	1.22–6.07	2	6.32	5.98–6.65
Linear	Scour Depth (m)	0	-	-	36	0.55	0.12–1.9	0	-	-
	Max. Horiz. Dim. (m)	0	-	-	34	62.2	7.0–280.5	0	-	-
	Water Depth (m) [1]	0	-	-	46	3.70	2.23–5.24	0	-	-

[1] Depth relative to MLLW

Table 38. Summary of strudel scour characteristics measured near the Sag., Kad., and Shav. Rivers, 1997–2017

Scour Type	Characteristic	Secondary Zone			Primary Zone			Tertiary Zone		
		Data Pts.	Mean (m)	Range (m)	Data Pts.	Mean (m)	Range (m)	Data Pts.	Mean (m)	Range (m)
Circular	Scour Depth (m)	143	0.49	0.09–3.23	433	0.78	0.09–7.59	0	-	-
	Max. Horiz. Dim. (m)	150	11.8	2.1–40.5	643	12.8	1.5–74.1	0	-	-
	Water Depth (m) [1]	150	1.38	0.91–2.01	643	2.54	1.01–5.27	0	-	-
Linear	Scour Depth (m)	5	0.47	0.24–0.76	29	0.61	0.15–2.47	0	-	-
	Max. Horiz. Dim. (m)	5	29.4	16.2–53.3	35	48.8	14.3–121.9	0	-	-
	Water Depth (m) [1]	6	1.34	1.19–1.52	35	2.35	1.07–3.54	0	-	-

[1] Depth relative to MLLW

Table 39. Summary of strudel scour characteristics measured near the Staines River, 2006–2010

Scour Type	Characteristic	Secondary Zone			Primary Zone			Tertiary Zone		
		Data Pts.	Mean (m)	Range (m)	Data Pts.	Mean (m)	Range (m)	Data Pts.	Mean (m)	Range (m)
Circular	Scour Depth (m)	25	0.27	0.13–0.45	26	0.67	0.15–1.72	0	-	-
	Max. Horiz. Dim. (m)	25	3.5	1.3–12.2	26	8.7	2.4–18.7	0	-	-
	Water Depth (m)[1]	25	1.78	1.60–1.95	26	2.62	1.31–3.24	0	-	-
Linear	Scour Depth (m)	0	-	-	1	0.30	-	0	-	-
	Max. Horiz. Dim. (m)	0	-	-	1	21.0	-	0	-	-
	Water Depth (m)[1]	0	-	-	1	2.40	-	0	-	-

[1] Depth relative to MLLW

Table 40. Summary of maximum strudel scour dimensions measured during industry studies

Scour Type	Characteristic	Secondary Zone Dimension (River[2])	Primary Zone Dimension (River[2])	Tertiary Zone Dimension (River[2])
Circular	Scour depth (m)	0.45 (Sta.)–4.45 (Col.)	0.73 (Shav.)–7.59 (Sag.)	0.40 (Kup.)
	Max. Horizontal Dimension (m)	5.8 (Simp.)–57.6 (Col.)	13.4 (Simp.)–74.1 (Sag.)	6.4 (Kup.)
Linear	Scour depth (m)	0.64 (Kad.)–2.65 (Col.)	0.21 (Shav.)–2.47 (Sag.)	-
	Max. Horizontal Dimension (m)	25.3 (Kad.)–1,252.1 (Col.)	19.8 (Shav.)–280.5 (Kup.)	-

[1] Range of values is the lowest maximum and the highest maximum among the various industry studies.

[2] Colville = Col.; Simpson Lagoon = Simp.; Kuparuk = Kup.; Sagavanirktok = Sag.; Kadleroshilik = Kad.; Shaviovik = Shav.; Staines = Sta.

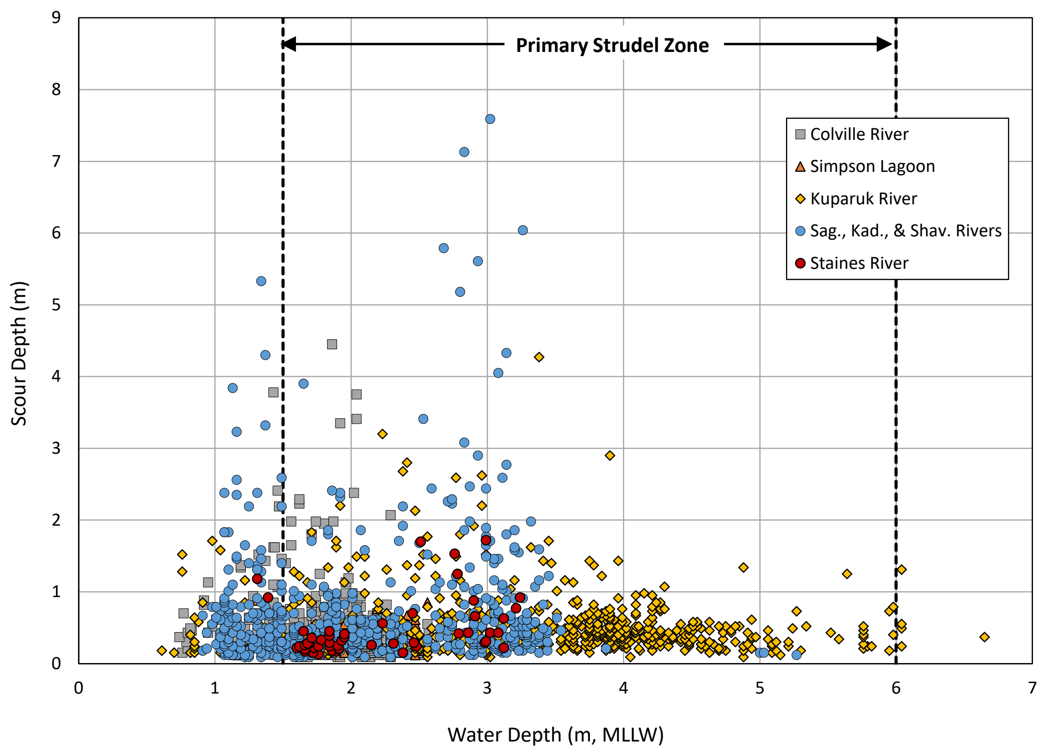

Figure 60. Strudel scour depth vs. water depth for circular scours, 1996–2020

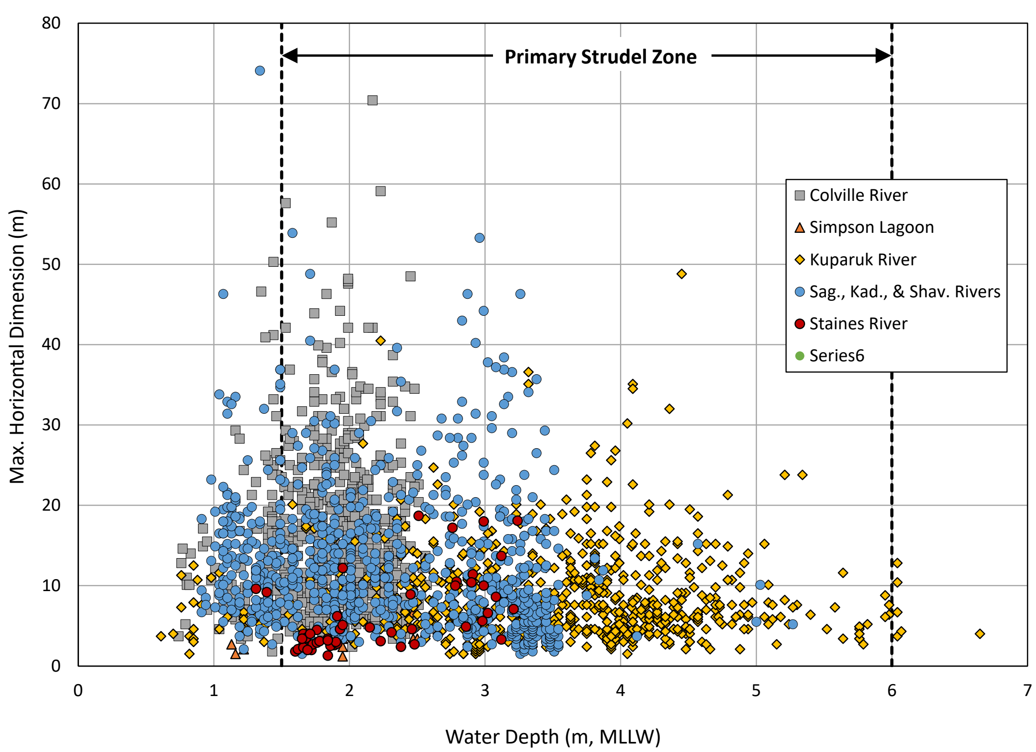

Figure 61. Strudel scour max. horizontal dim. vs. water depth for circular scours, 1996–2020

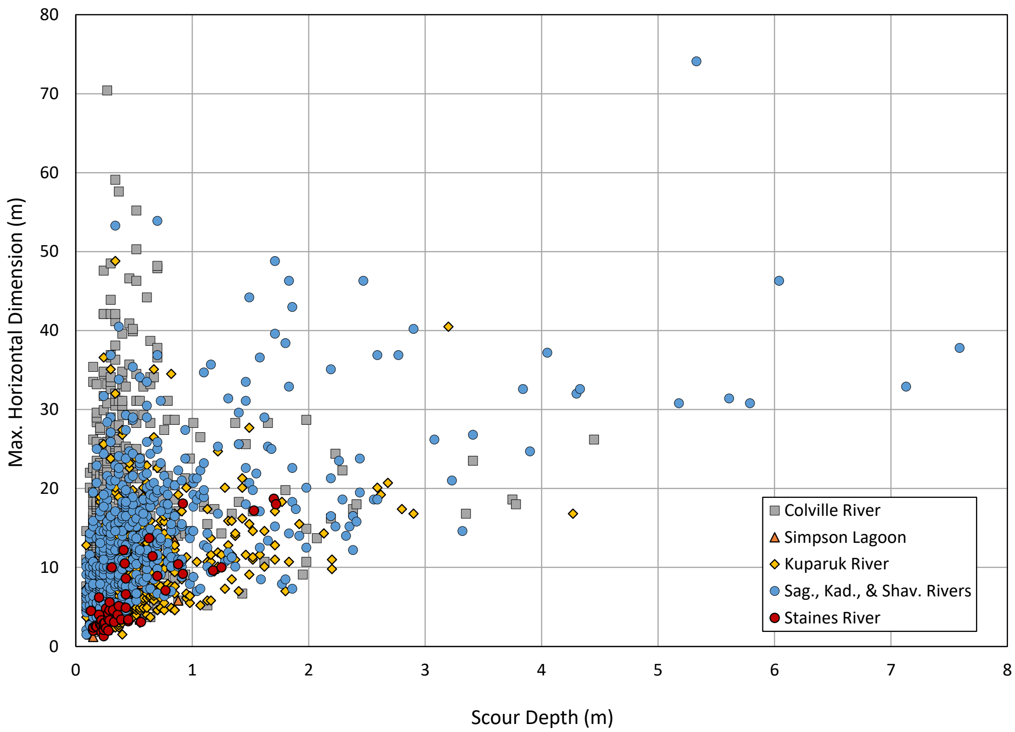

Figure 62. Strudel scour max. horizontal dim. vs. scour depth for circular scours, 1996–2020

12 Summary and Conclusions

The primary components of the study are a data product and a synthesis report. The data prepared as part of this study were compiled in a geodatabase that includes satellite imagery, interpreted overflood boundaries, isolines of probability of overflood occurrence, strudel drain and scour data, and an inventory of offshore ice roads for the 26-year study period from 1995 to 2020. The database consists of two volumes, each of which is described in detail in **Appendix C**. The principal study findings from the report are summarized below:

1. ***Overflood Boundary Mapping***: A total of 274 overflood boundaries were mapped over the 13-year period from 2008 through 2020. The peak overflood extents between 1995 and 2007 mapped as part of the 2009 Study were refined, as needed, based on newly available imagery. In addition, overflood boundaries missing from the 2009 Study due to lack of imagery at the time were mapped. Aside from one instance in 2019, the overflood edge was mapped for all watercourses in the study area over the 21-year MODIS-dominated era (2000 through 2020).

2. ***Overflood Occurrence Probability:*** Isolines of overflood probability were developed using the overflood extents mapped during the 21-year period from 2000 through 2020. The immediate region fronting all but one of the thirteen major rivers in the study area (Topagoruk River) flooded annually (100% probability of occurrence). In the central portion of the study area, between Cape Halkett and the Staines River, the entire coast flooded 25% of the time. Elsewhere, the flooded areas were discontinuous.

3. ***Correlation of River Overflood with Environmental Variables:*** Consistent with the 2009 Study findings, no meaningful correlations were identified between the annual overflood areas of the Colville, Kuparuk, and Sagavanirktok Rivers and environmental data related to streamflow, precipitation, snowpack, and air temperature. This indicates that the extent of river overflood onto the sea ice cannot readily be predicted by any single environmental variable for which historical data currently exist. The overflood phenomenon appears to be governed by interactions between a number of environmental forces, some of which (*e.g.*, soil moisture at high elevations at the onset of snowpack thawing, ice jams in distributary channels, roughness and snow cover on the sea ice, wind events during flooding, and the density of drainage features on the sea ice) are complex, for the most part poorly understood, or lack sufficient data to evaluate their contributions to the overall overflood process. In the absence of such direct correlations, the detailed long-term mapping of overflood boundaries in this study provides a valuable probabilistic assessment of potential hazards to coastal facilities based on past events. Investigations into the complex interactions governing river overflood is a recommended area of further research.

4. ***Long-Term Trends:*** The environmental and overflood data sets exhibit considerable year-to-year variability. However, clear trends in several parameters are evident over the 26-year study period. Both the end-of-winter snow water equivalent and average air temperature generally increased over the study period, while the streamflow and precipitation data exhibited inconsistent and weak trends. The annual overflood area within the study region decreased with time (rate $\approx$ 18 km^2/yr) and both the start and peak of overflood occurred earlier in the year (rate $\approx$ 0.4 days/yr).

5. ***Facility Hazards***: River overflood on the sea ice introduces two hazards to man-made facilities in the U.S. Beaufort Sea: interdiction of access to offshore facilities by flooding, and disturbance of the sea bottom above buried subsea pipelines by strudel scouring (which can compromise the integrity of the pipeline).

Rapid deterioration of the ice sheet can render ice roads impassable within the zone of river overflood, impacting both facilities access and oil spill response. At least some portion of every nearshore ice road mapped between 1995 and 2020 was located within the zone of river overflood and vulnerable to damage during break-up.

Strudel scouring can constitute a significant design consideration for subsea pipelines in nearshore areas adjacent to river and stream mouths. In the event that a strudel drain is located directly above a buried subsea pipeline, a sufficiently deep strudel scour may expose the pipeline and lead to an unsupported span. A strudel scour that forms directly over a buried pipeline also can remove the backfill material that is needed to prevent damage from ice keels and prevent upheaval buckling. An additional concern is that strudel drainage provides a potential mechanism to transport spilled oil below the ice sheet.

Strudel scour frequency and severity can be segregated into zones according to water depth. Strudel scouring typically is most common and severe in the Primary Strudel Zone, which extends offshore from the grounded landfast ice edge to approximately 6 m water depth. In the zone of grounded landfast ice (the "Secondary Strudel Zone") and offshore of the Primary Zone (the "Tertiary Strudel Zone"), scouring tends to be more modest and occur less frequently. When the major rivers in this region were considered, the Secondary Strudel Zone accounted for the greatest portion of the overflood area in any given year. On average, this zone encompassed 62% of the total overflood area. The Primary Strudel Zone accounted for 37% of the total overflood area, while the Tertiary Zone accounted for a mere 1%. Strudel zone and overflood occurrence information should be used to assess the hazard to prospective pipeline routes posed by strudel scouring in different coastal areas.

13 References

Arnborg, L., H. Walker, and J. Peippo, 1966, Water Discharge in the Colville River, 1962, *Geografiska Annaler: Series A, Physical Geography*, *48*(4), pp. 195–210.

ASF DAAC, 2021a, Alaska Satellite Facility, Sentinel-1, About, https://asf.alaska.edu/data-sets/sar-data-sets/sentinel-1/sentinel-1-about.

Atwater, S., 1991, 1989 Endicott Environmental Monitoring Program Final Report: Ice Break-up and Freeze-up, Prepared by Science Applications International Corporation for the U.S. Army Corps of Engineers, Anchorage, AK.

Barnes, P. and E. Reimnitz, 1976, Flooding of Sea Ice by Rivers of Northern Alaska. ETRS 1: A New Window on Our Planet. Richards, S. and Carter, W., editor. Menlo Park, CA, pp. 356-359. Geological Survey Professional Paper 929.

Barry, R., R. Moritz, and J. Rogers, 1979, Fast Ice Regimes of the Beaufort and Chukchi Sea Coasts, Alaska. Cold Regions Science and Technology. (1) pp. 129-152.

Bilello, M., 1960, Formation, Growth, and Decay of Sea Ice in the Canadian Arctic Archipelago, SIPRE Research Report 65, Hanover, NH.

Carlson, R., R. Seifert, D. Kane, 1977, Effects of Seasonability and Variability of Streamflow on Nearshore Coastal Areas, Final Report; (In) Environmental Assessment of the Alaskan Continental Shelf, Annual Reports 14:96-250. https://www.arlis.org/docs/vol1/OCSEAP2/Annual/OCSEAP-annual-1977-v14.pdf.

Coastal Frontiers Corporation, 1997, Northstar Development 1996 Pipeline Route Survey. Chatsworth, CA: BPXA. 72 pp. + appen.

Coastal Frontiers Corporation, 1998, Liberty Development 1997 Pipeline Route Survey. Chatsworth, CA: BPXA, 62 pp. + appen.

Coastal Frontiers Corporation, 2001, Northstar Pipeline Trench Backfill Program, Winter 2001. Chatsworth, CA: BPXA

Coastal Frontiers Corporation, 2006, Oooguruk Development 2005 Bathymetric Survey Program. Chatsworth, CA: Pioneer Natural Resources. 30 pp. + appen.

Coastal Frontiers Corporation, 2007, Sivulliq Development 2006 Nearshore Survey Program. Chatsworth, CA: Shell International Exploration and Production Inc. 40 pp. + appen.

Coastal Frontiers Corporation, 2014, 2014 River Overflood Mapping for Sivulliq Area. Moorpark, CA: Shell Exploration and Production Co. 19 pp.

Coastal Frontiers Corporation, 2016, Smith Bay 2016 River Overflood and Sea Ice Reconnaissance_Rev1, memorandum to Ben Anglen, Caelus Energy Alaska, LLC.

Coastal Frontiers Corporation and Vaudrey and Associates, Inc., 2021, 2020-21 Freeze-Up Study of Arctic Sea Ice in the Alaskan Beaufort and Chukchi Seas, prepared for Bureau of Safety and Environmental Enforcement, U.S. Dept. of the Interior, Moorpark, CA, 212 pp. + appen.

Coastal Frontiers Corporation and Vaudrey and Associates, Inc., 2022, 2021 Break-Up Study of Arctic Sea Ice in the Alaskan Beaufort and Chukchi Seas, prepared for Bureau of Safety and Environmental Enforcement, U.S. Dept. of the Interior, Moorpark, CA, 212 pp. + appen.

Craig, J., K. Sherwood, and P. Johnson, 1985, Geological Report for the Beaufort Sea Planning Area, Alaska – Regional Geology, Petroleum Geology, Environment Geology. U.S. Department of the Interior, Minerals Management Service, Anchorage, AK. 192 pp. Report No.: OCS Report MMS 85-0111. *https://www.boem.gov/sites/default/files/boem-newsroom/Library/Publications/1985/85_0111.pdf*.

DF Dickins, Vaudrey and Associates Inc., and Coastal Frontiers Corporation, 1999, Sea Ice Overflood Limits Affecting the Liberty Pipeline Route: Results of a Literature Search and Satellite Image Analysis. For BP Exploration (Alaska), Anchorage (proprietary, see published summary Dickins *et al*., 2001).

Dickins, D., G. Hearon, K. Morris, K. Ambrosius, and W. Horowitz, 2011, Mapping Sea Ice Overflood using Remote Sensing: Alaska Beaufort Sea. Cold Regions Science and Technology. 65(3):275-285.

Dickins, D., and E. Owens, 2002, Annual Ice Cycle at the Mouth of the Colville River and Implications for Oil Transport. Proceedings 2002 Arctic and Marine Oil Spill Conference (published with permission of ConocoPhillips Alaska based on a previous study completed in 1999, proprietary).

Dickins, D., G. Hearon, and K. Vaudrey, 2001, Sea Ice Overflood in Stefansson Sound, Alaskan Beaufort Sea. In Proceedings 16th International Conference on Port and Ocean Engineering Under Arctic Conditions, Ottawa, pp. 193-202.

ESA, 2021a, Earth Online, About ERS, *https://earth.esa.int/eogateway/missions/ers#instruments-section*.

Hearon, G., D. Dickins, K. Ambrosius, and K. Morris, 2009, Mapping Sea Ice Overflood Using Remote Sensing: Smith Bay to Camden Bay. Report prepared by DF Dickins Associates, Coastal Frontiers Corporation, Aerometric, and The Geophysical Institute, University of Alaska for U.S. Department of the Interior, Minerals Management Service, Alaska OCS Region. 127 p. Report No.: OCS Study MMS 2009-017. Contract M06PC00034. *https://espis.boem.gov/final%20reports/4871.pdf*.

JAXA, 2021a, Advanced Land Observing Satellite, About ALOS, Overview and Objectives, *https://www.eorc.jaxa.jp/ALOS/en/index_e.htm*.

LaBelle, J., J. Wise, R. Voelker, R. Schulze, and G. Wohl, 1983, Alaska Marine Ice Atlas, Arctic Environmental Information and Data Service. University of Alaska, Anchorage.

Lanan, G., T. Cowin, B. Hazen, D. Maguire, J. Hall, and C. Perry, 2008, Oooguruk Offshore Arctic Flowline Design and Construction. Offshore Technology Conference, Houston, Texas, USA, May 2008. *https://doi.org/10.4043/19353-MS*.

Leidersdorf, C., G. Hearon, K. Vaudrey, and G. Swank, 2007, Strudel Scour Formation off Arctic River Deltas. Proc., 30th International Conference on Coastal Engineering, Vol. 5, World Scientific, Hackensack, NJ, pp. 5312-5324.

McClelland Engineers Inc., 1982, Duck Island/Sag Delta Development Project, Strudel Scour Investigation, Ventura, CA, 47 pp. + appen.

Milbert, D., 2001, GPS Fluctuations over Time on May 2, 2000. Interagency GPS Executive Board, Washington, D.C., 4 pp. *https://www.gps.gov/systems/gps/modernization/sa/data/*

Natural Resources Conservation Service (NRCS), 2021, National Water and Climate Center, *https://www.nrcs.usda.gov/wps/portal/wcc/home/*

NASA, 2021a, Moderate Resolution Imaging Spectroradiometer data and products, *https://modis.gsfc.nasa.gov/data*.

NOAA, 2022a, Local Climatological Data, *https://www.ncdc.noaa.gov/cdo-web/datatools/lcd*

NOAA, 2022b, Climate at a Glance, National Centers for Environmental Information, *https://www.ncdc.noaa.gov/cag/county/time-series/AK-185/tavg/1/4/1895-2022*

Norton, D. and G. Weller, 1984, The Beaufort Sea: Background, History, and Perspective. (In) The Alaskan Beaufort Sea. Barnes, P.W. and Reimnitz, E. Editors. Elsevier. *https://doi.org/10.1016/B978-0-12-079030-2.50007-1*

Reimnitz, E. and E. Kempema, 1982, High Rates of Bedload Transport Measured from Infilling Rate of Large Strudel-scour Craters in the Beaufort Sea, Alaska. U.S. Geological Survey, Menlo Park, CA. 18 p. Open File Report 82-588. *https://pubs.usgs.gov/of/1982/0588/report.pdf*

Reimnitz, E., C. Rodeick, and S. Wolf, 1974, Strudel Scour: A Unique Arctic Marine Geologic Phenomenon. Journal of Sedimentary Research, *44*, pp. 409–420.

Stuefer S., D. Kane, and K. Dean, 2020, Snow Water Equivalent Measurements in Remote Arctic Alaska Watersheds. AGU Water Resources Research, 56(4). *https://doi.org/10.1029/2019WR025621*

Trans-Alaska Pipeline System Owners (TAPS), 2001, Environmental Report for Trans-Alaska Pipeline System Right-of-Way Renewal. Anchorage, AK: TAPS Owners.

U.S. Geological Survey, 2021a, National Hydrography Dataset (ver. USGS National Hydrography Dataset Best Resolution (NHD) for Hydrologic Unit (HU) 4 - 1906 (published 20201202)), accessed January 1, 2021 at URL *https://www.sciencebase.gov/catalog/item/5a3a5264e4b0d05ee8b59f1f*U.S. Geological Survey, 2021b, Landsat Satellite Missions, *https://www.usgs.gov/core-science-systems/nli/landsat/landsat-satellite-missions?qt-science_support_page_related_con=0#qt-science_support_page_related_con*.

U.S. Geological Survey, 2021c, Landsat 5, *https://www.usgs.gov/core-science-systems/nli/landsat/landsat-5?qt-science_support_page_related_con=0#qt-science_support_page_related_con*.

U.S. Geological Survey, 2021d, Landsat 7, *https://www.usgs.gov/core-science-systems/nli/landsat/landsat-7?qt-science_support_page_related_con=0#qt-science_support_page_related_con*.

U.S. Geological Survey, 2021e, Landsat 8, *https://www.usgs.gov/core-science-systems/nli/landsat/landsat-8?qt-science_support_page_related_con=0#qt-science_support_page_related_con*.

U.S. Geological Survey, 2021f, Earth Resources Observation and Science Center Archive - Sentinel-2, *https://www.usgs.gov/centers/eros/science/usgs-eros-archive-sentinel-2?qt-science_center_objects=0#qt-science_center_objects*.

U.S. Geological Survey, 2021g, Earth Resources Observation and Science Center Archive - ISRO Resourcesat 1 and Resourcesat 2, *https://www.usgs.gov/centers/eros/science/usgs-eros-archive-isro-resourcesat-1-and-resourcesat-2-liss-3?qt-science_center_objects=0#*.

U.S. Geological Survey, 2021h, National Water Information System: Web Interface, *http://waterdata.usgs.gov*

Vaudrey, K., 1984, Breakup Study of the Alaskan Beaufort and Upper Chukchi Seas, 1983 Season. AOGA Project 224, Vaudrey & Associates, Inc., San Luis Obispo, CA.

Vaudrey, K., 1985, Breakup Study of the Alaskan Beaufort and Upper Chukchi Seas, 1984 Season. AOGA Project 274, Vaudrey & Associates, Inc., San Luis Obispo, CA.

Vaudrey, K., 1986, Breakup Study of the Alaskan Beaufort and Upper Chukchi Seas, 1985 Season. AOGA Project 319, Vaudrey & Associates, Inc., San Luis Obispo, CA.

Walker, H., 1974, The Colville River and the Beaufort Sea: Some interactions. In J. Reed and J. Sater (Eds.), *The Coast and Shelf of the Beaufort Sea, Proceedings of a symposium on Beaufort Sea Coast and Shelf Research* (pp. 513–540). The Arctic Institute of North America.

Appendix A: Satellite Platforms

TERRA AND AQUA MISSIONS: MODIS

Agency: National Aeronautics and Space Administration

The Moderate Resolution Imaging Spectroradiometer (MODIS) instrument currently operates onboard the National Aeronautics and Space Administration (NASA) Terra and Aqua satellites, which were launched in 1999 and 2002, respectively. Terra's orbit is timed so that it passes from north to south across the equator in the morning, while Aqua passes south to north over the equator in the afternoon. Terra MODIS and Aqua MODIS view the entire Earth's surface every 1 to 2 days. The sensor has a viewing swath width of 2,330 km, measures 36 spectral bands, and acquires data at three spatial resolutions: 250 m for bands 1 and 2, 500 m for bands 3 to 7, and 1,000 m for bands 8 to 36 (NASA, 2021a).

The MODIS instrument is not able to penetrate cloud cover. Nevertheless, a basic understanding of the timing and magnitude of the overflood extents can be derived in partially-cloudy conditions. Notwithstanding the relatively low resolution of MODIS imagery, it is generally sufficient to provide an accurate estimate of peak overflood extents in cloudless conditions. While the sensor's inability to penetrate cloud cover renders the imagery obsolete in completely cloudy conditions, a basic understanding of the overflood timing and magnitude of the overflood extents can be derived. The strength of MODIS resides in the combination of its daily repeat cycle and wide acquisition swath.

Available Data

MODIS imagery is available through NASA's Worldview portal. The portal provides full-resolution, georeferenced scenes within user-defined bounds. The bounds selected for this study are the 69°N and 72°N parallels and the 157°W and 141°W meridians.

The MODIS products typically used for overflood assessment are daily Corrected Reflectance images (NASA, 2021b). The Corrected Reflectance algorithm utilizes MODIS Level 1B data (the calibrated, geolocated radiances) to provide natural-looking images by removing gross atmospheric effects, such as Rayleigh scattering, from MODIS visible bands 1-7. The algorithm was developed by the original MODIS Rapid Response team to address the needs of the fire monitoring community who want to see smoke.

Two band combinations were used for this project:

Bands 1-4-3: These are so-called true-color or natural color images because this combination of wavelengths is similar to what the human eye would see (**Figure 1A**).

Bands 7-2-1: This band combination enhances flooded areas and can be used to distinguish snow and ice from clouds. In the 7-2-1 band combination, liquid water appears very dark, sediments in water appear dark blue, ice and snow appear as bright turquoise, and clouds appear white (**Figure 1B**).

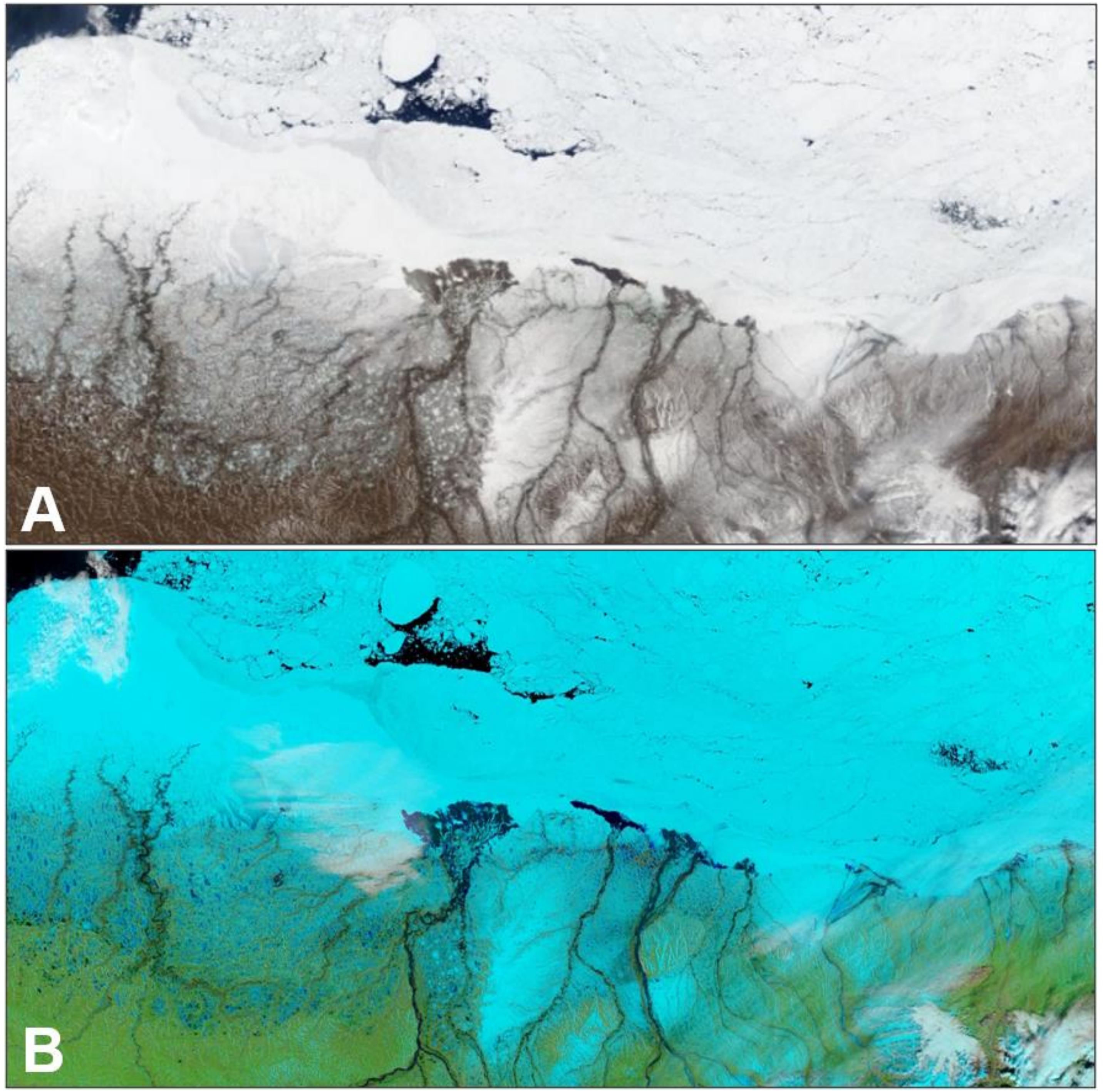

Figure 1. MODIS images in 1-4-3 (panel A) and 7-2-1 (panel B) band combinations (May 29th, 2020) showing overflood along the North Slope of Alaska coast.
Image source: NASA, 2021c

LANDSAT MISSIONS: Landsat 8, 7, and 5

Agencies: National Aeronautics and Space Administration and United States Geological Survey

The Landsat Missions originated as a combined effort of the Department of the Interior, NASA, and the Department of Agriculture to develop and launch the first civilian Earth observation system (USGS, 2021a). Since the launch of Landsat 1 in 1972, they have a comprehensive historical archive of optical imagery for Alaska (**Figure 2**).

Figure 2. Landsat Missions over time
Image source: USGS, 2021a

The following three satellites provided coverage of the study area between 2008 and 2020:

Landsat 8
(2013-present)
Landsat 8 is the more recently-launched satellite and carries the Operational Land Imager (OLI) and the Thermal Infrared Sensor (TIRS) instruments. A Landsat 8 scene size is 185 km x 180 km, with an overlap varying from 7% at the equator to approximately 85% at extreme latitudes. Spatial resolution of Landsat 8 products is typically 30 m (USGS, 2021b). The satellite has a 16-day repeat cycle, but the increased overlap in polar regions results in considerably higher image frequency in the study area.

Landsat 7
(1999-present)
Landsat 7 closely resembles Landsat 8 in terms of imagery spatial resolution, swath, overlap, and repeat cycle. There is an eight-day offset between the two satellites, resulting in a combined repeat cycle of eight days. Unfortunately, since June 2003 the Enhanced Thematic Mapper (ETM+) sensor on board of Landsat 7 has acquired and delivered data with gaps caused by the Scan Line Corrector failure. As a result, Landsat 7 scenes only have 78% of their pixels remaining (USGS, 2021c).

Landsat 5
(1984-2013)
Landsat 5 carried the Multispectral Scanner (MSS) and the Thematic Mapper (TM) sensors, and produced imagery products similar to those of Landsat 7 and 8 in terms of resolution, swath, overlap, and repeat cycle. The orbits of the Landsat 5 and 7 satellites were offset to give eight-day coverage to any area from one of the sensors (USGS, 2021d).

Available Data

The United States Geological Survey is the primary distributor of Landsat products. The imagery, which is distributed through different data portals such as Earth Explorer and Glovis, are available at three processing levels (USGS, 2021e):

Level-1 Products: The main Landsat products, they are distributed as a single compressed folder which contains data from each optical band in Geospatial Tagged Image File Format (GeoTIFF), ancillary files, and a metadata text file. Layers must be stacked in specific combinations to create usable analysis-ready products.

LandsatLook Products: Full resolution images derived from Landsat Level-1 data products. The images are compressed and stretched to create a product optimized for image selection and visual interpretation, but should not be used for automated scientific analysis. Scenes are available as Natural Color Image (a composite of three bands to show a “natural” looking image) and as Thermal Image (a one-band gray scale image that displays the thermal properties of the scene). Individual images are available as GeoTIFF files of approximately one tenth of the size of the Level-1 product bundle, and do not include associated comprehensive metadata. Examples of LandsatLook products from the Landsat 8 and Landsat 7 platforms are shown in **Figure 3**.

Level-2 and Level-3 Products: These are application-specific science products that the USGS has developed from Landsat Level-1 data. Examples of Level-2 and Level-3 products are Landsat Surface Temperature and Landsat Burned Area.

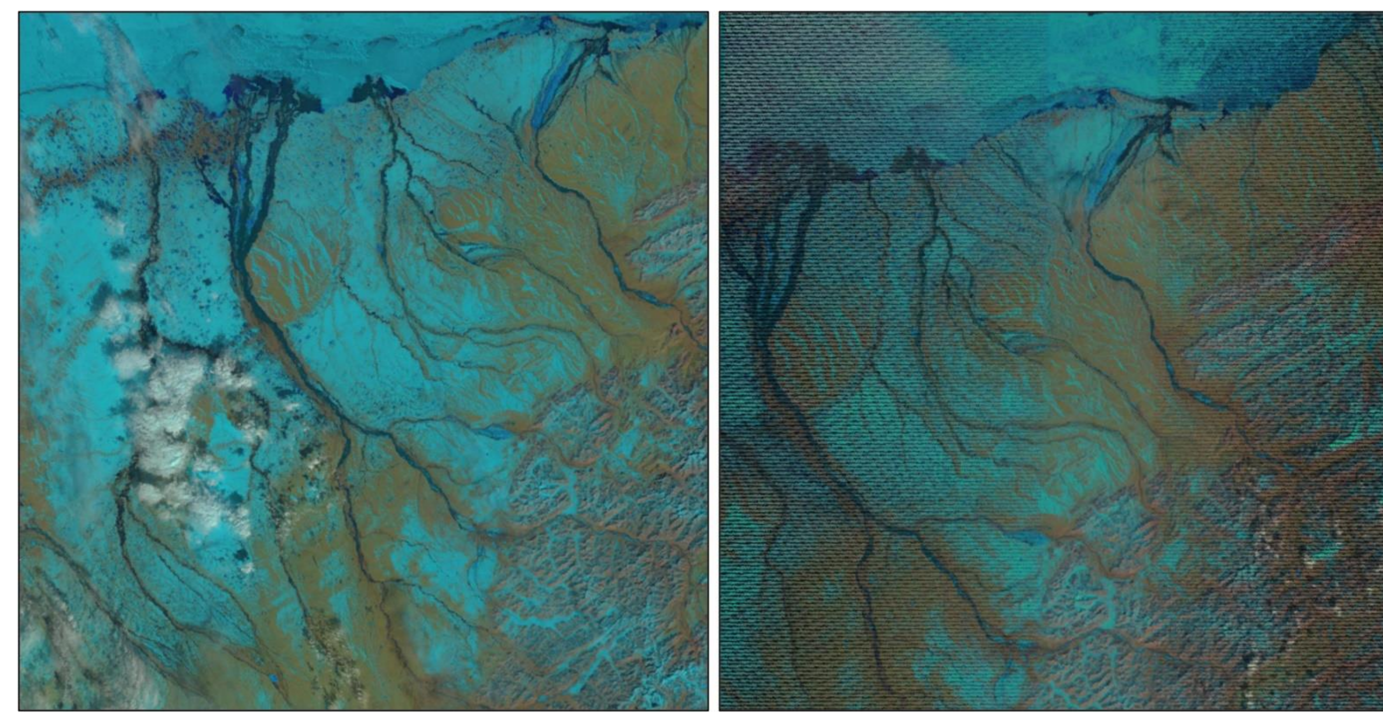

Figure 3. Landsat 8 image (left; May 19th, 2015) and Landsat 7 image (right; May 20th, 2015) showing the overflood of the Sagavanirktok, Shaviovik, and Staines Rivers
Image source: USGS, 2021f

SENTINEL MISSIONS: Sentinel 1

Agency: European Space Agency

The Sentinels are a new fleet of satellites developed in the framework of the European Space Agency (ESA) Copernicus Program to replace and enhance older Earth observation missions which have reached retirement, such as the ERS mission. Two of the Sentinel missions were identified as potential sources of imagery for the current project, Sentinel-1 and Sentinel-2 (described in the next frame).

Sentinel-1
(2014-present)
The first in the series, Sentinel-1 includes twin polar-orbiting satellites that each carry C-band Synthetic Aperture Radar, together providing all-weather, day-and-night imagery of Earth's surface (ASF DAAC, 2021a). Sentinel-1A was launched in 2014, and Sentinel-1B in 2016. They orbit 180° apart, imaging the entire Earth every six days.

The SAR instrument may acquire data in four modes: Interferometric Wide swath (IW), Extra Wide swath (EW), Wave (WV), and Stripmap (SM). The characteristics of each mode are described in **Table 1** and illustrated by **Figure 4**.

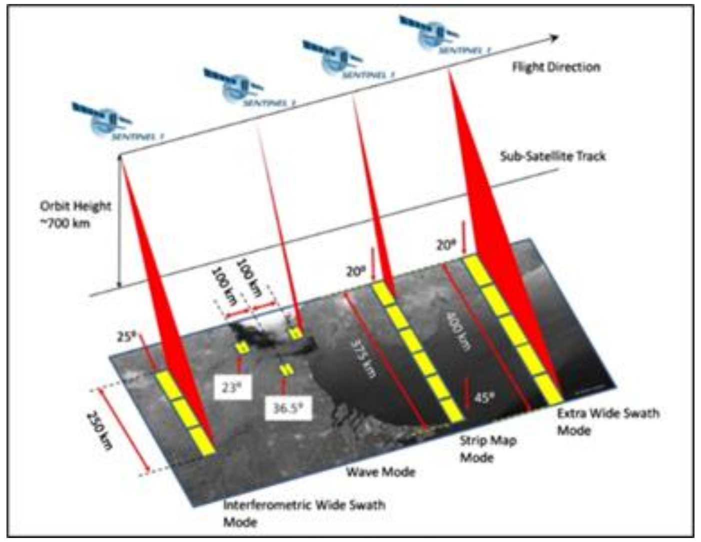

Figure 4. Sentinel-1 product modes
image source : ESA, 2021a

Table 1. Sentinel-1 product modes (after ASF DAAC, 2021b)

Beam Mode	Description	Polarization	Spatial Resolution	Swath Width
Interferometric Wide swath (IW)	Data is acquired in three swaths using the Terrain Observation with Progressive Scanning SAR (TOPSAR) imaging technique. IW is Sentinel-1's primary operational mode over land.	HH+HV, VV+VH, HH or VV	5 m x 20 m	250 km
Extra Wide swath (EW)	Data is acquired in five swaths using the TOPSAR imaging technique. EW mode provides very large swath coverage at the expense of spatial resolution.	HH+HV, VV+VH, HH or VV	20 m x 40 m	410 km
Wave (WV)	Data is acquired in small scenes called "vignettes", situated at regular intervals of 100 km along track. WV is Sentinel-1's operational mode over open ocean.	VV	5 m x 20 m	20 km
Stripmap (SM)	A standard SAR stripmap imaging mode used in rare circumstances to support emergency management services.	HH+HV, VV+VH, HH or VV	5 m	80 km

Available Data

For each acquisition mode, Sentinel-1 data products distributed by ESA include:

Raw Level-0 Data: Compressed and unfocused SAR raw data from which all other products are produced (ESA, 2021b). For the data to be usable, they need to be processed using focusing software.

Processed Level-1 Products: The products intended for most users, Level-1 data can be processed into either Single Look Complex (SLC) and/or Ground Range Detected (GRD) products. SLC products consist of focused SAR data, geo-referenced using orbit and attitude data from the satellite, and provided in slant-range geometry. They preserve phase information and are processed at the natural pixel spacing. GRD products consist of focused SAR data that have been detected, multi-looked and projected to ground range using the Earth ellipsoid model WGS84. Pixel values represent detected amplitude, and phase information is lost. The resulting product has approximately square resolution pixels and square pixel spacing with reduced speckle at a cost of reduced spatial resolution (ESA, 2021c).

Level-2 Ocean Products: Geolocated geophysical products derived from Level-1 data. Examples of Level-2 products include ocean wind fields, ocean swell spectra, and surface radial velocity (ESA, 2021d).

Level-0 and Level-1 data also are available to U.S. users through the Alaska Satellite Facility Distributed Active Archive Center (ASF DAAC). For the current study, Level-1 products processed by the ASF DAAC were selected as most appropriate for analysis. Two examples are provided in **Figure 5**.

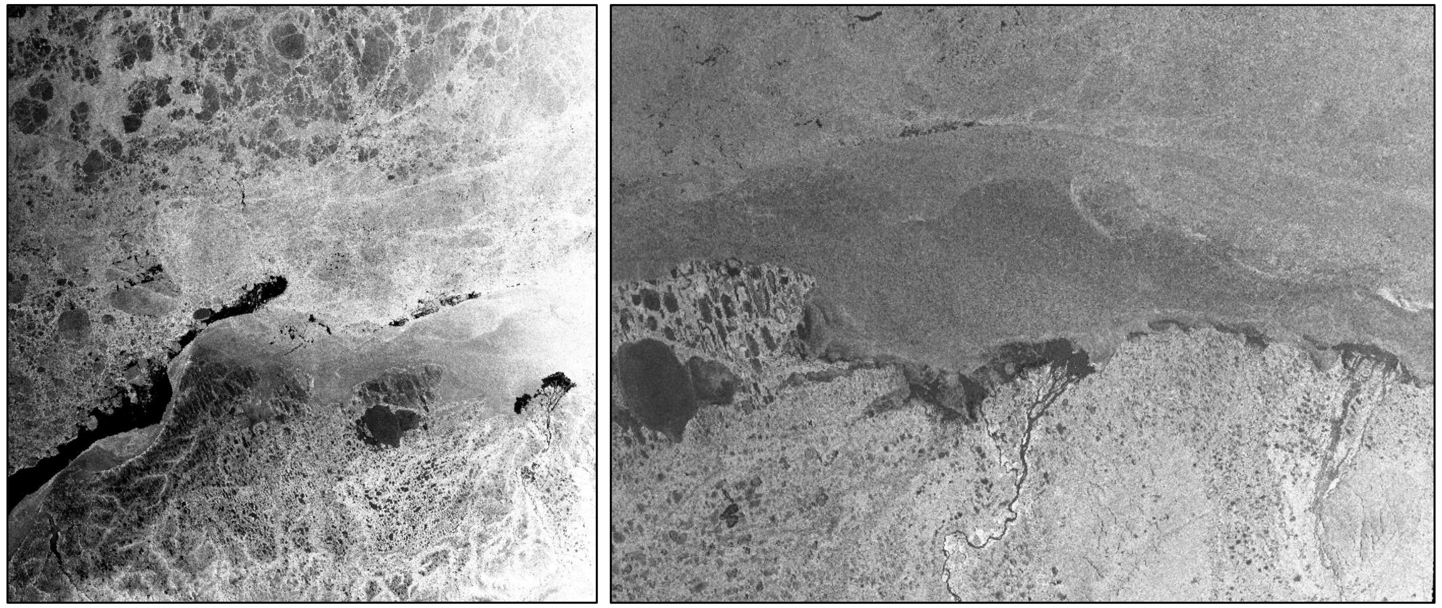

Figure 5. Sentinel-1 EW image (left; May 23rd, 2015) and IW image (right; May 20th, 2015) showing the overflood of the Colville River
Image source: ASF DAAC, 2021c

SENTINEL MISSIONS: Sentinel 2

Agency: European Space Agency

The Sentinels are a new fleet of satellites developed in the framework of the European Space Agency Copernicus Program to replace and enhance older Earth observation missions which have reached retirement, such as the ERS mission. Two of the Sentinel missions were identified as potential sources of imagery for the current project, Sentinel-1 (described in the previous frame) and Sentinel-2.

Sentinel-2
(2015-present)
Sentinel-2 is a polar-orbiting, multispectral high-resolution imaging mission for land monitoring. Similar to Sentinel-1, the mission is composed of two twin satellites. Sentinel-2A was launched in 2015, and Sentinel-2B followed in 2017. The two satellites operate with 10-day repeat cycles, resulting in a combined repeat cycle of five days (**Figure 6**). The Multispectral Instrument (MSI) samples 13 spectral bands: four bands at 10 m, six bands at 20 m, and three bands at 60 m spatial resolution (USGS, 2021g).

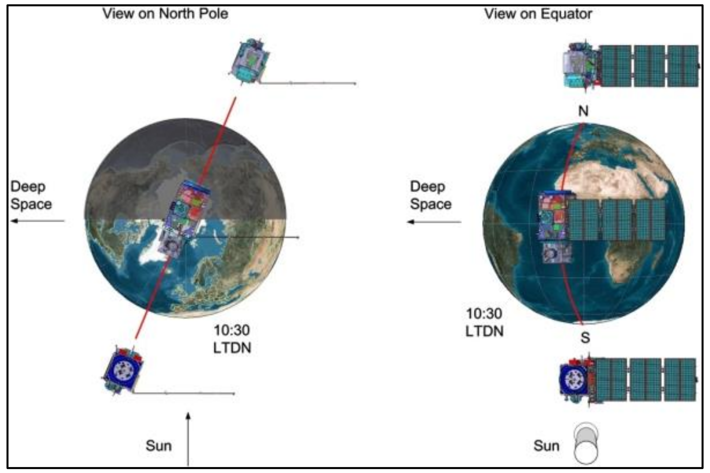

Figure 6. Twin-satellite orbital configuration of Sentinel-2
Image source: ESA, 2021e

Available Data

Sentinel-2 data consist of the following products:

Level-0, Level-1A, and Level-1B products: Sub-image granules 25 km across track and 23 km along track in size. These products are not made available to users (ESA, 2021f).

Level-1C (Top-Of-Atmosphere Reflectance) and Level-2A (Bottom-Of-Atmosphere Reflectance): Publicly-available orthorectified products that are provided as 100 km x 100 km tiles with ancillary satellite telemetry data, auxiliary information, and quality indicator data. Processing includes radiometric and geometric corrections along with orthorectification to generate highly accurate geolocated products (ESA, 2021g). Products are resampled to a pixel size of 10, 20 and 60 m depending on the native resolution of the different spectral bands. ESA provides Sentinel-2 products in Sentinel Standard Archive Format for Europe (SAFE) format. The SAFE format consists of a folder containing image data for each band, a true color image composite, quality indicators, auxiliary data, and metadata.

A partnership between ESA and the USGS allows for the latter to distribute Level-1C data. The USGS repackages Sentinel-2 products on a per tile basis in a compressed file format similar to that used for Landsat imagery. In addition, Full Resolution Browse images also are available from the USGS for all Sentinel-2 tiles. This product is a simulated natural color composite image created from three selected bands (11, 8A, 4) with a ground resolution of 20 m (USGS, 2021g). An example is provided in **Figure 7**.

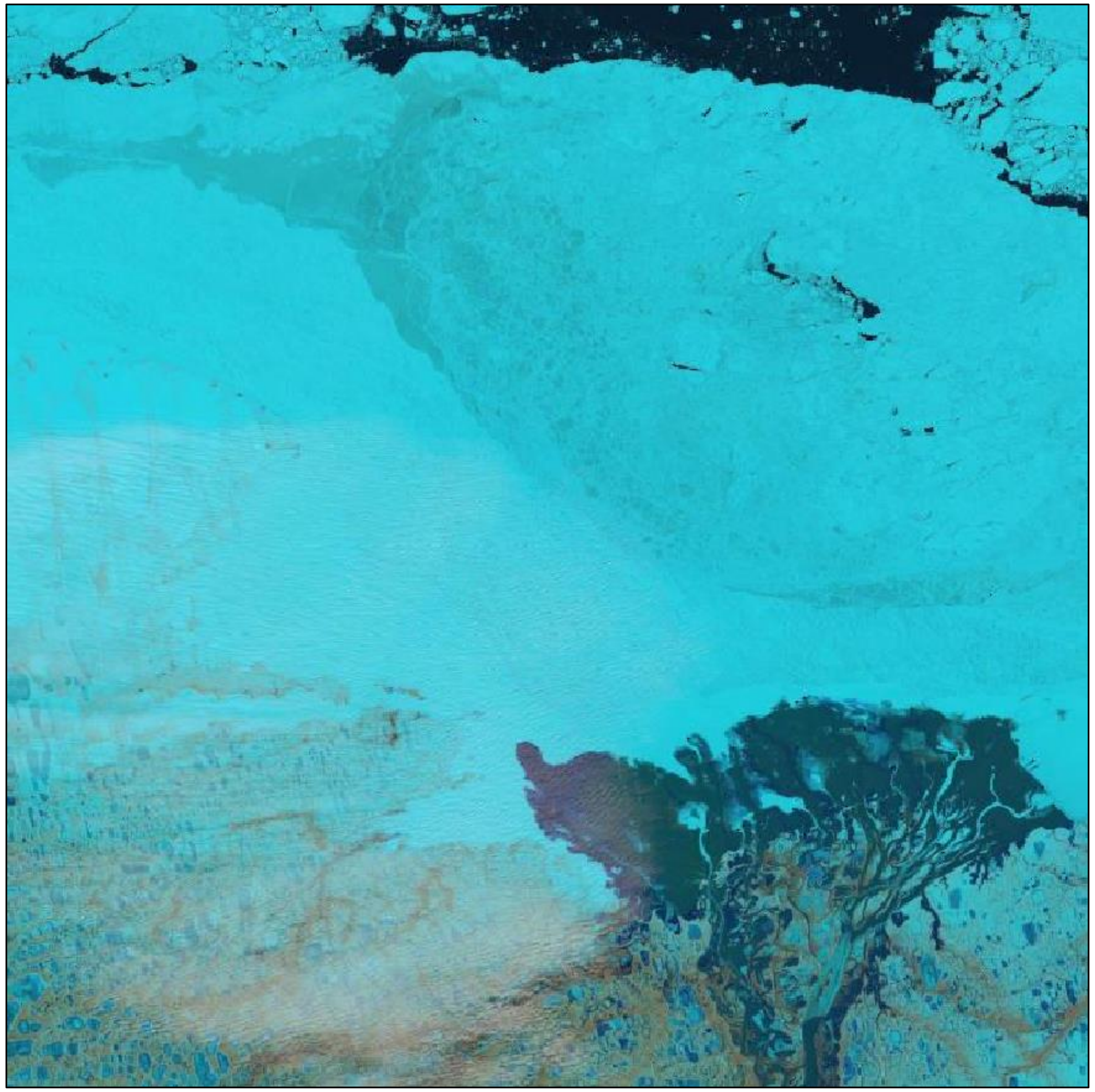

Figure 7. Sentinel-2 EW image of Colville River Delta on May 29th, 2020
Image source: USGS, 2021h

RESOURCESAT MISSIONS: Resourcesat-2A

Agency: Indian Space Research Organization

The Indian Space Research Organization's Indian Remote Sensing (IRS) Resourcesat satellites provide high-resolution multispectral images for land and water resource management (USGS, 2021i). Resourcesat-1 was launched in 2003, followed by Resourcesat-2 in 2011 and Resourcesat-2A in 2016. The satellites operate in a sun-synchronous orbit at an altitude of 817 km, and acquire imagery in four spectral bands very similar to the Landsat mission. The wavelengths range from Visible and Near-Infrared (VNIR) to Shortwave Infrared (SWIR).

Generally, Resourcesat imagery is not freely available. However, a collaborative effort between ISRO and the USGS provides open access to selected Resourcesat-2A products acquired from August 2016 to present (USGS, 2021i). The products that are open to all users, including scientific and commercial users, are acquired by two distinct sensors (**Figure 8**):

The ***Advanced Wide Field Sensor (AWiFS)***, which covers a 740-km orbital swath at a resolution of 56 m with a 5-day repeat cycle; and

The ***Linear Imaging Self Scanning Sensor (LISS-3)***, which covers a 140-km orbital swath at a spatial resolution of 24 m with a 24-day repeat cycle.

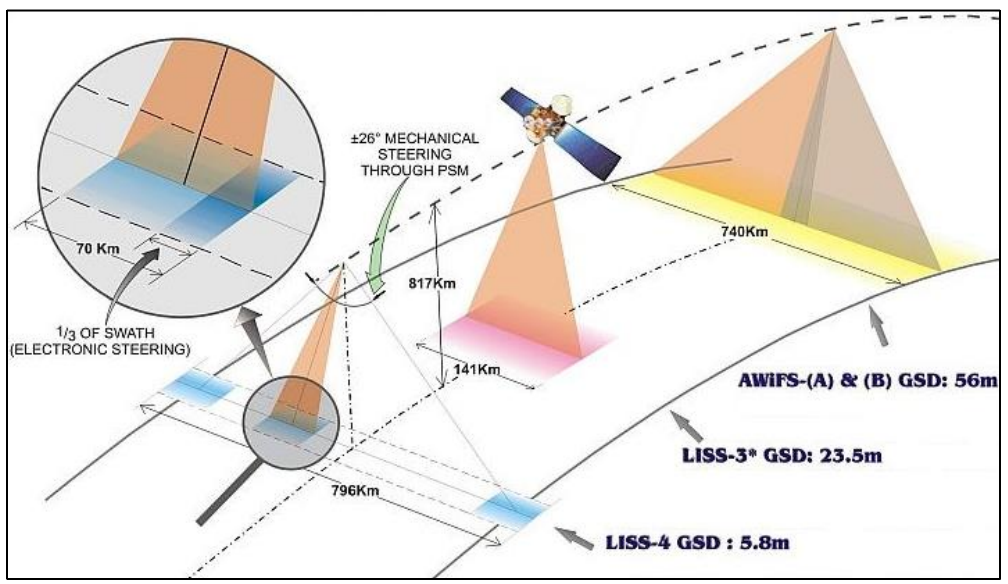

Figure 8. Resourcesat-2A sensors
Image source: ESA, 2021h

Available Data

Products are distributed by the USGS through the EarthExplorer data portal. Imagery is provided as a compressed bundle that includes one file for each of the four spectral bands in GeoTIFF format, plus metadata (USGS, 2021i). As in the case of Landsat and Sentinel-2 products, georeferenced Full Resolution Browse (FRB) images also are available from the USGS. In the case of Resourcesat, this product is a simulated natural color composite image created from three bands (5, 4, and 3). Examples of AWiFS and LISS-3 images are provided in **Figures 9** and **10**.

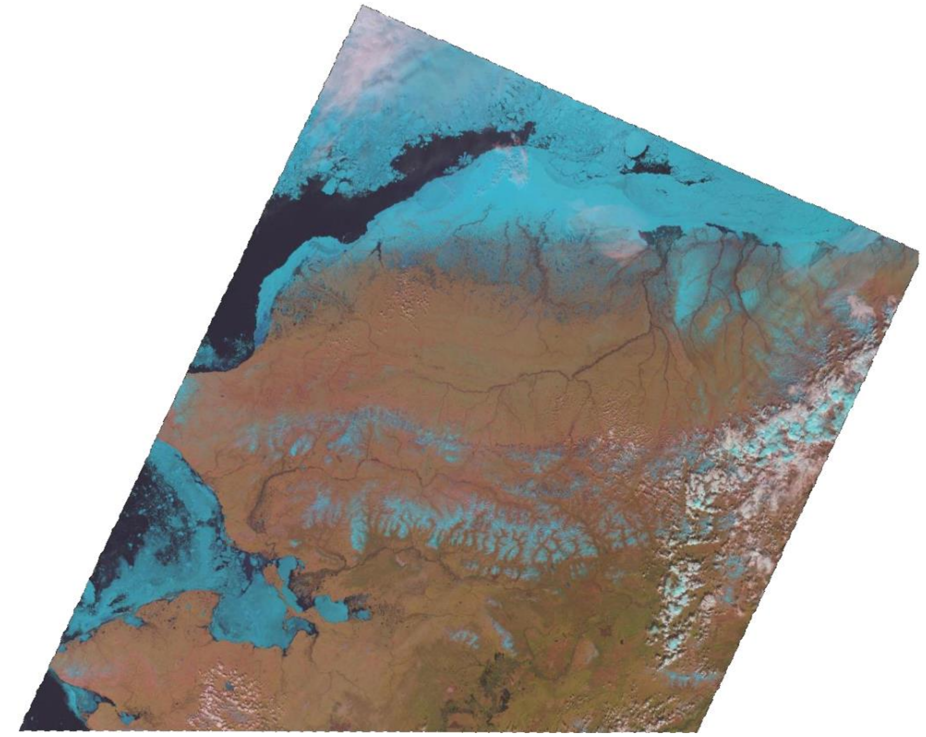

Figure 9. Resourcesat-2A AWiFS image (May 29th, 2020)
Image source: USGS, 2021j

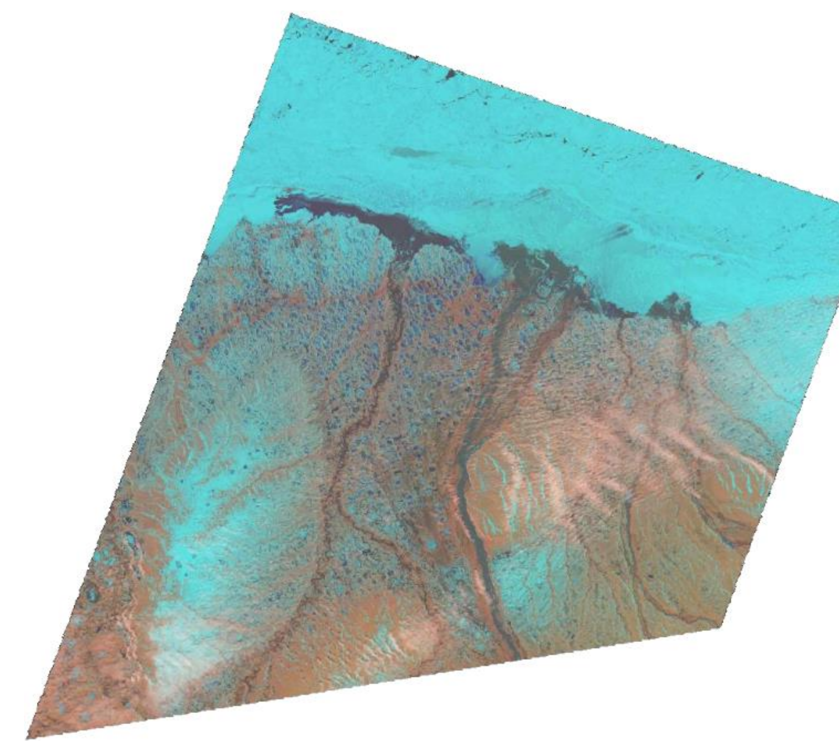

Figure 10. Resourcesat-2A LISS-3 image (May 30th, 2020)
Image source: USGS, 2021k

ALOS MISSIONS: ALOS Daichi

Agency: Japanese Aerospace Exploration Agency

The Advanced Land Observing Satellite (ALOS), also known as Daichi, was a mission of the Japanese Aerospace Exploration Agency developed to contribute to the fields of mapping, disaster monitoring, and resource surveying (JAXA, 2021a). The satellite was operative between 2006 and 2011, and was followed by the ALOS-2 mission in 2014. Daichi carried two sensors of interest for the current study: the Phased Array type L-band Synthetic Aperture Radar (PALSAR), and the Advanced Visible and Near Infrared Radiometer type 2 (AVNIR-2).

PALSAR was an active microwave sensor using L-band frequency to achieve cloud-free and day-and-night land observation (JAXA, 2021b). It had two fine beam modes: single polarization (FBS/DSN) and dual polarization (FBD), as well as a polarimetric mode (PLR). Lastly, the ScanSAR wide beam (WB1, WB2; **Figure 11**) provided wider image swaths at the expense of image resolution. **Table 2** summarizes the resolution and swath for each beam mode.

Table 2. ALOS PALSAR product modes (after: JAXA, 2021b)

Beam Mode	FBS, DSN (fine resolution)	FBD (fine resolution)	WB1, WB2 (ScanSAR)	Polarimetric
Polarization	HH or VV	HH+HV or VV+VH	HH or VV	HH+HV+VV+VH
Spatial Resolution	10 m	20 m	100 m	30 m
Swath Width	70 km	70 km	250-350 km	30 km

AVNIR-2 was an optical sensor for observing land and coastal zones (JAXA, 2021c). Imagery products have a spatial resolution of 10 m and a swath width of 70 km. Unfortunately, because coverage in the current project study area is very limited, AVNIR-2 imagery was excluded from further consideration.

Available Data

Selected ALOS imagery is available free of charge to U.S. users through NASA's ASF DAAC, as long as it is used for peaceful purposes only. The SAR products are provided at three processing levels (ASF DAAC, 2021d):

Raw Level-1.0 Data: Unprocessed, raw SAR data from which all other products are produced.

Processed Level-1.1 and 1.5 Products: The products intended for most users, Level-1 data can be processed into either single-look slant-range imagery (Level-1.1) and/or projected to ground range (Level 1.5). These formats are equivalent to Sentinel-1 SLC and GRD products.

Radiometrically and Terrain-Corrected (RTC) Products: These products are created by the ASF from JAXA data in an effort to make SAR data accessible to a broader community of users by post-processing the scenes (ASF DAAC, 2021e). The download bundle contains RTC files in GIS-ready GeoTIFF format for each polarization available, and ancillary files and metadata. Products are produced at 12.5-m or 30-m resolutions. Examples are provided in **Figures 11** and **12**. The RTC scenes greatly simplify data processing and storage relative to the Level-1 products. However, not all ALOS PALSAR imagery is processed to RTC by the ASF.

Figure 11. ALOS PALSAR ScanSAR image (May 30th, 2009)
Image source: ASF DAAC, 2021f

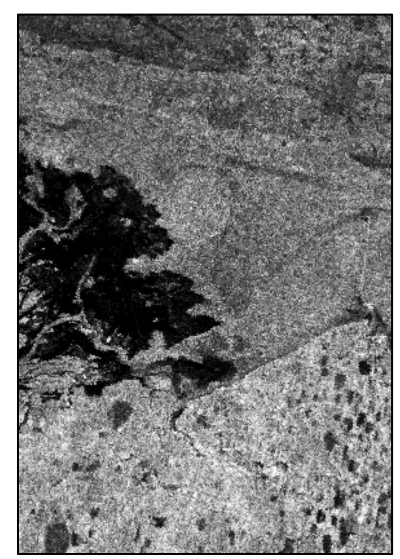

Figure 12. ALOS PALSAR fine resolution image (May 21st, 2009)
Image source: ASF DAAC, 2021f

ERS MISSIONS: ERS-2

Agency: European Space Agency

The European Remote Sensing (ERS) program was the European Space Agency's first earth observation effort, and it was developed to provide environmental monitoring in the microwave spectrum (ESA, 2021i). ERS-1 was launched in 1991 and remained operational through the year 2000. A virtually identical follow-up mission, ERS-2, provided data between 1995 and 2011.

Both satellites followed a near-circular, polar sun-synchronous orbit at an altitude of 785 km. The missions' range of instruments were capable of monitoring the land, oceans, and atmosphere (ESA, 2021i). The ERS products investigated for the current project are the high-resolution imagery obtained in Image Mode by the Synthetic Aperture Radar instrument onboard of ERS-2. The characteristics of these products are summarized in **Table 3**.

Table 3. Characteristics of ERS-2 SAR products acquired in Image Mode (after: ASF DAAC, 2021g)

Parameter	Description
Frequency/Wavelength	5.3 GHz/C-band 5.6 cm
Polarization	VV
Spatial Resolution	26 m across track; between 6 and 30 m along track
Swath Width	100 km
Repeat Cycle	3 days

Available Data

A subset of ERS-2 SAR data is now free and open via the ASF DAAC by agreement between NASA and ESA. The spatial coverage of the available imagery, which includes the current study area, is shown in **Figure 13**.

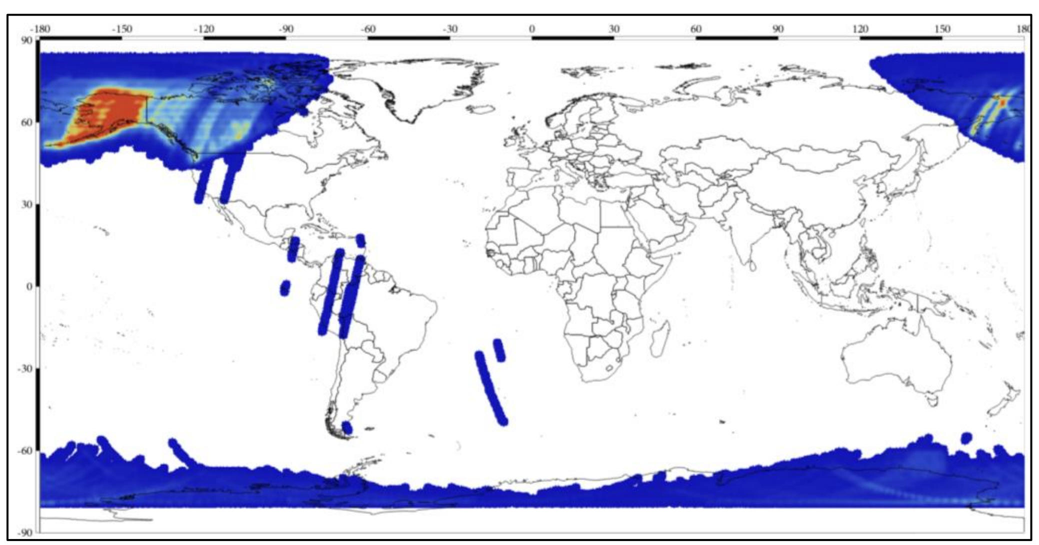

Figure 13. ERS-2 SAR product coverage in the ASF DAAC archive
Image source: ASF DAAC, 2021g

ERS-2 SAR data are provided at two processing levels:

Raw Level-0 Data: Unprocessed, raw SAR data.

Processed Level-1 Products: Processed image products in Committee on Earth Observation Satellites (CEOS) format. In order to fully integrate these products into a GIS environment, they need to be geocoded.

For the current study, CEOS-formatted data granules were geocoded and transformed to GeoTIFF format using the ASF MapReady utility. An example of the imagery is given in **Figure 14**.

Figure 14. ERS-2 Synthetic Aperture Radar image of Colville River delta (May 20th, 2009)
Image source: ASF DAAC, 2021h

References

ASF DAAC, 2021a, Alaska Satellite Facility, Sentinel-1, About, *https://asf.alaska.edu/data-sets/sar-data-sets/sentinel-1/sentinel-1-about*.

ASF DAAC, 2021b, Alaska Satellite Facility, Sentinel-1, Data and Imagery, *https://asf.alaska.edu/data-sets/sar-data-sets/sentinel-1/sentinel-1-data-and-imagery*.

ASF DAAC, 2021c, Copernicus Sentinel-1 dataset, accessed through ASF DAAC, *https://asf.alaska.edu*.

ASF DAAC, 2021d, Alaska Satellite Facility PALSAR Products, *https://asf.alaska.edu/data-sets/sar-data-sets/alos-palsar/alos-palsar-about*.

ASF DAAC, 2021e, ALOS PALSAR, Radiometric Terrain Correction, *https://asf.alaska.edu/data-sets/sar-data-sets/alos-palsar/alos-palsar-about*.

ASF DAAC, 2021f, JAXA/METI ALOS PALSAR 2009 dataset, accessed through ASF DAAC, *https://asf.alaska.edu*.

ASF DAAC, 2021g, ERS-1 SAR Data, *https://asf.alaska.edu/data-sets/sar-data-sets/ers-1*.

ASF DAAC, 2021h, ESA ERS-2 dataset, accessed through ASF DAAC, *https://asf.alaska.edu*.

ESA, 2021a, Sentinel-1 User Guide, Acquisition Modes, *https://sentinel.esa.int/web/sentinel/user-guides/sentinel-1-sar/acquisition-modes*.

ESA, 2021b, Sentinel-1 User Guide, Product Types and Processing Levels, Level 0, https://*sentinel.esa.int/web/sentinel/user-guides/sentinel-1-sar/product-types-processing-levels/level-0*.

ESA, 2021c, Sentinel-1 User Guide, Product Types and Processing Levels, Level 1, *https://sentinel.esa.int/web/sentinel/user-guides/sentinel-1-sar/product-types-processing-levels/level-1*.

ESA, 2021d, Sentinel-1 User Guide, Product Types and Processing Levels, Level 2, *https://sentinel.esa.int/web/sentinel/user-guides/sentinel-1-sar/product-types-processing-levels/level-2*.

ESA, 2021e, Sentinel-2 Mission Overview, *https://sentinel.esa.int/web/sentinel/missions/sentinel-2/overview*.

ESA, 2021f, Sentinel-2 MSI User Guide, Product Types, Level 0, *https://sentinel.esa.int/web/sentinel/user-guides/sentinel-2-msi/product-types/level-0*.

ESA, 2021g, Sentinel-2 MSI User Guide, Product Types, *https://sentinel.esa.int/web/sentinel/user-guides/sentinel-2-msi/product-types*.

ESA, 2021h, eoPortal Directory, Resourcesat-2, *https://earth.esa.int/web/eoportal/satellite-missions/r/resourcesat-2*

ESA, 2021i, Earth Online, About ERS, *https://earth.esa.int/eogateway/missions/ers#instruments-section*.

JAXA, 2021a, Advanced Land Observing Satellite, About ALOS, Overview and Objectives, *https://www.eorc.jaxa.jp/ALOS/en/index_e.htm*.

JAXA, 2021b, Advanced Land Observing Satellite, About ALOS, PALSAR, *https://www.eorc.jaxa.jp/ALOS/en/index_e.htm*.

JAXA, 2021c, Advanced Land Observing Satellite, About ALOS, AVNIR-2, *https://www.eorc.jaxa.jp/ALOS/en/index_e.htm*.

NASA, 2021a, Moderate Resolution Imaging Spectroradiometer data and products, *https://modis.gsfc.nasa.gov/data*.

NASA, 2021b, Worldview Snapshots Frequently Asked Questions, *https://earthdata.nasa.gov/faq/worldview-snapshots-faq*.

NASA, 2021c, Terra MODIS True Color and 7-2-1 Correct Reflectance datasets, accessed through Worldview Snapshots, part of the Earth Observing System Data and Information System, *https://wvs.earthdata.nasa.gov*.

NOAA, 2021, NOAA/NASA Joint Polar Satellite System Program, *https://www.jpss.noaa.gov*.

USGS, 2021a, Landsat Satellite Missions, *https://www.usgs.gov/core-science-systems/nli/landsat/landsat-satellite-missions?qt-science_support_page_related_con=0#qt-science_support_page_related_con*.

USGS, 2021b, Landsat 8, *https://www.usgs.gov/core-science-systems/nli/landsat/landsat-8?qt-science_support_page_related_con=0#qt-science_support_page_related_con*.

USGS, 2021c, Landsat 7, *https://www.usgs.gov/core-science-systems/nli/landsat/landsat-7?qt-science_support_page_related_con=0#qt-science_support_page_related_con*.

USGS, 2021d, Landsat 5, *https://www.usgs.gov/core-science-systems/nli/landsat/landsat-5?qt-science_support_page_related_con=0#qt-science_support_page_related_con*.

USGS, 2021e, Earth Resources Observation and Science Center Archive, Landsat Archives, *https://www.usgs.gov/centers/eros/science/usgs-eros-archive-landsat-archives-landsat-8-oli-operational-land-imager-and?qt-science_center_objects=0#qt-science_center_objects*.

USGS, 2021f, Landsat 8 and 7 Collection 1 LandsatLook dataset, accessed through Earth Resources Observation and Science Center Archive, EarthExplorer Tool, *https://earthexplorer.usgs.gov*.

USGS, 2021g, Earth Resources Observation and Science Center Archive, Sentinel-2, *https://www.usgs.gov/centers/eros/science/usgs-eros-archive-sentinel-2?qt-science_center_objects=0#qt-science_center_objects*.

USGS, 2021h, Sentinel-2 Level-1C TOA dataset, accessed through Earth Resources Observation and Science Center Archive, EarthExplorer Tool, *https://earthexplorer.usgs.gov*.

USGS, 2021i, Earth Resources Observation and Science Center Archive, ISRO Resourcesat 1 and Resourcesat 2, *https://www.usgs.gov/centers/eros/science/usgs-eros-archive-isro-resourcesat-1-and-resourcesat-2-liss-3?qt-science_center_objects=0#*.

USGS, 2021j, ISRO Resourcesat-2A AWiFS dataset, accessed through Earth Resources Observation and Science Center Archive, EarthExplorer Tool, *https://earthexplorer.usgs.gov*.

USGS, 2021k, ISRO Resourcesat-2A LISS-3 dataset, accessed through Earth Resources Observation and Science Center Archive, EarthExplorer Tool, *https://earthexplorer.usgs.gov*.

Appendix B: Composite Overflood Extent Boundaries, 1995–2020

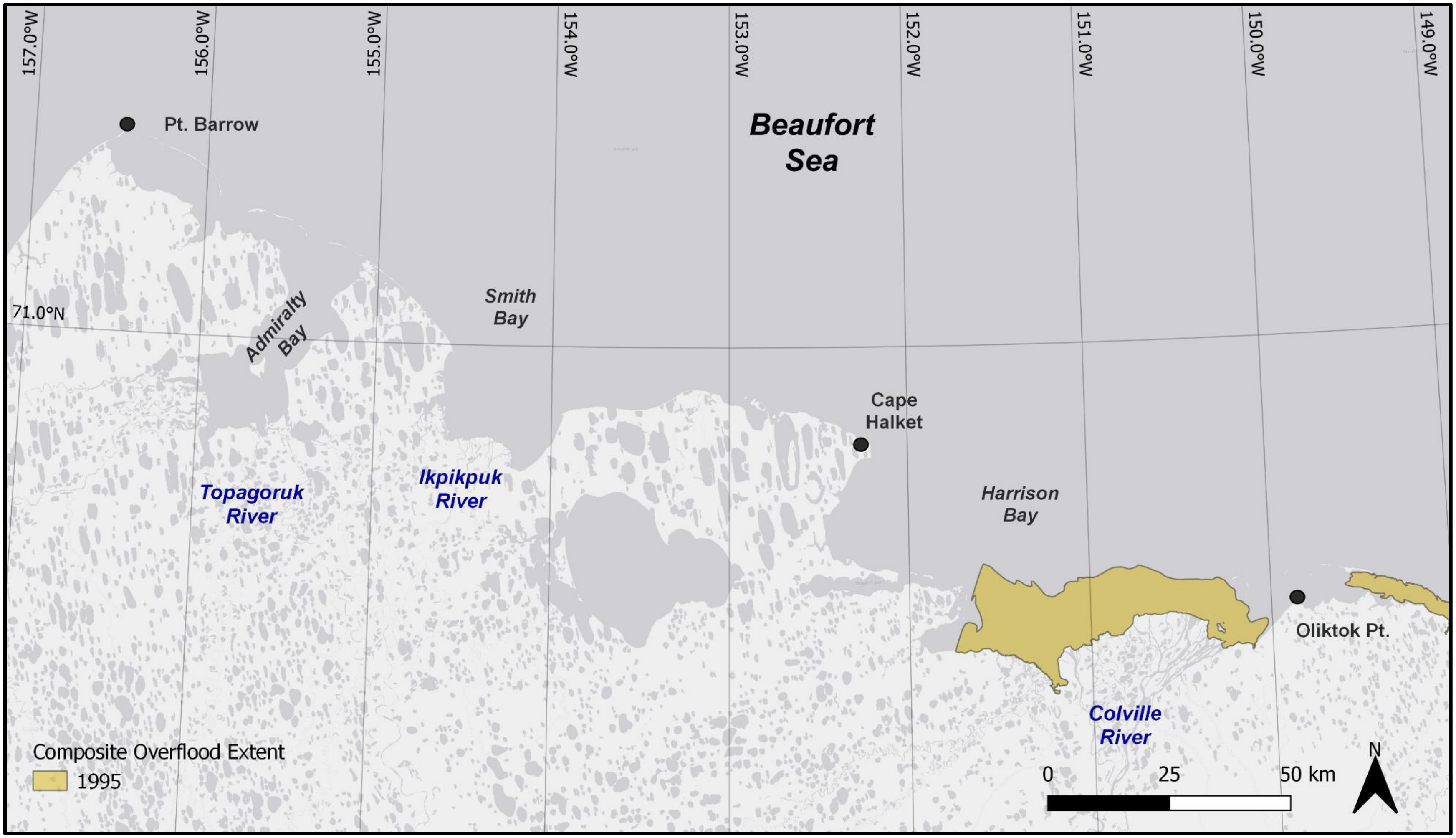

Figure 1. Composite overflood extent, west study region, 1995

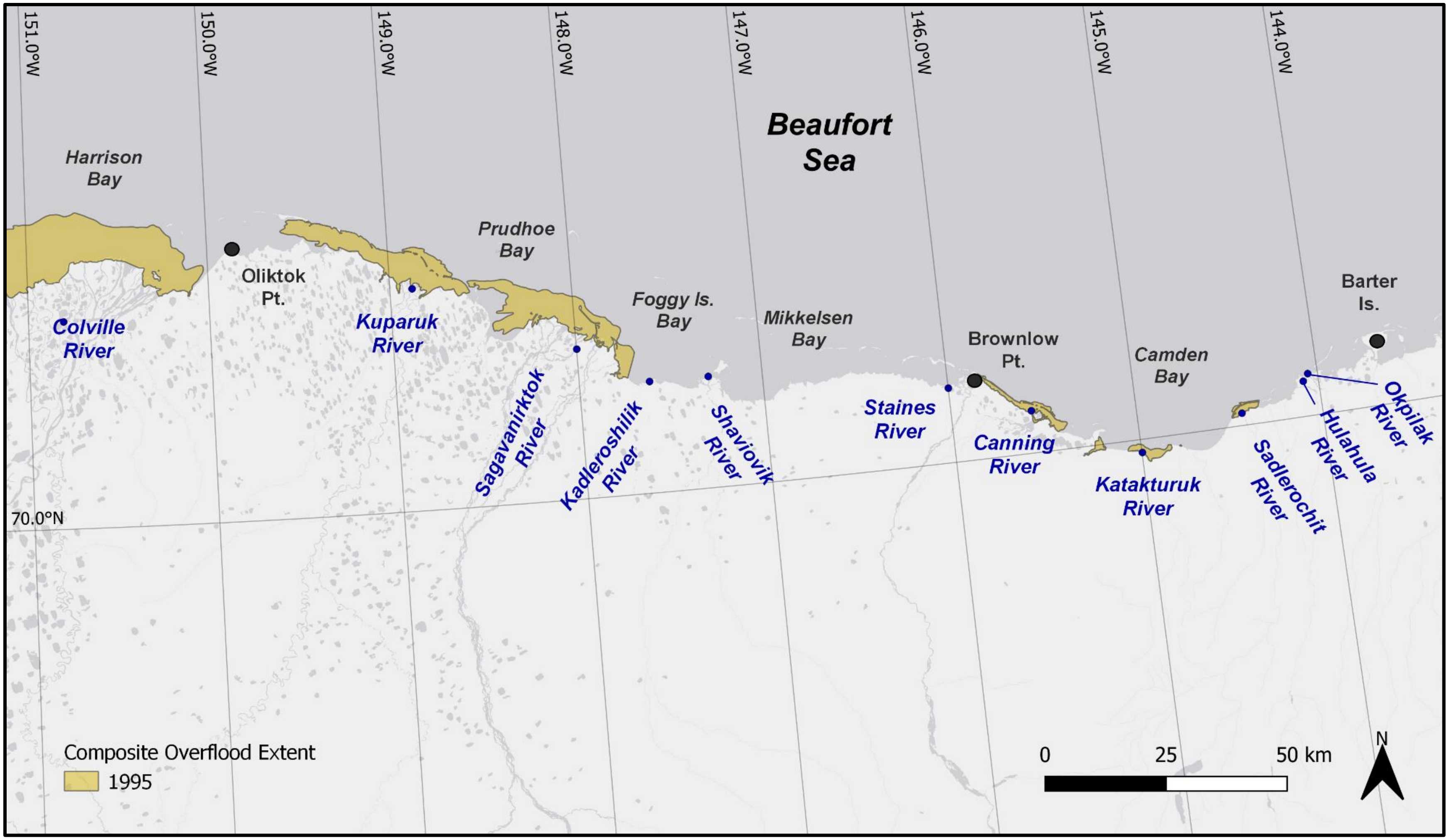

Figure 2. Composite overflood extent, east study region, 1995

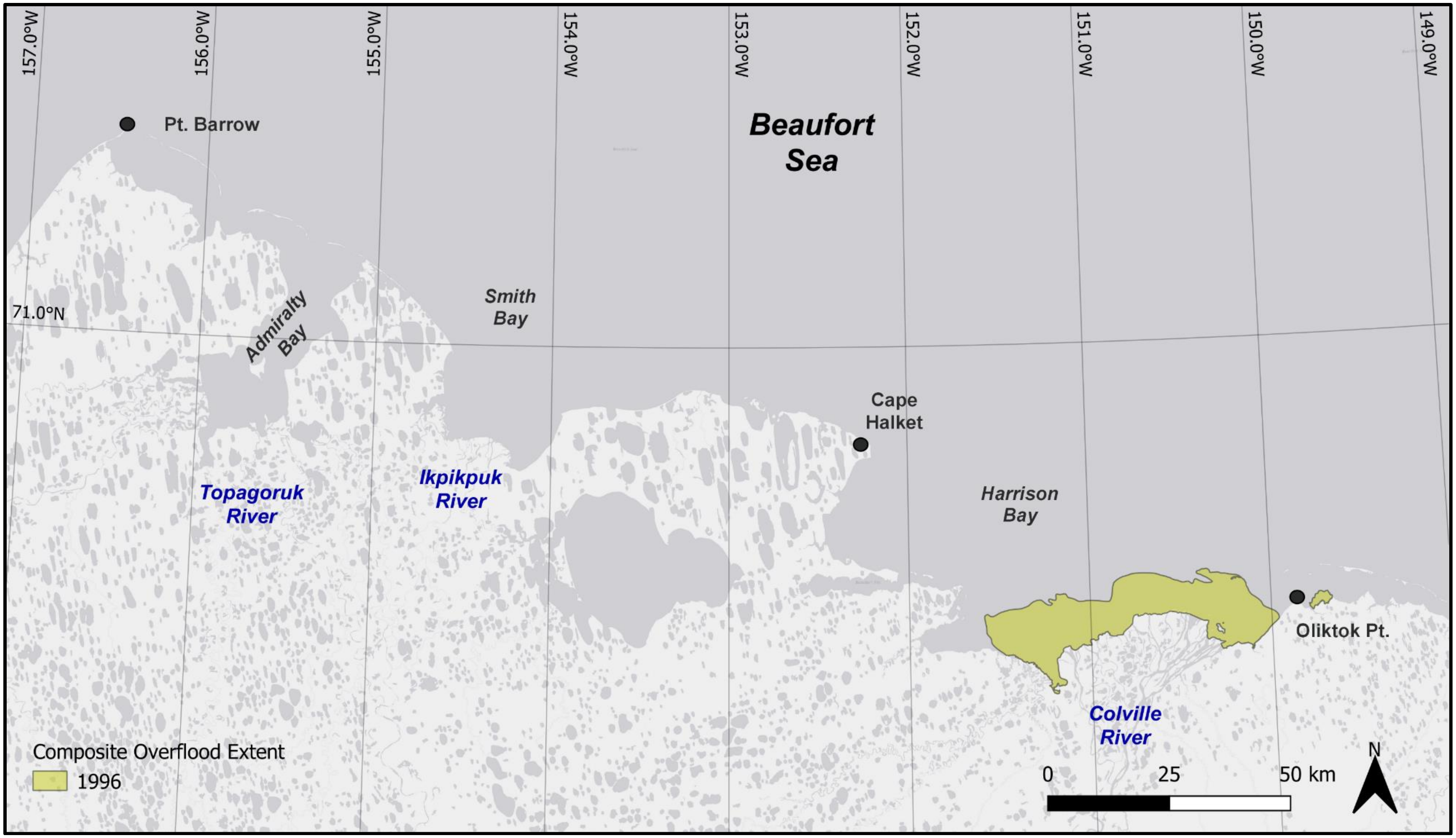

Figure 3. Composite overflood extent, west study region, 1996

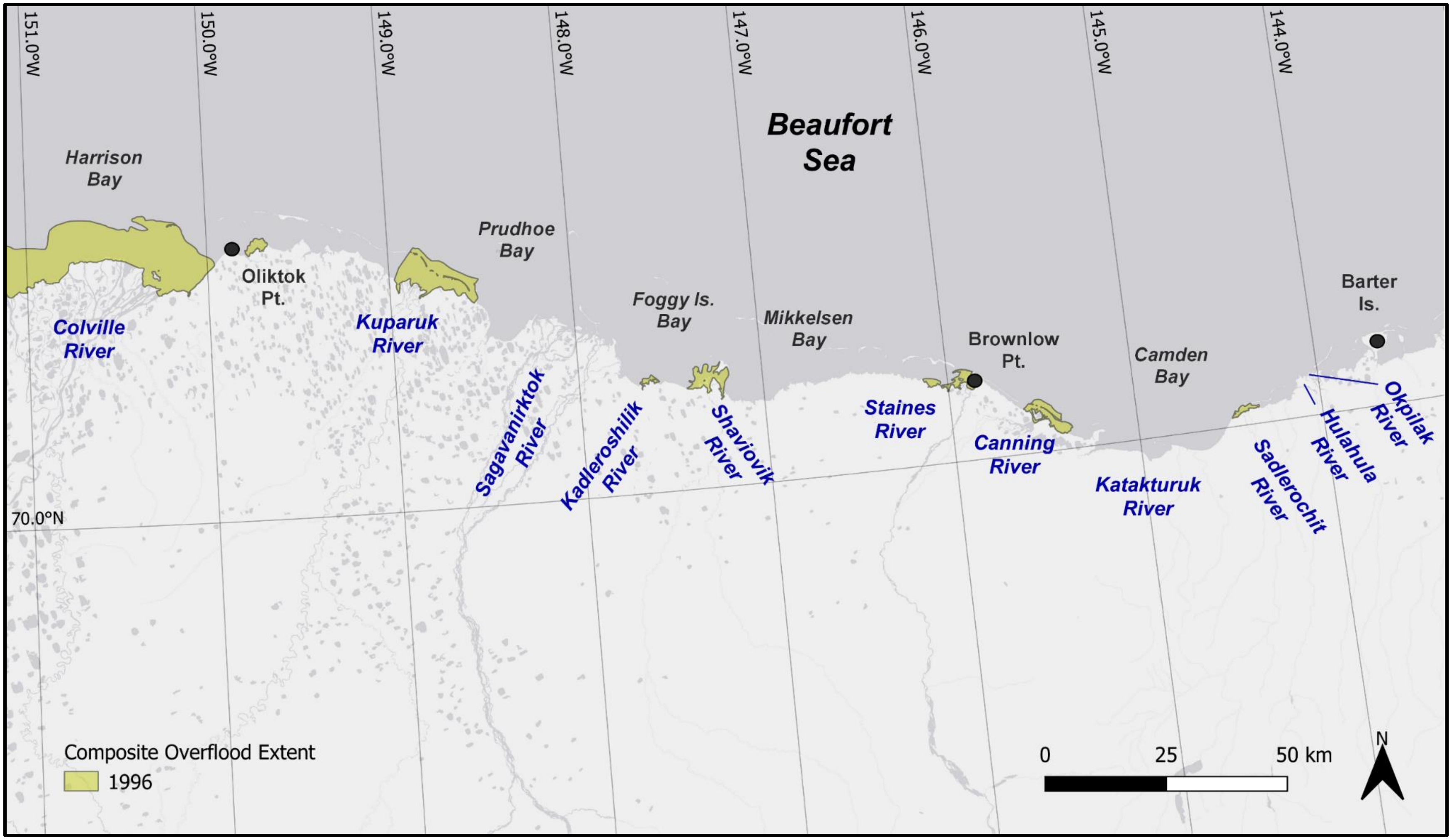

Figure 4. Composite overflood extent, east study region, 1996

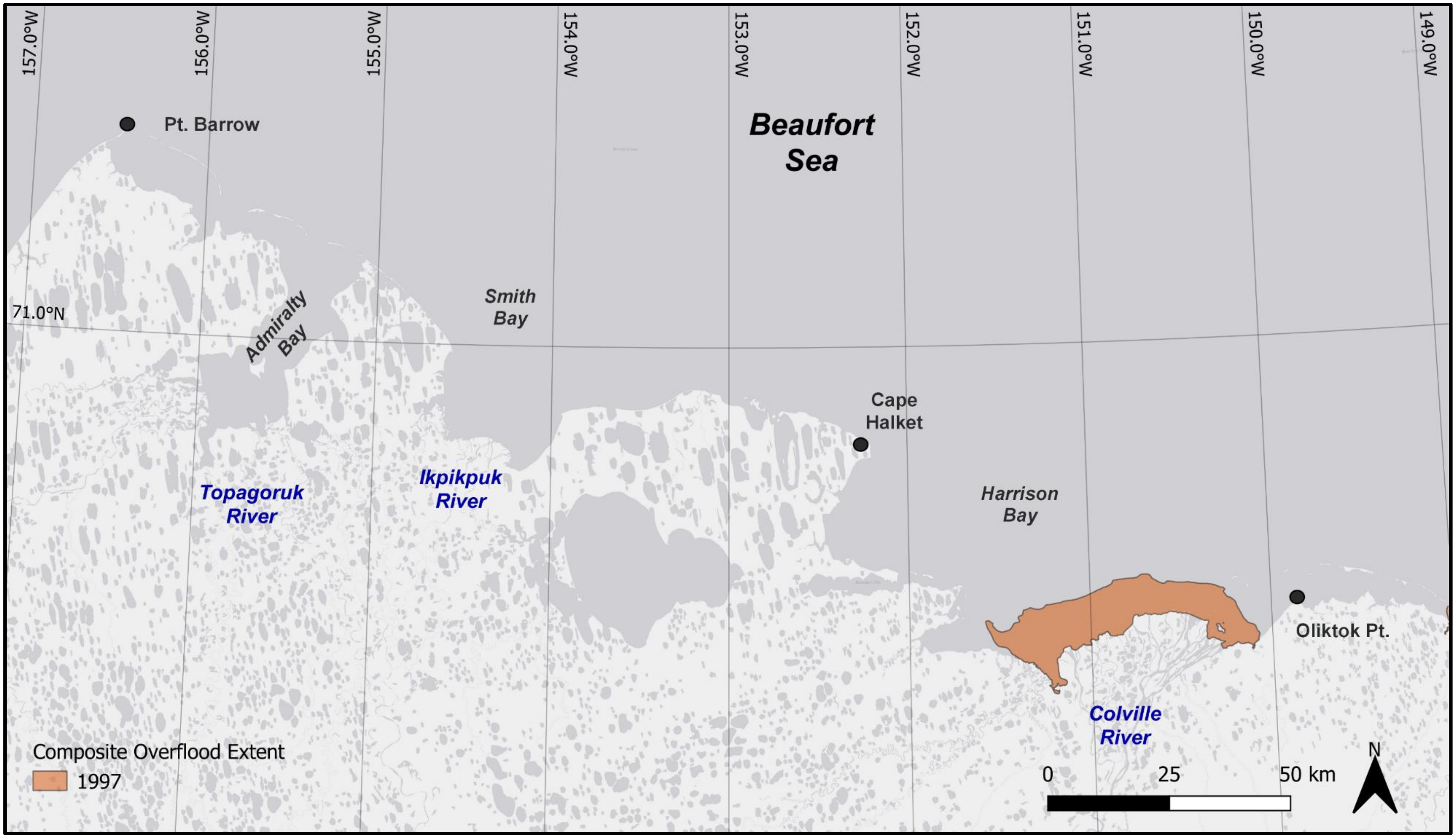

Figure 5. Composite overflood extent, west study region, 1997

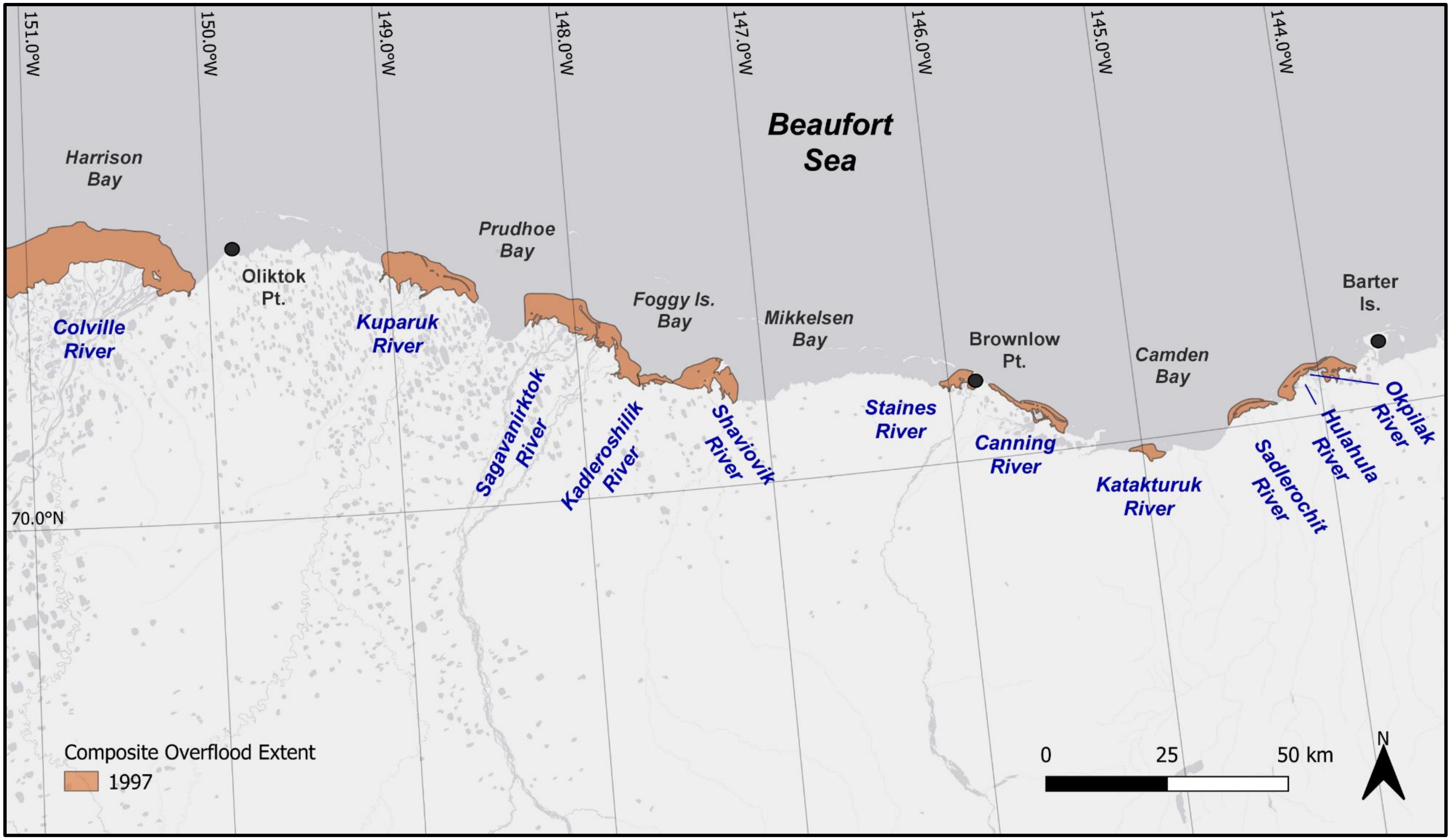

Figure 6. Composite overflood extent, east study region, 1997

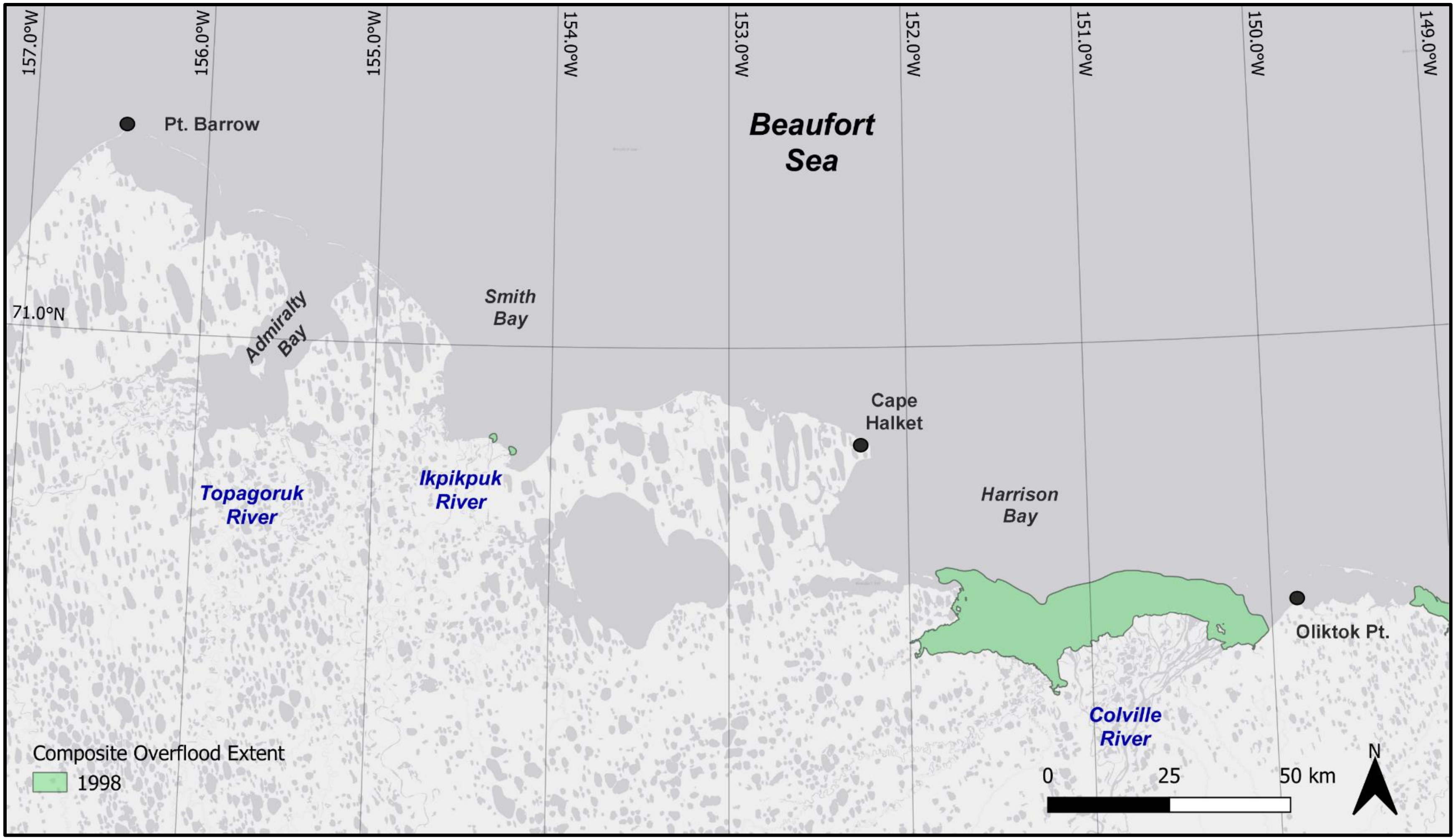

Figure 7. Composite overflood extent, west study region, 1998

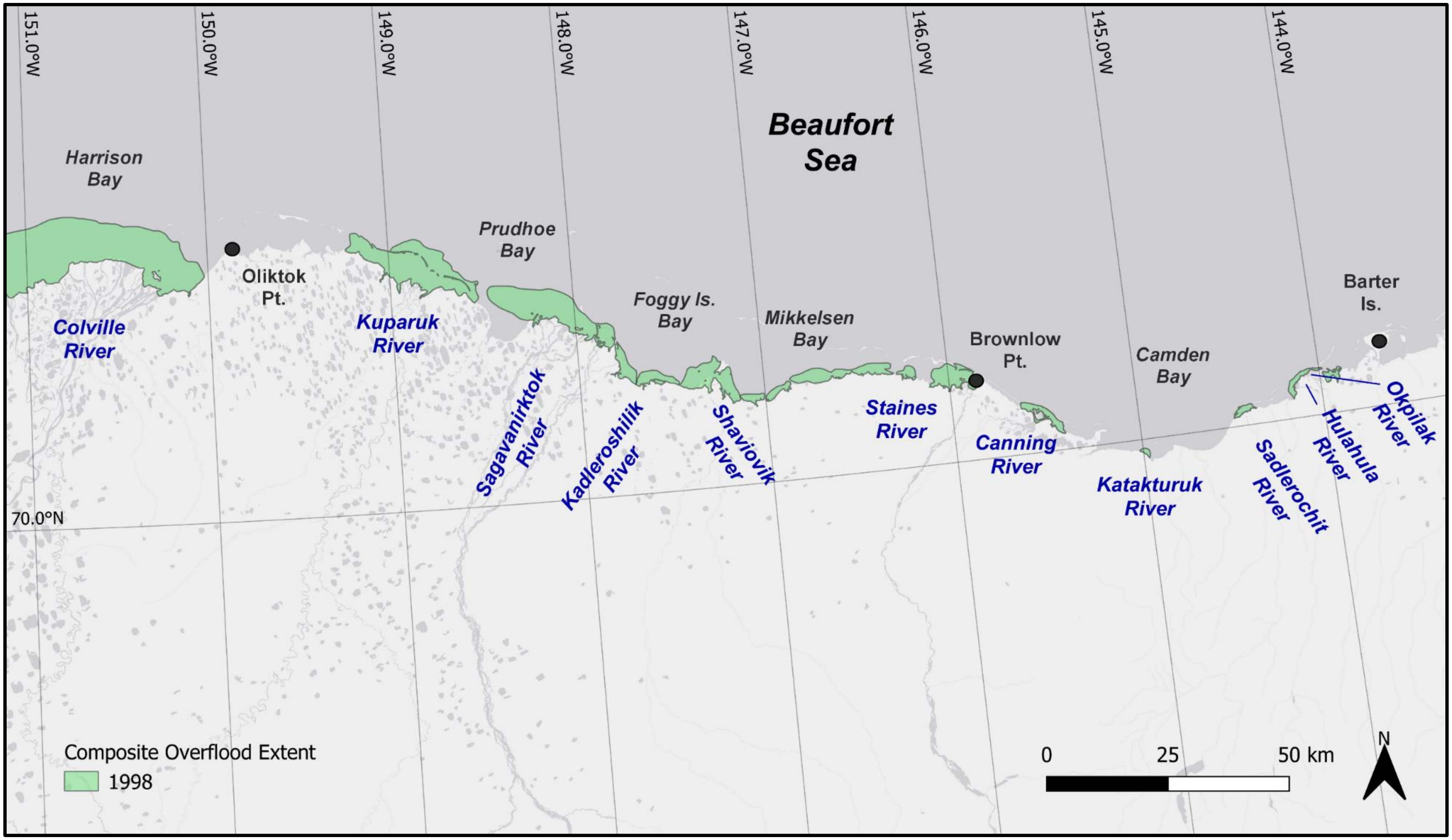

Figure 8. Composite overflood extent, east study region, 1998

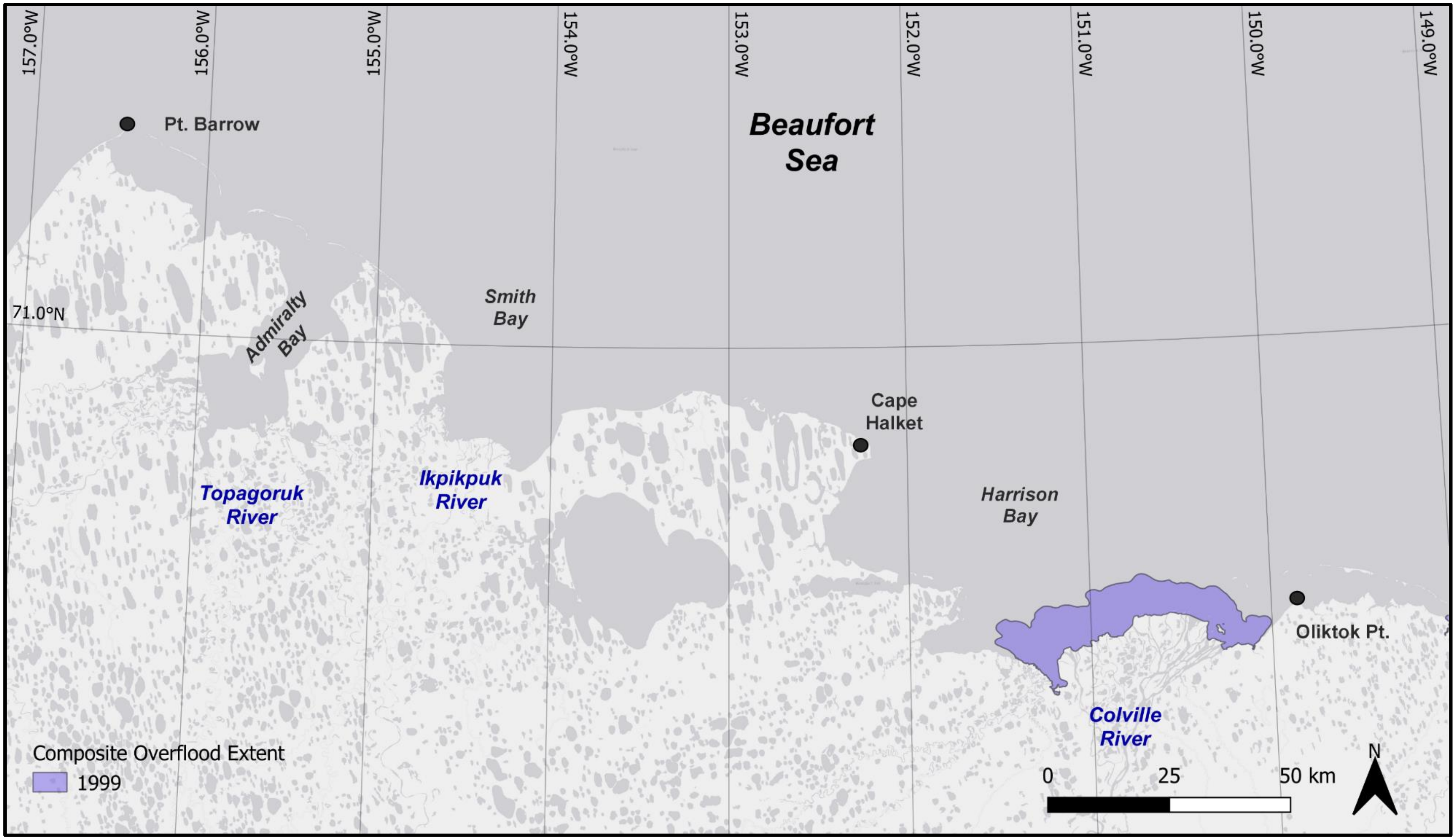

Figure 9. Composite overflood extent, west study region, 1999

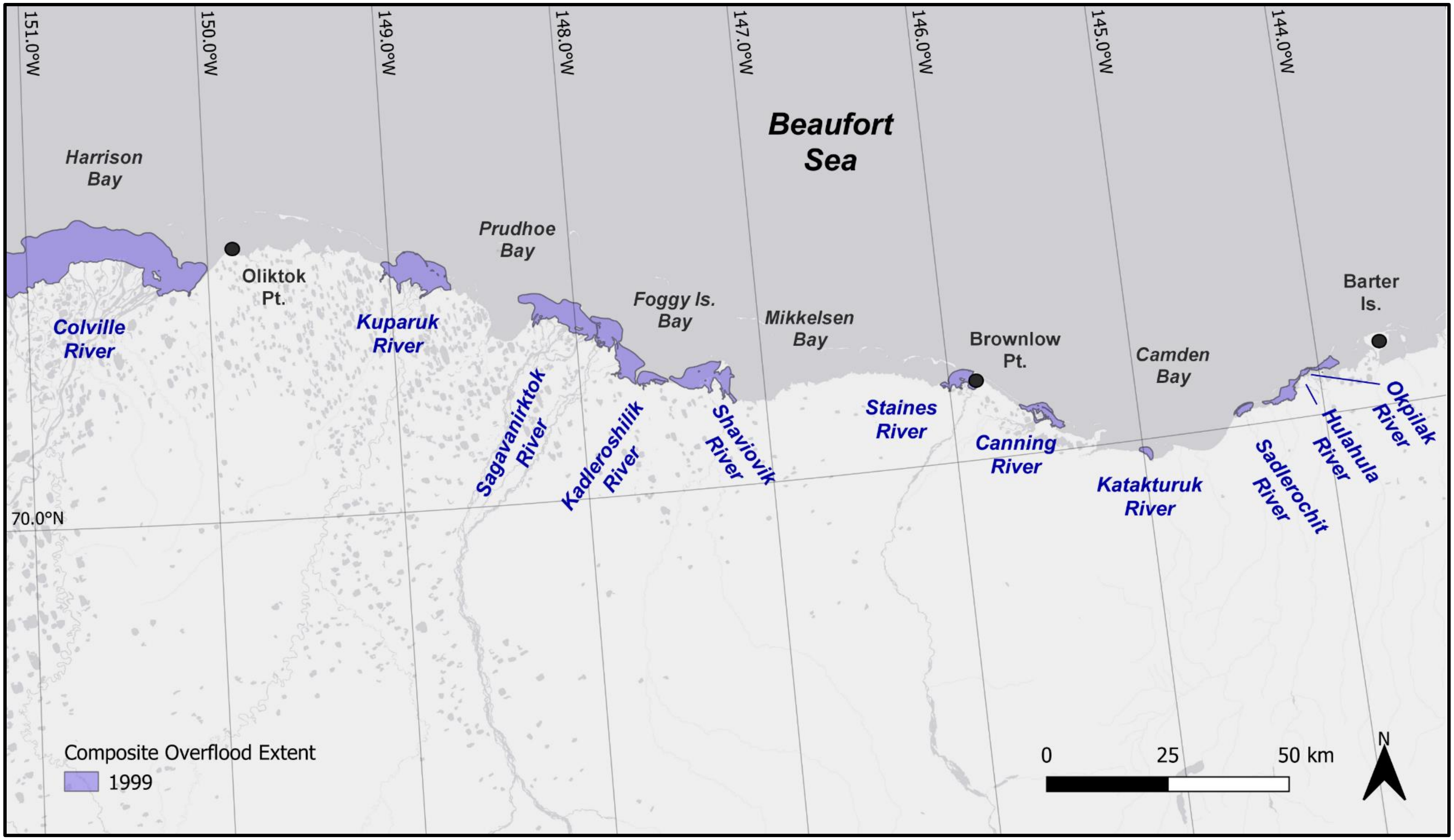

Figure 10. Composite overflood extent, east study region, 1999

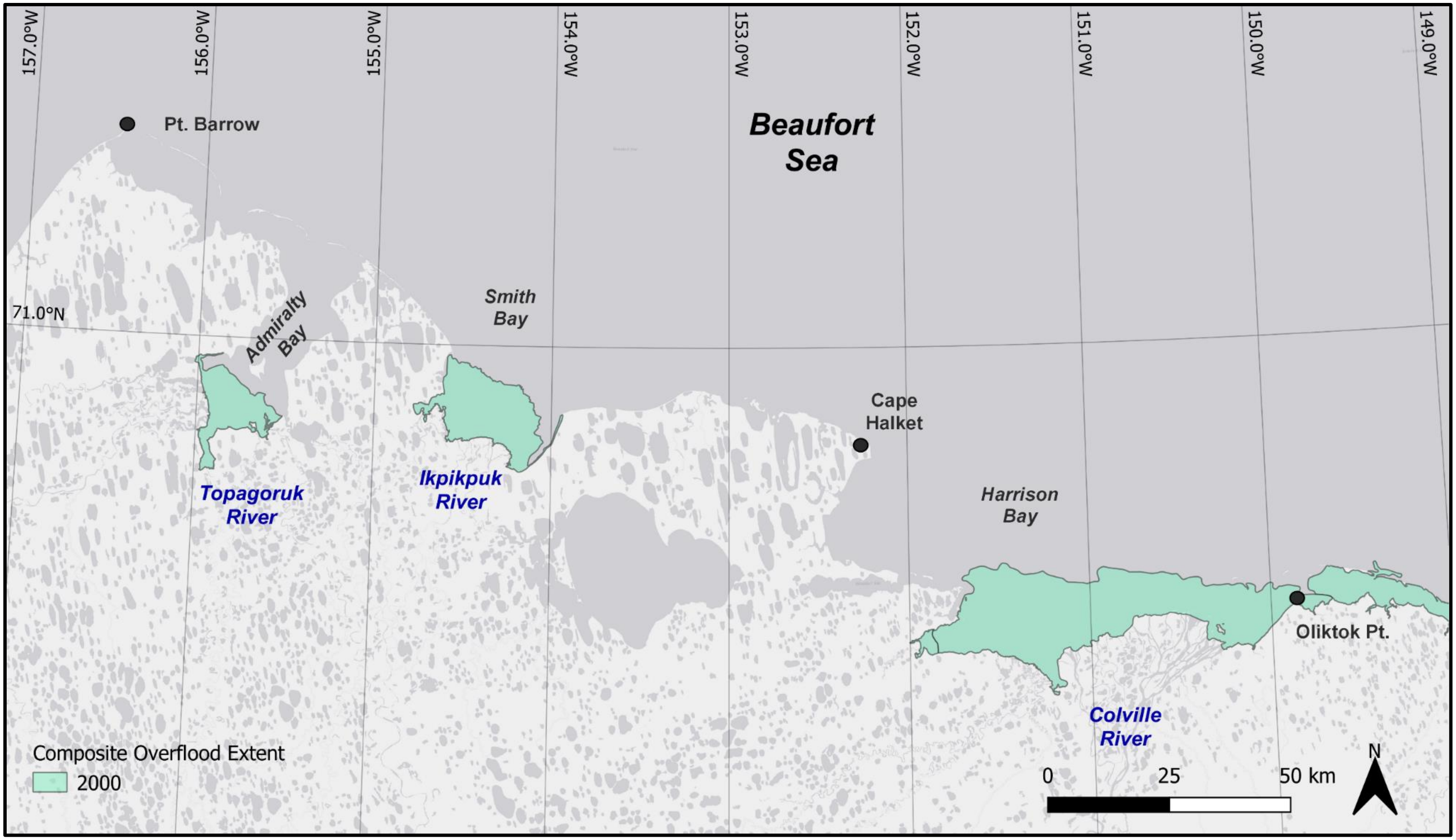

Figure 11. Composite overflood extent, west study region, 2000

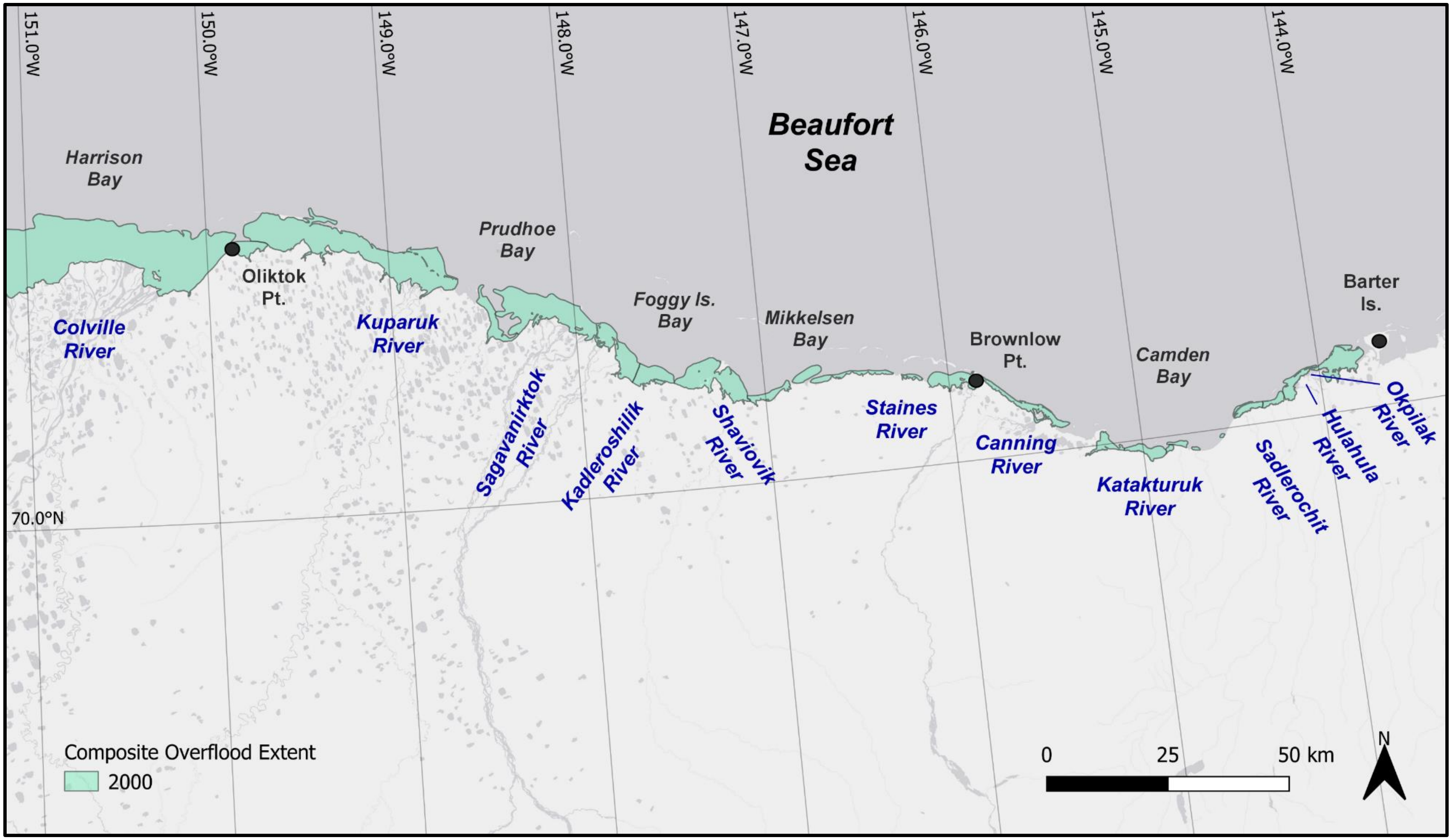

Figure 12. Composite overflood extent, east study region, 2000

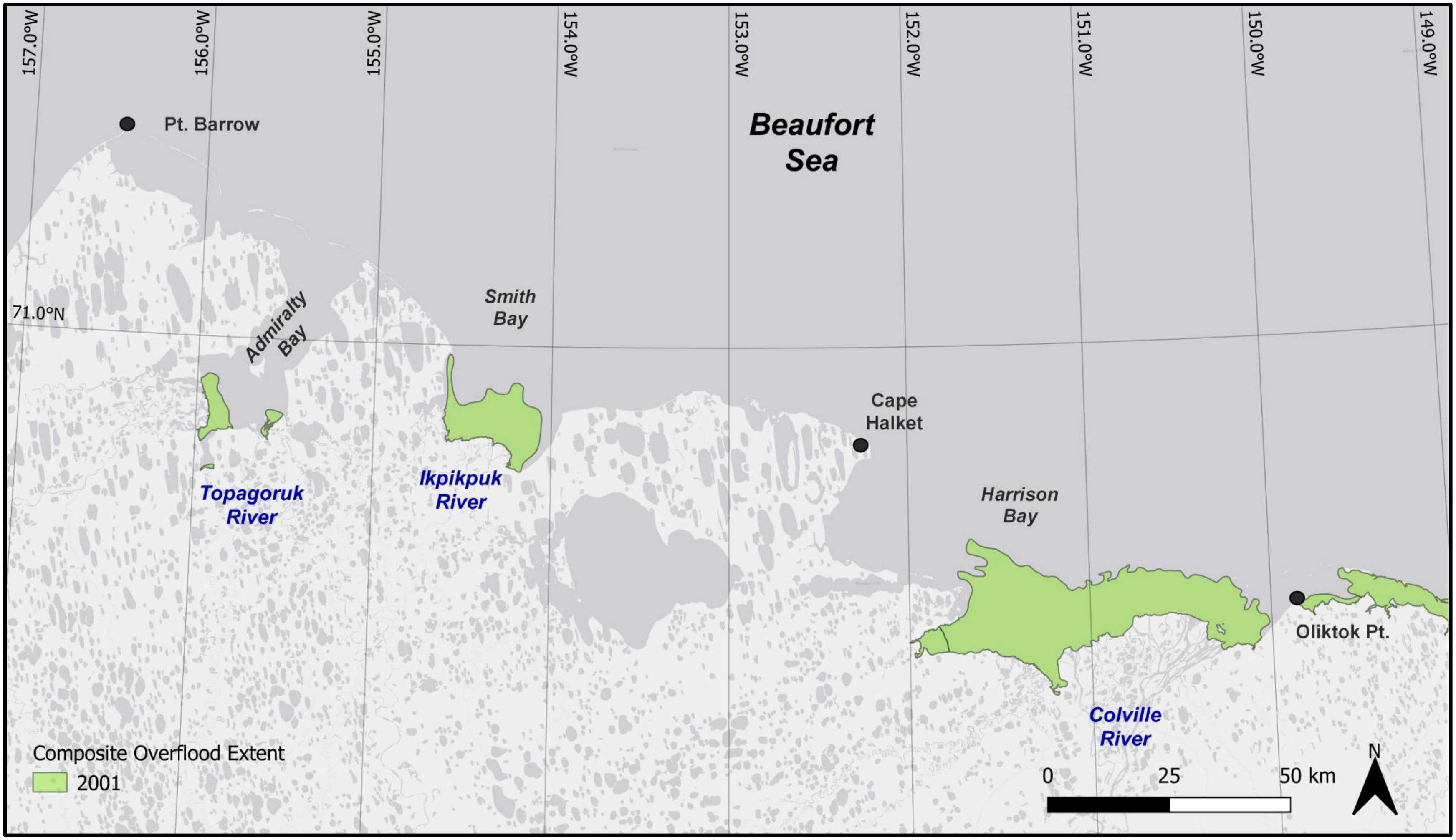

Figure 13. Composite overflood extent, west study region, 2001

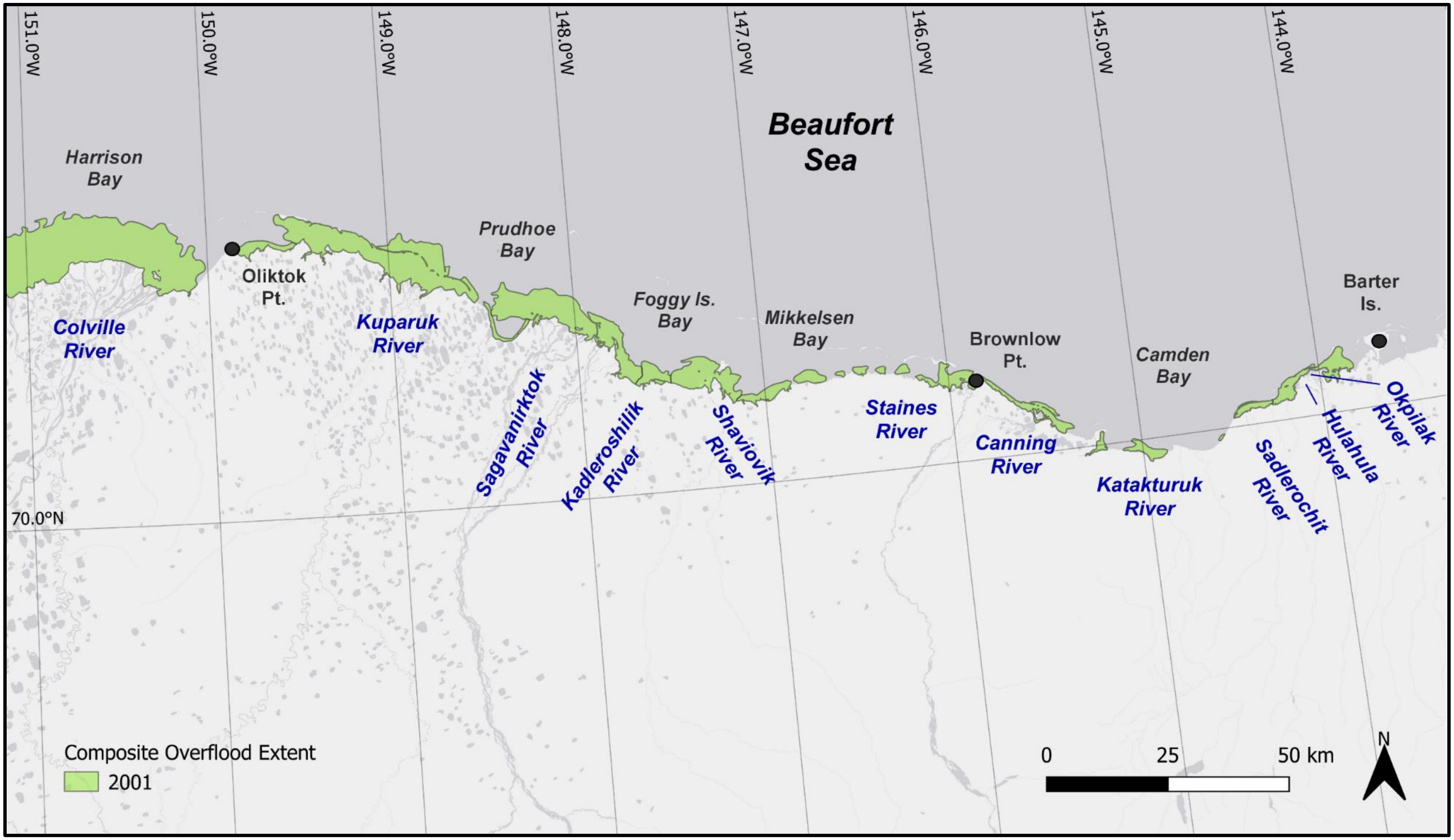

Figure 14. Composite overflood extent, east study region, 2001

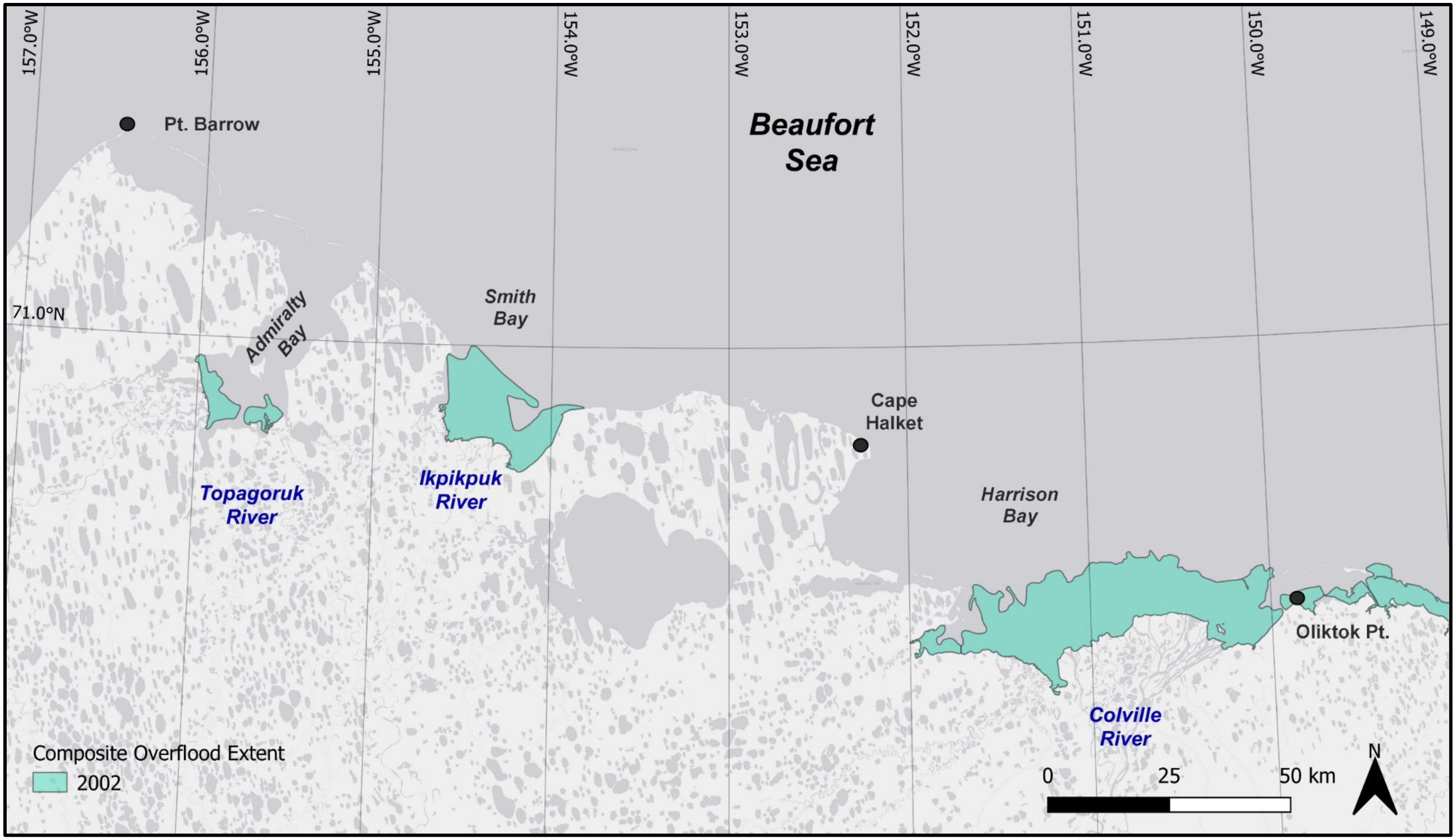

Figure 15. Composite overflood extent, west study region, 2002

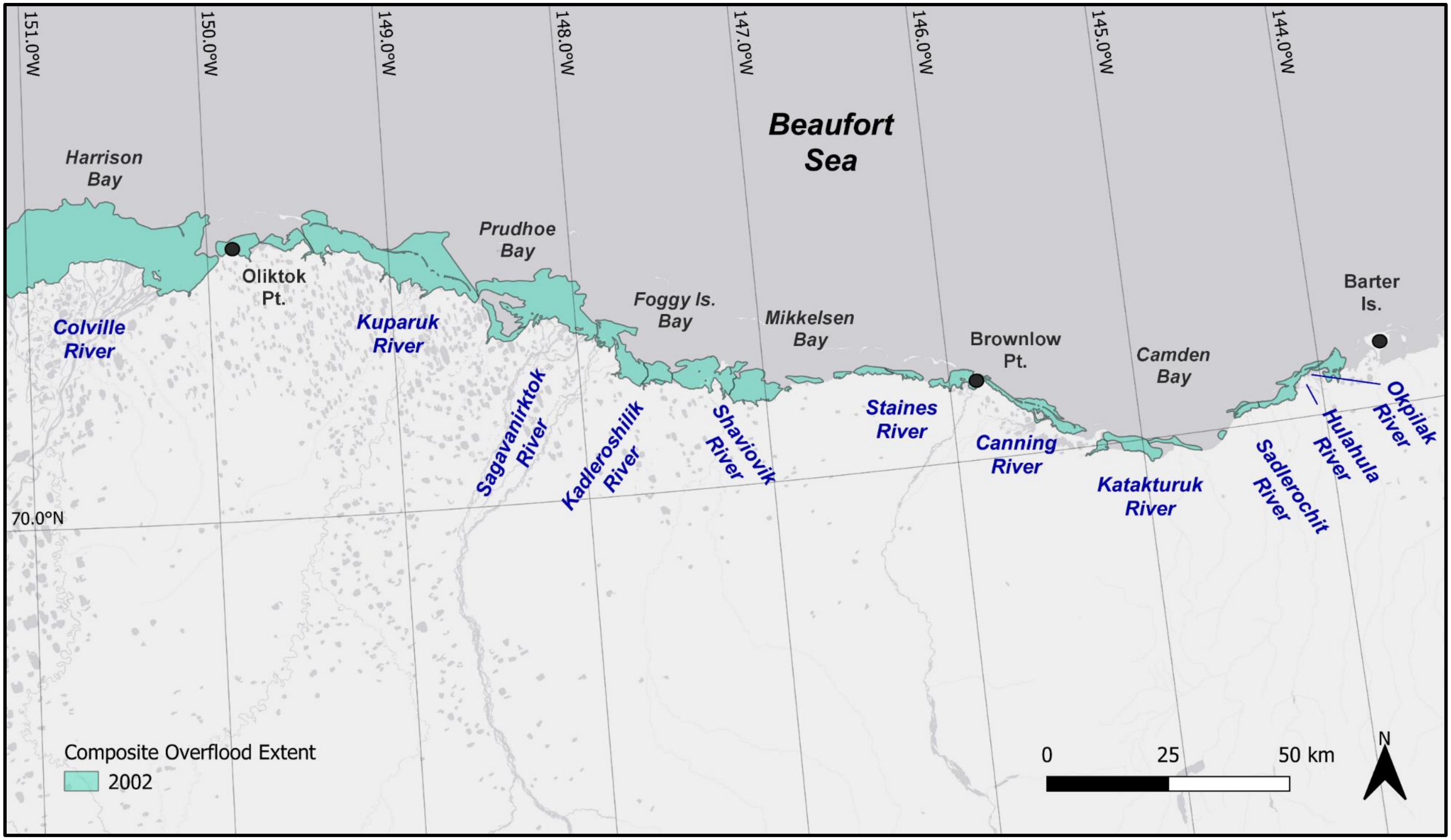

Figure 16. Composite overflood extent, east study region, 2002

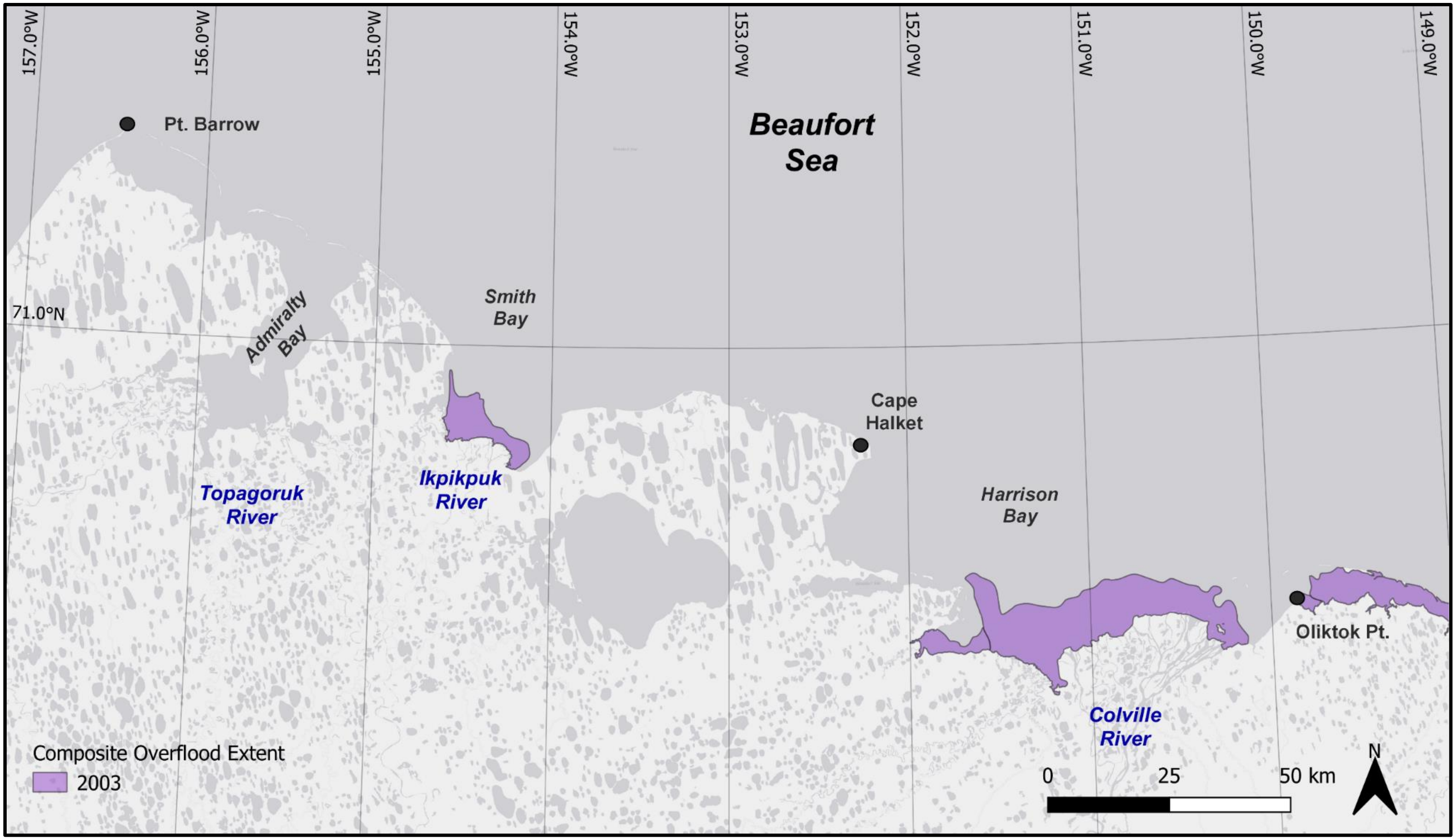

Figure 17. Composite overflood extent, west study region, 2003

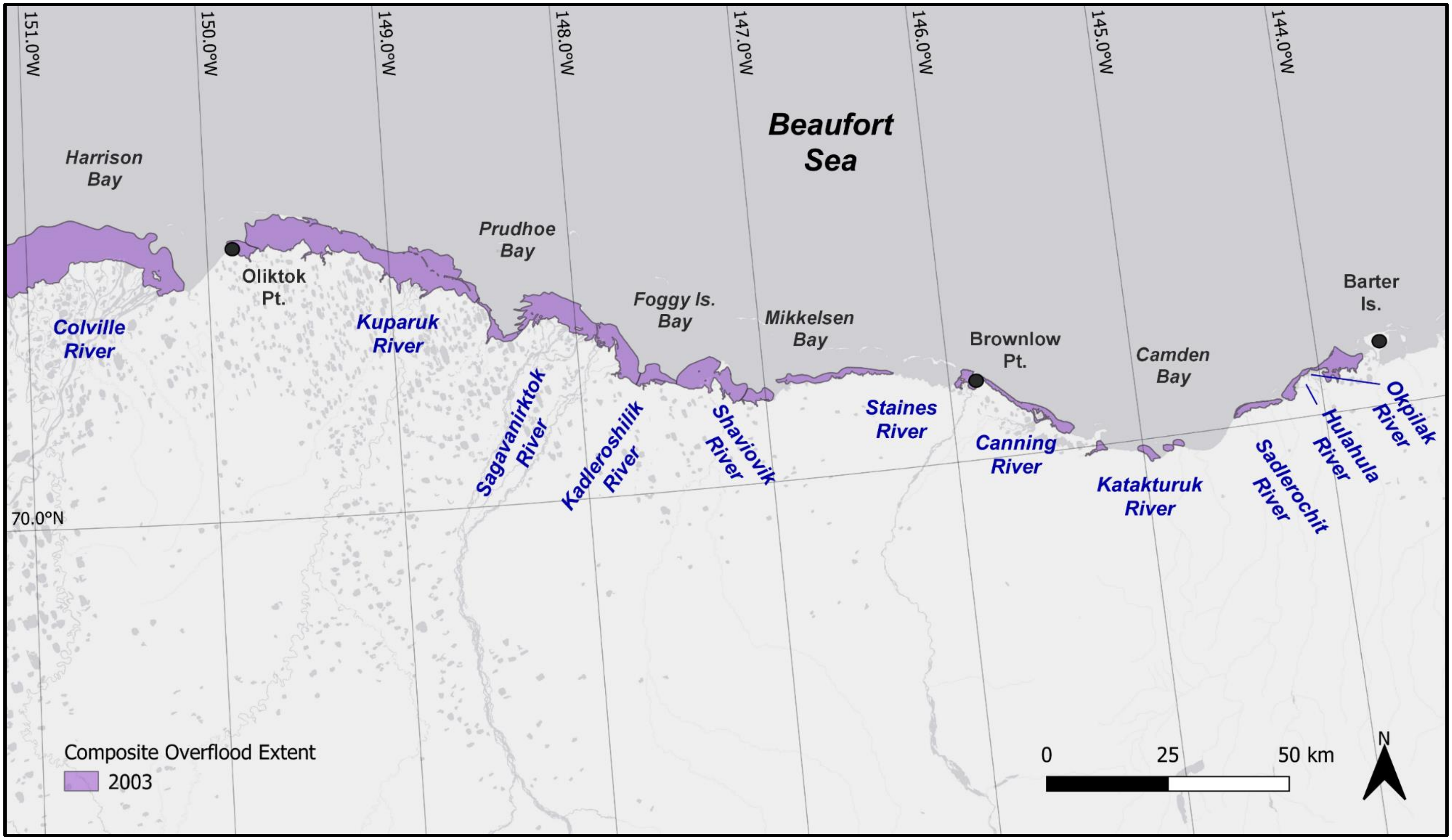

Figure 18. Composite overflood extent, east study region, 2003

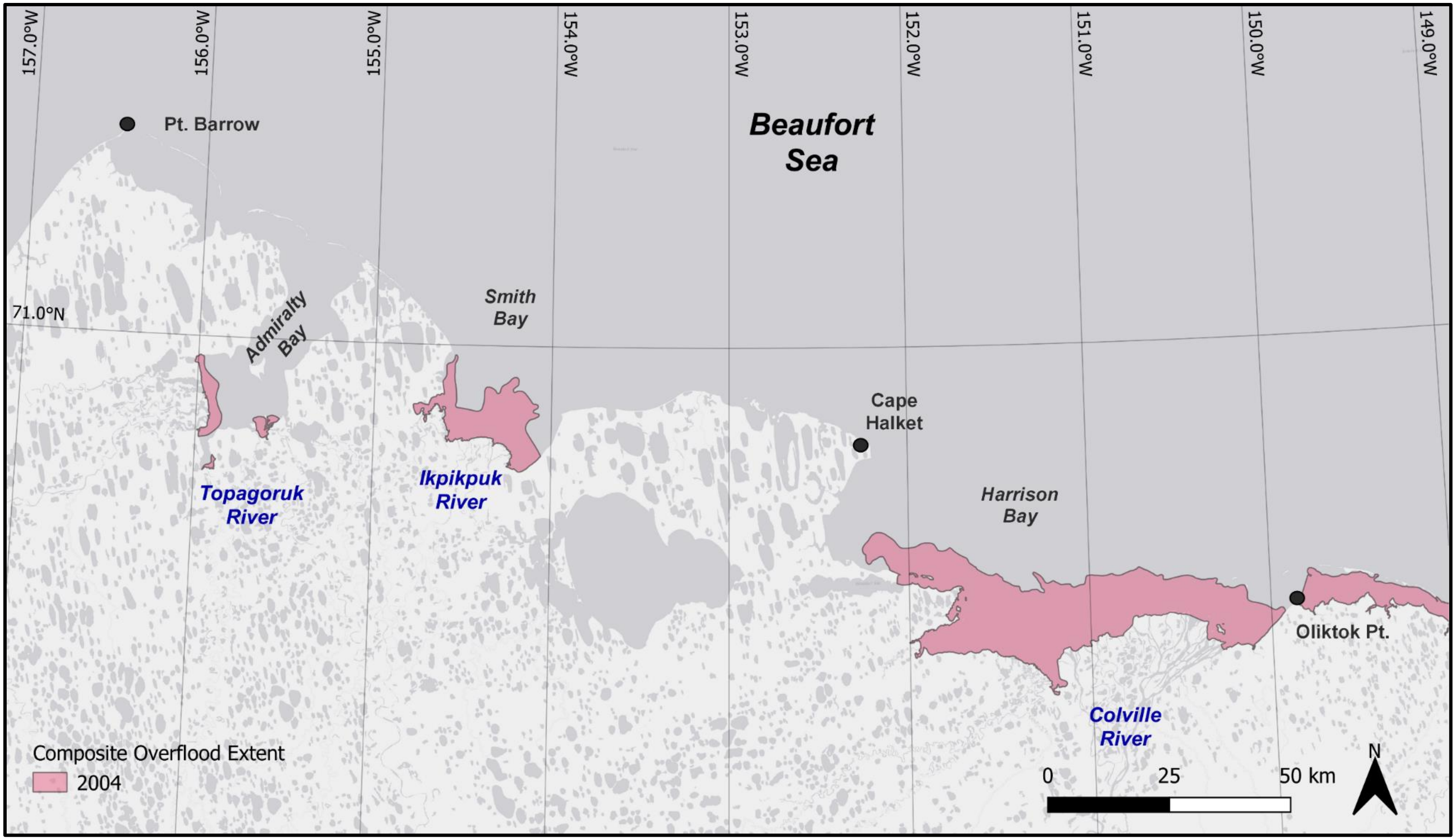

Figure 19. Composite overflood extent, west study region, 2004

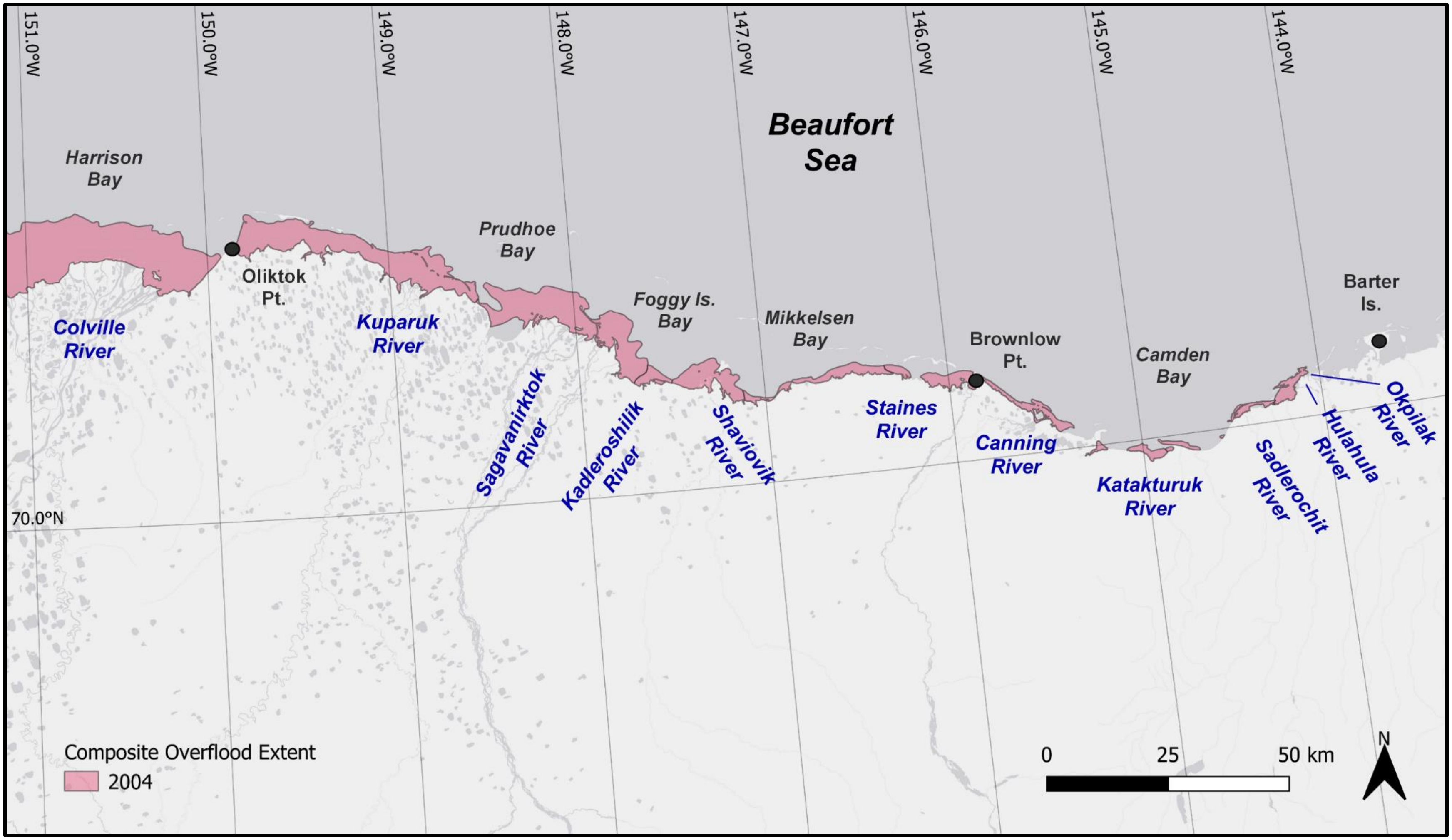

Figure 20. Composite overflood extent, east study region, 2004

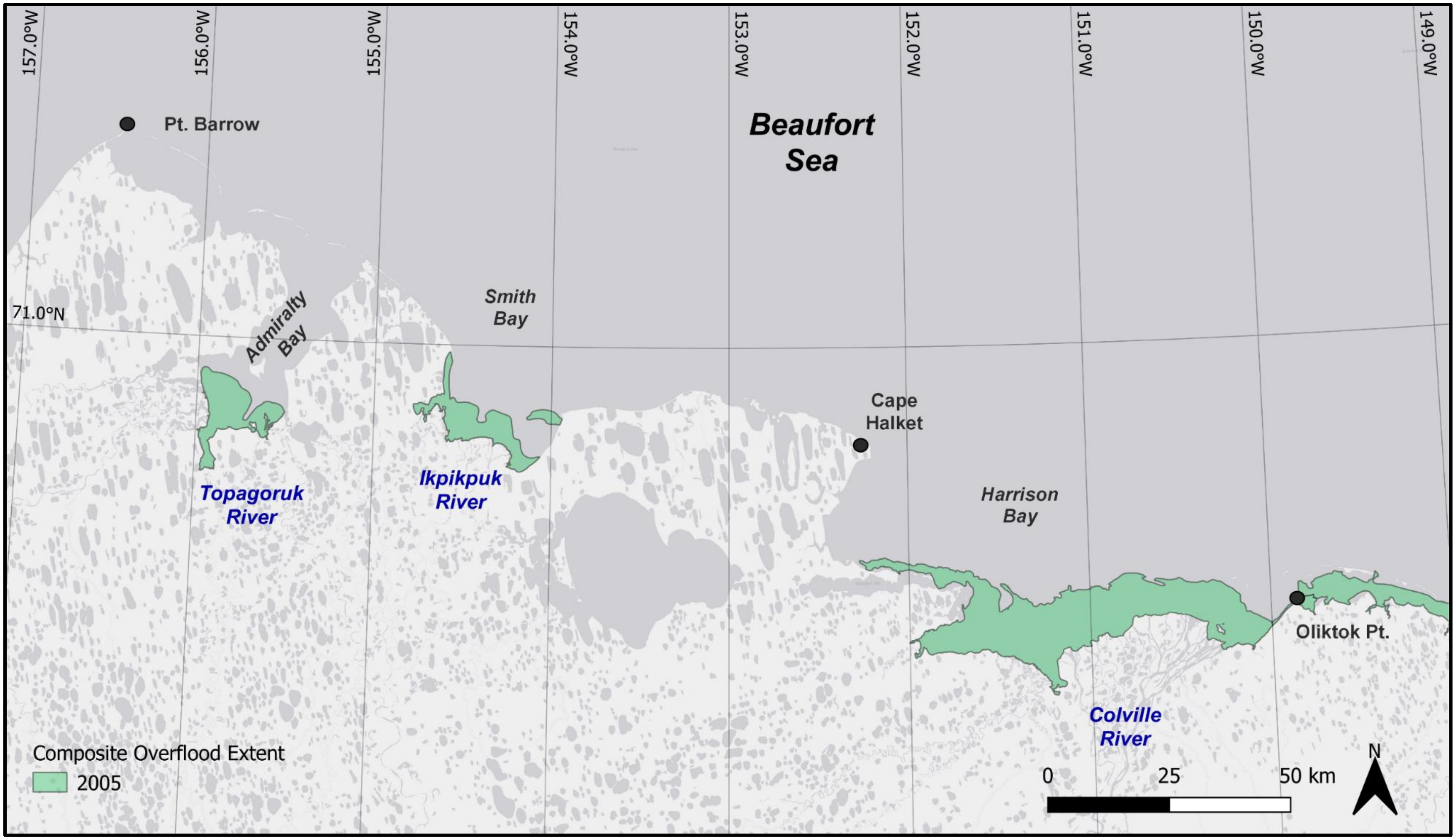

Figure 21. Composite overflood extent, west study region, 2005

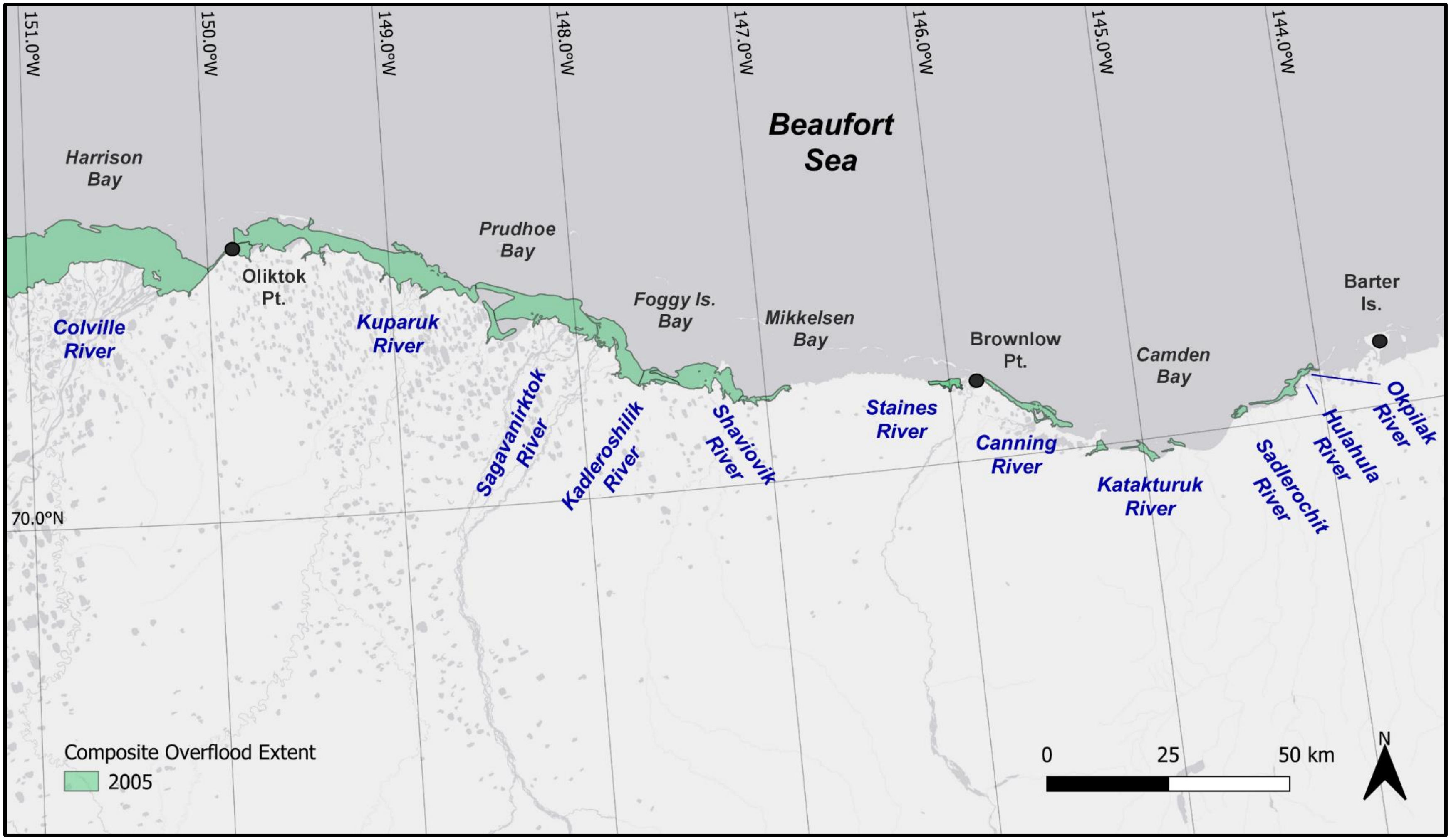

Figure 22. Composite overflood extent, east study region, 2005

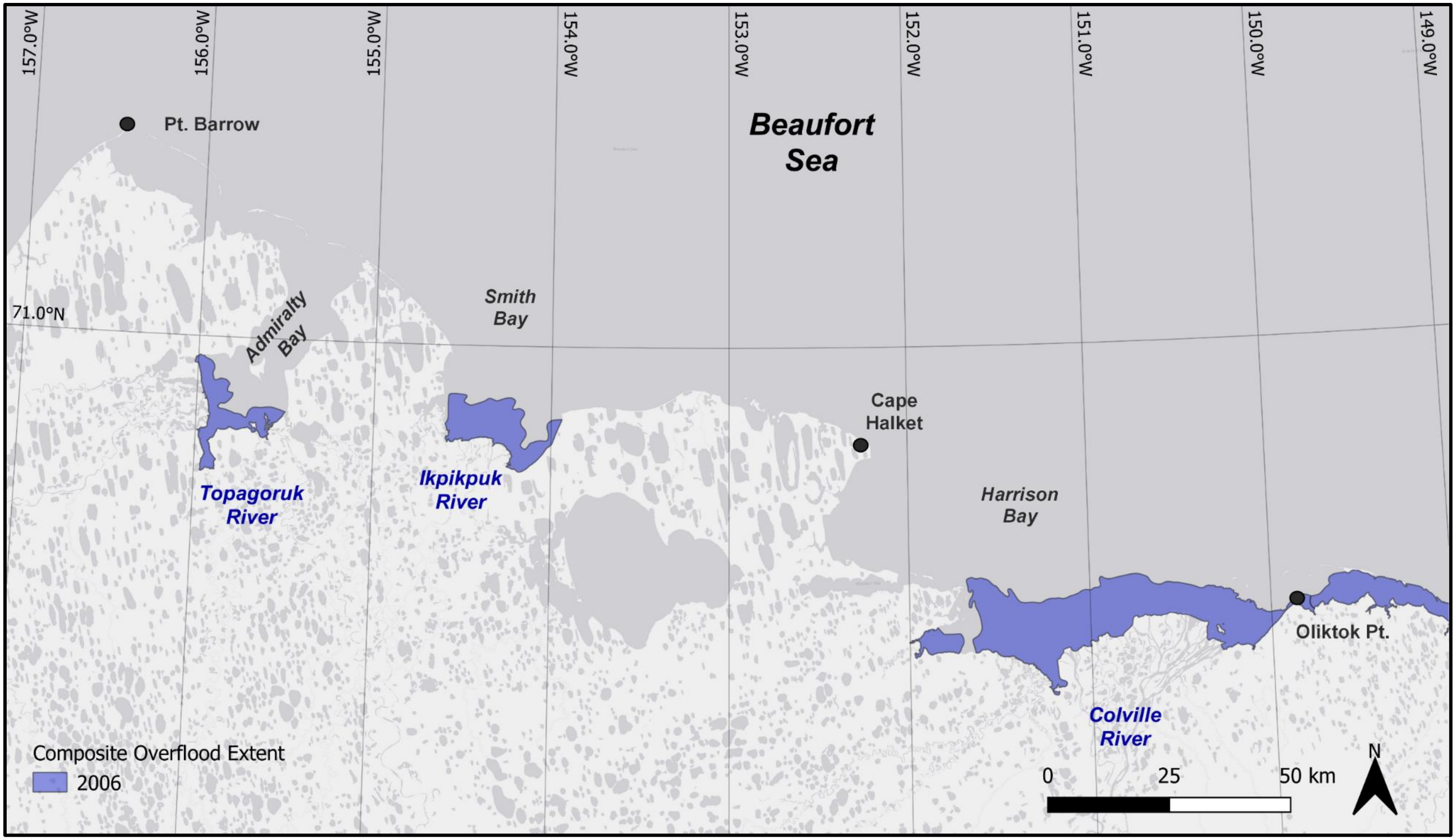

Figure 23. Composite overflood extent, west study region, 2006

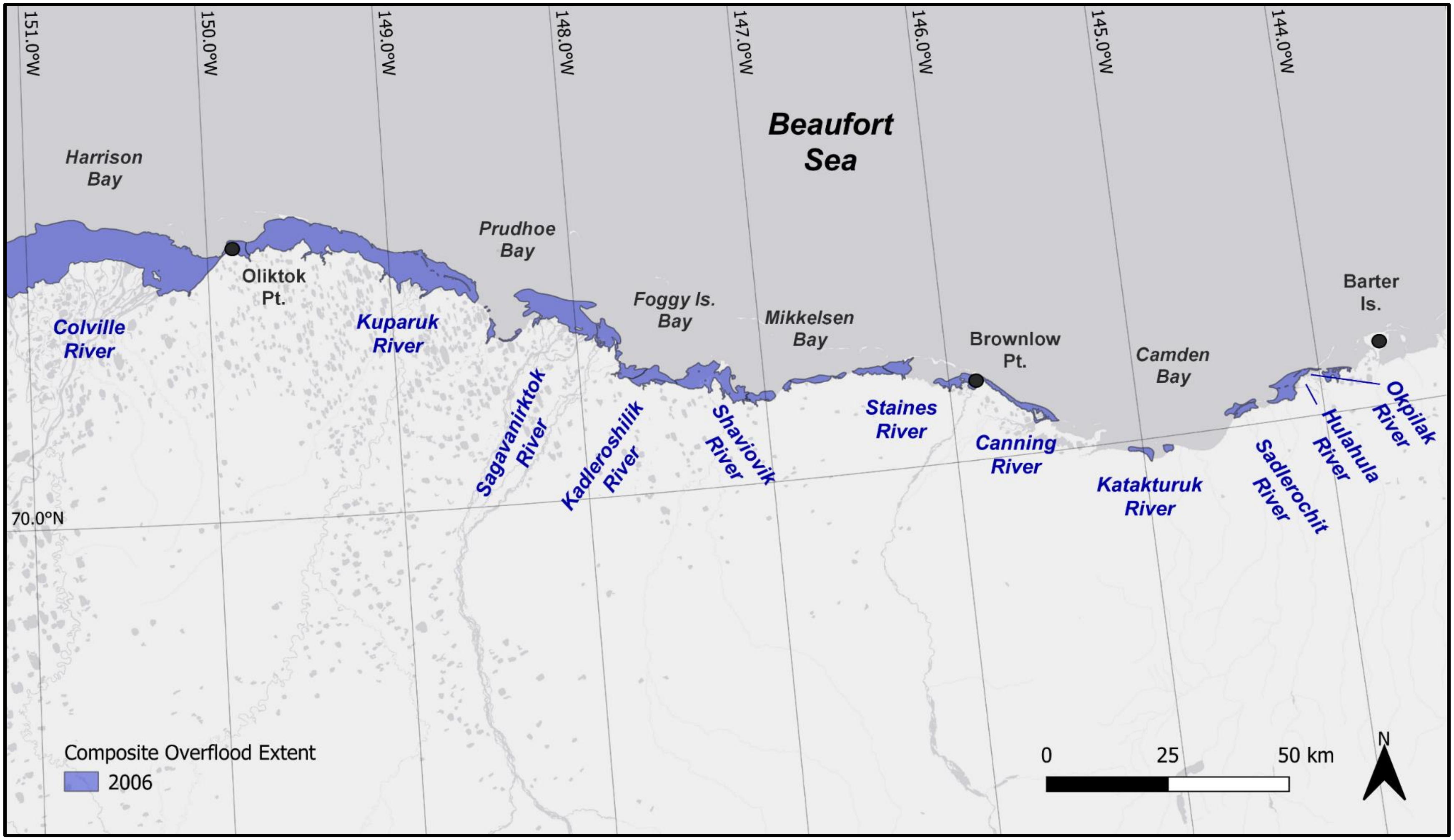

Figure 24. Composite overflood extent, east study region, 2006

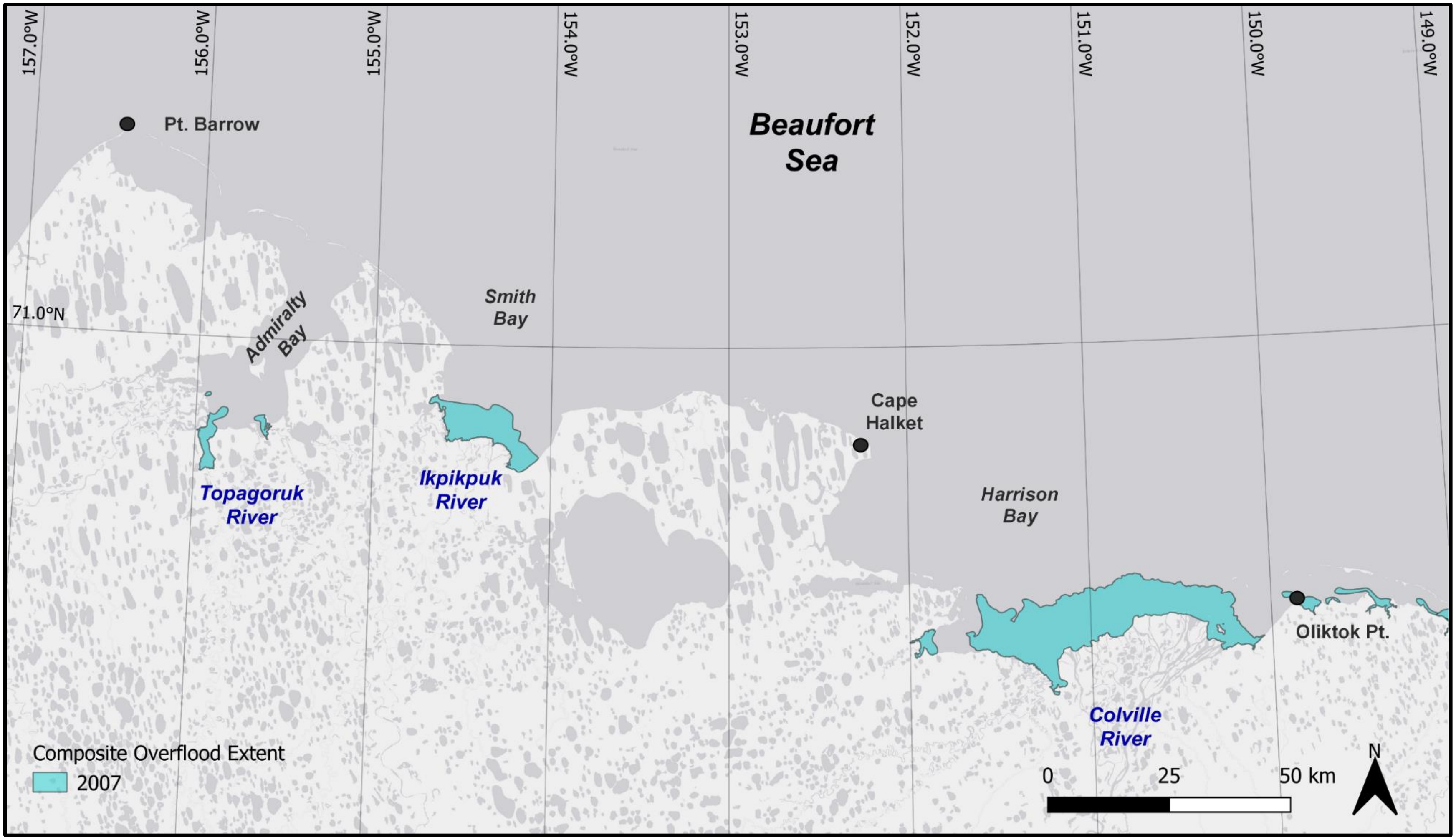

Figure 25. Composite overflood extent, west study region, 2007

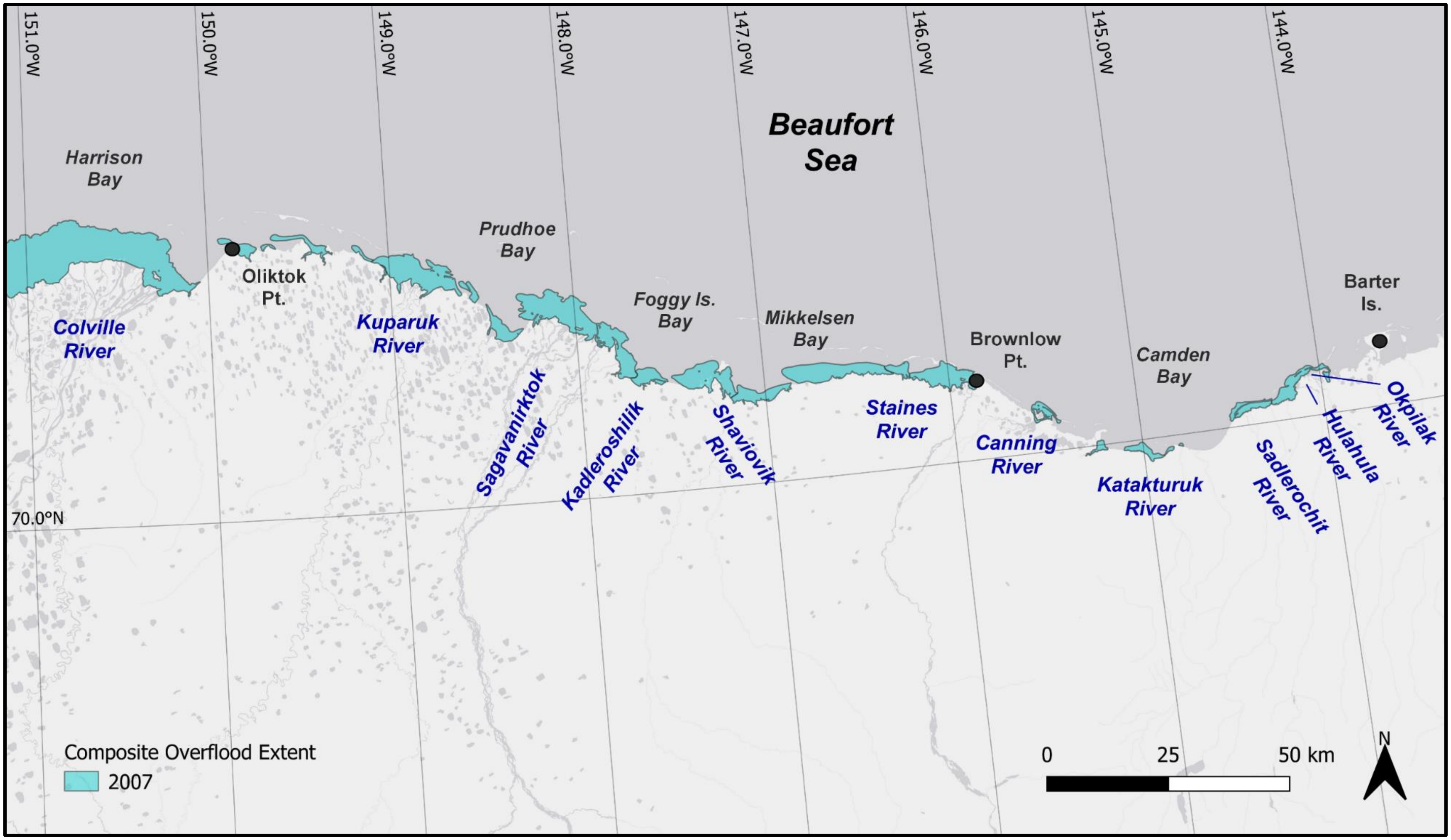

Figure 26. Composite overflood extent, east study region, 2007

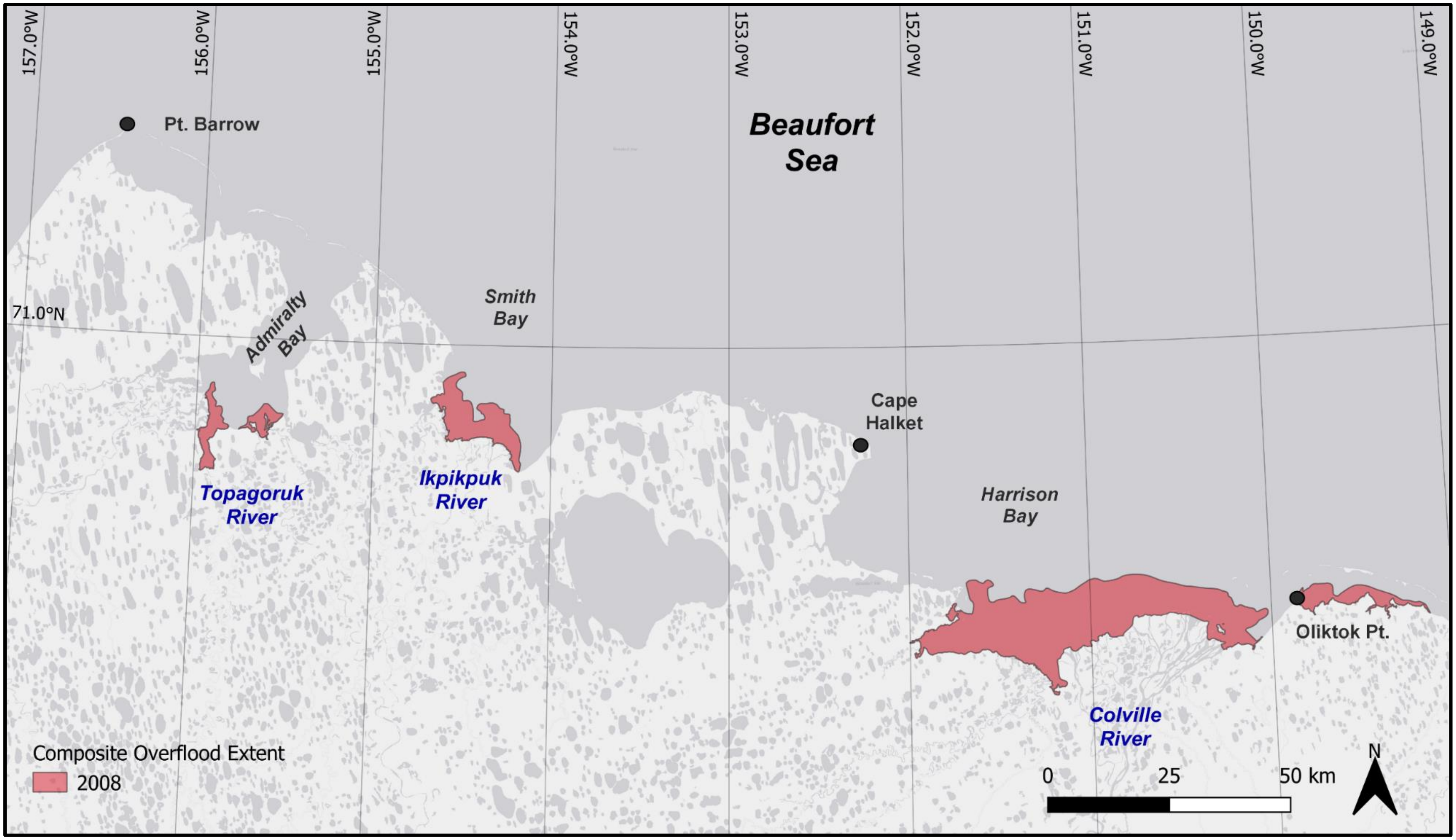

Figure 27. Composite overflood extent, west study region, 2008

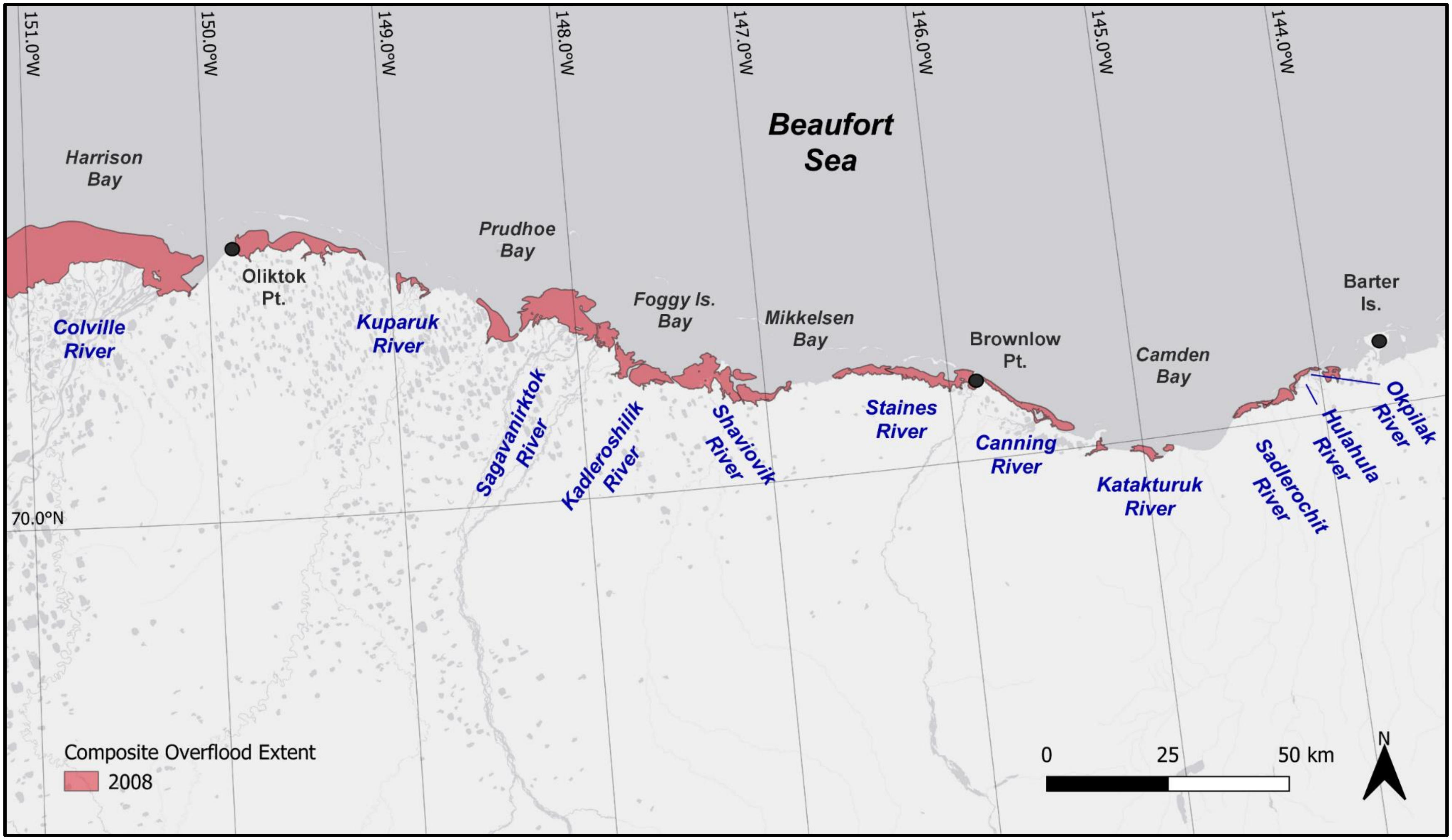

Figure 28. Composite overflood extent, east study region, 2008

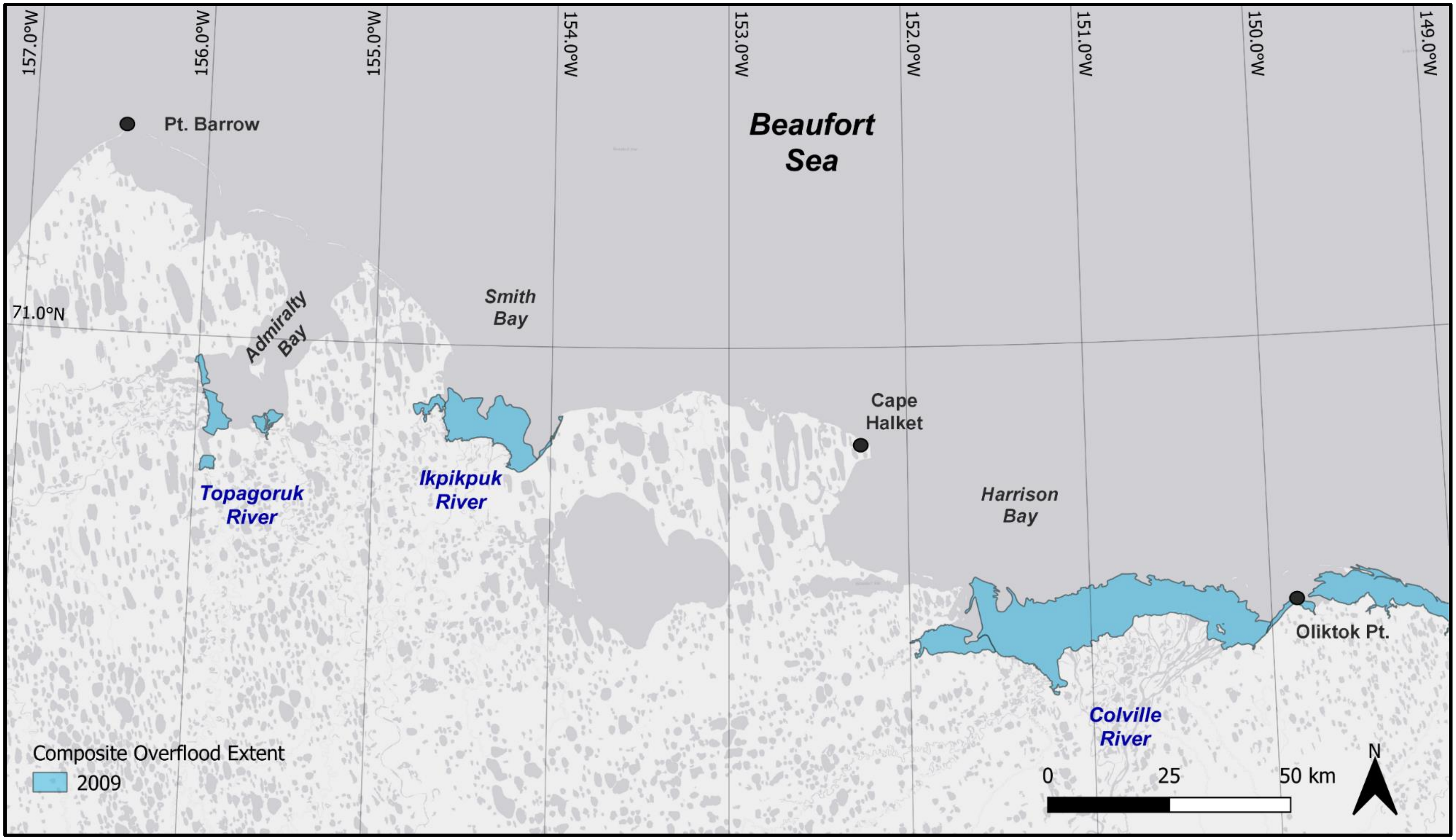

Figure 29. Composite overflood extent, west study region, 2009

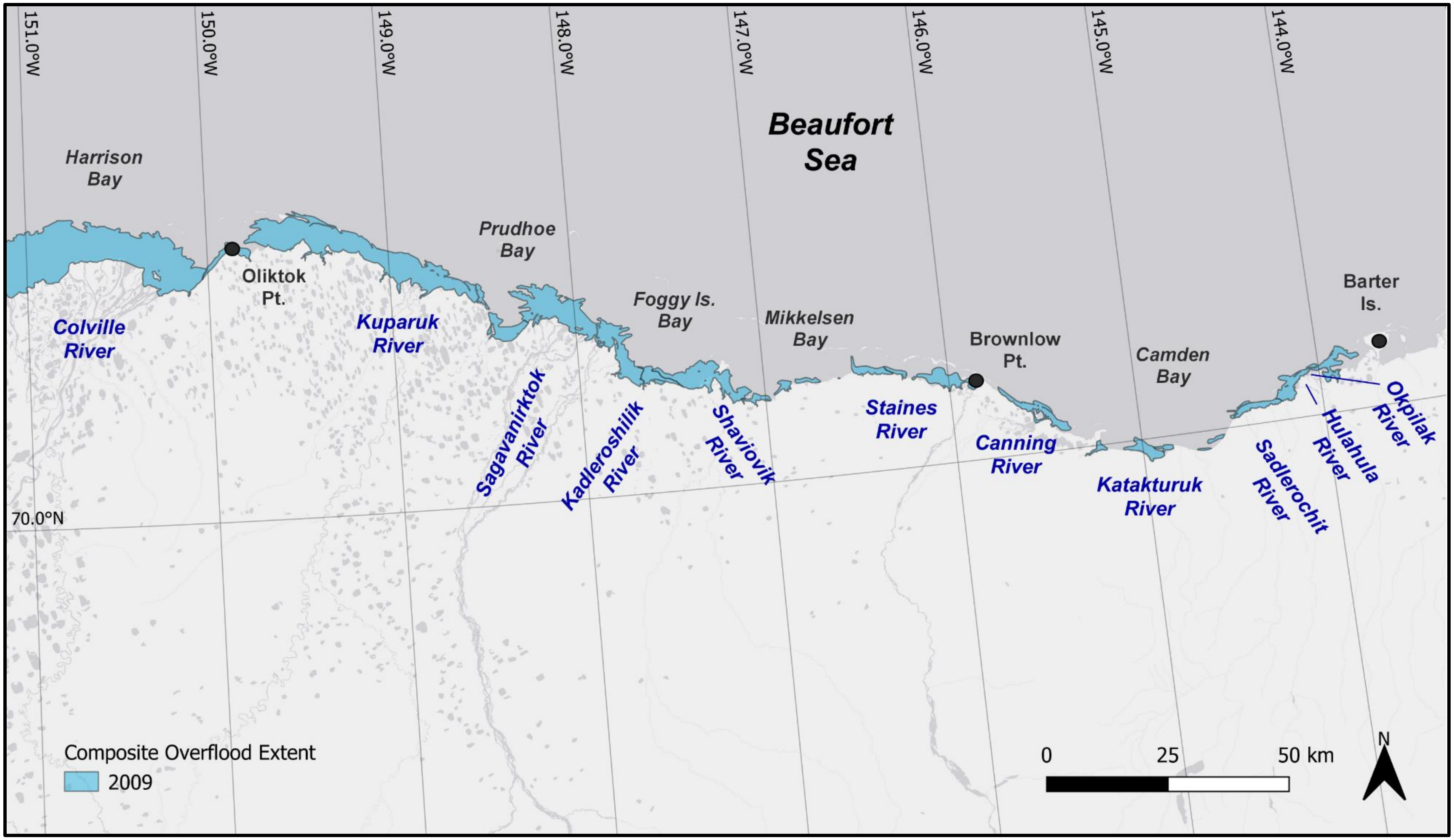

Figure 30. Composite overflood extent, east study region, 2009

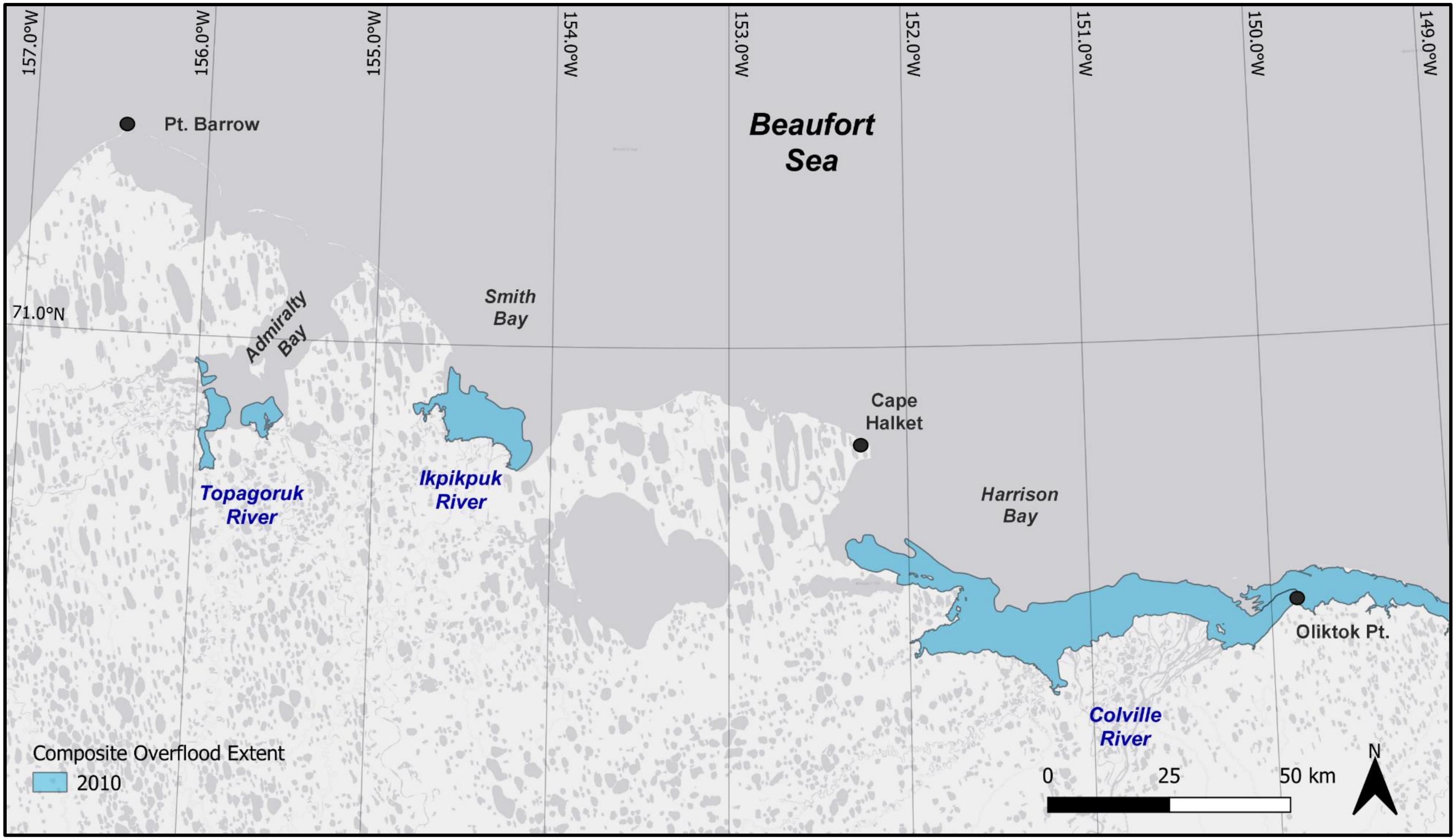

Figure 31. Composite overflood extent, west study region, 2010

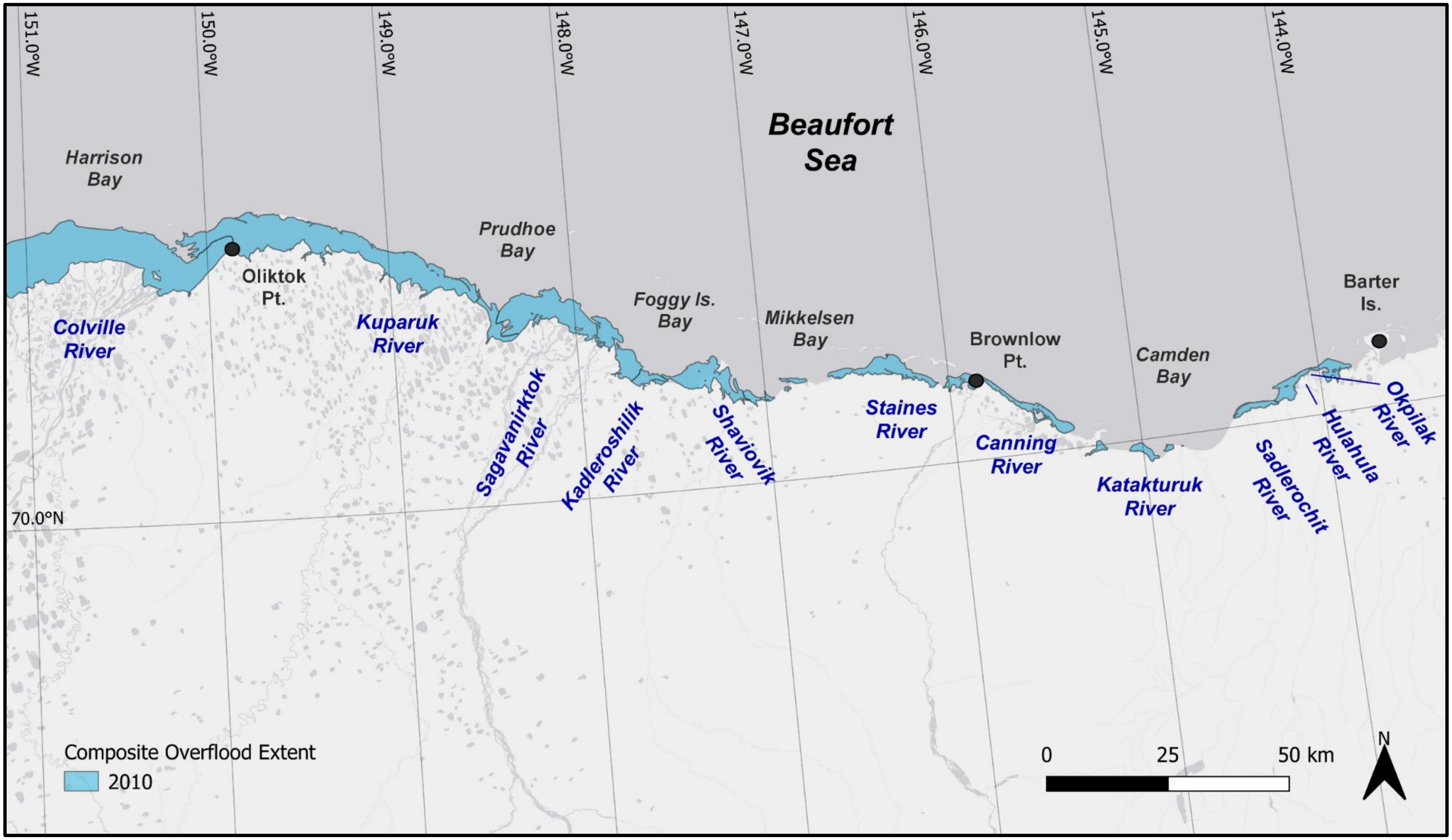

Figure 32. Composite overflood extent, east study region, 2010

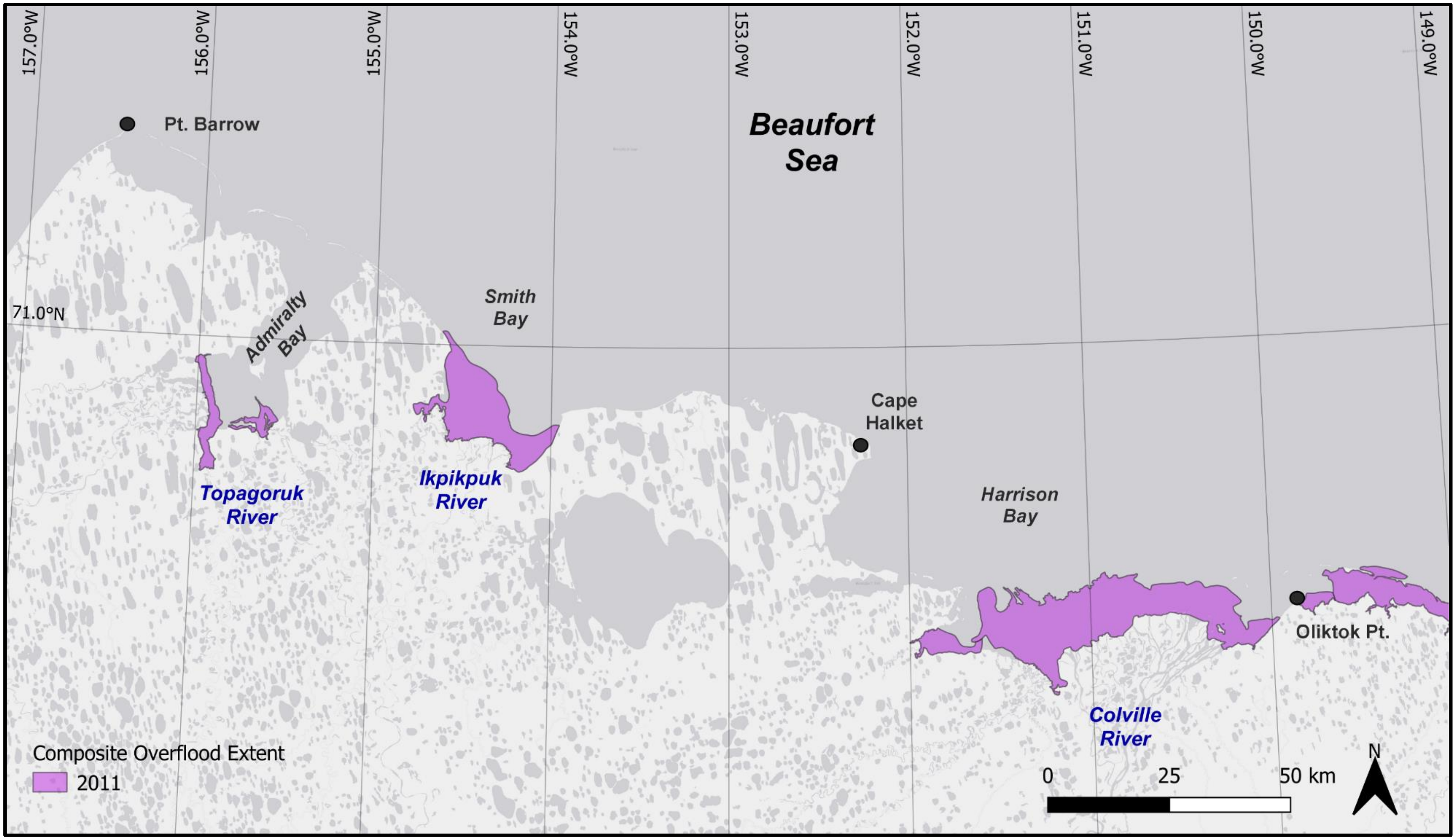

Figure 33. Composite overflood extent, west study region, 2011

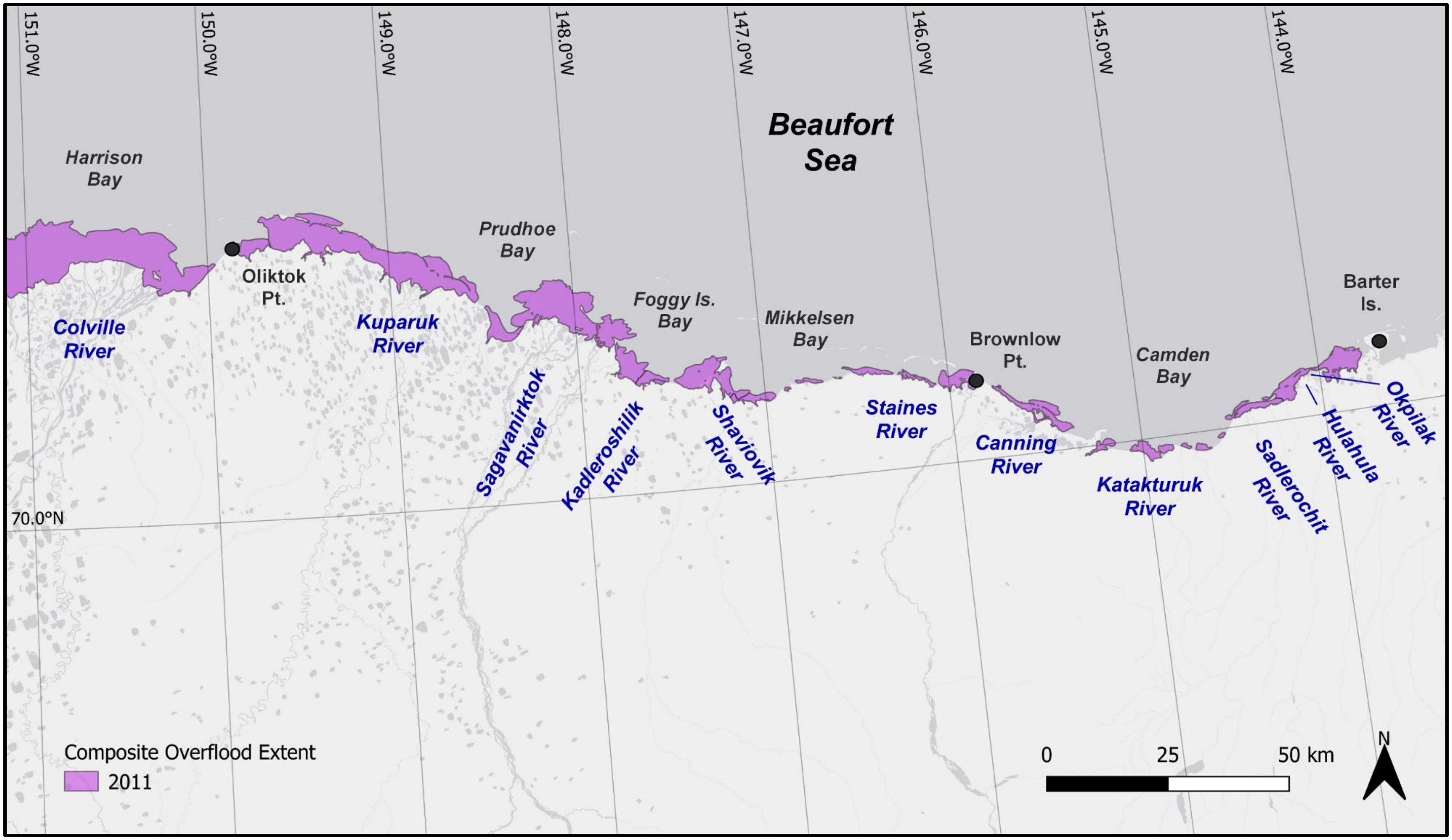

Figure 34. Composite overflood extent, east study region, 2011

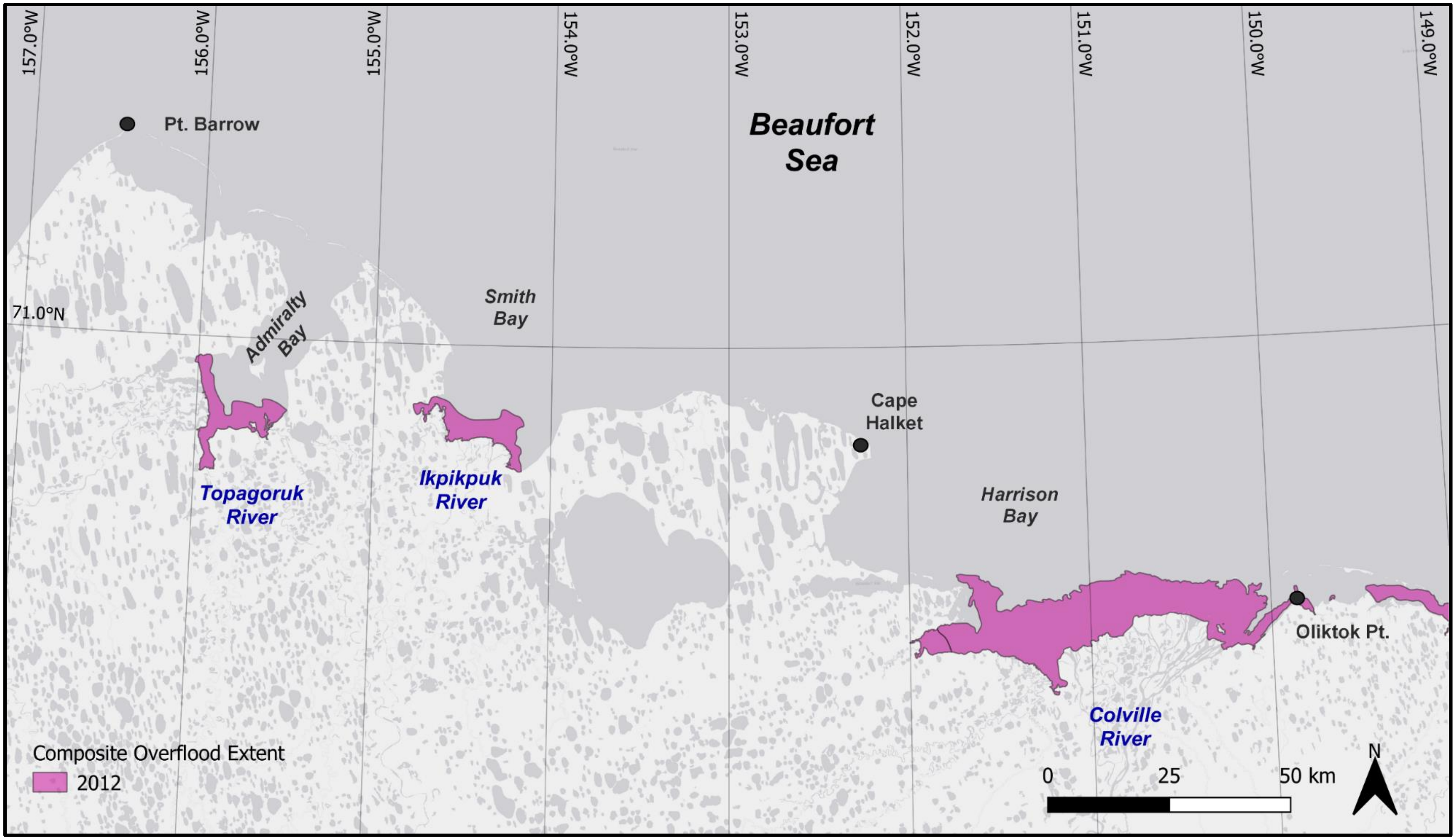

Figure 35. Composite overflood extent, west study region, 2012

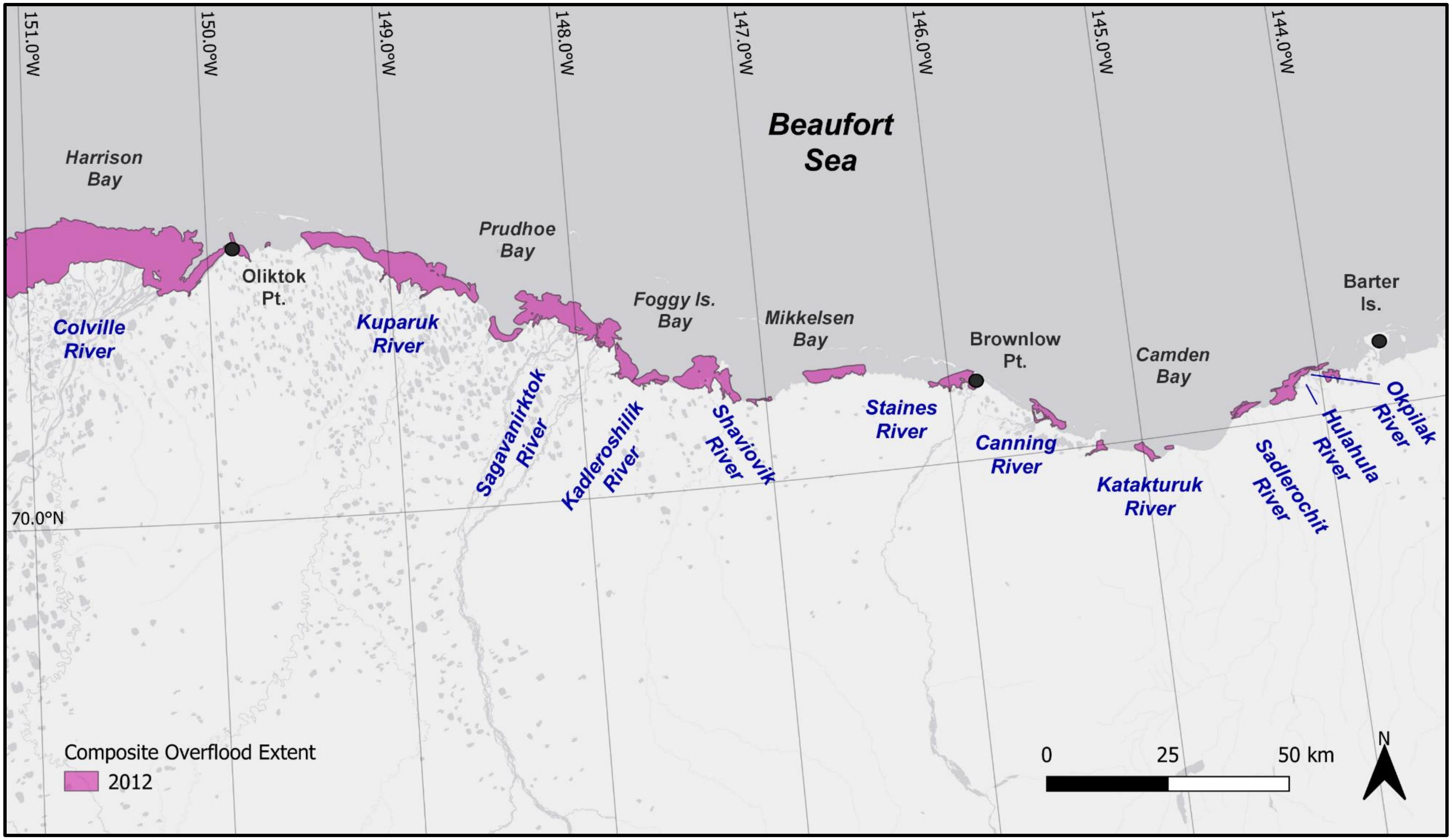

Figure 36. Composite overflood extent, east study region, 2012

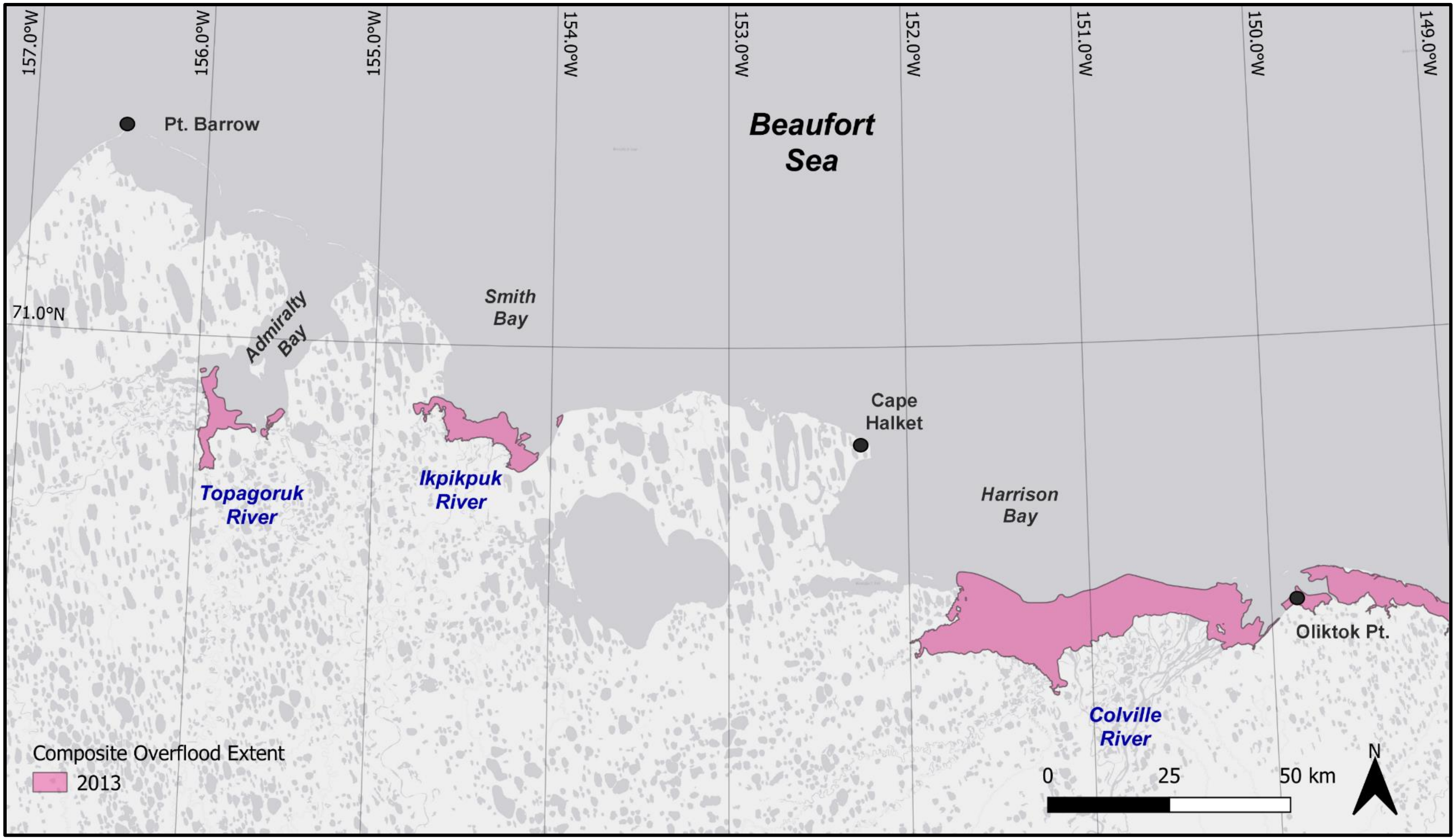

Figure 37. Composite overflood extent, west study region, 2013

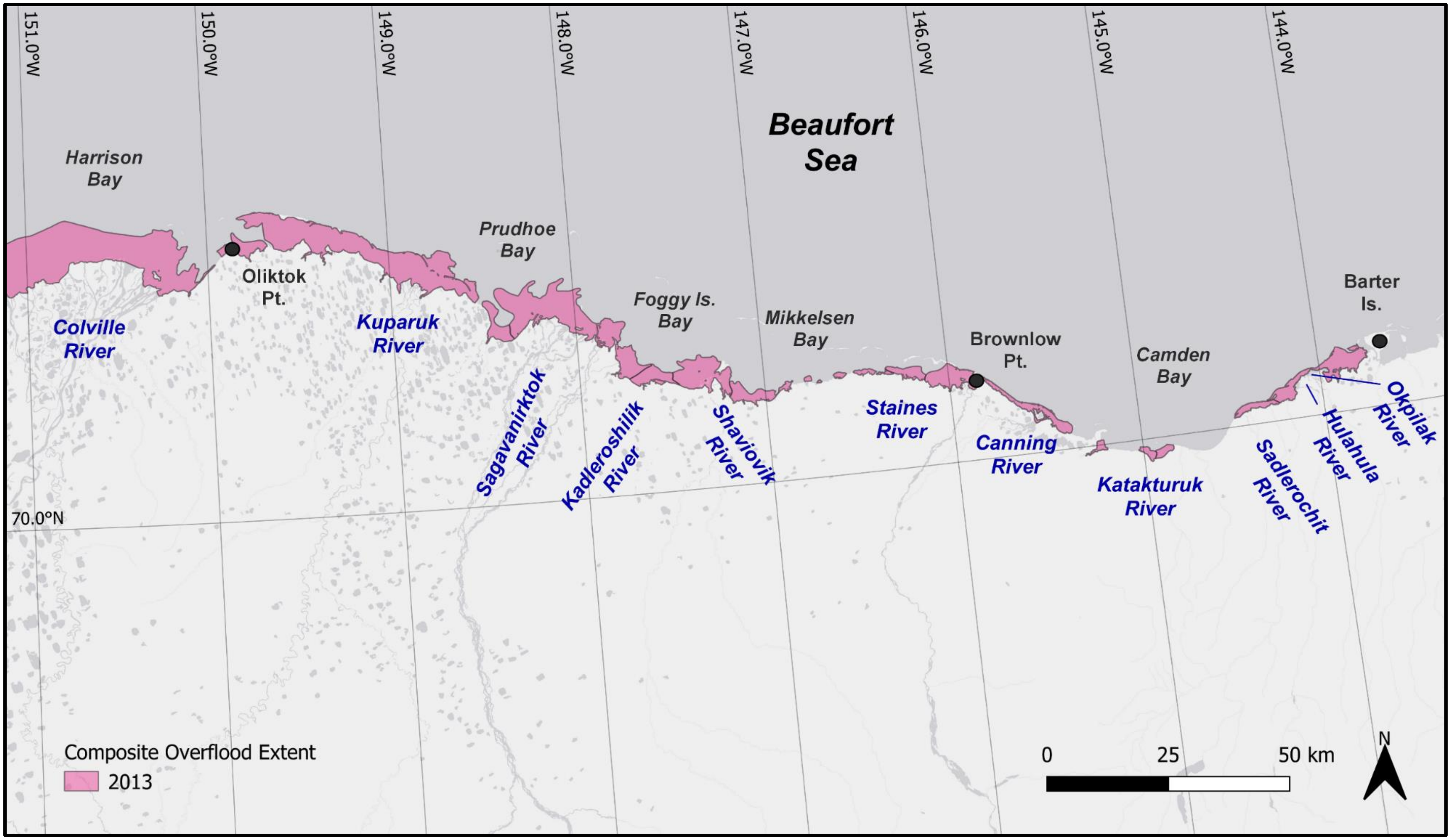

Figure 38. Composite overflood extent, east study region, 2013

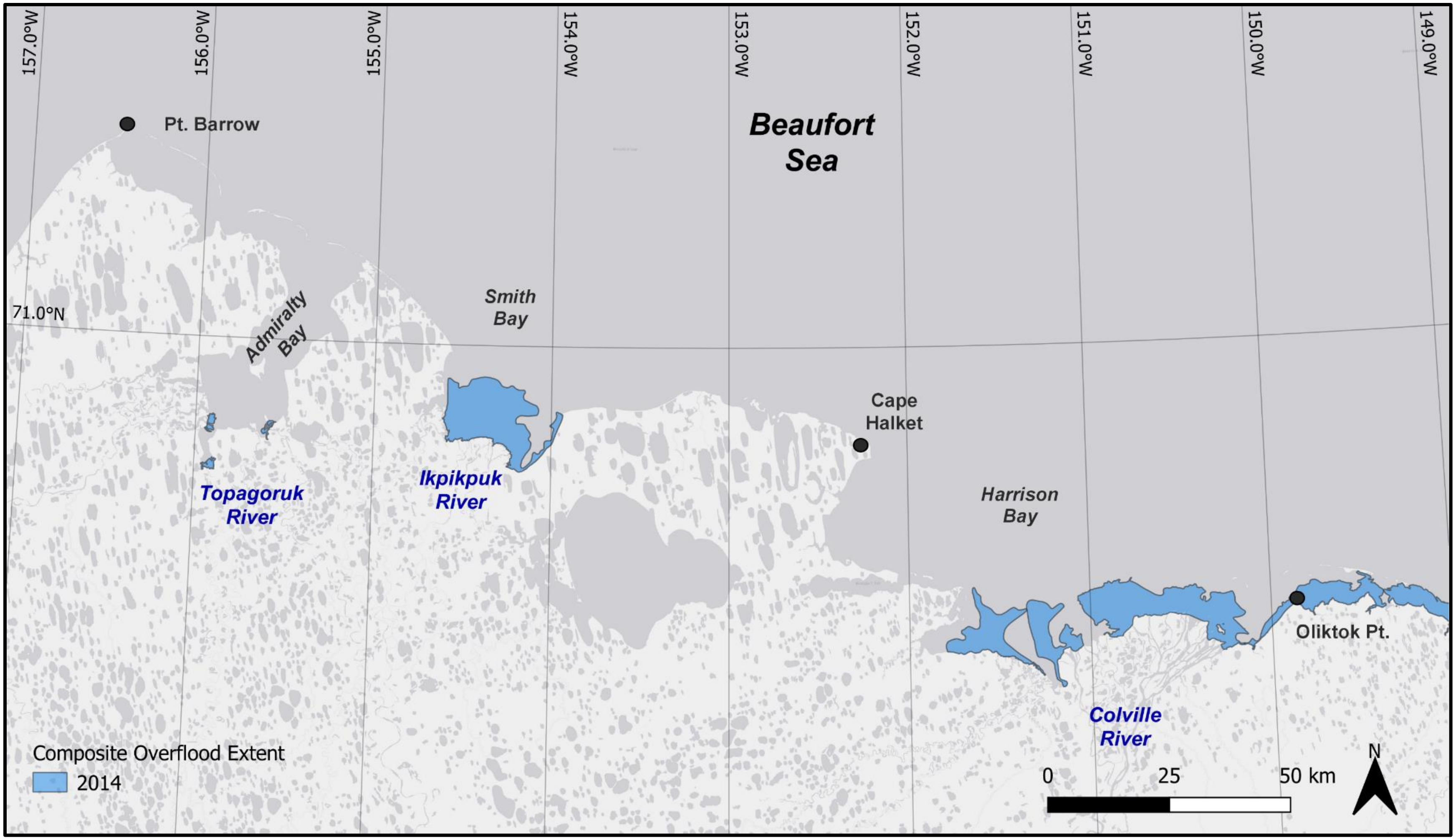

Figure 39. Composite overflood extent, west study region, 2014

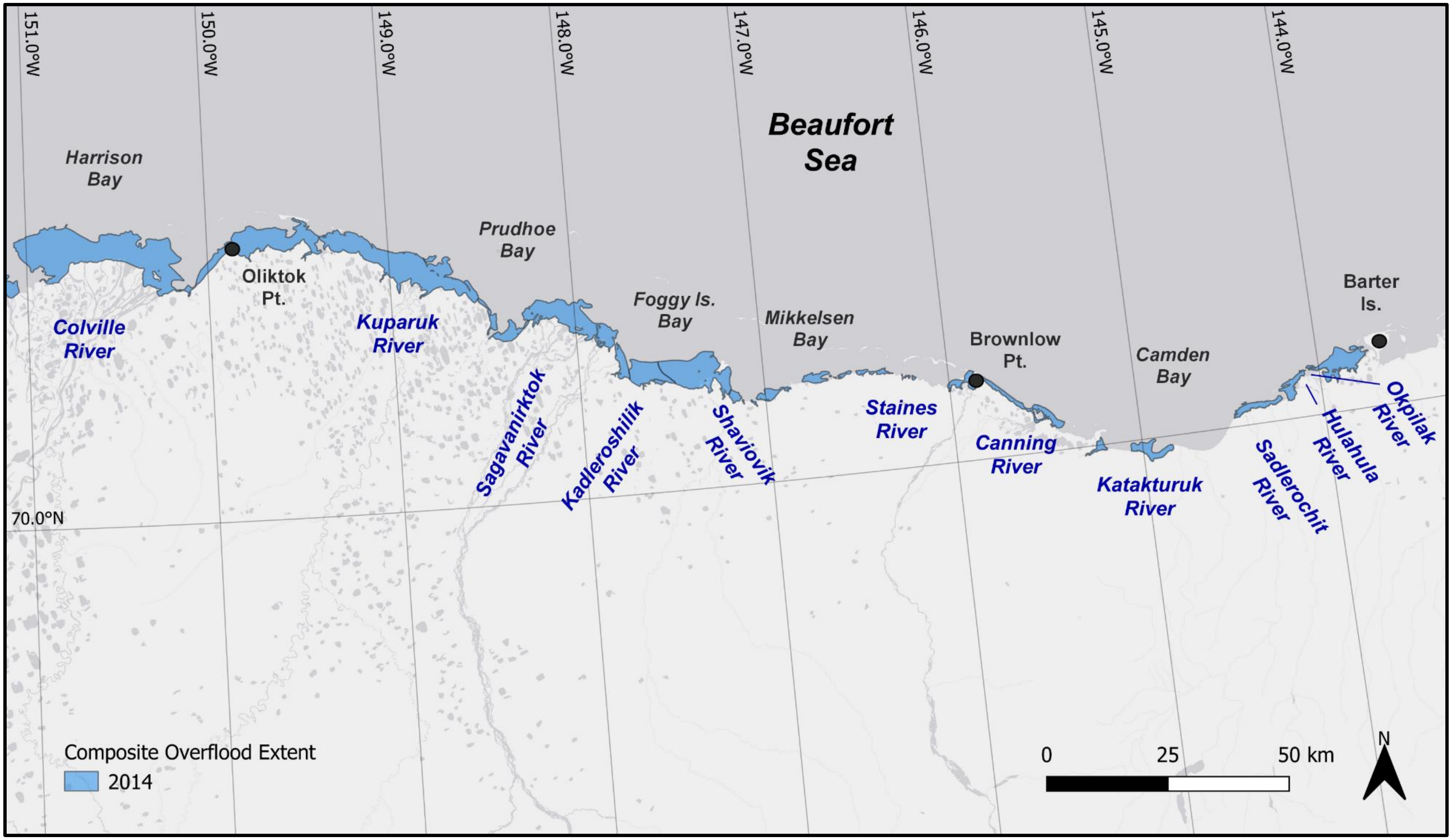

Figure 40. Composite overflood extent, east study region, 2014

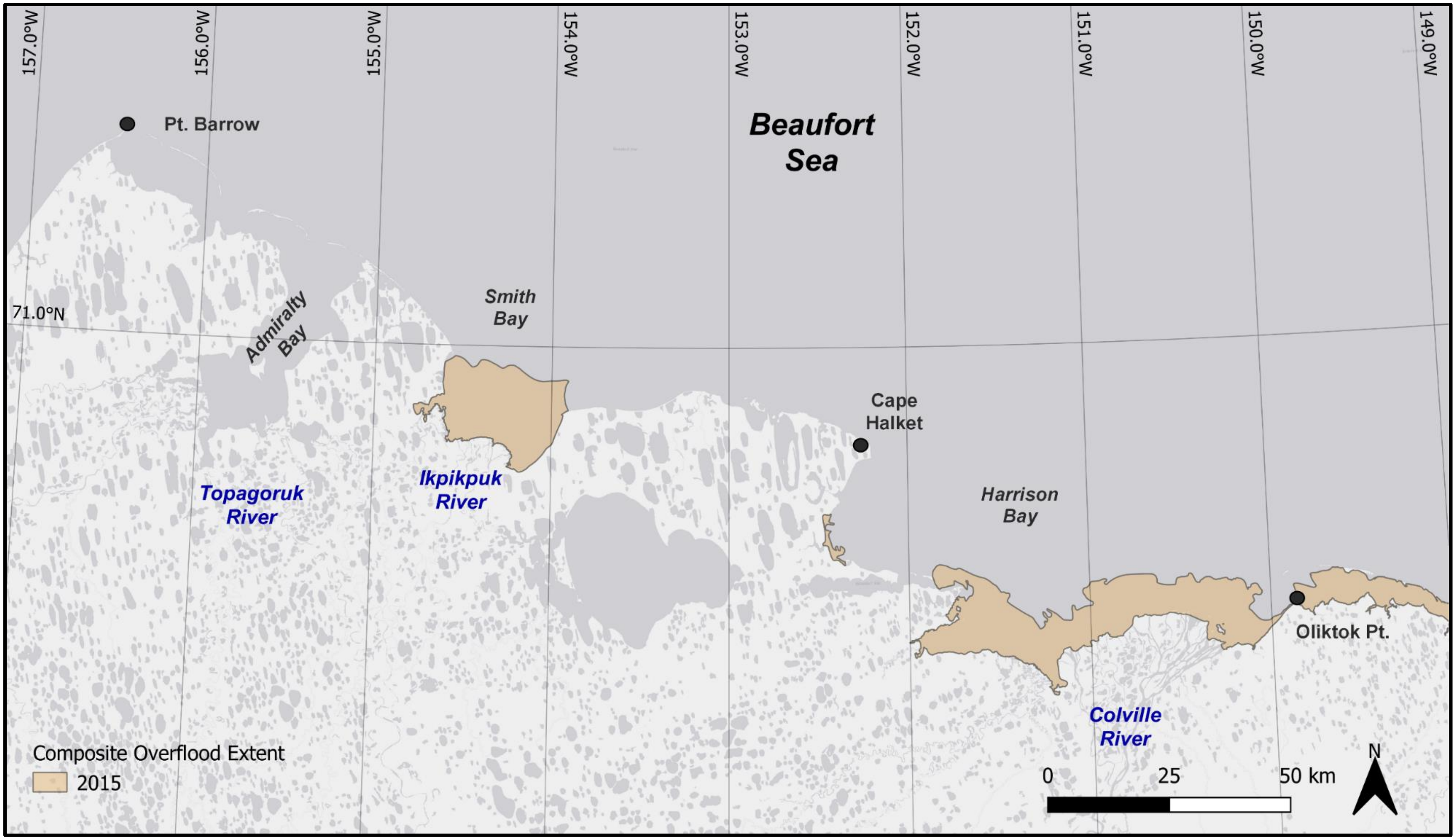

Figure 41. Composite overflood extent, west study region, 2015

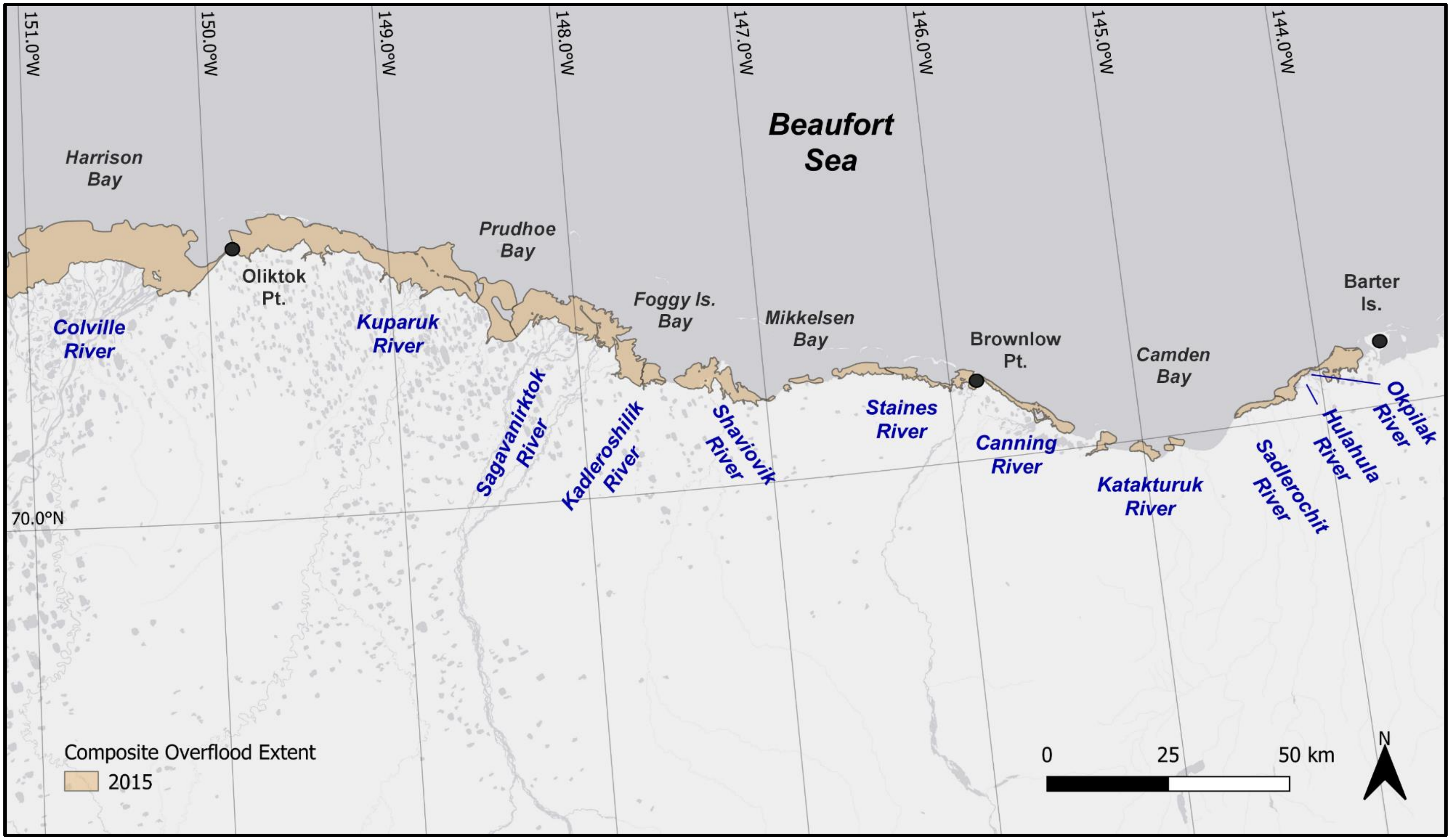

Figure 42. Composite overflood extent, east study region, 2015

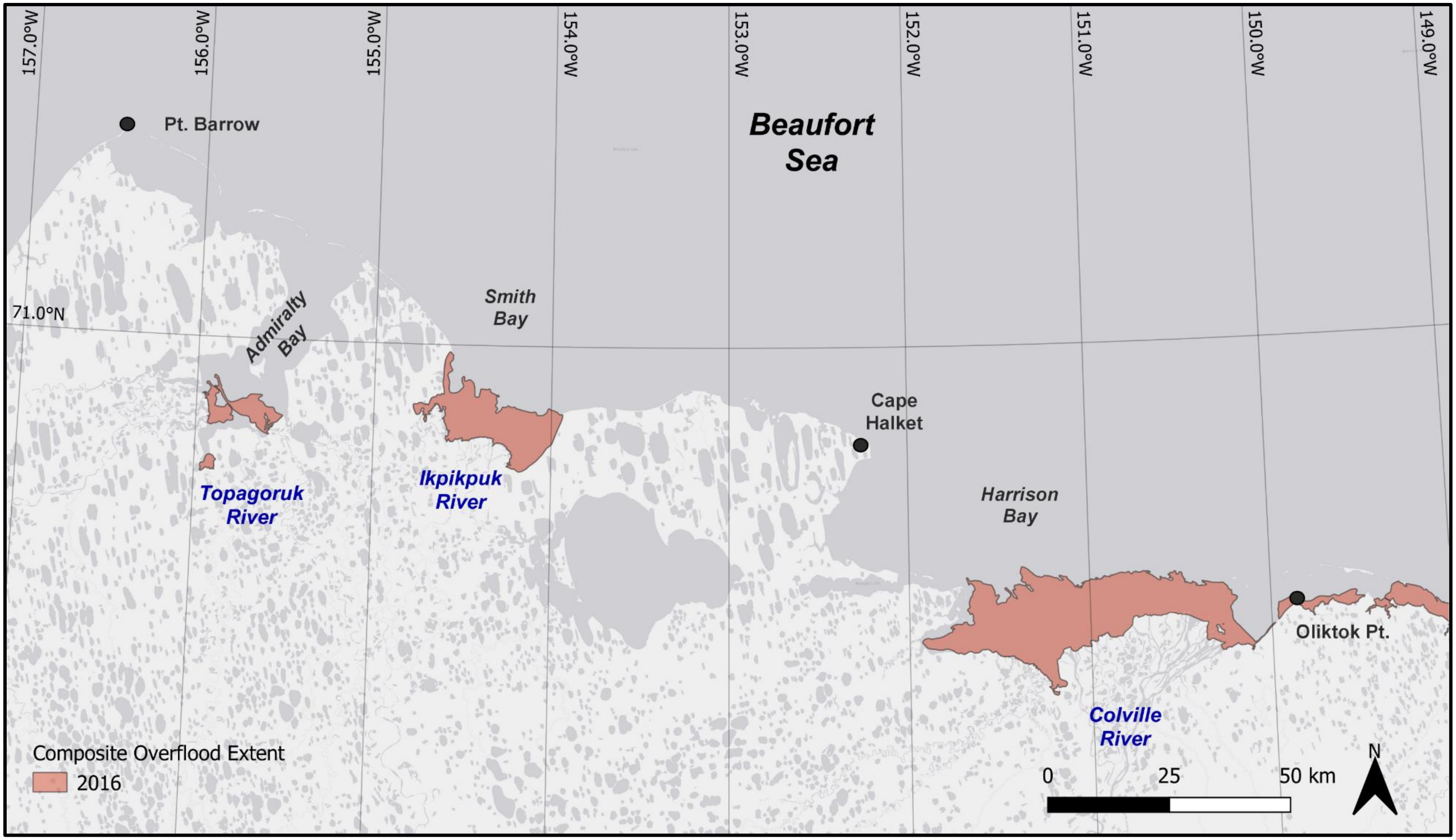

Figure 43. Composite overflood extent, west study region, 2016

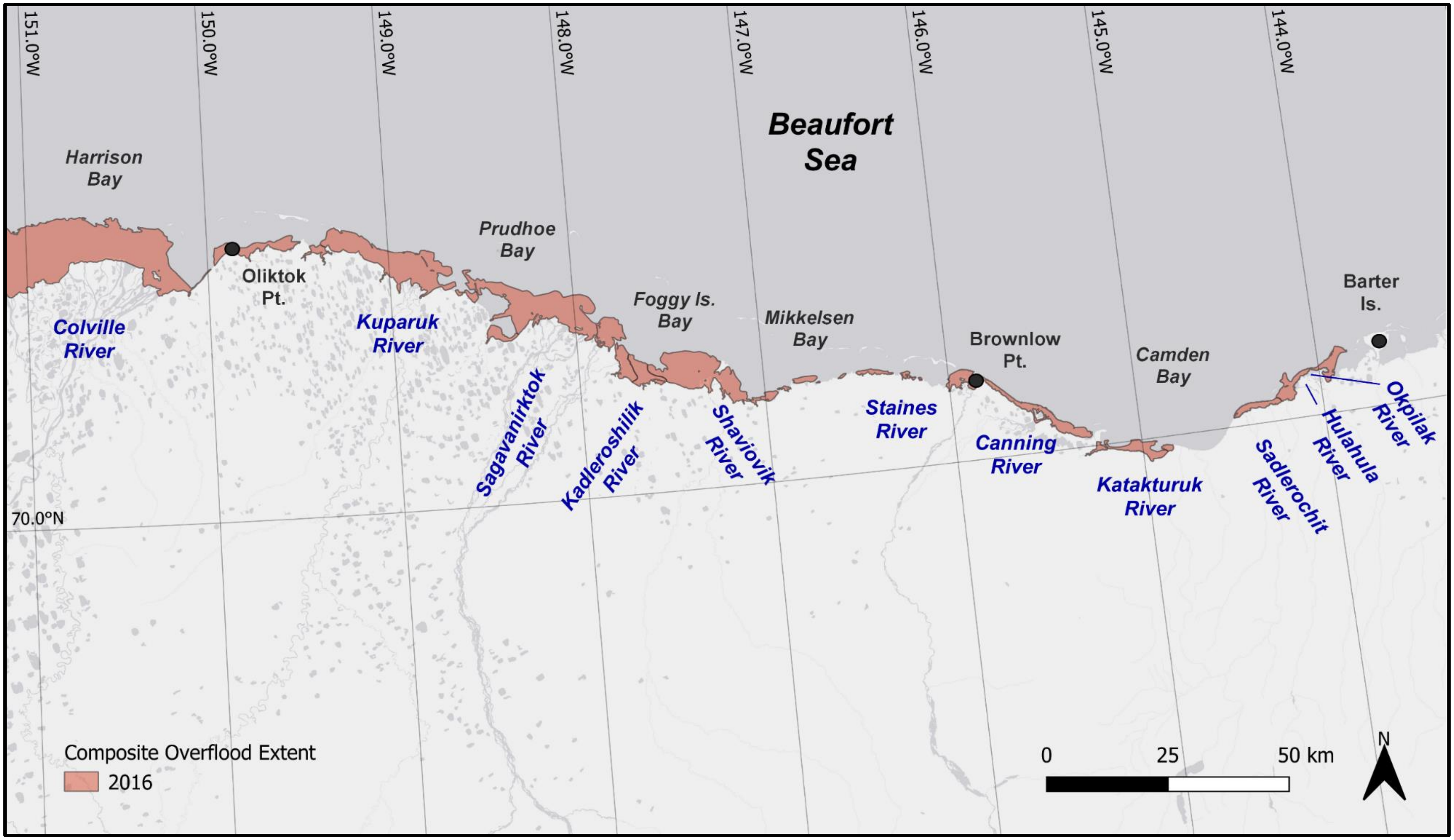

Figure 44. Composite overflood extent, east study region, 2016

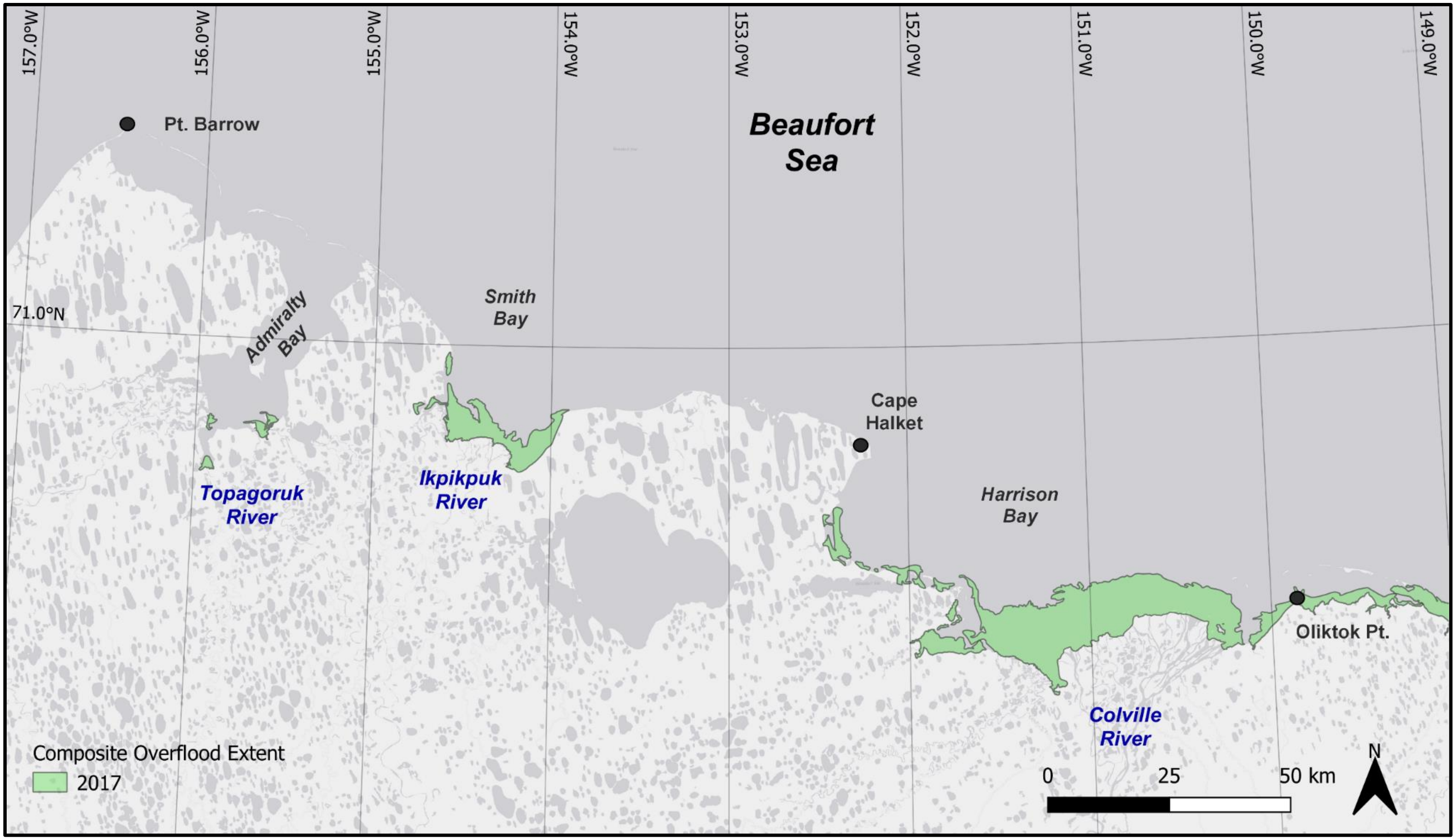

Figure 45. Composite overflood extent, west study region, 2017

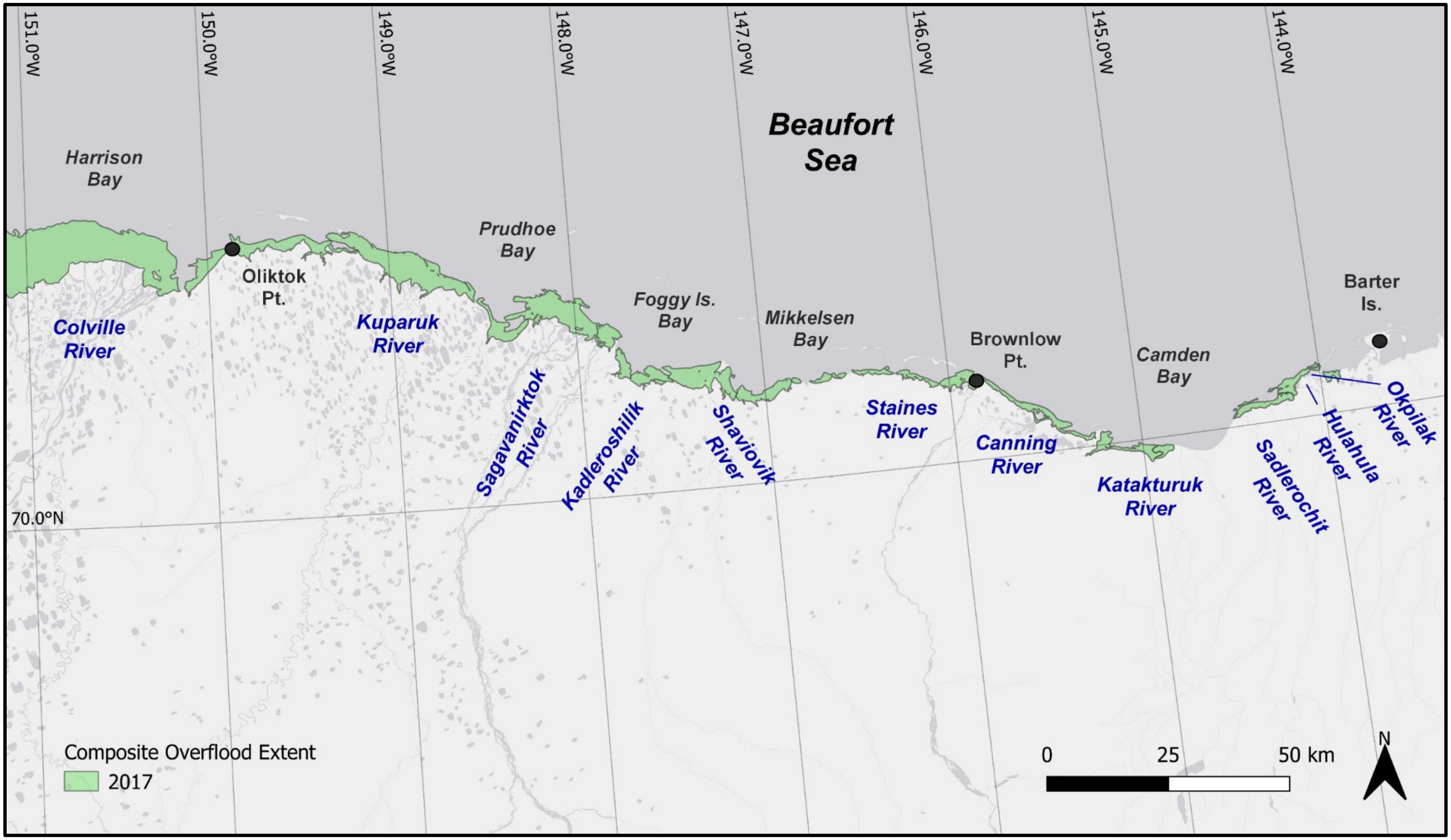

Figure 46. Composite overflood extent, east study region, 2017

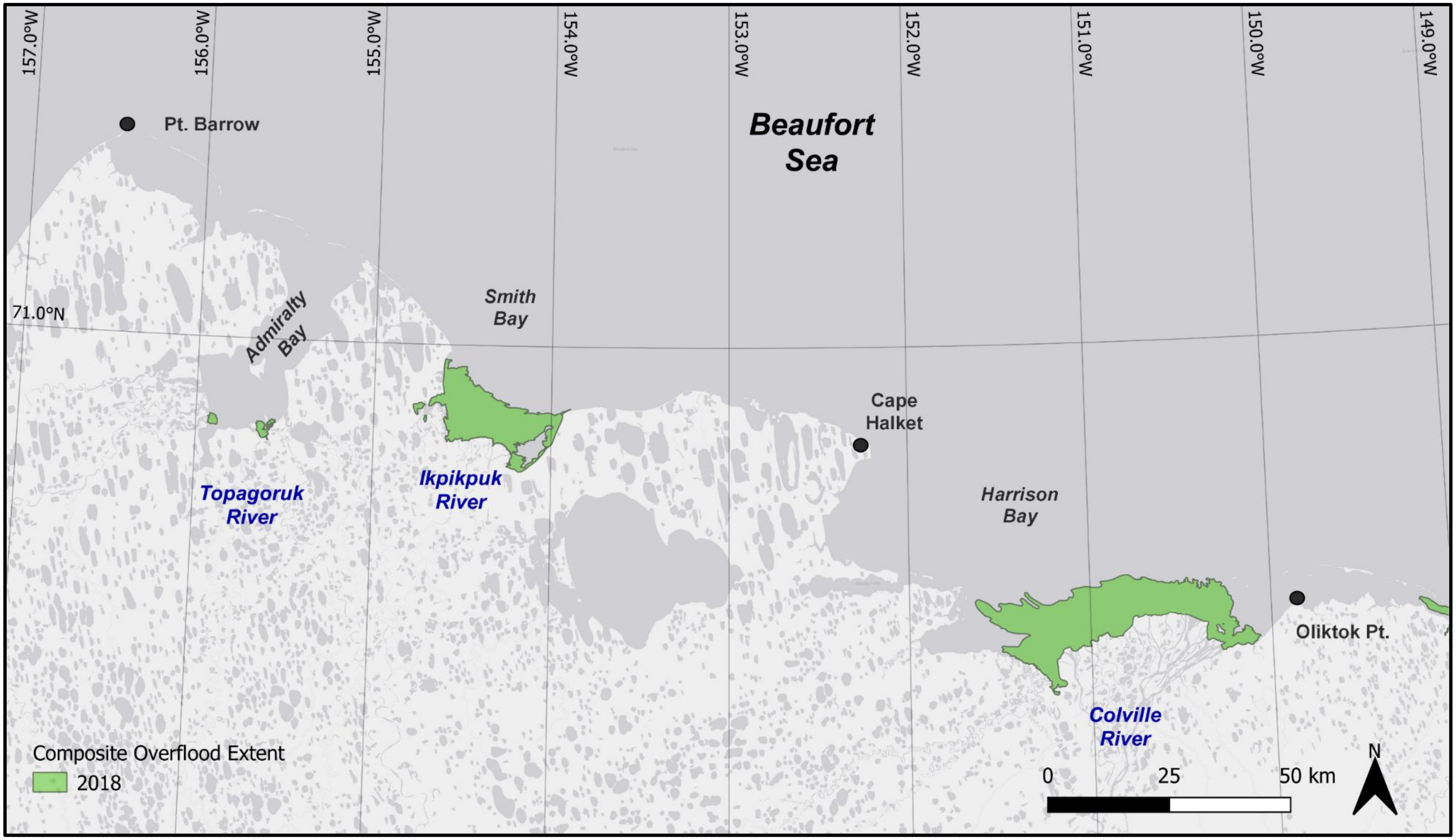

Figure 47. Composite overflood extent, west study region, 2018

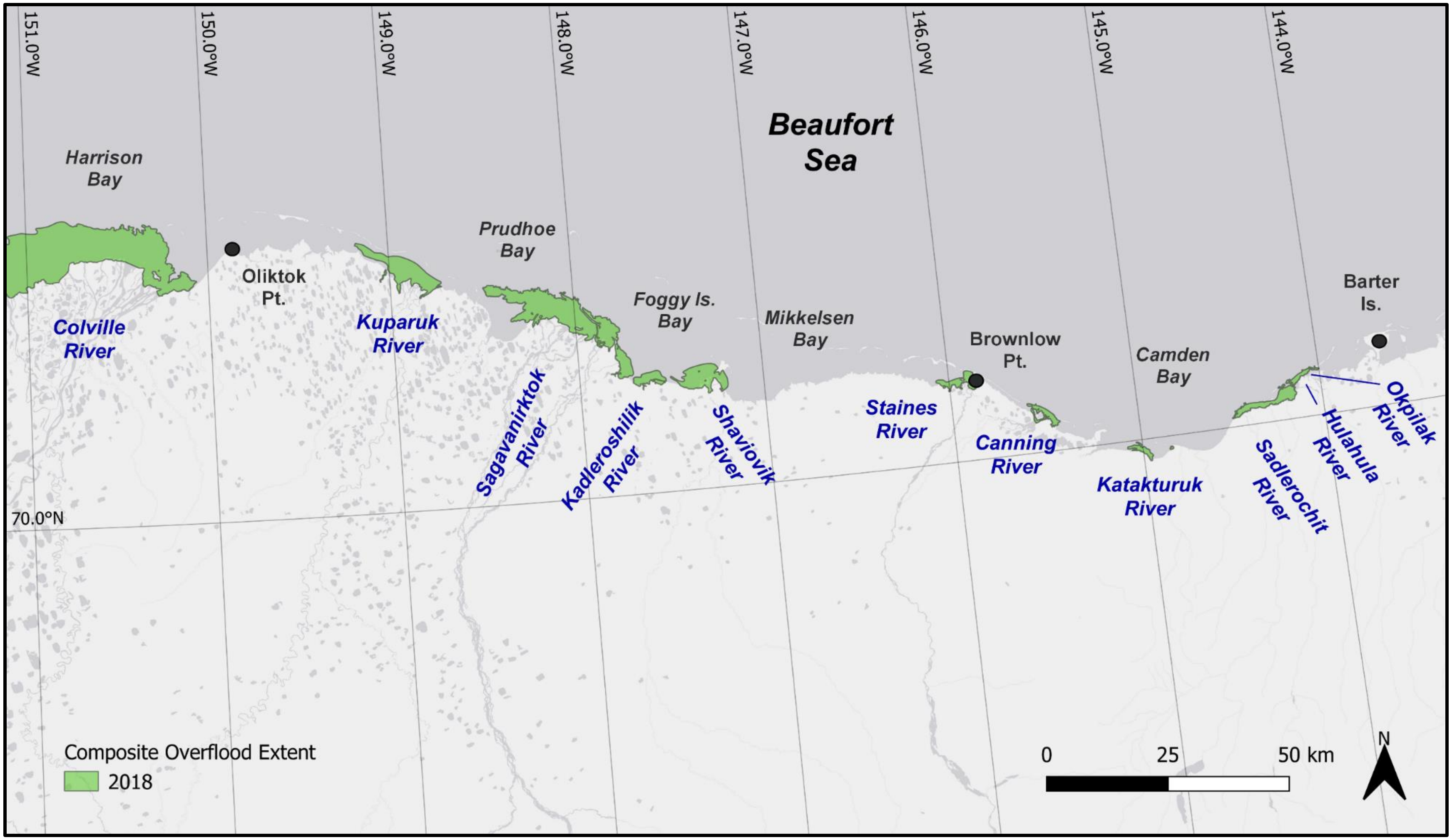

Figure 48. Composite overflood extent, east study region, 2018

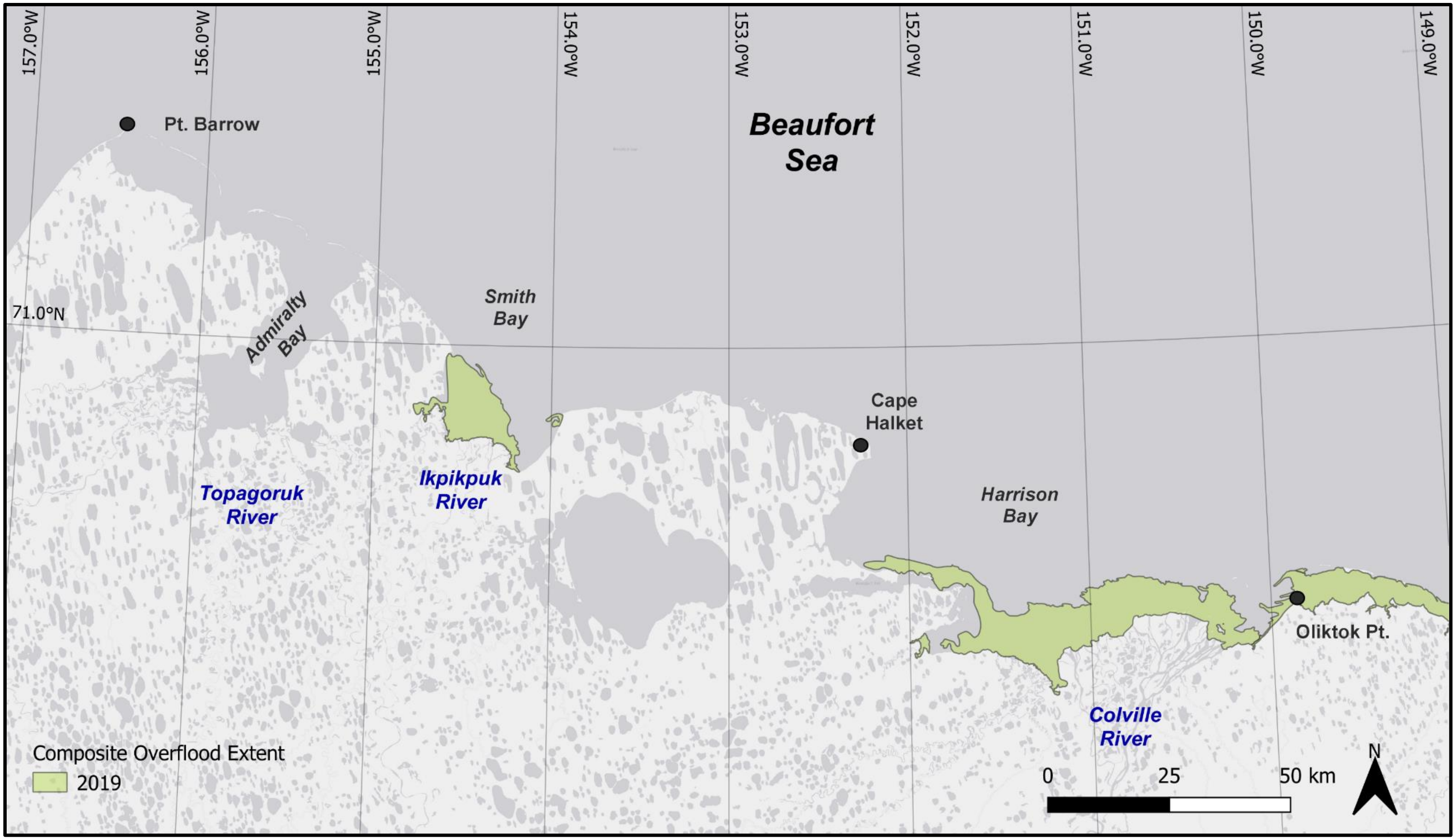

Figure 49. Composite overflood extent, west study region, 2019

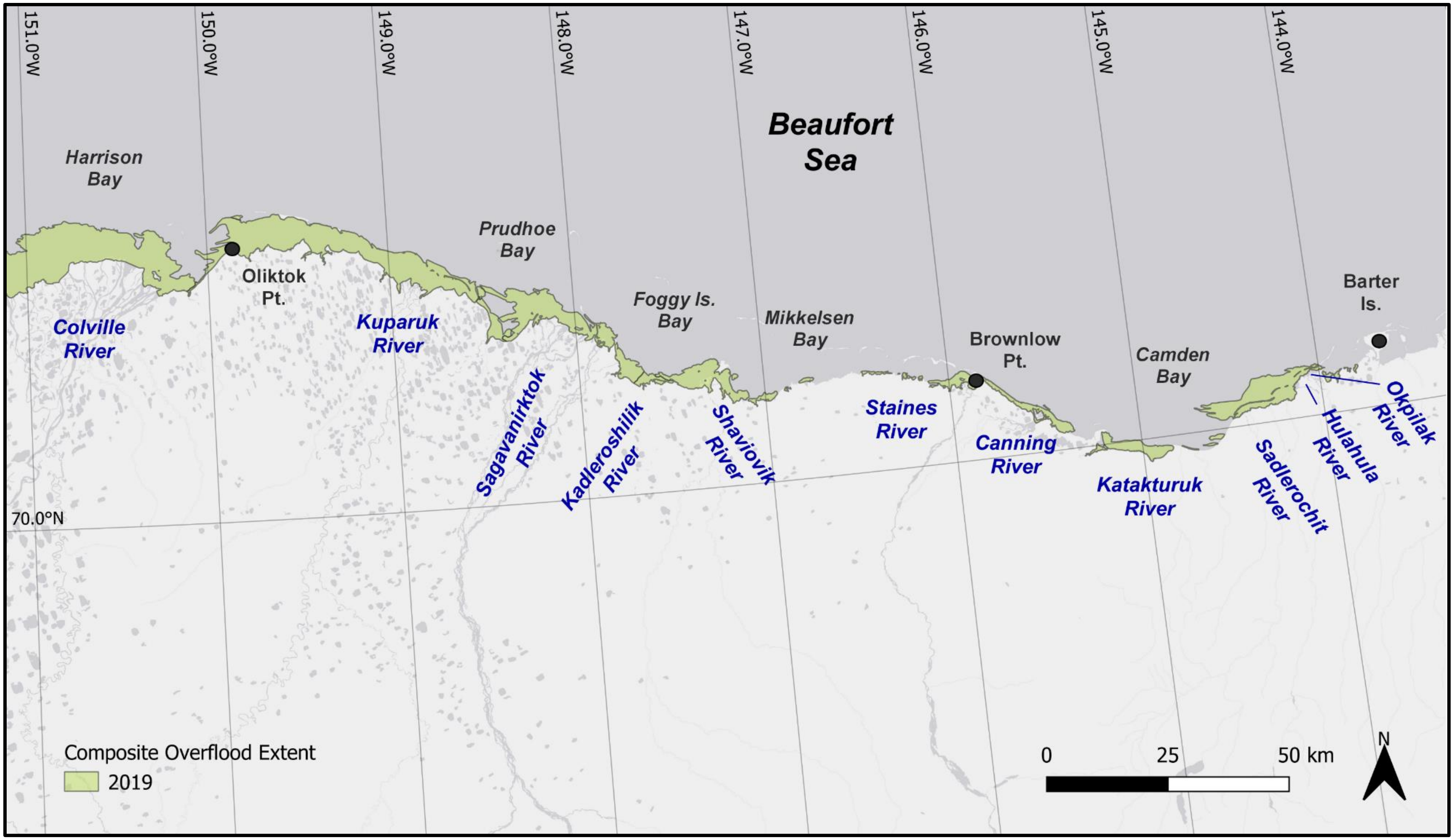

Figure 50. Composite overflood extent, east study region, 2019

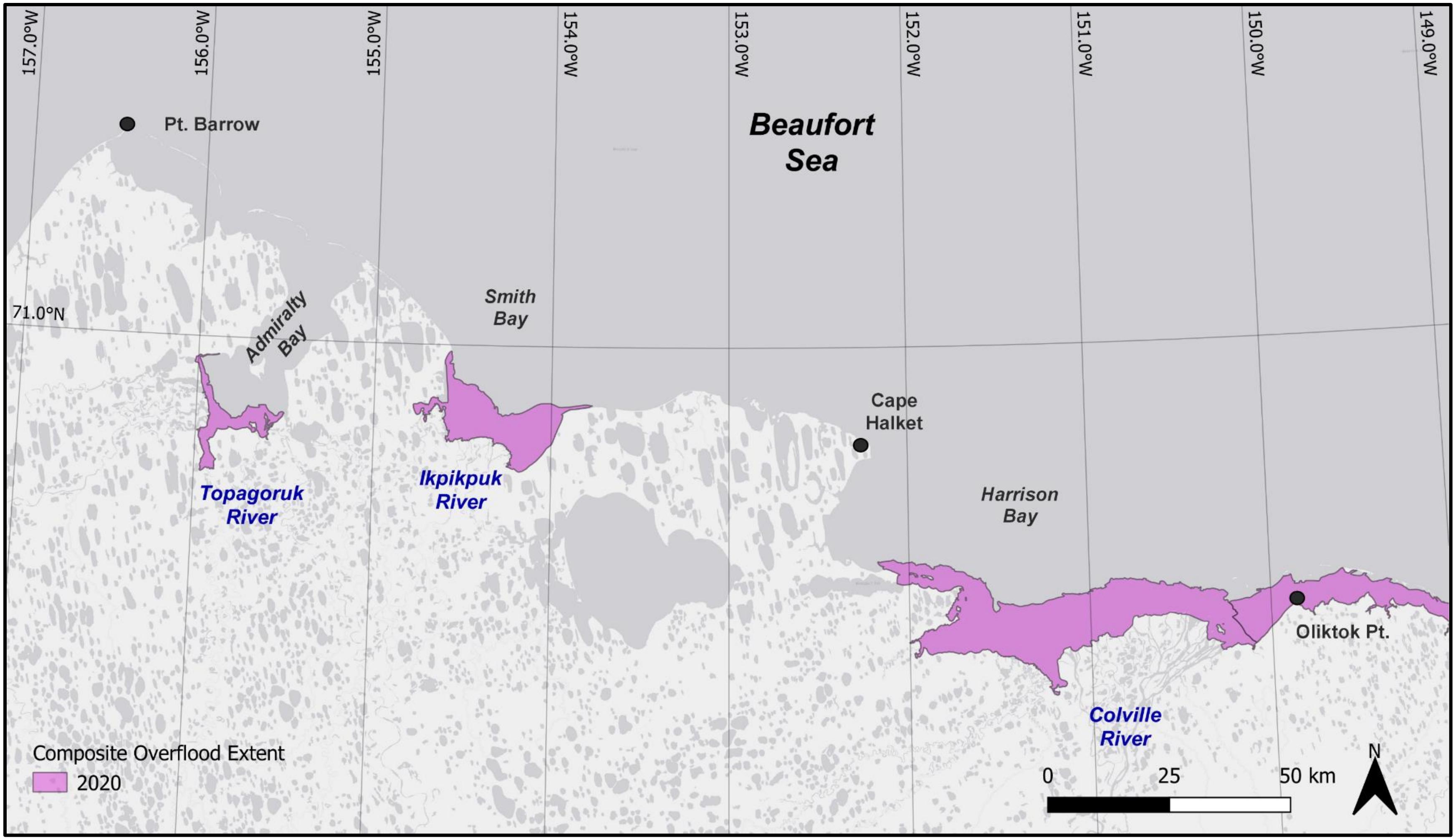

Figure 51. Composite overflood extent, west study region, 2020

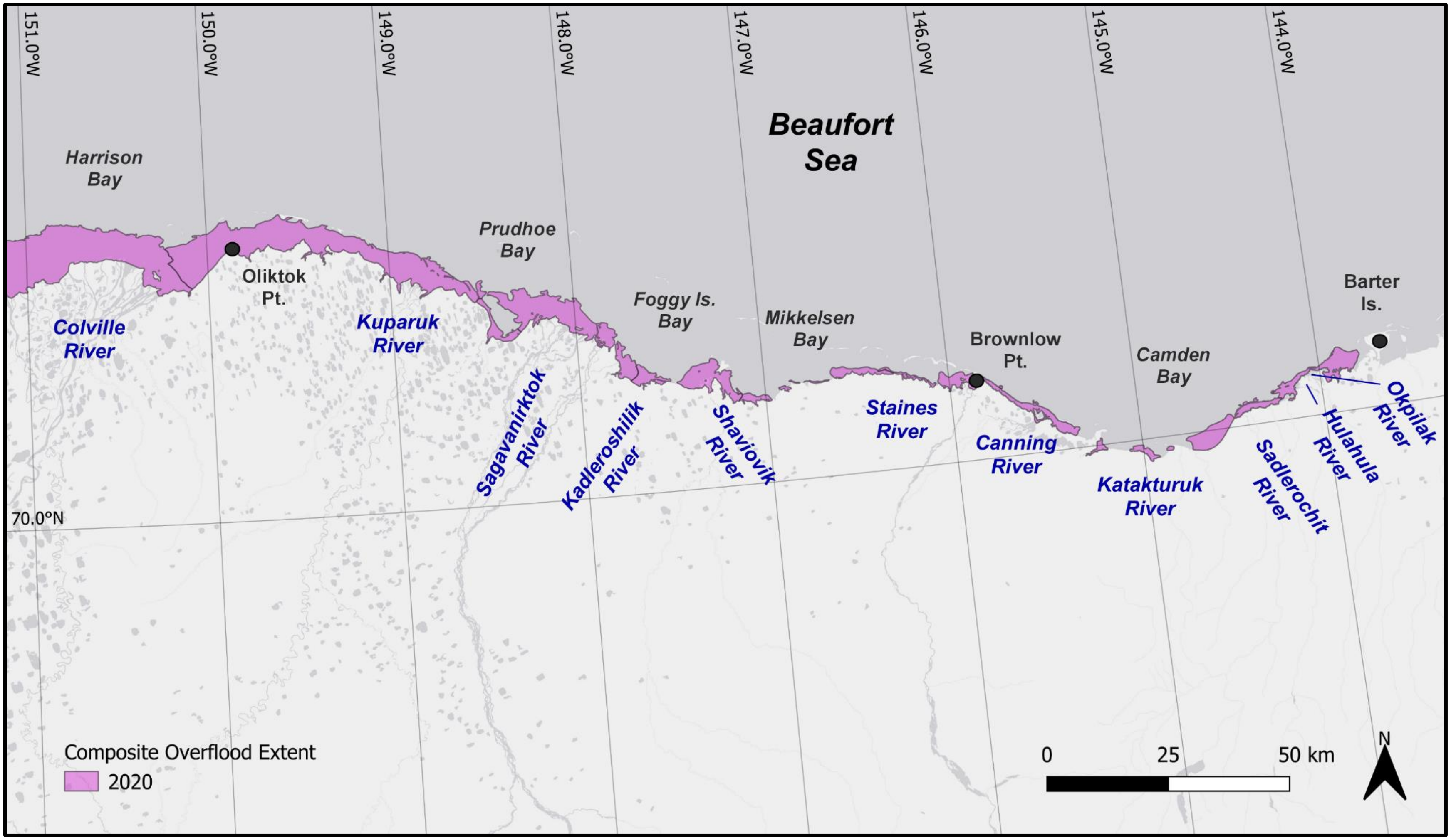

Figure 52. Composite overflood extent, east study region, 2020

Appendix C. Geodatabase Documentation

Update of the River Overflood on Sea Ice and Strudel Scour in the U.S. Beaufort Sea

Geodatabase Documentation

US Department of the Interior
Bureau of Ocean Energy Management
Alaska OCS Region, Anchorage, AK

Update of the River Overflood on Sea Ice and Strudel Scour in the U.S. Beaufort Sea

Geodatabase Documentation

March 2022

Authors:
Gregory Hearon
Ana Plana Casado
Christopher Scott

Prepared under Contract No. M0121C0001
By
Coastal Frontiers Corporation
882A Patriot Drive
Moorpark, CA 93021

Contents

List of Tables

List of Abbreviations and Acronyms

AWiFS	Advanced Wide Field Sensor
BOEM	Bureau of Ocean Energy Management
CSA	Canadian Space Agency
ESA	European Space Agency
GIS	Geographic Information Systems
HU8	Level 8 Hydrologic Unit
ISRO	Indian Space Research Organization
JAXA	Japanese Aerospace Exploration Agency
LISS-3	Linear Imaging Self Scanning Sensor
MLLW	Mean Lower Low Water
MMS	Mineral Management Service
MODIS	Moderate Resolution Imaging Spectroradiometer
NAD83	North American Datum of 1983
NASA	National Aeronautics and Space Administration
NOS	National Ocean Service
SAR	Synthetic Aperture Radar
USGS	United States Geological Survey
UTM	Universal Transverse Mercator

1 Introduction

This document describes the river overflood geodatabase developed by Coastal Frontiers Corporation on behalf of the U.S. Department of the Interior, Bureau of Ocean Energy Management (BOEM) as part of the project *Update of the River Overflood on Sea Ice and Strudel Scour in the U.S. Beaufort Sea*. Detailed information regarding the overflood processes is provided in the project's Final Report, which also includes extensive analysis of the products contained in the geodatabase. The documentation presented herein is intended to be used in concert with the Final Report, and thus does not contain information on the workflows used and assumptions made to develop the dataset.

The present geodatabase builds on, updates, and supersedes the geodatabase created in 2009 in the framework of the Mineral Management Service (MMS) project *Mapping Sea Ice Overflood Using Remote Sensing: Smith Bay to Camden Bay* (Hearon *et al.*, 2009).

2 Points of Contact

Scientific inquiries regarding the geodatabase products and underlying assumptions should be directed to:

Gregory Hearon, P.E.
Principal Investigator
Coastal Frontiers Corporation
882A Patriot Drive, Moorpark, California 93021
(818) 341-8133
ghearon@coastalfrontiers.com

Inquiries regarding data access and dissemination should be directed to:

Caryn Smith
Contracting Officer's Representative
U.S. Department of the Interior
Bureau of Ocean Energy Management Alaska Regional Office
3801 Centerpoint Drive, Mailstop AM 500, Anchorage, Alaska 99503
(907) 334-5248
caryn.smith@boem.gov

3 Geodatabase Structure

The geodatabase consists of two volumes:

OVERFLOOD_DATA.GDB: Primary geodatabase containing the river overflood data and auxiliary information compiled for the project. This product is intended for most end-users, and must be utilized in concert with the Final Report. Unless specifically stated, the horizontal datum of all datasets provided in the geodatabase is Universal Transverse Mercator (UTM) Zone 5N, relative to the North American Datum of 1983 (NAD83), with units of meters. The EPSG code is 26905. Depths are given in meters relative to the National Ocean Service (NOS) Mean Lower Low Water (MLLW) vertical datum. Unless otherwise stated, missing values are specified as "Null."

IMAGERY_BANK.GDB: Supporting geodatabase containing the raw satellite imagery used to derive the overflood extents for the period 1995–2020. This product is intended for experienced end-users interested in studying the dataset used to derive the overflood extents presented in OVERFLOOD_DATA.GDB. The scenes composing the geodatabase are third-party products provided as is. The contents of each geodatabase are described in Sections 4 and 5 below, respectively.

4 River Overflood Data

The OVERFLOOD_DATA.GDB geodatabase is composed of three distinct feature datasets and one table. The geodatabase structure is listed in **Table 1** and described in detail in the sub-sections that follow.

Table 1. Contents of OVERFLOOD_DATA.GDB

Feature Dataset	Feature Class	Name
1	-	**Overflood_Extent_Data**
	1.1	overflood_extent_1995_thru_2020
	1.2	overflood_extent_yearly_envelope_1995_thru_2020
	1.3	overflood_extent_maximum_envelope_1995_thru_2020
	1.4	overflood_extent_from_field_surveys_1995_thru_2020
	1.5	overflood_extent_pre_1995
	1.6	overflood_extent_probability_contours_2000_thru_2020
2	-	**Drain_and_Strudel_Scour_Data**
	2.1	circular_drains_and_short_crack_drains_1995_thru_2020
	2.2	long_crack_drains_1995_thru_2020
	2.3	circular_strudel_scours_1995_thru_2020
	2.4	linear_strudel_scours_1995_thru_2020
	2.5	drain_and_strudel_search_areas_1995_thru_2020
	2.6	strudel_zones
	2.7	strudel_zones_with_overflood_extent_yearly_envelope_1995_thru_2020
3	-	**Auxiliary_Data**
	3.1	alaska_north_slope_coast
	3.2	alaska_north_slope_bathymetry
	3.3	environmental_data_stations
	3.4	WBDHU8 (hydrologic_units)
	3.5	ice_roads
Table	-	**image_catalog**

4.1 Overflood Extent Data Feature Classes

4.1.1 Overflood Extent, 1995–2020

Feature class name: *overflood_extent_1995_thru_2020*

Feature class type: geometry - polygons

Description: Peak (cumulated maximum) overflood extent for each river, stream, or creek within the study area during each of the 26 river break-up seasons between 1995 and 2020. Data sources include field surveys and satellite imagery. The feature attributes are provided in **Table 2**. In 2019, the start of overflood in Admiralty Bay was identified; however, the available imagery was insufficient to map the peak overflood extent. A feature with no geometry is included (OBJECTID = 418) for this special case.

Table 2. Attribute description: overflood_extent_1995_thru_2020

Field Name	Field Type	Field Length	Description
FEATURE	string	254	Type of feature documented. All features in this class are categorized as "overflood extent."
YEAR	integer	4	Overflood season of the documented overflood extent.
WBD_HU8	string	254	Name of the level 8 hydrologic unit (HU8) containing the river, stream, or creek from which the overflood originated. HU8 are those defined by the United States Geological Survey (USGS) Watershed Boundary Dataset (USGS, 2021a) provided in feature class *WBDHU8*.
RIVER	string	254	Name of the river, stream, or creek from which the flood waters originated. Names correspond to those documented in various USGS topographic maps (USGS, 2021b). Bodies of water for which a name is not provided are categorized as "unnamed." Notes: 1. When the flood waters from multiple streams merge offshore and cannot be accurately assigned to individual rivers, this field lists all the contributing bodies of water. 2. When flood waters of a stream reach an area previously occupied by another stream for which the overflood extent was accurately documented, the overlapping area is assigned to the first stream. Exception: due to their importance for data analysis, flood waters from the Colville, Kuparuk, and Sagavanirktok Rivers are always assigned to those rivers.
OF_START	date	10	Overflood start date. Corresponds to the day when river discharge was first detected on the sea ice adjacent to a river mouth. Notes: 1. Overflood start dates are only documented when determined with an accuracy of ±2 days (or ±1 day for the Colville, Kuparuk, and Sagavanirktok Rivers). 2. No data value is "09/09/9999."
OF_PEAK	date	10	Overflood peak date. Corresponds to the day when the maximum overflood extent was registered. Notes: 1. The overflood of major rivers progresses heterogeneously in different directions. As a result, on a given day the flood water boundary can be advancing in one region while retreating in another. In these cases, the peak date is defined as the last day during which flood waters advanced anywhere in the region. 2. Overflood peak dates are only documented when determined with an accuracy of ±2 days (or ±1 day for the Colville, Kuparuk, and Sagavanirktok Rivers). 3. No data value is "09/09/9999."
OF_AREA	integer	6	Area, in square kilometers, covered by the flood waters when the maximum overflood extent was registered. Notes: 1. Areas are ellipsoidal relative to the GRS 1980 ellipsoid. 2. Areas are rounded to the nearest square kilometer. 3. Areas less than 0.5 square kilometers are assigned a value of 0.
CONFIDENCE	string	254	Level of confidence attributed to the geometry of the overflood extent. This is a qualitative assessment to describe how well the mapped overflood extent matches the actual maximum overflood that occurred for the river, stream, or creek under consideration. A description of the confidence levels used is provided in **Table 3**.
SOURCE	string	254	Source of the overflood extent data. Data sources include satellite imagery and field surveys (helicopter or hovercraft). Notes: 1. When satellite imagery was utilized, the list of the specific scenes used is provided in the field "IMAGERY." 2. When field surveys were utilized, the date and type of survey is noted in this field. Additional detail pertaining to field surveys conducted between 1995 and 2020 is provided in feature class *overflood_extent_from_field_surveys_1995_thru_2020*.

(continued)

Table 2. Attribute description: overflood_extent_1995_thru_2020 (continued)

Field Name	Field Type	Field Length	Description
IMAGERY	string	254	List of satellite images used to trace the overflood extent. Scenes are identified by their short name in the following format: **TTT_YYYYMMDDL** Where: **TTT** is the imagery type (see **Table 4**) **YYYYMMDD** is the date of image capture (local time) **L** is a unique identifier ("A", "B", or "C") used to differentiate images captured on the same date Image details are summarized in feature class *image_catalog*, and the scenes themselves are compiled in the Imagery Bank geodatabase.

Table 3. Confidence levels

Confidence Level	Description
high	Clear and abundant satellite imagery or survey data available. High degree of confidence that the derived geometry accurately matches the true maximum overflood extent.
medium-high	Mostly clear and abundant satellite imagery or survey data available. High degree of confidence that the derived geometry accurately matches the true overflood extent in most of the region. Uncertainties exist in isolated locations, and/or the overflood edge is diffuse due to light cloud cover.
medium	The available satellite imagery and survey data are sufficient to derive a meaningful overflood extent, but in certain areas the linework heavily relies on the interpretation of scarce/flawed data. This is generally the case when abundant cloud cover is present intermittently during the overflood season and limited Synthetic Aperture Radar (SAR) images are available.
medium-low	The available satellite imagery and survey data are sufficient to derive a meaningful overflood extent, but the linework heavily relies on the interpretation of scarce/flawed data. This is generally the case when abundant cloud cover is present throughout the overflood season and no SAR images are available, or when the overflood extent is very small.
low (1995–99)	Confidence level reserved for overflood extents from the pre-MODIS era (pre-2000). It reflects the lack of daily data covering the entire study area, which could have resulted in a general under-estimation of overflood areas relative to the MODIS era. Caution must be used when including these data in numerical analysis.

Table 4. Abbreviations for satellite imagery types

Short Name	Description
ERS	ERS-2 image (European Space Agency, ESA)
LS5	Landsat 5 image (USGS/National Aeronautics and Space Administration, NASA)
LS7	Landsat 7 image (USGS/NASA)
LS8	Landsat 8 image (USGS/NASA)
MOD	Moderate Resolution Imaging Spectroradiometer (MODIS) image (NASA)
PAL	ALOS PALSAR image (Japanese Aerospace Exploration Agency, JAXA)
R2A	Resourcesat-2A Advanced Wide Field Sensor (AWiFS) image, (Indian Space Research Organization, ISRO)
R2L	Resourcesat-2A Linear Imaging Self Scanning Sensor (LISS-3) image (ISRO)
RAD	Radarsat (Canadian Space Agency, CSA)
SE1	Sentinel-1 image (ESA)
SE2	Sentinel-2 image (ESA)

4.1.2 Overflood Extent Yearly Envelope, 1995–2020

Feature class name: *overflood_extent_yearly_envelope_1995_thru_2020*

Feature class type: geometry - polygons

Description: Combined peak overflood extent for all rivers, streams, and creeks in the study area during each of the 26 river break-up seasons between 1995 and 2020. Base data for this feature class are those contained in feature class *overflood_extent_1995_thru_2020*. The feature attributes are provided in **Table 5**.

Table 5. Attribute description: overflood_extent_yearly_envelope_1995_thru_2020

Field Name	Field Type	Field Length	Description
FEATURE	string	254	Type of feature documented. All features in this class are categorized as "overflood extent."
YEAR	integer	4	Overflood season of the documented overflood extent.
OF_AREA	integer	6	Area, in square kilometers, covered by the maximum flood extent at all rivers, streams, and creeks in the study region. Notes: 1. Area is ellipsoidal relative to the GRS 1980 ellipsoid. 2. Area is rounded to the nearest square kilometer.

4.1.3 Overflood Extent Maximum Envelope, 1995–2020

Feature class name: *overflood_extent_maximum_envelope_1995_thru_2020*

Feature class type: geometry - polygons

Description: Boundary of all overflood extents mapped between 1995 and 2020. Base data for this feature class are contained in feature class *overflood_extent_1995_thru_2020*. Feature attributes are provided in **Table 6**.

Table 6. Attribute description: overflood_extent_maximum_envelope_1995_thru_2020

Field Name	Field Type	Field Length	Description
FEATURE	String	254	Type of feature documented. All features in this class are categorized as "overflood extent."

4.1.4 Overflood Extent Derived from Field Surveys, 1995–2020

Feature class name: *overflood_extent_from_field_surveys_1995_thru_2020*

Feature class type: geometry - lines

Description: Peak overflood extent for various rivers in the study area derived from helicopter and hovercraft surveys performed by Coastal Frontiers between 1995 and 2020. Feature attributes are provided in **Table 7**. The information in this feature class was analyzed alongside the satellite imagery presented in Section 5 in order to derive the final dataset presented in feature class *overflood_extent_1995_thru_2020*. The information is provided for archival purposes only.

Table 7. Attribute description: overflood_extent_from_field_surveys_1995_thru_2020

Field Name	Field Type	Field Length	Description
FEATURE	string	254	Type of feature documented. All features in this class are categorized as "overflood extent."
YEAR	integer	4	Overflood season of the documented overflood extent.
DATE	date	10	Date of the survey (local time).
TYPE	string	254	Type of survey (by helicopter or, in a limited number of occasions, by hovercraft).
RIVER	string	254	Name of the river or rivers from which the flood waters originated. Names correspond to those documented in various USGS topographic maps (USGS, 2021b). Bodies of water for which a name is not provided by the USGS are categorized as "unnamed."

4.1.5 Overflood Extent, Pre-1995

Feature class name: *overflood_extent_pre_1995*

Feature class type: geometry - lines

Description: Peak overflood extent for various rivers in the study area during overflood seasons pre-dating 1995. Data sources include field surveys and satellite imagery. Feature attributes are provided in **Table 8**. The information is provided for archival purposes only.

Table 8. Attribute description: overflood_extent_pre_1995

Field Name	Field Type	Field Length	Description
FEATURE	string	254	Type of feature documented. All features in this class are categorized as "overflood extent."
YEAR	integer	4	Overflood season of the documented overflood extent.
RIVER	string	254	Name of the river or rivers from which the flood waters originated. Names correspond to those documented in various USGS topographic maps (USGS, 2021b).
SOURCE	string	254	Source of the overflood extent data. Data sources include satellite imagery and field surveys. Notes: 1. When satellite imagery was utilized, the specific scene in noted in this field. 2. When survey data was utilized, the date of the survey is noted in this field.

4.1.6 Overflood Extent Probability Contours, 2000–2020

Feature class name: *overflood_extent_probability_contours_2000_thru_2020*

Feature class type: geometry - lines

Description: Isolines of annual overflood occurrence probability derived from the 21 annual overflood extents between 2000 and 2020. The base data used to derive the contours are provided in feature class *overflood_extent_yearly_envelope_1995_thru_2020*. The contours have been smoothed for presentation purposes. Feature attributes are provided in **Table 9**.

Table 9. Attribute description: overflood_extent_probability_contours_2000_thru_2020

Field Name	Field Type	Field Length	Description
FEATURE	string	254	Type of feature documented. All features in this class are categorized as “overflood extent probability contour.”
PROB	integer	3	Probability of flood waters reaching the location in any given year, in percent. Probabilities of 0%, 10%, 25%, 50%, 75%, 90%, and 100% are provided.

4.2 Drain and Strudel Scour Data Feature Classes

4.2.1 Circular Drains and Short Crack Drains, 1995–2020

Feature class name: *circular_and_short_crack_drains_1995_thru_2020*

Feature class type: geometry - points

Description: Circular and short crack drain data obtained from field surveys performed by Coastal Frontiers during the overflood seasons between 1995 and 2020. Feature attributes are provided in **Table 10**. It should be noted that the field surveys did not encompass the entire study region. The search areas included as part each field survey are provided in feature class *drain_and_strudel_search_areas_1995_thru_2020*.

Table 10. Attribute description: circular_and_short_crack_drains_1995_thru_2020

Field Name	Field Type	Field Length	Description
FEATURE	string	254	Type of feature documented. All features in this class are categorized as “drain.”
YEAR	integer	4	Overflood season during which the documented drain formed.
TYPE	string	254	Type of drain: circular, short crack (less than 15.2 m long), or unknown.
RIVER	string	254	Name of the river, stream, or creek from which the flood waters where the drain was found originated. Names correspond to those documented in various USGS topographic maps (USGS, 2021b). Bodies of water for which a name is not provided by the USGS are categorized as “unnamed”. If the specific river that flooded the drain could not be determined with a high degree of confidence, all of the possible sources are listed.
ZONE	string	254	Strudel formation zone where the drain occurred. The zones are provided in feature class *strudel_zones*.
DRAIN_SA	string	254	Description of the area thoroughly searched for drains. Typically, the area corresponds to a monitoring corridor along a route of interest (*e.g.,* pipeline route). See feature class *drain_and_strudel_search_areas_1995_thru_2020* for additional detail.
NORTHING	real	10	Northing of the drain center. Horizontal datum is UTM Zone 5N, NAD83, with units of meters.
EASTING	real	10	Easting of the drain center. Horizontal datum is UTM Zone 5N, NAD83, with units of meters.
LAT	real	10	Latitude of the drain center (NAD83).
LON	real	10	Longitude of the drain center (NAD83).
LOCATION	string	254	This field notes if the drain was located inside or outside of the pre-established monitoring corridor delineated in field “DRAIN_SA.” “No corridor” indicates that a pre-established monitoring corridor was not used as part of the strudel search.

4.2.2 Long Crack Drains, 1995–2020

Feature class name: *long_crack_drains_1995_thru_2020*

Feature class type: geometry - lines

Description: Long crack drain data obtained from field surveys performed by Coastal Frontiers during the overflood seasons between 1995 and 2020. Feature attributes are provided in **Table 11**. It should be noted that the field surveys did not encompass the entire study region. The search areas included as part each field survey are provided in feature class *drain_and_strudel_search_areas_1995_thru_2020*.

Table 11. Attribute description: long_crack_drains_1995_thru_2020

Field Name	Field Type	Field Length	Description
FEATURE	string	254	Type of feature documented. All features in this class are categorized as “drain.”
YEAR	integer	4	Overflood season during which the documented drain formed.
TYPE	string	254	Type of drain. All features in this class are categorized as “long crack.”
RIVER	string	254	Name of the river, stream, or creek from which the flood waters where the drain was found originated. Names correspond to those documented in various USGS topographic maps (USGS, 2021b). Bodies of water for which a name is not provided by the USGS are categorized as “unnamed”. If the specific river that caused the drain could not be determined with a high degree of confidence, all of the possible source streams are listed in this field.
ZONE	string	254	Strudel formation zone where the drain occurred. The zones are provided in feature class *strudel_zones*.
DRAIN_SA	string	254	Description of the area thoroughly searched for drains. Typically, the area corresponds to a monitoring corridor along a route of interest (*e.g.,* pipeline route). See feature class *drain_and_strudel_search_areas_1995_thru_2020* for additional detail.
LOCATION	string	254	This field notes if the drain was located inside or outside of the pre-established monitoring corridor delineated in field “DRAIN_SA”. “No corridor” indicates that a pre-established monitoring corridor was not used as part of the strudel search.
LENGTH	integer	4	Approximate length of the crack, in meters.

4.2.3 Circular Strudel Scours, 1995–2020

Feature class name: *circular_strudel_scours_1995_thru_2020*

Feature class type: geometry - points

Description: Circular strudel scour data derived from bathymetric surveys performed by Coastal Frontiers and others during the open water seasons between 1995 and 2020. Feature attributes are provided in **Table 12**. It should be noted that the field surveys did not encompass the entire study region. The search areas included as part each field survey are provided in feature class *drain_and_strudel_search_areas_1995_thru_2020*.

Table 12. Attribute description: circular_strudel_scours_1995_thru_2020

Field Name	Field Type	Field Length	Description
FEATURE	string	254	Type of feature documented. All features in this class are categorized as “strudel scour.”
YEAR	integer	4	Overflood season during which the documented strudel formed (for new strudels), or year when the strudel was found (for relict strudels).
AGE	string	6	“New” strudels correspond to features formed in the same year that they were first surveyed. “Relict” strudels correspond to features found outside the corresponding overflood extent. The latter are included in the geodatabase for data archival purposes.
TYPE	string	254	Type of strudel scour. All features in this class are categorized as “circular.”
RIVER	string	254	Name of the river, stream, or creek from which the flood waters that caused the strudel scour originated. Names correspond to those documented in various USGS topographic maps (USGS, 2021b). Bodies of water for which a name is not provided by the USGS are categorized as “unnamed.” If the specific river that caused the strudel scour could not be determined with a high degree of confidence, all of the possible source streams are listed in this field.
ZONE	string	254	Strudel formation zone where the strudel scour was found. The zones are provided in feature class *strudel_zones*.
WATER_D	real	6	Water depth at the location of the strudel scour. Vertical datum is NOS MLLW, in units of meters.
SCOUR_D	real	6	Scour depth relative to the surrounding sea floor, in units of meters. Value is “Null” in those cases where the scour was imaged only with side-scan sonar (scour depth not measured).
HORIZONTAL	real	6	Maximum horizontal dimension of the scour at the depth of the surrounding sea floor, in units of meters.
SCOUR_SA	string	254	Description of the area thoroughly searched for strudel scours. The area generally includes several pre-planned survey lines and, if a drain search was performed during break-up, the locations of the mapped drains. See feature class *drain_and_strudel_search_areas_1995_thru_2020* for additional detail.
DRAIN_SA	string	254	Description of the area thoroughly searched for drains. Typically, the area corresponds to a monitoring corridor along a route of interest (*e.g.,* pipeline route). See feature class *drain_and_strudel_search_areas_1995_thru_2020* for additional detail.
NORTHING	real	10	Northing of deepest point of the scour. Horizontal datum is UTM Zone 5N, NAD83, with units of meters.
EASTING	real	10	Easting of deepest point of the scour. Horizontal datum is UTM Zone 5N, NAD83, with units of meters.
LAT	real	10	Latitude of deepest point of the scour (NAD83).
LON	real	10	Longitude of deepest point of the scour (NAD83).
LOCATION	string	254	This field notes if the scour was located inside or outside of the pre-established monitoring corridor delineated in field “SCOUR_SA.” “No corridor” indicates that a pre-established monitoring corridor was not used as part of the strudel search.

4.2.4 Linear Strudel Scours, 1995–2020

Feature class name: *linear_strudel_scours_1995_thru_2020*

Feature class type: geometry - points

Description: Linear strudel scour data derived from bathymetric surveys performed by Coastal Frontiers and others during the open water seasons between 1995 and 2020. Feature attributes are provided in **Table 13**. It should be noted that the field surveys did not encompass the entire study region. The search areas included as part each field survey are provided in feature class *drain_and_strudel_search_areas_1995_thru_2020*.

Table 13. Attribute description: linear_strudel_scours_1995_thru_2020

Field Name	Field Type	Field Length	Description
FEATURE	string	254	Type of feature documented. All features in this class are categorized as "strudel scour."
YEAR	integer	4	Overflood season during which the documented strudel formed (for new strudels), or year when the strudel was found (for relict strudels).
AGE	string	6	"New" strudels correspond to features formed in the same year that they were first surveyed. "Relict" strudels correspond to features found outside the corresponding overflood extent. The latter are included in the geodatabase for archival purposes.
TYPE	string	254	Type of strudel scour. All features in this class are categorized as "linear."
RIVER	string	254	Name of the river, stream, or creek from which the flood waters that caused the strudel scour originated. Names correspond to those documented in various USGS topographic maps (USGS, 2021b). Bodies of water for which a name is not provided by the USGS are categorized as "unnamed". If the specific river that caused the strudel scour could not be determined with a high degree of confidence, all of the possible source streams are listed in this field.
ZONE	string	254	Strudel formation zone where the strudel scour was found. The zones are provided in feature class *strudel_zones*.
WATER_D	real	6	Water depth at the location of the strudel scour. Vertical datum is NOS MLLW, in units of meters.
SCOUR_D	real	6	Scour depth relative to the surrounding sea floor, in units of meters. Value is "Null" in those cases where the scour was imaged only with side-scan sonar (scour depth not measured).
HORIZONTAL	real	6	Maximum horizontal dimension of the scour at the depth of the surrounding sea floor, in units of meters. Corresponds to the length of the feature measured along the scour orientation.
SCOUR_ORNT	integer	3	Orientation of the scour, in units of degrees relative to Grid North (UTM Zone 5N, NAD83).
SCOUR_SA	string	254	Description of the area thoroughly searched for strudel scours. The area generally includes several pre-planned survey lines and, if a drain search was performed during break-up, the locations of the mapped drains. See feature class *drain_and_strudel_search_areas_1995_thru_2020* for additional detail.
DRAIN_SA	string	254	Description of the area thoroughly searched for drains. Typically, the area corresponds to a monitoring corridor along a route of interest (*e.g.,* pipeline route). See feature class *drain_and_strudel_search_areas_1995_thru_2020* for additional detail.
NORTHING	real	10	Northing of deepest point of the scour. Horizontal datum is UTM Zone 5N, NAD83, with units of meters.
EASTING	real	10	Easting of deepest point of the scour. Horizontal datum is UTM Zone 5N, NAD83, with units of meters.
LAT	real	10	Latitude of deepest point of the scour (NAD83).
LON	real	10	Longitude of deepest point of the scour (NAD83).
LOCATION	string	254	This field notes if the scour was located inside or outside of the pre-established monitoring corridor delineated in field "SCOUR_SA." "No corridor" indicates that a pre-established monitoring corridor was not used as part of the strudel search.

4.2.5 Drain and Strudel Search Areas, 1995–2020

Feature class name: *drain_and_strudel_search_areas_1995_thru_2020*

Feature class type: geometry - polygons

Description: Spatial coverage of the drain and strudel scour surveys performed by Coastal Frontiers between 1995 and 2020. Feature attributes are provided in **Table 14**. The coverages have been trimmed to include only the flooded portion of the search area based on feature class *overflood_extent_from_field_surveys_1995_thru_2020*. Empty features correspond to years when either a drain search was not conducted, or a drain search was planned, but the flood waters did not reach the monitoring corridor. In both cases, a strudel search was conducted using the data acquired along the pipeline monitoring survey transects.

Table 14. Attribute description: drain_and_strudel_search_areas_1995_thru_2020

Field Name	Field Type	Field Length	Description
FEATURE	string	254	Type of feature documented. All features in this class are categorized as "search area."
YEAR	integer	4	Overflood season during which the search was undertaken.
RIVER	string	254	Name of the river, stream, or creek from which the flood waters that were searched originated. Names correspond to those documented in various USGS topographic maps (USGS, 2021b). Bodies of water for which a name is not provided by the USGS are categorized as "unnamed."
DRAIN_SA	string	254	Description of the area thoroughly searched for drains. Typically, the area corresponds to a monitoring corridor along a route of interest (*e.g.,* pipeline route).
SCOUR_SA	string	254	Description of the area thoroughly searched for strudel scours. The area generally includes several pre-planned survey lines and, if a drain search was performed during break-up, the locations of the mapped drains.

4.2.6 Strudel Zones

Feature class name: *strudel_zones*

Feature class type: geometry - polygons

Description: The three zones of strudel scour formation identified by Leidersdorf, *et al.* (2007). The Primary Strudel Zone is defined as the region between the 1.5-m and 6.1-m isobaths. The Secondary Strudel Zone is located landward of the 1.5-m isobath, and the Tertiary Strudel Zone is located offshore of the Primary Strudel Zone. Feature attributes are provided in **Table 15**.

Table 15. Attribute description: strudel_zones

Field Name	Field Type	Field Length	Description
FEATURE	string	254	Type of feature documented. All features in this class are categorized as "strudel zone."
ZONE	string	254	Strudel formation zone (Leidersdorf, *et al.*, 2007). **Primary Strudel Zone:** region between the 1.5-m and 6.1-m isobaths **Secondary Strudel Zone:** region located landward of the 1.5-m isobath **Tertiary Strudel Zone:** region located offshore of the Primary Strudel Zone The bathymetric contours used to define the three strudel zones are provided as feature class *alaska_north_slope_bathymetry*.

4.2.7 Strudel Zones and Overflood Extent Yearly Envelope, 1995–2020

Feature class name: *strudel_zones_and_overflood_extent_yearly_envelope_1995_thru_2000*

Feature class type: geometry - polygons

Description: The combined peak overflood extent for all rivers, streams, and creeks in the study area during each of the 26 river break-up seasons between 1995 and 2020 (feature class *overflood_extent_yearly_envelope_1995_thru_2020*) classified according to the three zones of strudel scour formation (feature class *strudel_zones*). Feature attributes are provided in **Table 16**.

Table 16. Attribute desc.: strudel_zones_and_overflood_extent_yearly_envelope_1995_thru_2000

Field Name	Field Type	Field Length	Description
FEATURE	string	254	Type of feature documented. All features in this class are categorized as “overflood extent by strudel zone.”
YEAR	Integer	4	Overflood season of the documented overflood extent.
ZONE	string	254	Combined peak overflood extent for all rivers, streams, and creeks in the study area classified by strudel formation zone (Leidersdorf, *et al.*, 2007). **Primary Strudel Zone:** region between the 1.5-m and 6.1-m isobaths **Secondary Strudel Zone:** region located landward of the 1.5-m isobath **Tertiary Strudel Zone:** region located offshore of the Primary Strudel Zone The bathymetric contours used to define the three strudel zones are provided as feature class *alaska_north_slope_bathymetry*.

4.3 Auxiliary Data Feature Classes

4.3.1 Alaska North Slope Coastline

Feature class name: *alaska_north_slope_coast*

Feature class type: geometry - polygons

Description: Alaska North Slope coastline used as the landward boundary for the study. It is a simplified version of that contained in the original study geodatabase (Hearon *et al.*, 2009). The linework should be considered to be approximate, as the Alaskan Arctic coast has experienced differential erosion and accretion between 1995 and 2020. Feature attributes are provided in **Table 17**.

Table 17. Attribute description: alaska_north_slope_coast

Field Name	Field Type	Field Length	Description
LandType	string	254	“mainland” or “island.”

4.3.2 Alaska North Slope Bathymetry

Feature class name: *alaska_north_slope_bathymetry*

Feature class type: geometry - lines

Description: Bathymetric contours used to derive the strudel zones presented in feature class *strudel_zones*. It is a simplified version of that contained in the original study geodatabase (Hearon *et al.*, 2009). Updates to the original study geodatabase include removal of contours exceeding 15.2 m, and refinement of the contours on the far east end of the study area. The linework should be considered to be approximate, as the primary data set used to develop the contours was acquired in the 1950's. Feature attributes are provided in **Table 18**.

Table 18. Attribute description: alaska_north_slope_bathymetry

Field Name	Field Type	Field Length	Description
WATER_D	Real	6	Water depth below National Ocean Service (NOS) Mean Lower Low Water (MLLW) in units of meters.
SOURCE	String	254	Source used to develop bathymetric contours.

4.3.3 Environmental Data Stations

Feature class name: *environmental_data_stations*

Feature class type: geometry - points

Description: Location of the meteorological stations and river streamflow monitoring sites used in the analysis of the overflood data presented in the geodatabase. Feature attributes are provided in **Table 19**, while the project's Final Report describes the analysis methods and results.

Table 19. Attribute description: environmental_data_stations

Field Name	Field Type	Field Length	Description
AGENCY	string	254	Reporting agency.
NAME	string	254	Station name.
DATA_PRIM	string	254	Primary environmental data reported by the station and of interest for overflood studies.
DATA_SEC	string	254	Secondary environmental data reported by the station and of interest for overflood studies.
PERIOD	string	254	Period of operation in years. Note, data gaps may exist.

4.3.4 Hydrologic Units

Feature class name: *WBDHU8*

Feature class type: geometry - polygons

Description: USGS Watershed Boundary Dataset (WBD) 8-digit Hydrologic Unit (HU8) data for Arctic Alaska. The dataset is provided as is from the USGS without modification (USGS, 2021a). Feature attributes are provided in **Table 20**. The associated XML file submitted with the geodatabase (\FGDC Metadata\OVERFLOOD_DATA\Auxiliary Data\WBDHU8.xml) provides a complete description of the dataset.

Table 20. Attribute description: WBDHU8

Field Name	Field Type	Field Length	Description
OBJECTID	integer	10	Internal feature number
TNMID	string	40	Unique 40-character field that identifies each element in the geodatabase exclusively.
MetaSource	string	40	Unique identifier that links the element to the metadata tables.
SourceData	string	100	Brief description of the type of base data used to update or change the current WBD.
SourceOrig	string	130	Description of the agency that created the base data used to improve the WBD
SourceFeat	string	40	Identifies the parent of the feature if the feature is the result of a split or merge.
LoadDate	date	10	Date when the data were loaded into the official USGS WBD ArcSDE geodatabase
GNIS_ID	Integer	10	Preassigned numeric field that uses a unique number to relate the name of the hydrologic unit to the GNIS names geodatabase.
AreaAcres	real	18	Area in acres calculated at the 12-digit hydrologic unit from the intrinsic area value maintained by the GIS software.
AreaSqKm	real	18	Area in square kilometers calculated at the 12-digit hydrologic unit from the intrinsic area value maintained by the GIS software.
Name	string	120	Name refers to the GNIS name for the geographic area in which the hydrologic unit is located.
ReferenceG	string	50	Unknown field. No documentation provided by USGS.
States	string	50	The States or outlying area attribute identifies the State(s) or outlying areas that the hydrologic unit falls within or touches.
HUC8	string	8	Unique 8-digit hydrologic unit code.
Shape_Leng	real	18	Unknown field. No documentation provided by USGS.
Shape_Area	real	18	Unknown field. No documentation provided by USGS.

4.3.5 Ice Roads

Feature class name: *ice_roads*

Feature class type: geometry - lines

Description: Location of the offshore ice roads constructed between 1995 and 2020. The linework was provided by industry partners or was identified in satellite imagery. Feature attributes are provided in **Table 21**.

Table 21. Attribute description: ice_roads

Field Name	Field Type	Field Length	Description
YEAR	integer	4	Overflood year during which the ice road was in place.
SOURCE	string	254	Data provider. If identified on satellite imagery, the value is “SATELLITE.”

4.4 Image Catalog (Table)

Table name: *image_catalog*

Description: Summary of the 344 satellite imagery scenes used in the development of feature class *overflood_extent_1995_thru_2020*. The imagery is provided as a bundle in the supporting geodatabase IMAGERY_BANK.GDB (Section 5). The catalog fields are given in **Table 22**.

Table 22. Attribute description: image_catalog

Field Name	Field Type	Field Length	Description
SHORT_N	string	254	Project-specific image name in the following format: **TTT_YYYYMMDDL** Where: **TTT** is the imagery type (see **Table 4**) **YYYYMMDD** is the date of image capture (local time) **L** is a unique identifier (“A”, “B”, or “C”) used to differentiate images captured on the same date The scenes are compiled in the Imagery Bank geodatabase.
LONG_N	string	254	Original name of the image file, as obtained from the data provider.
DATE	date	-	Date of image capture (local time).
RES	real	6	Image spatial resolution, in units of meters.
SATELLITE	string	254	Satellite platform or constellation.
SENSOR	string	254	Satellite sensor acquiring the image.
PRODUCT	string	254	Specific product type or acquisition mode.
PROVIDER	string	254	Data provider.
ORIGINATOR	string	254	Data originator.

5 Imagery Bank

The 344 satellite images listed in the *image_catalog* feature class are provided as a bundle in the IMAGERY_BANK.GDB geodatabase. Scenes are categorized by image type. The images are provided as is. The only modification is appending the project-specific name to the image name. The image catalog includes references to the data provider and source. The imagery collections are listed in **Table 23**.

Table 23. Contents of IMAGERY_BANK.GDB

Collection	Imagery Source
1	ERS-2 (ESA)
2	Landsat 5 (USGS/NASA)
3	Landsat 7 (USGS/NASA)
4	Landsat 8 (USGS/NASA)
5	Moderate Resolution Imaging Spectroradiometer (MODIS, NASA)
6	ALOS PALSAR (JAXA)
7	Resourcesat-2A Advanced Wide Field Sensor (AWiFS, ISRO)
8	Resourcesat-2A Linear Imaging Self Scanning Sensor (LISS-3, ISRO)
9	Sentinel-1 image (ESA)
10	Sentinel-2 image (ESA)
11	Radarsat (CSA)

6 References

Hearon, G., D. Dickins, K. Ambrosius, and K. Morris. 2009. Mapping Sea Ice Overflood Using Remote Sensing: Smith Bay to Camden Bay. Report prepared by DF Dickins Associates, Coastal Frontiers Corporation, Aerometric, and The Geophysical Institute, University of Alaska for U.S. Department of the Interior, Minerals Management Service, Alaska OCS Region. 127 p. Report No.: OCS Study MMS 2009-017. Contract M06PC00034. *https://espis.boem.gov/final%20reports/4871.pdf*.

Leidersdorf, C.B., G.E. Hearon, K.D. Vaudrey, and G. Swank. 2007. Strudel Scour Formation off Arctic River Deltas. Proc., 30th International Conference on Coastal Engineering, Vol. 5, World Scientific, Hackensack, New Jersey, p. 5312-5324.

U.S. Geological Survey, 2021a, National Hydrography Dataset (ver. USGS National Hydrography Dataset Best Resolution (NHD) for Hydrologic Unit (HU) 4 - 1906 (published 20201202)), accessed January 1, 2021 at URL *https://www.sciencebase.gov/catalog/item/5a3a5264e4b0d05ee8b59f1f*

U.S. Geological Survey, 2021b, National Geologic Map Database (topoView), accessed at URL *https://ngmdb.usgs.gov/topoview/*

Appendix D: Correlations between Environmental Parameters and Overflood

This appendix contains figures illustrating the correlation between each of the paired environmental and overflood parameters presented in Section 9 of the main report. Please see Section 9 for more information.

1 Correlation between Environmental Parameters and Streamflow

1.1 Colville River Streamflow

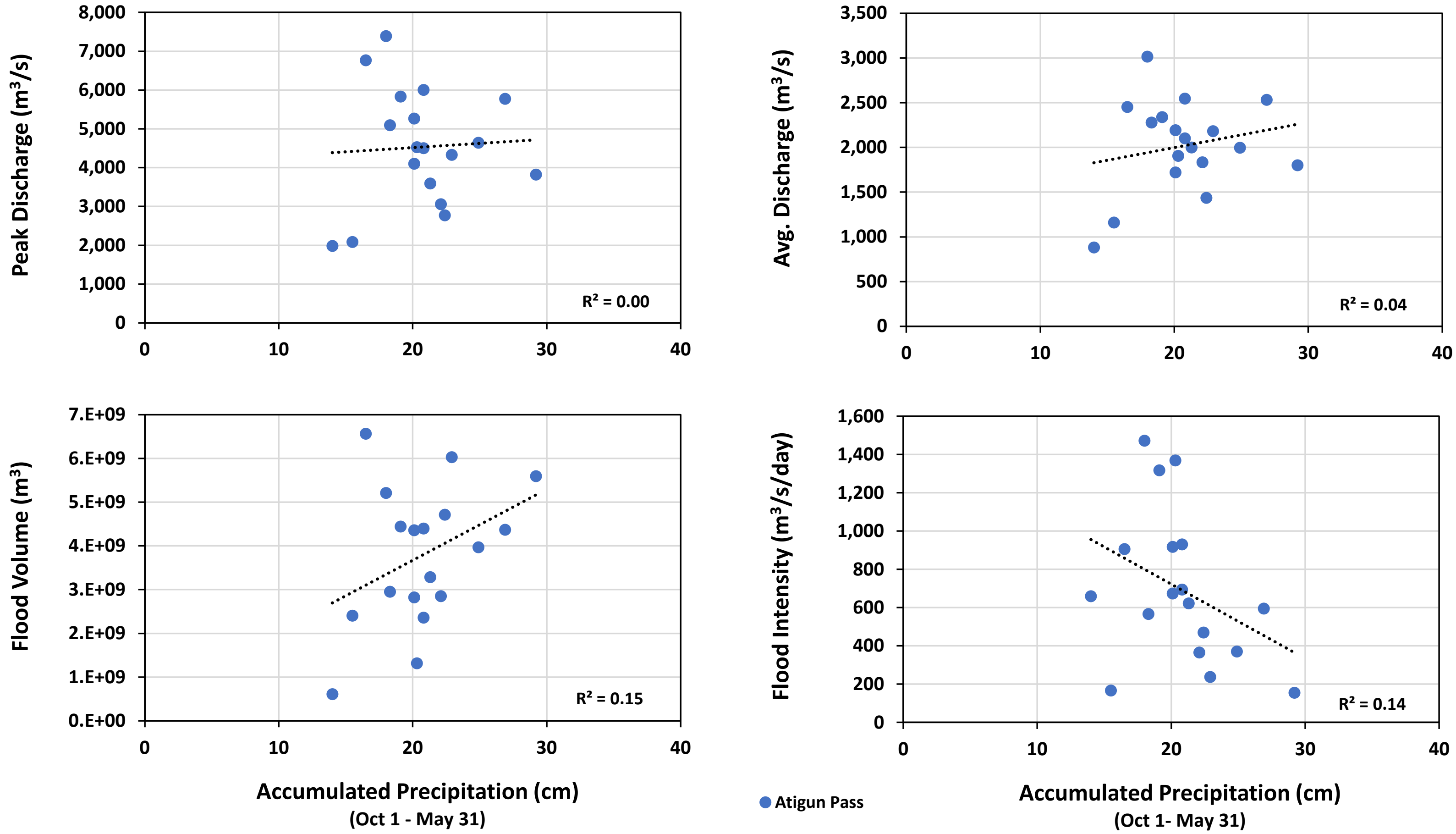

Figure 1. Correlation between precipitation (Atigun Pass) and streamflow (Colville River)

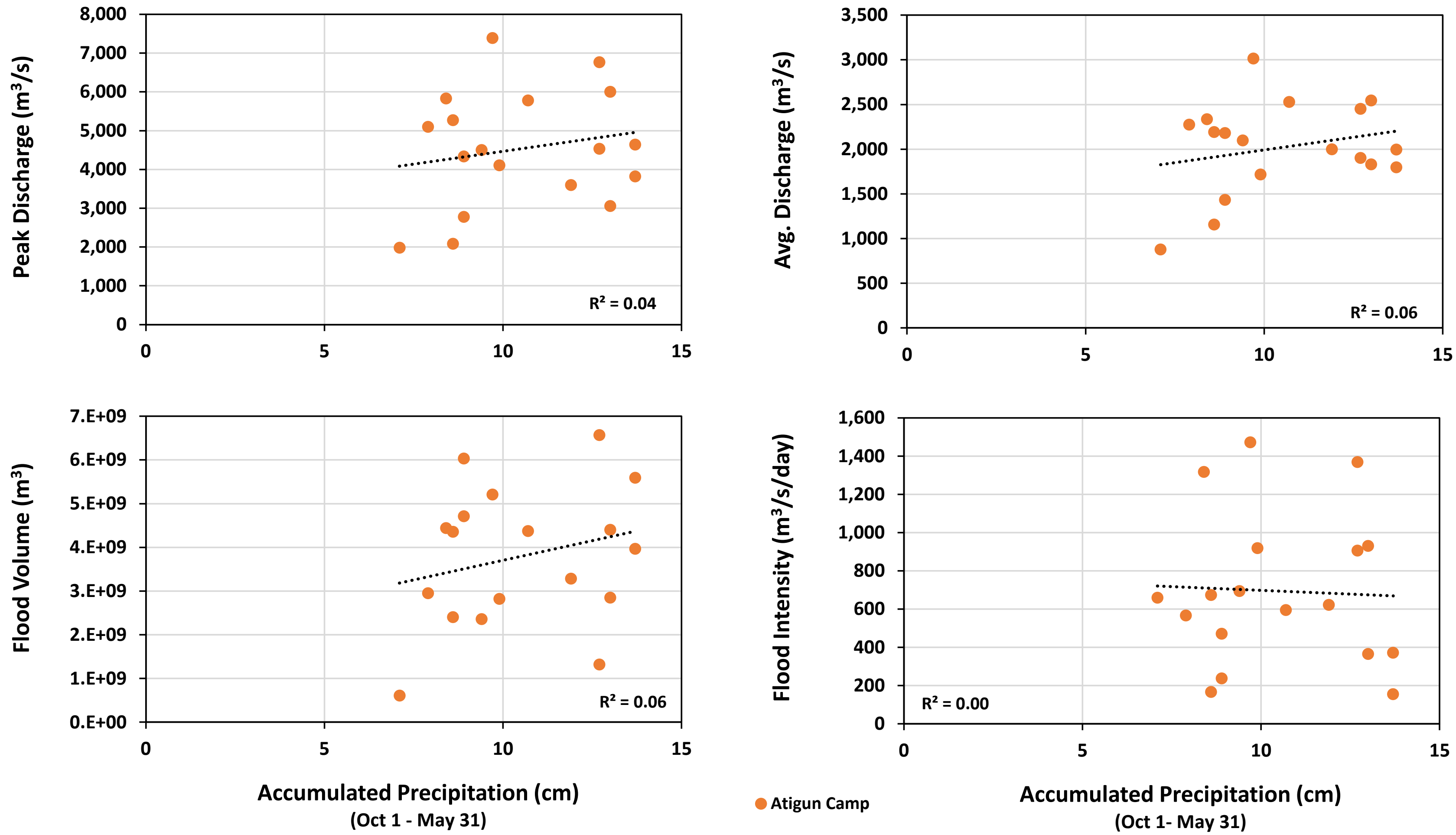

Figure 2. Correlation between precipitation (Atigun Camp) and streamflow (Colville River)

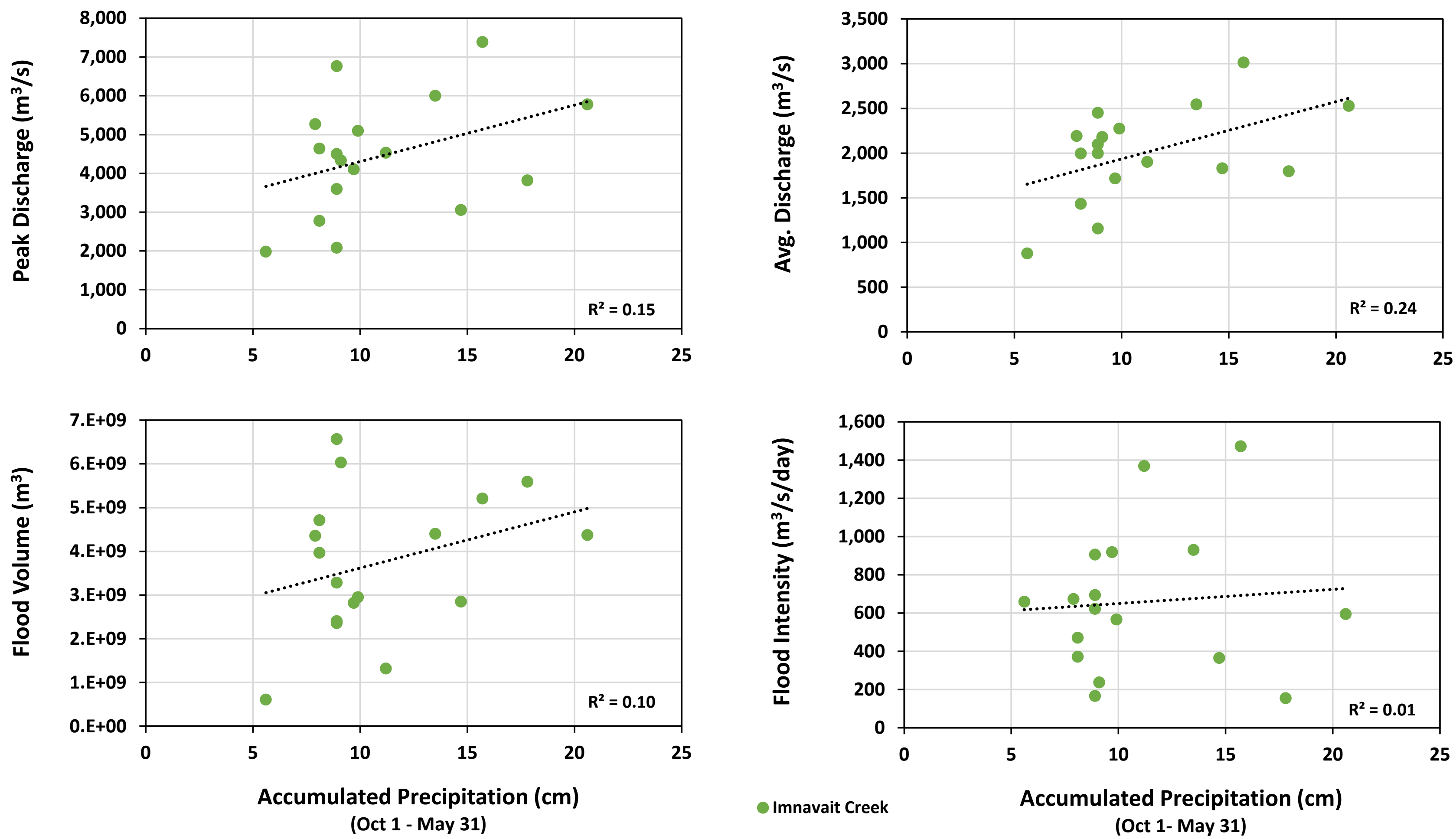

Figure 3. Correlation between precipitation (Imnavait Creek) and streamflow (Colville River)

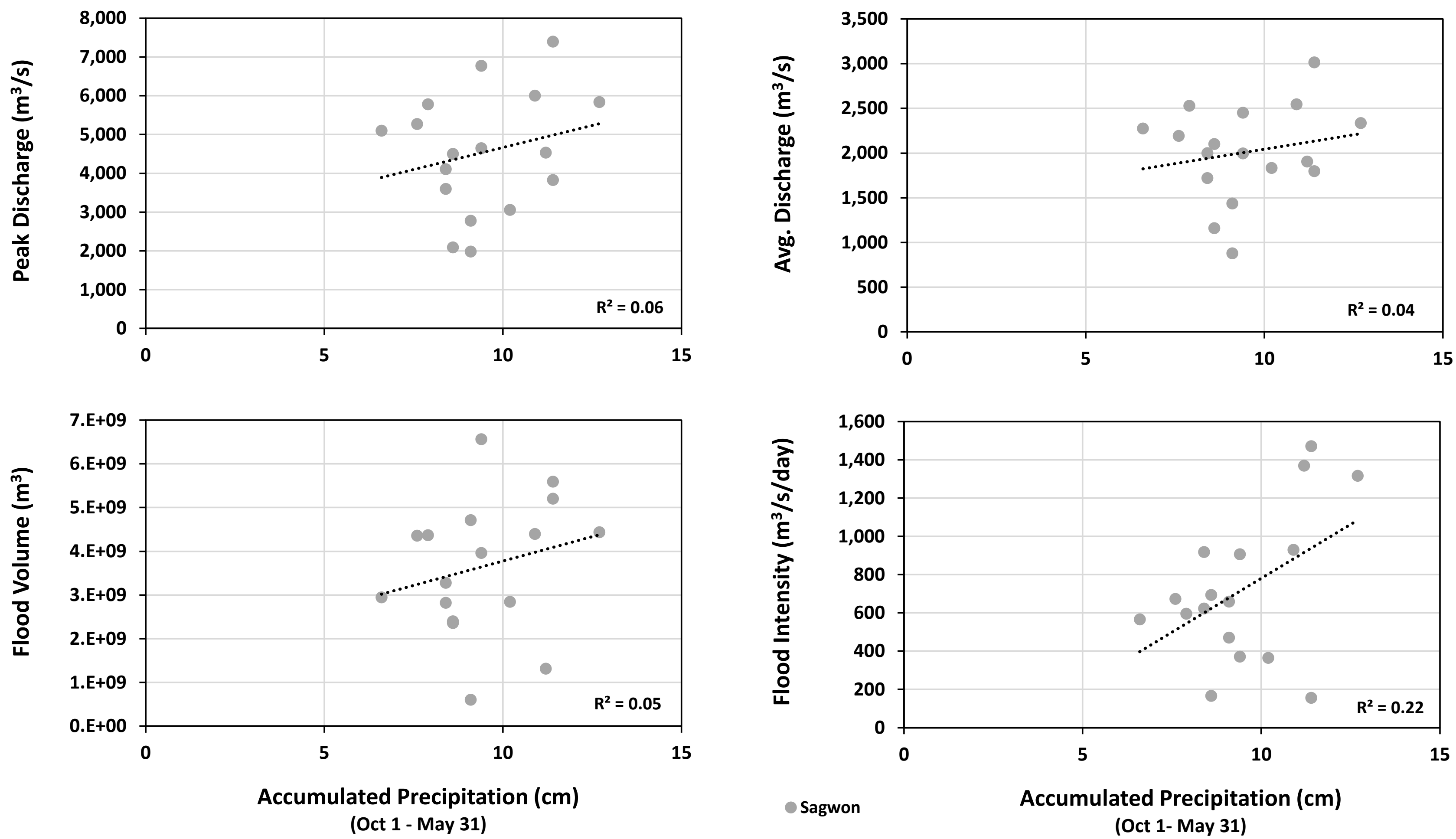

Figure 4. Correlation between precipitation (Sagwon) and streamflow (Colville River)

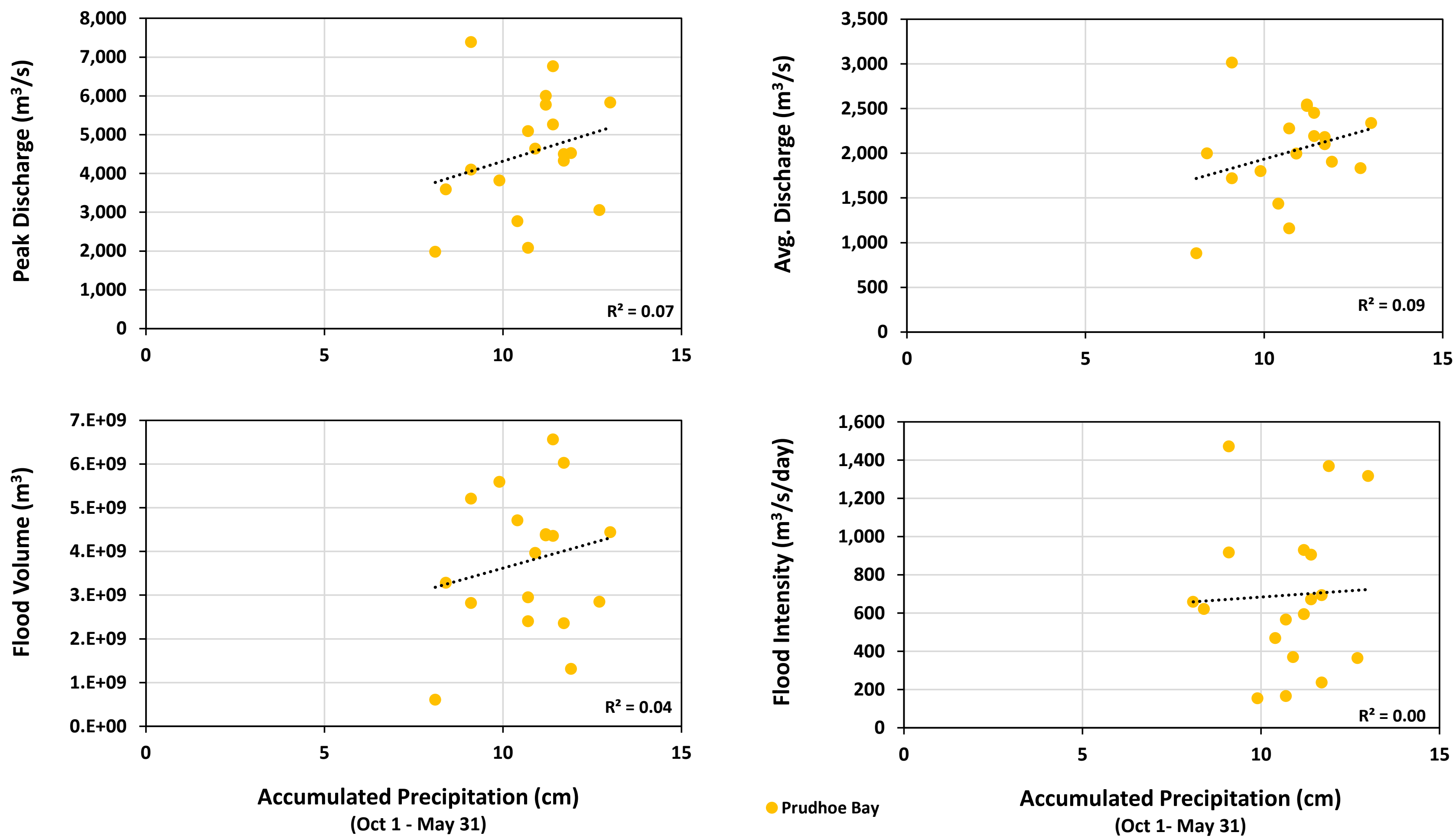

Figure 5. Correlation between precipitation (Prudhoe Bay) and streamflow (Colville River)

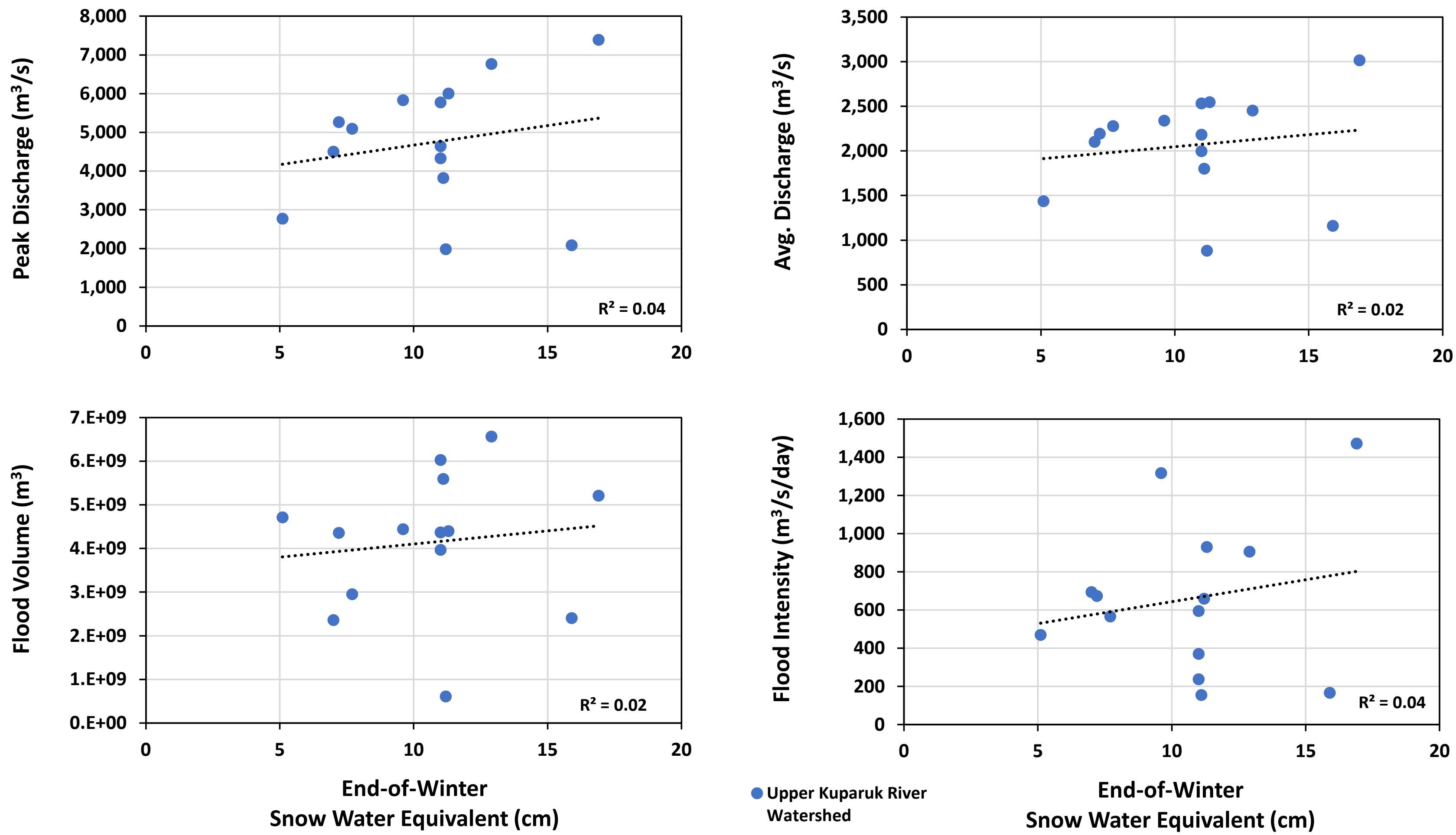

Figure 6. Correlation between end-of-winter SWE (Upper Kuparuk River Watershed) and streamflow (Colville River)

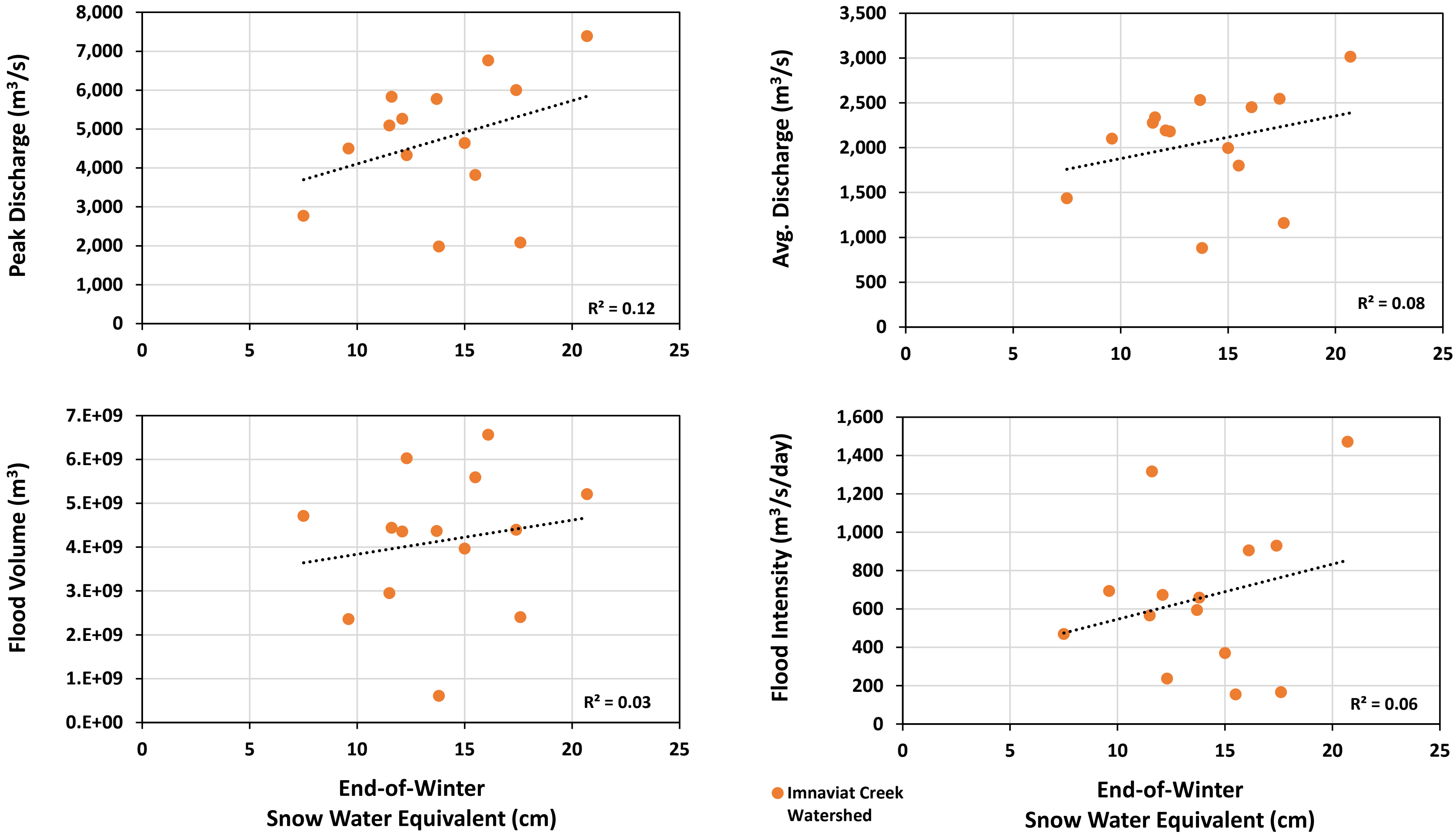

Figure 7. Correlation between end-of-winter SWE (Imnaviat Creek Watershed) and streamflow (Colville River)

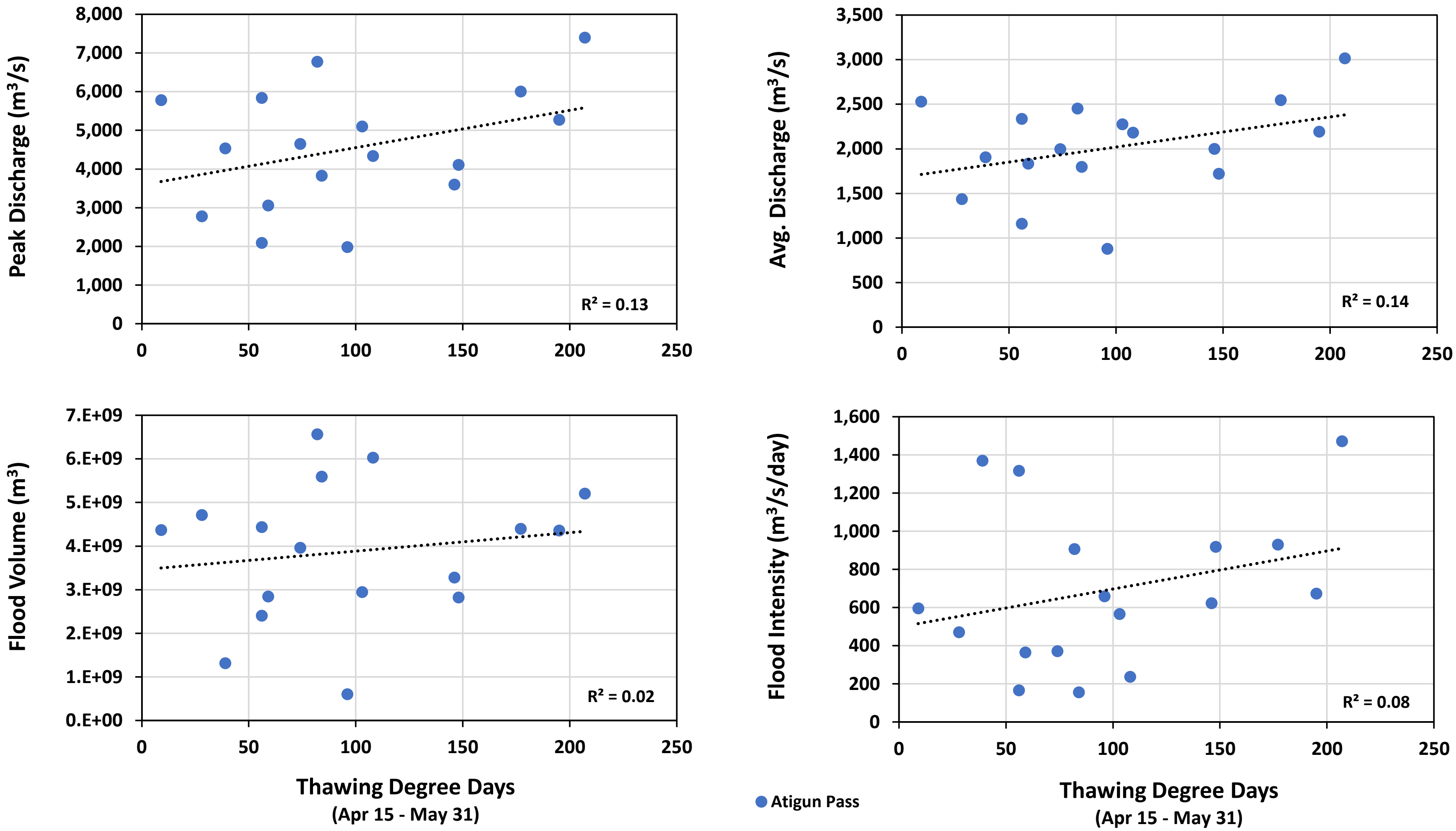

Figure 8. Correlation between TDD (Atigun Pass) and streamflow (Colville River)

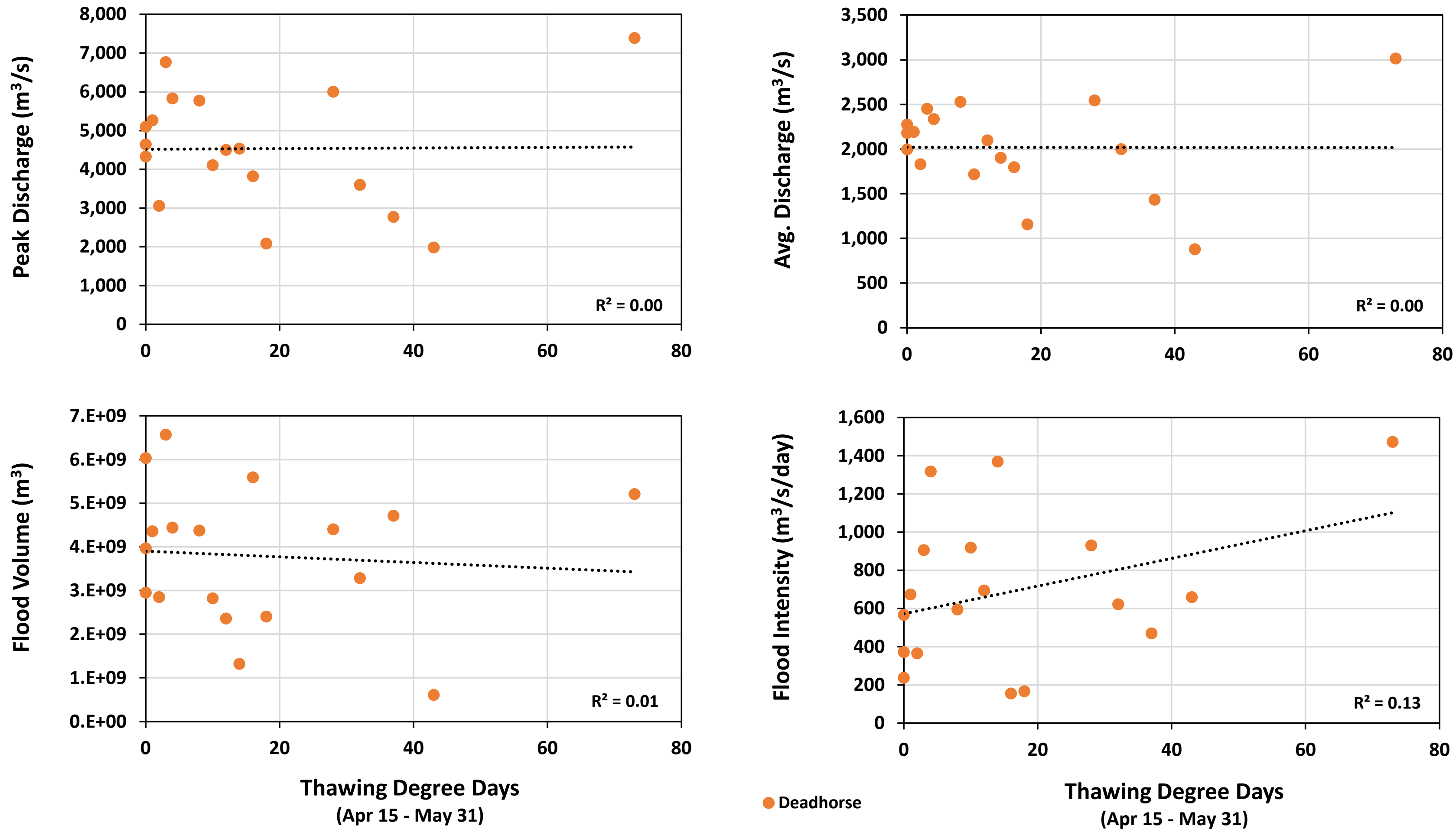

Figure 9. Correlation between TDD (Deadhorse) and streamflow (Colville River)

1.2 Kuparuk River Streamflow

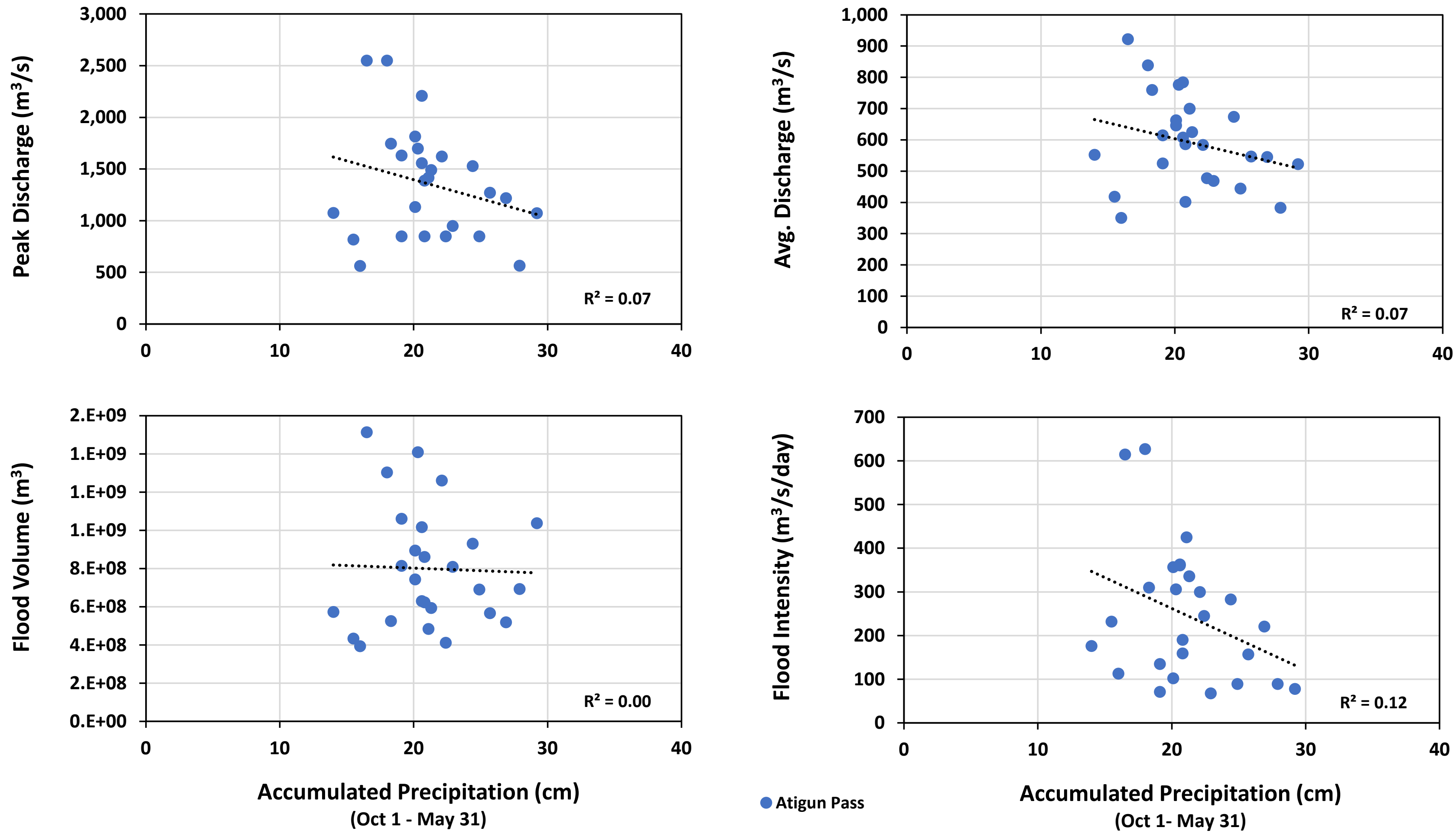

Figure 10. Correlation between precipitation (Atigun Pass) and streamflow (Kuparuk River)

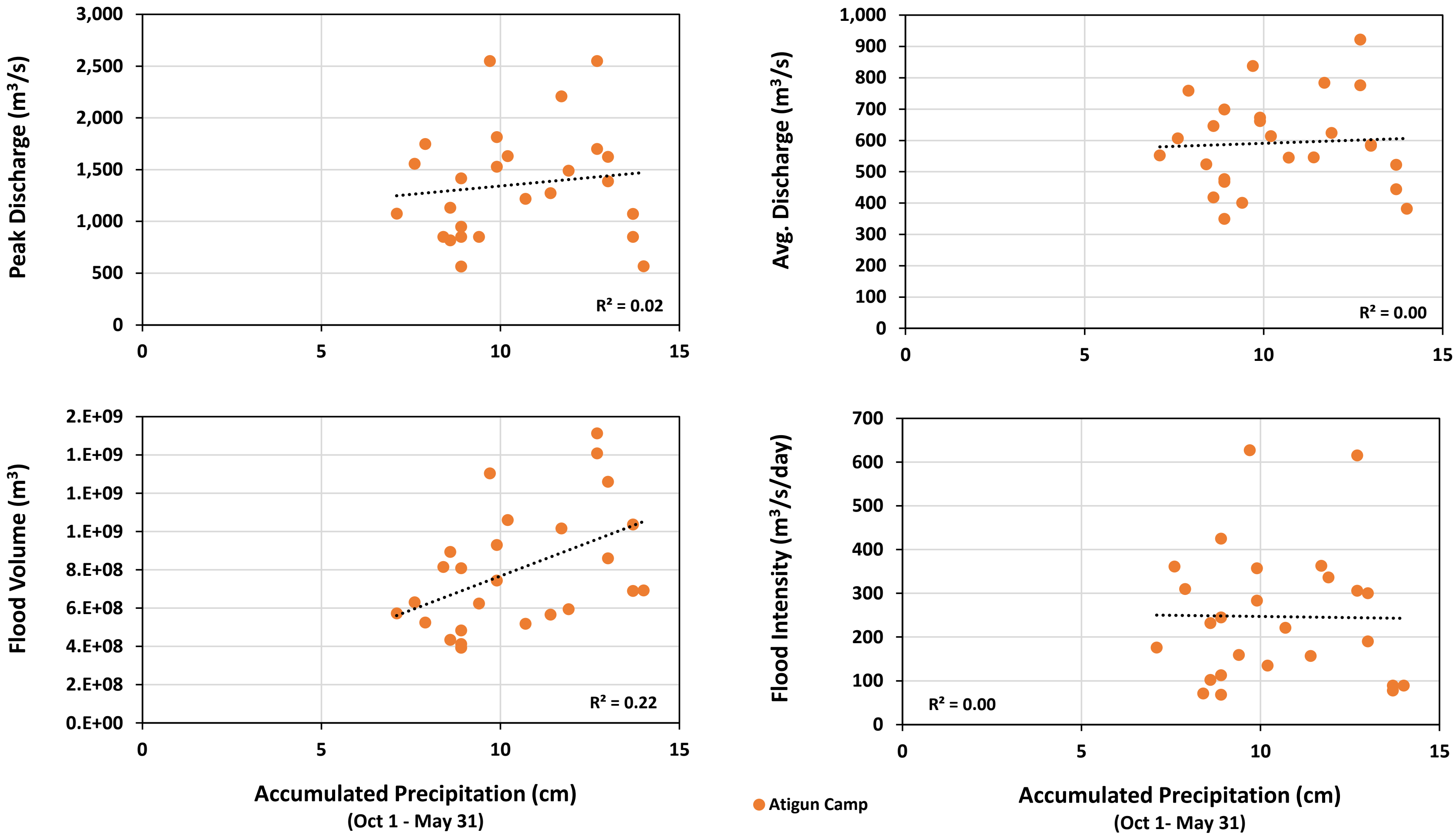

Figure 11. Correlation between precipitation (Atigun Camp) and streamflow (Kuparuk River)

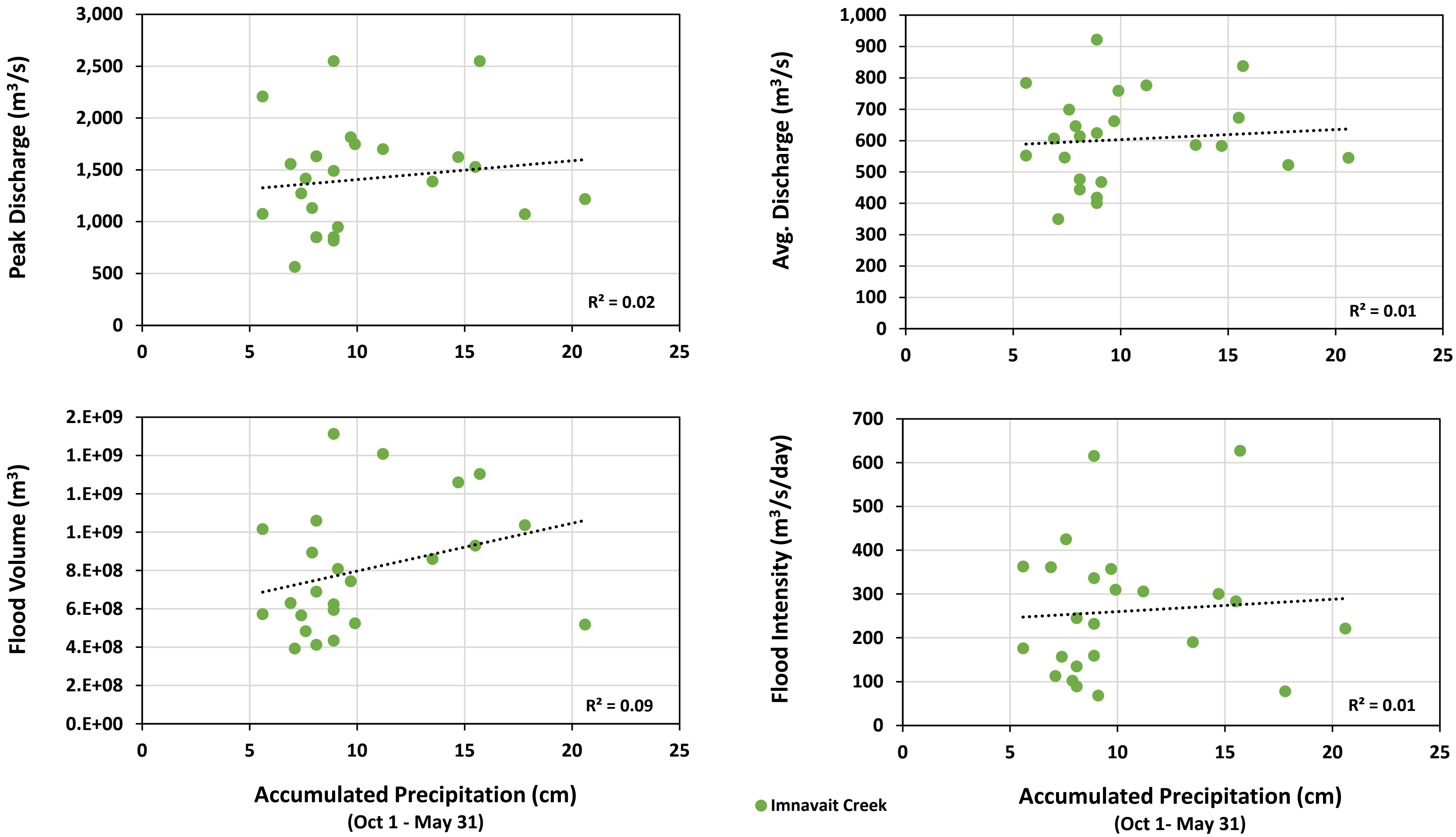

Figure 12. Correlation between precipitation (Imnavait Creek) and streamflow (Kuparuk River)

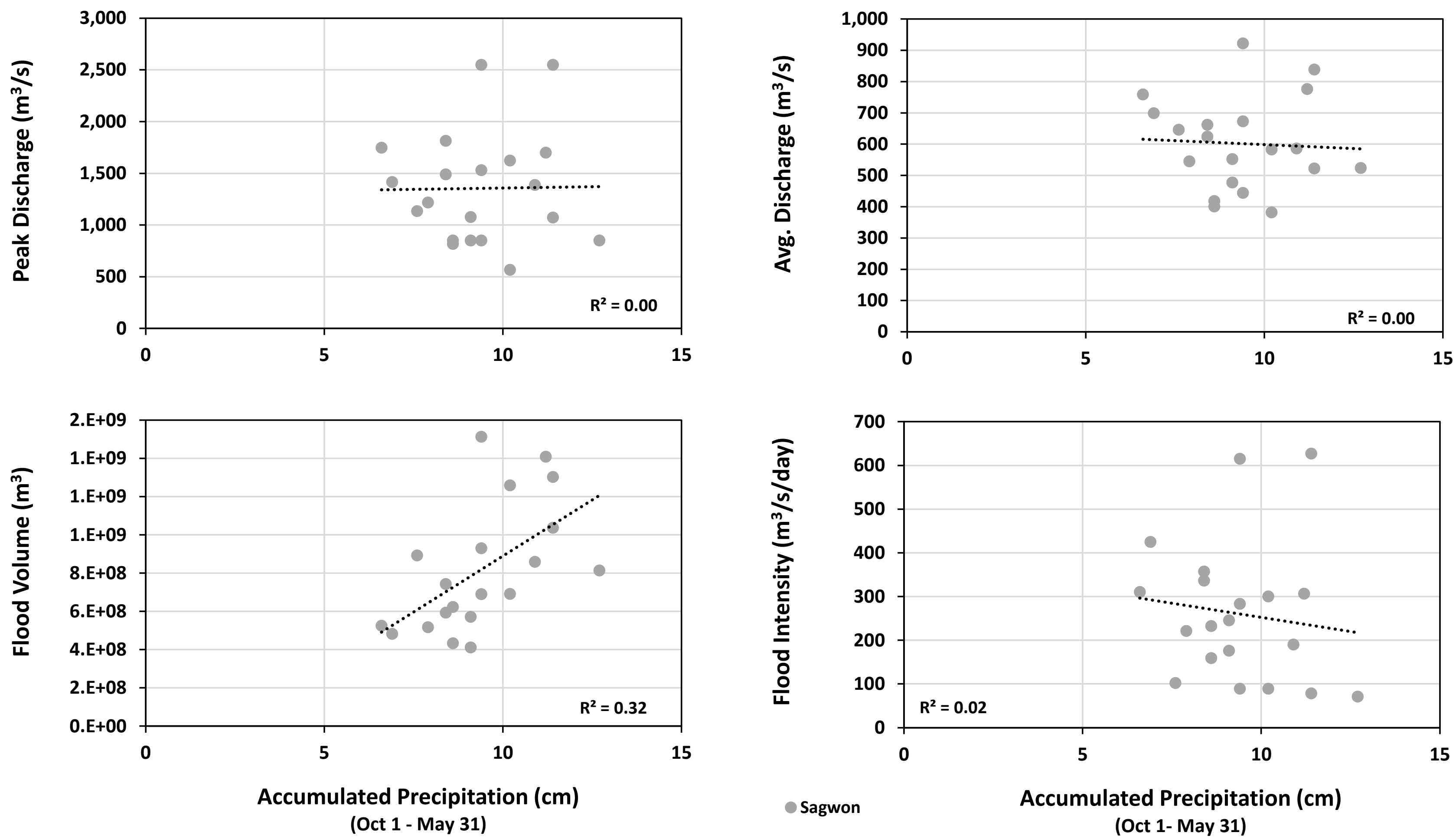

Figure 13. Correlation between precipitation (Sagwon) and streamflow (Kuparuk River)

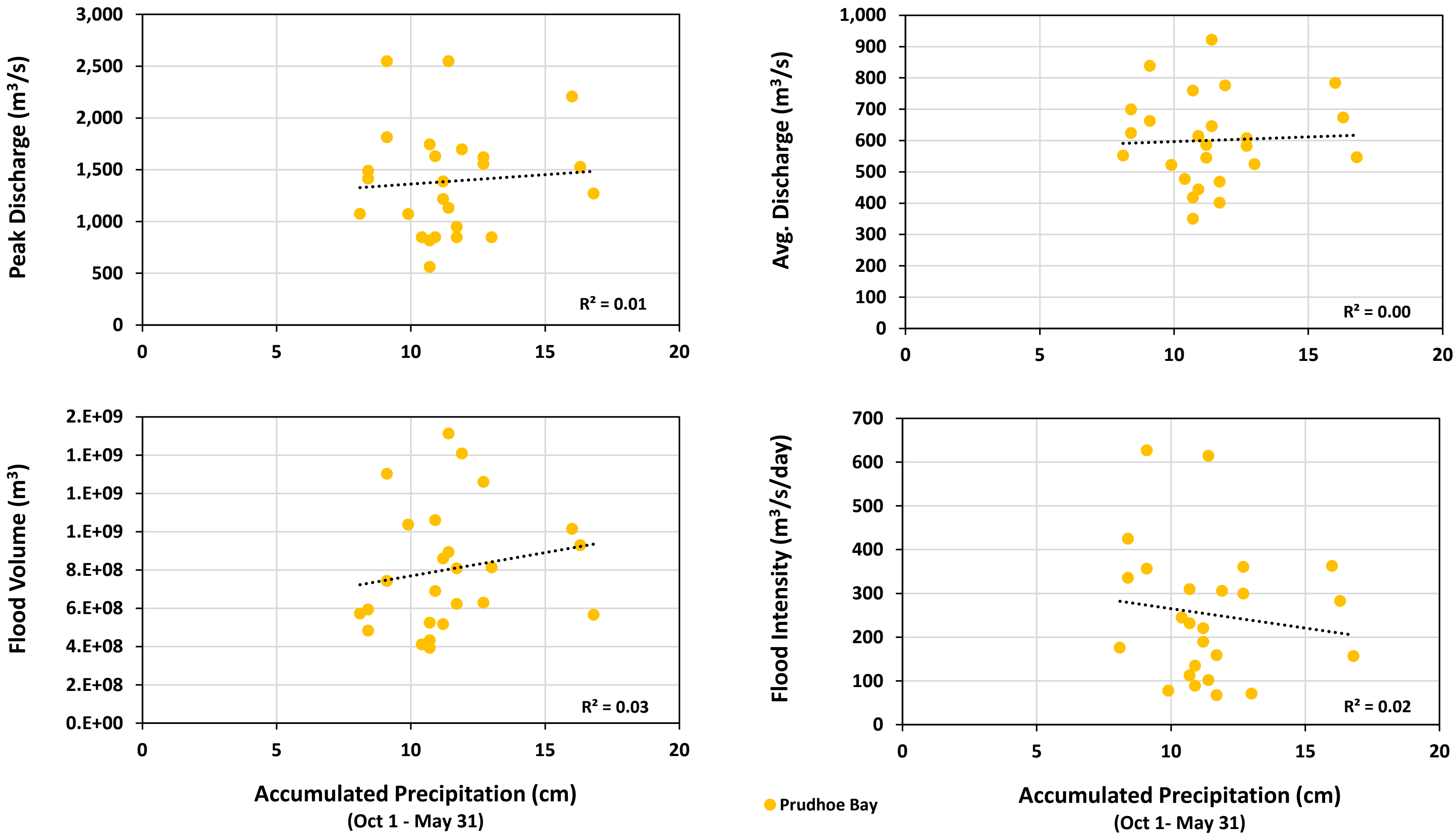

Figure 14. Correlation between precipitation (Prudhoe Bay) and streamflow (Kuparuk River)

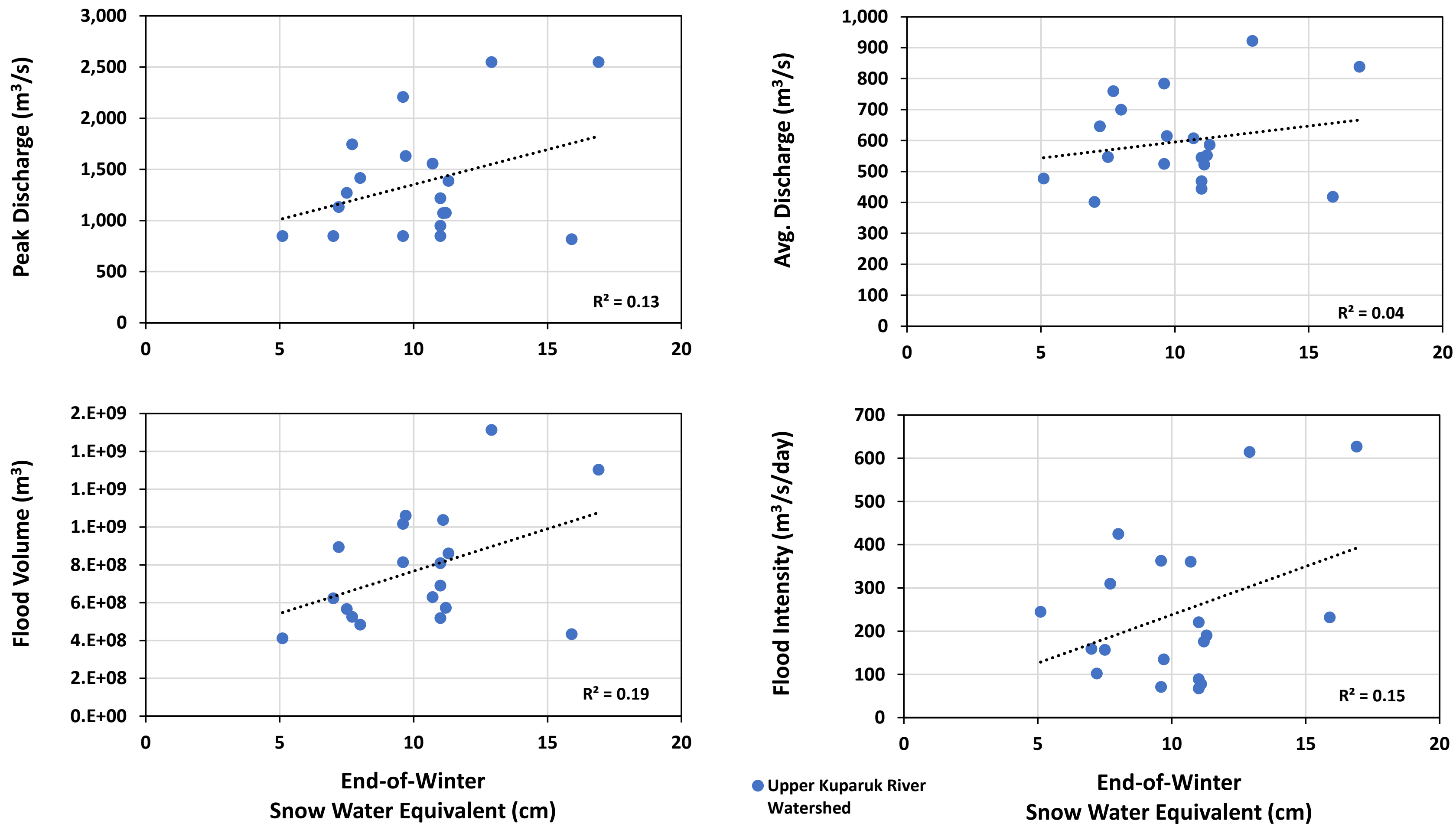

Figure 15. Correlation between end-of-winter SWE (Upper Kuparuk River Watershed) and streamflow (Kuparuk River)

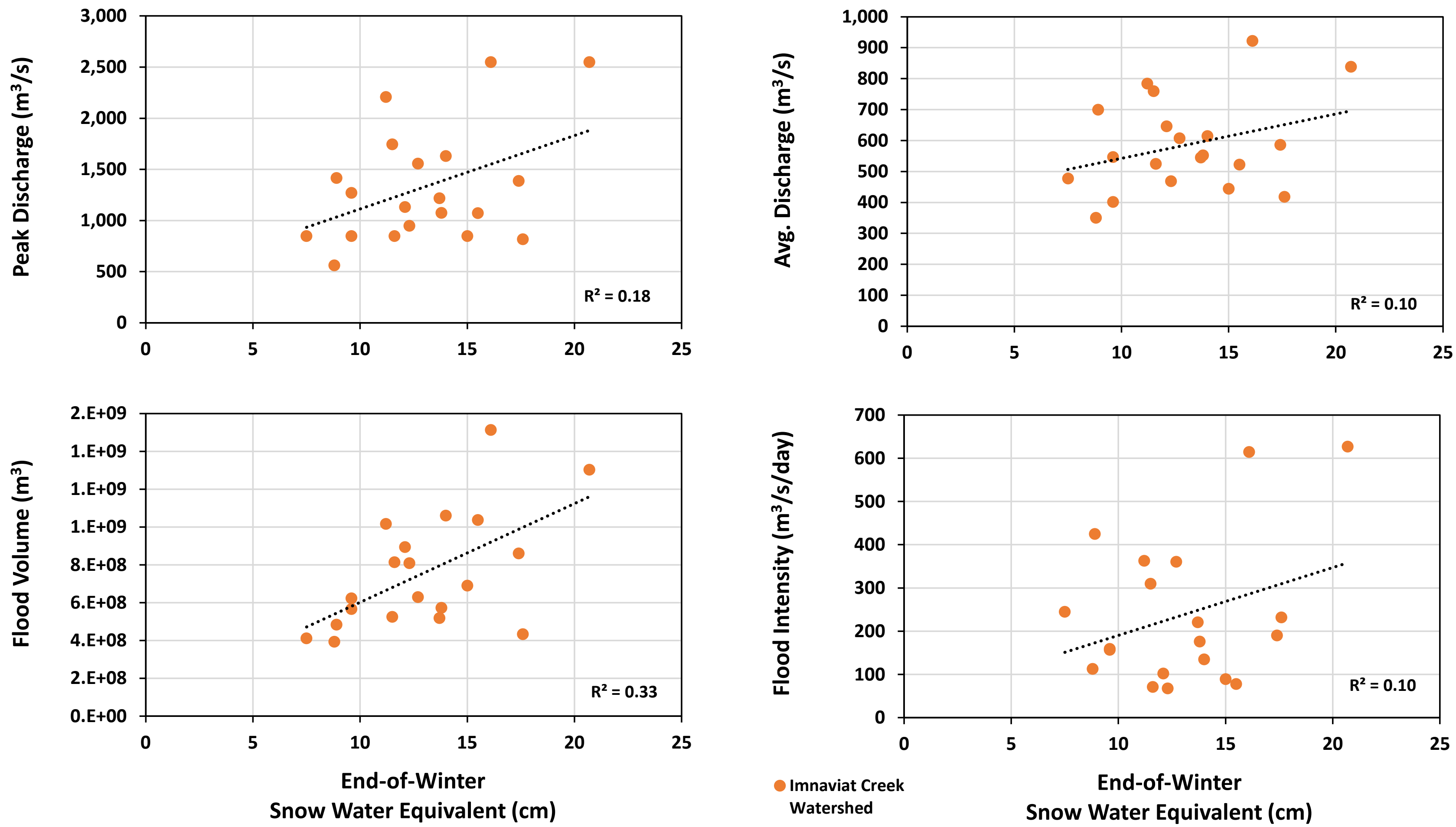

Figure 16. Correlation between end-of-winter SWE (Imnavait Creek Watershed) and streamflow (Kuparuk River)

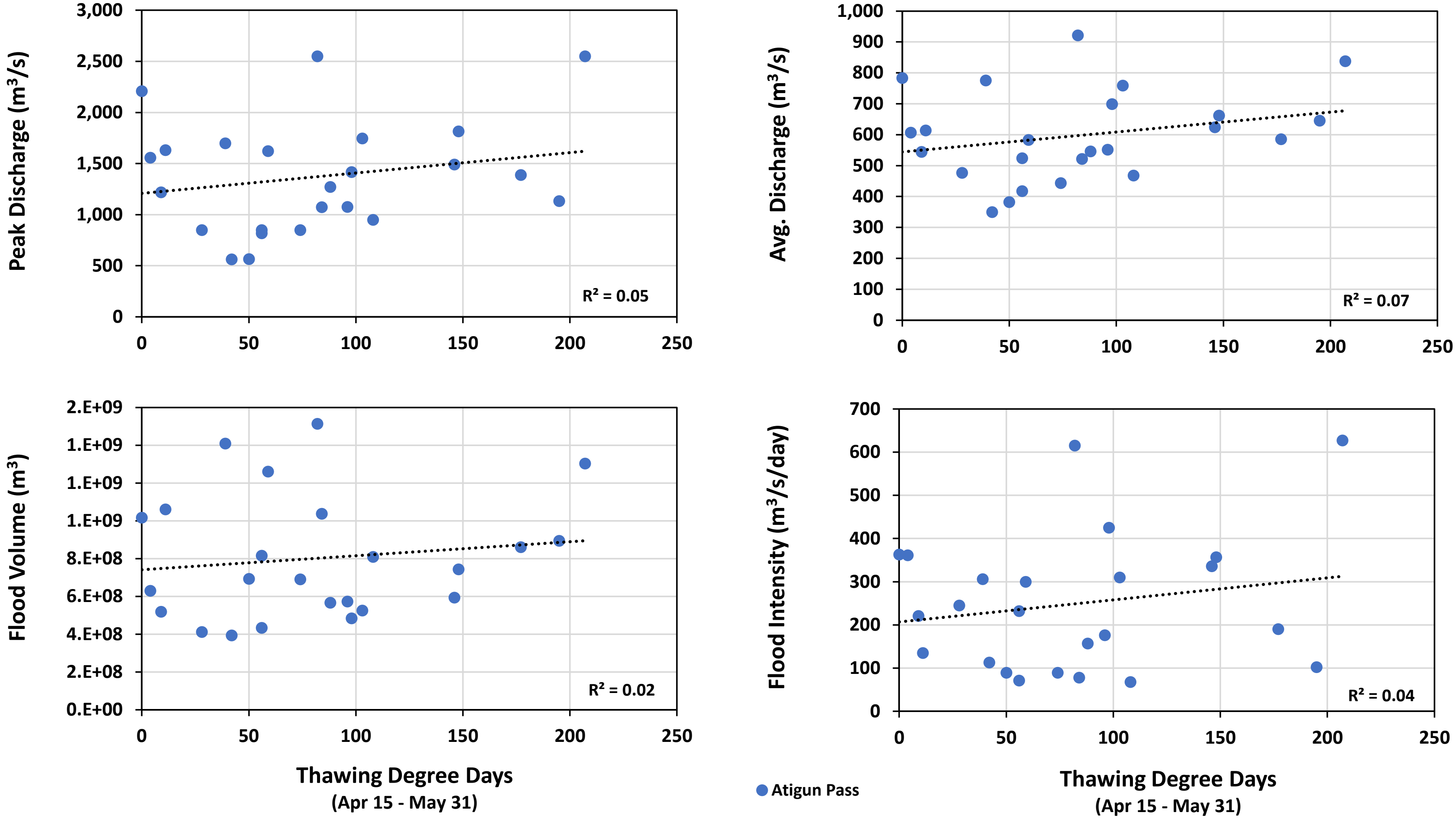

Figure 17. Correlation between TDD (Atigun Pass) and streamflow (Kuparuk River)

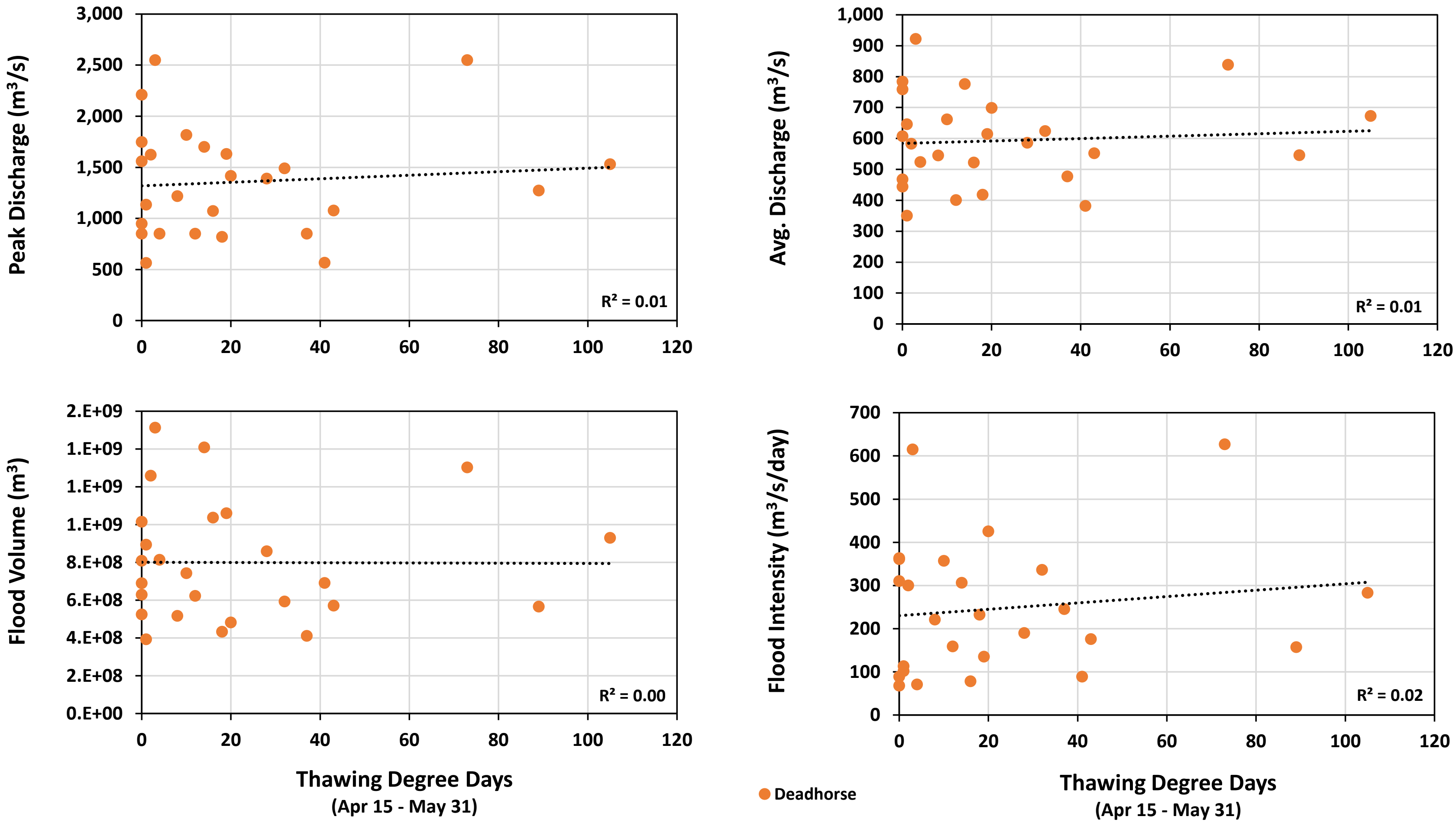

Figure 18. Correlation between TDD (Deadhorse) and streamflow (Kuparuk River)

1.3 Sagavanirktok River Streamflow

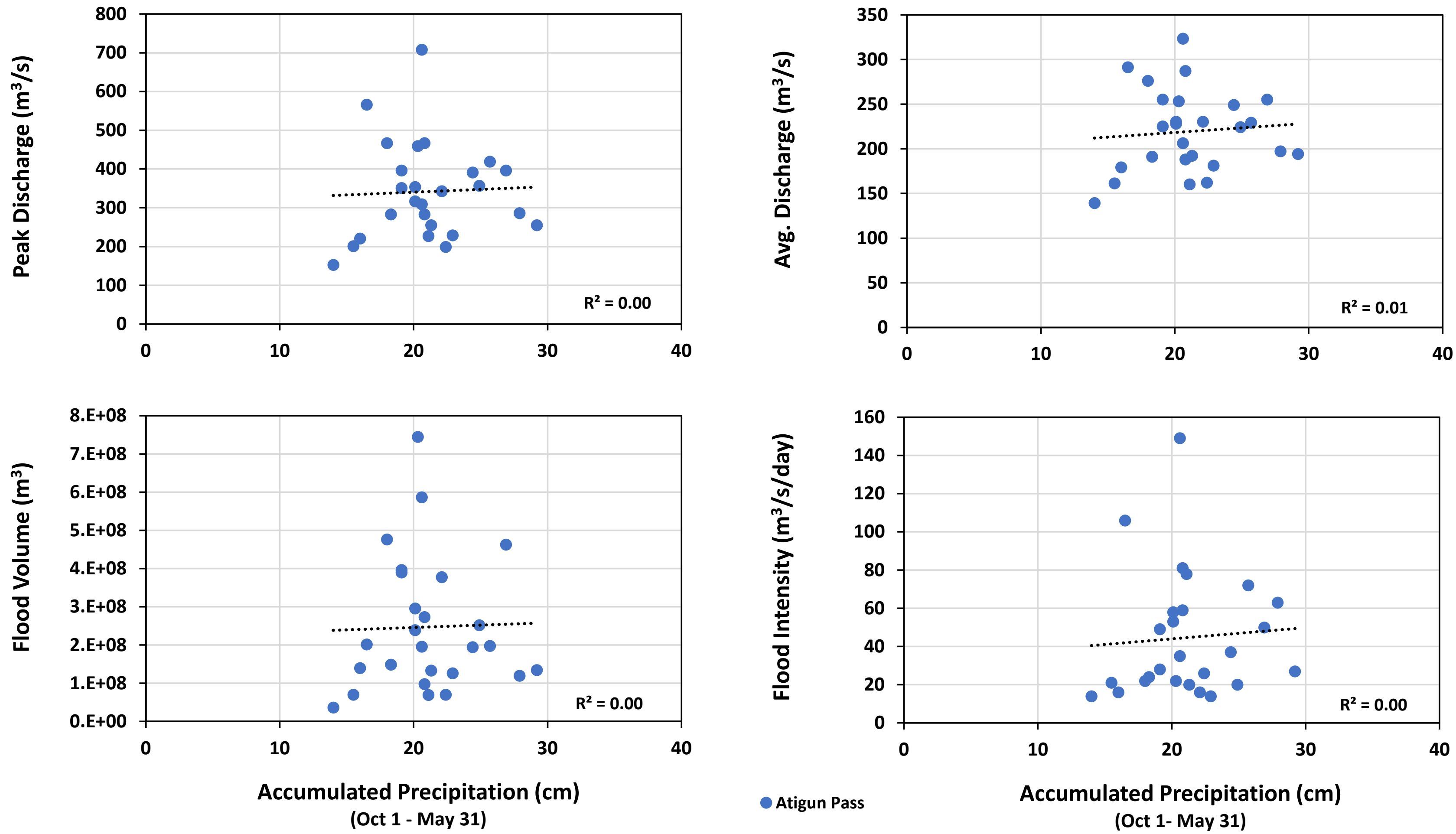

Figure 19. Correlation between precipitation (Atigun Pass) and streamflow (Sagavanirktok River)

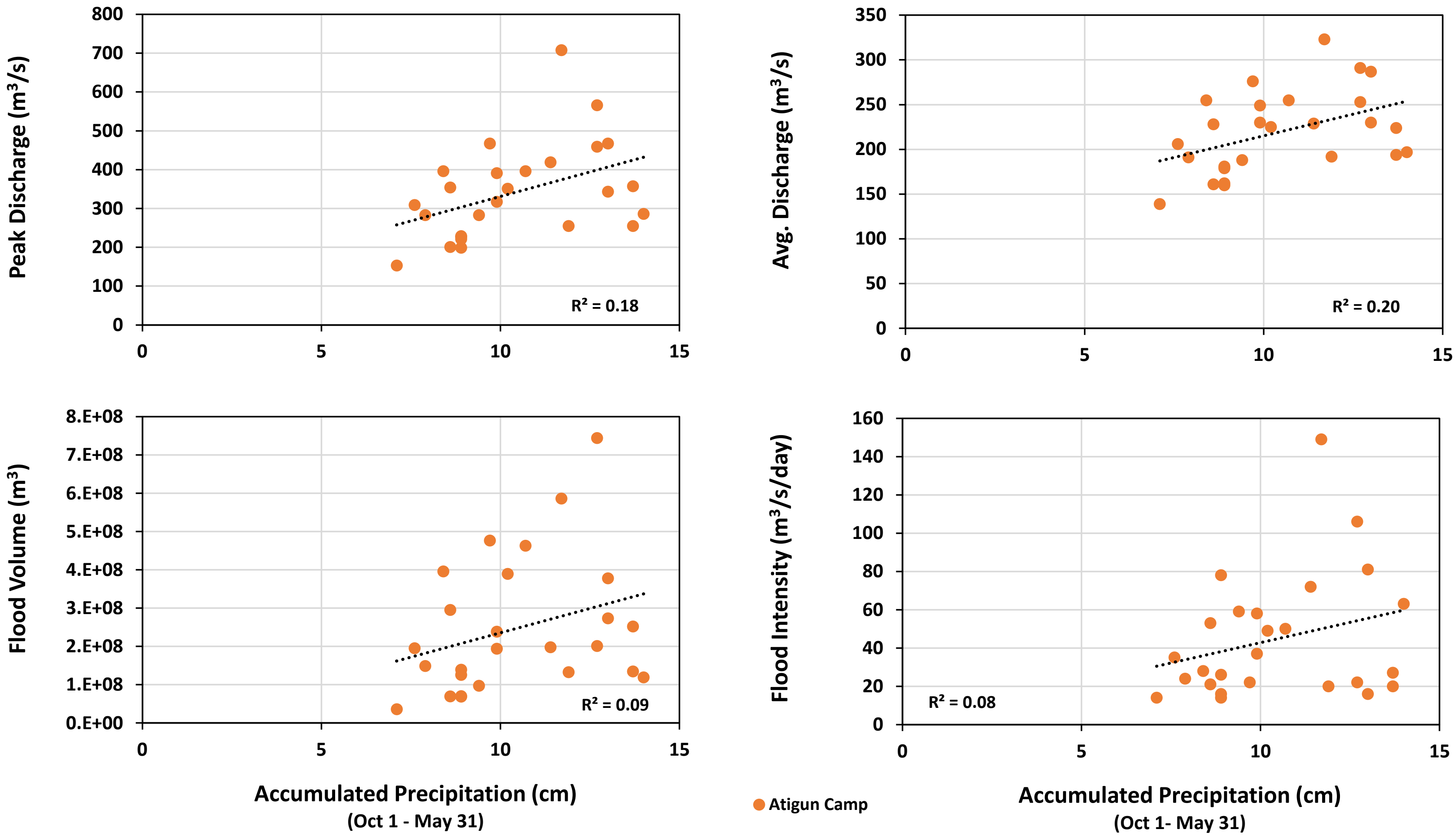

Figure 20. Correlation between precipitation (Atigun Camp) and streamflow (Sagavanirktok River)

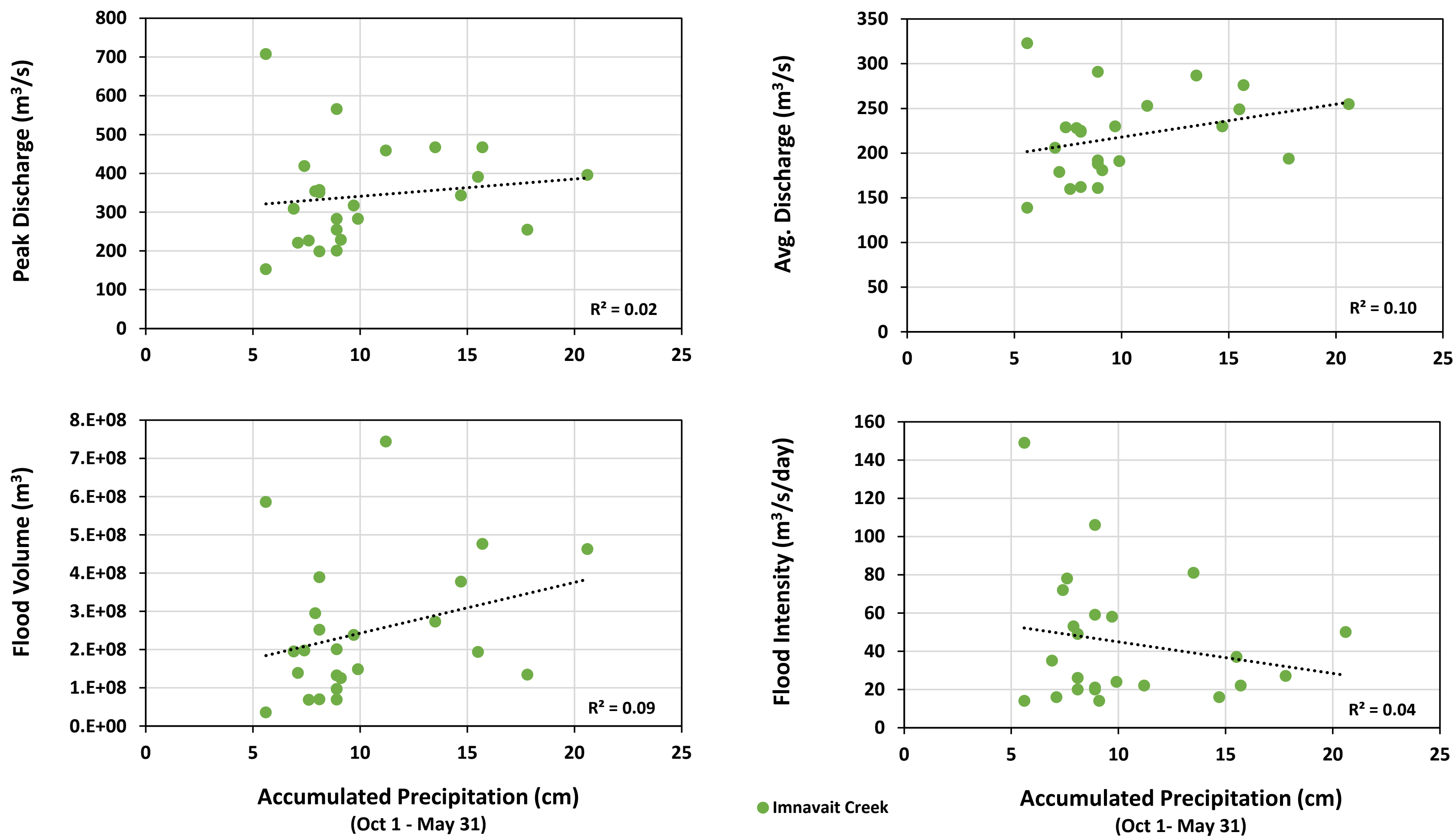

Figure 21. Correlation between precipitation (Imnavait Creek) and streamflow (Sagavanirktok River)

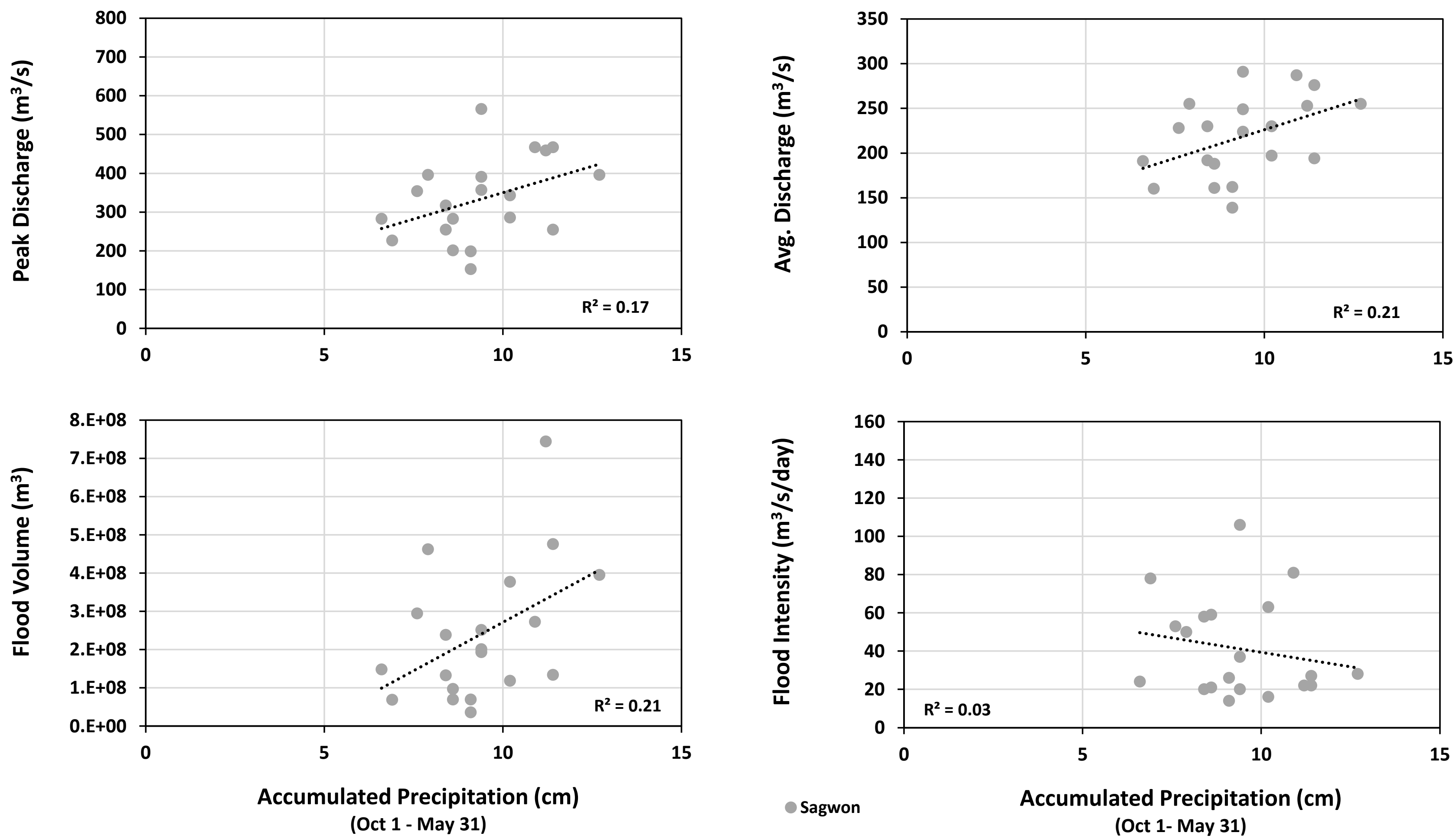

Figure 22. Correlation between precipitation (Sagwon) and streamflow (Sagavanirktok River)

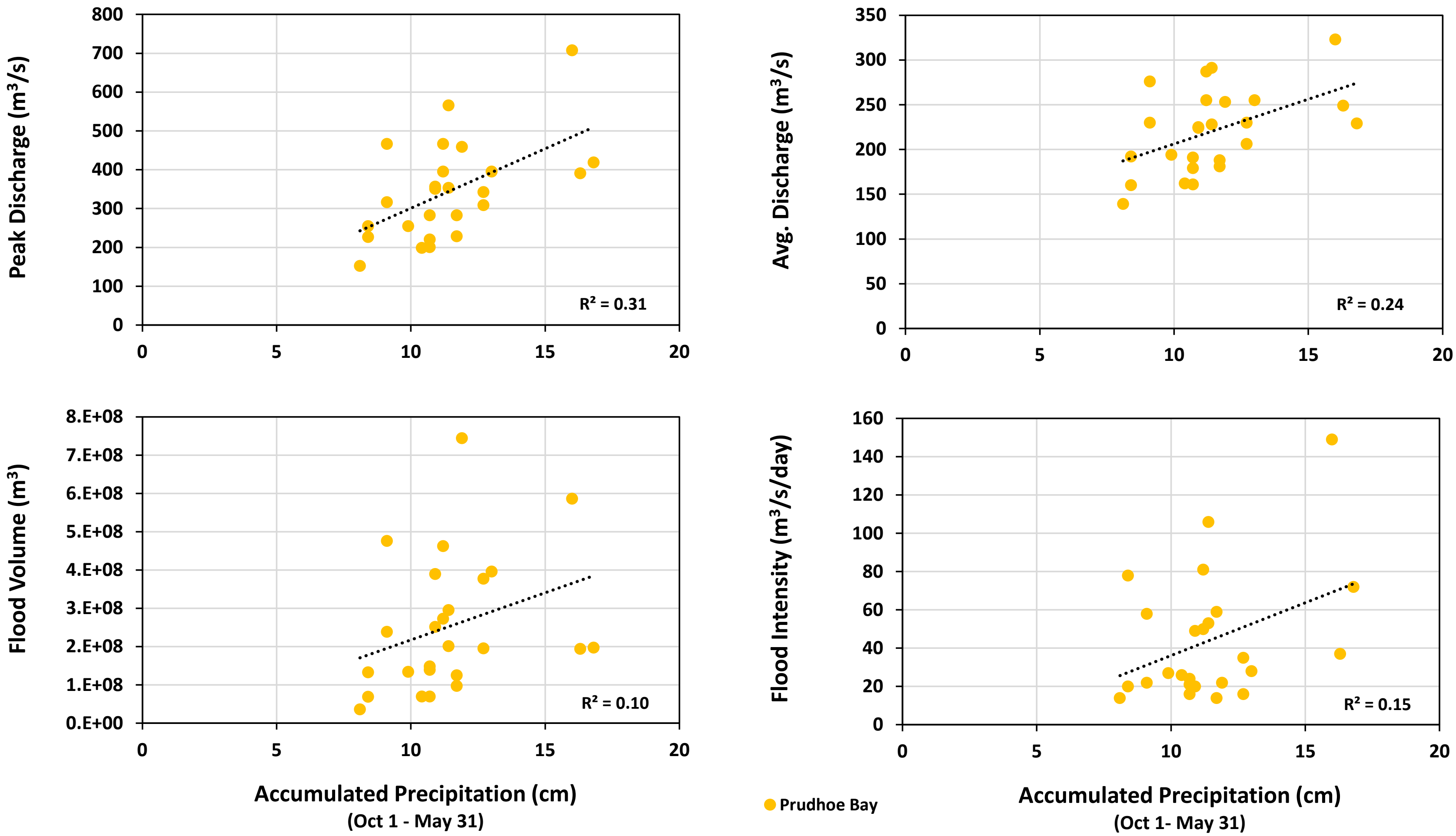

Figure 23. Correlation between precipitation (Prudhoe Bay) and streamflow (Sagavanirktok River)

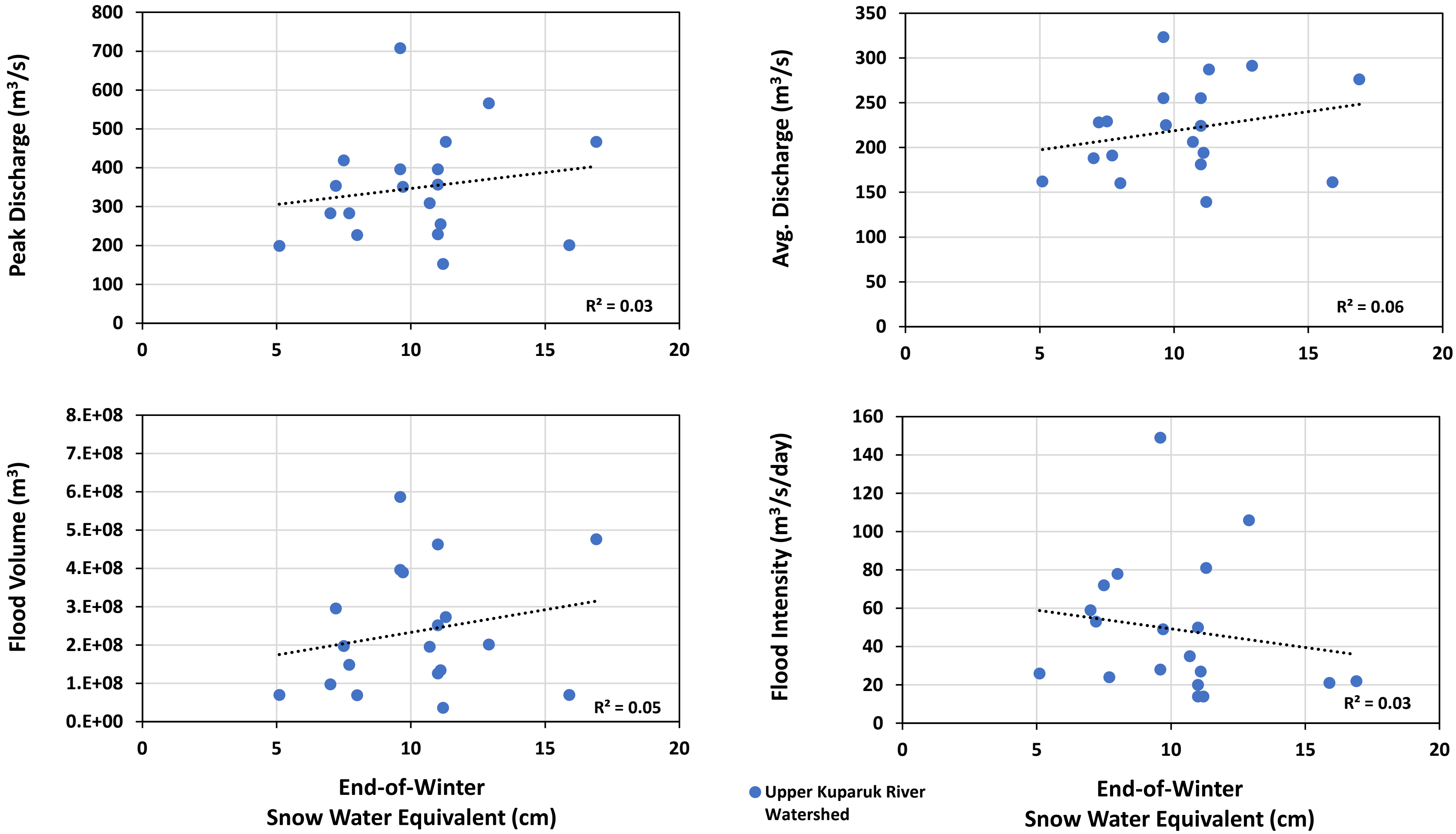

Figure 24. Correlation between end-of-winter SWE (Upper Kuparuk River Watershed) and streamflow (Sagavanirktok River)

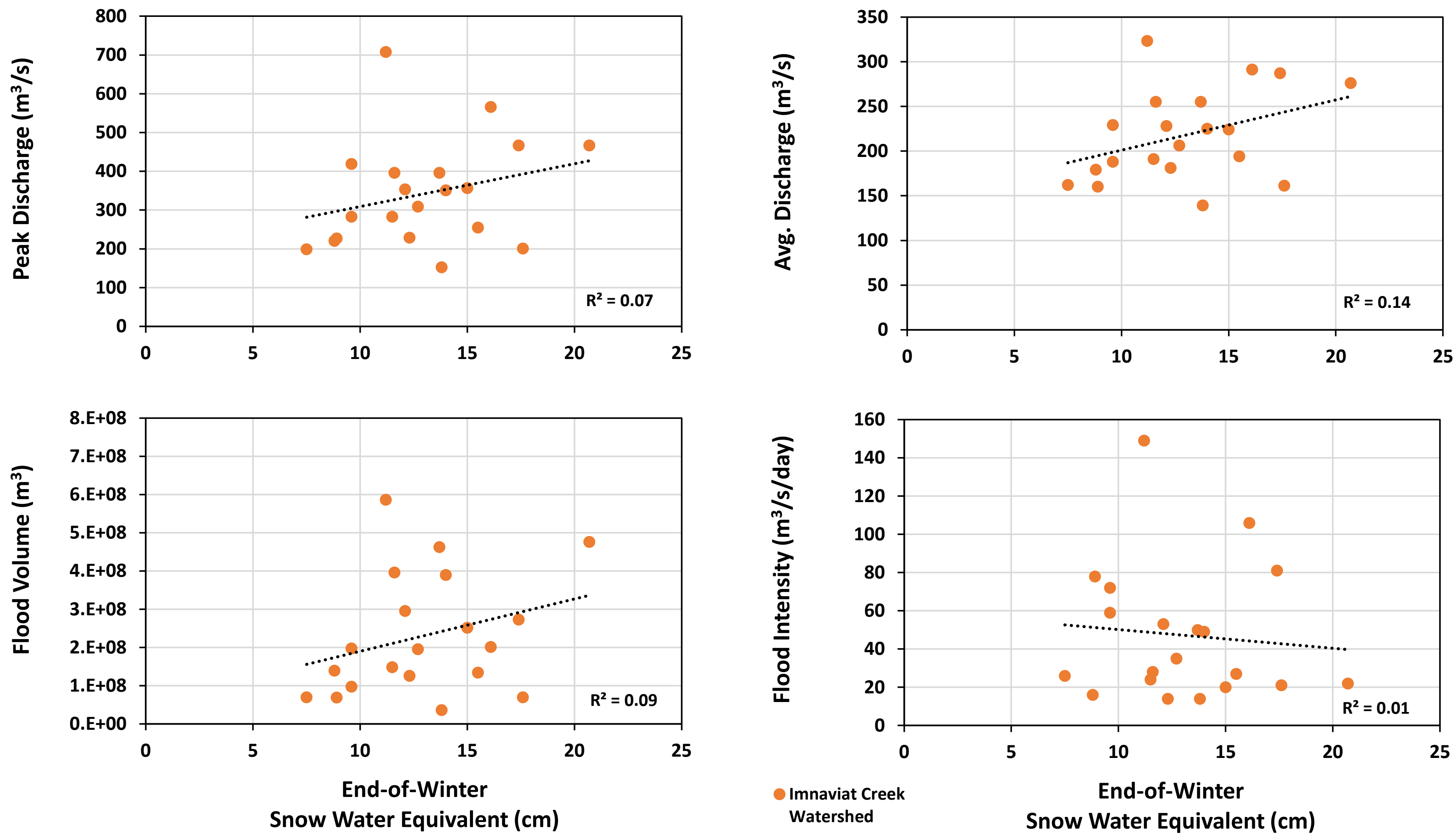

Figure 25. Correlation between end-of-winter SWE (Imnavait Creek Watershed) and streamflow (Sagavanirktok River)

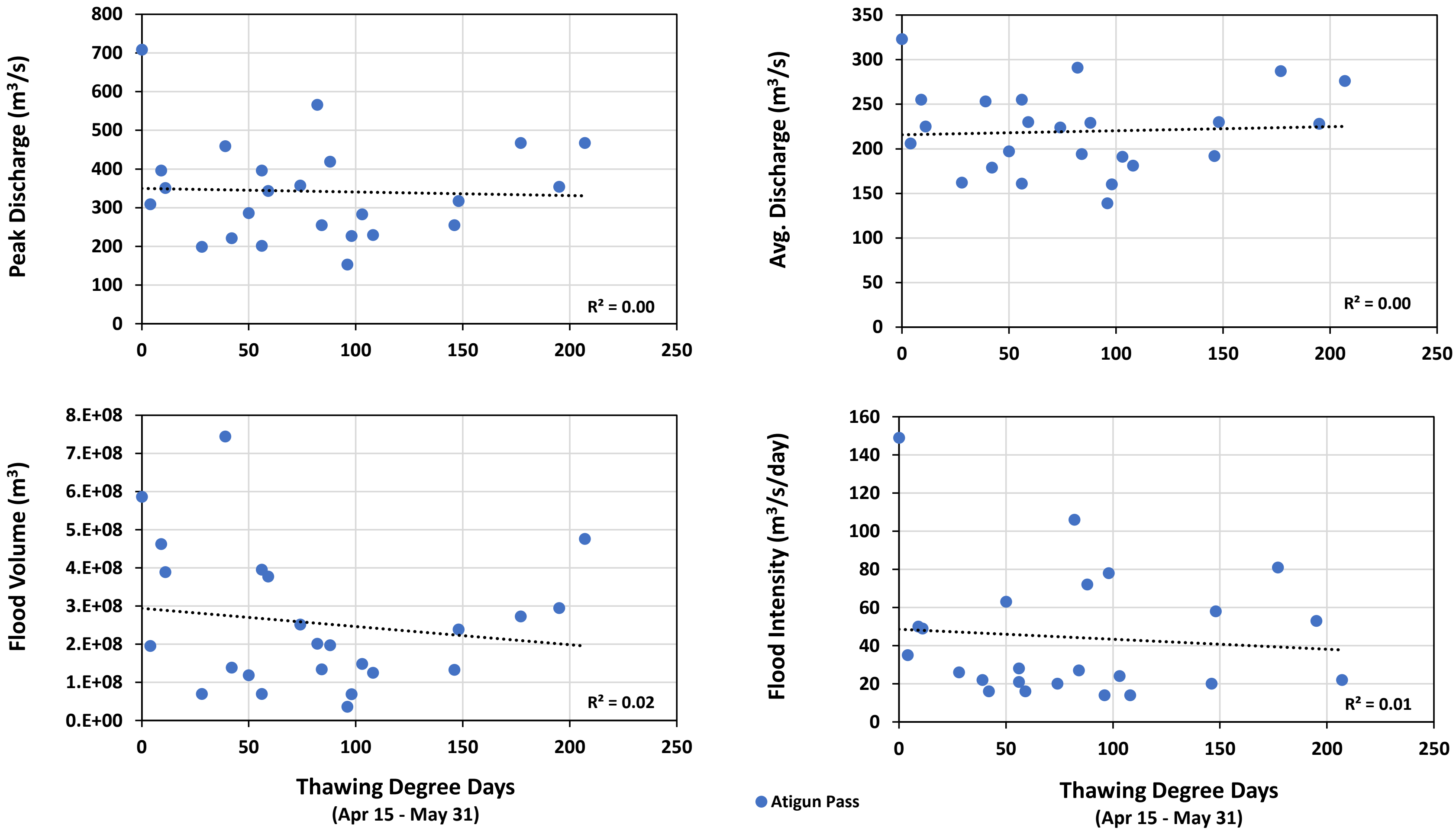

Figure 26. Correlation between TDD (Atigun Pass) and streamflow (Sagavanirktok River)

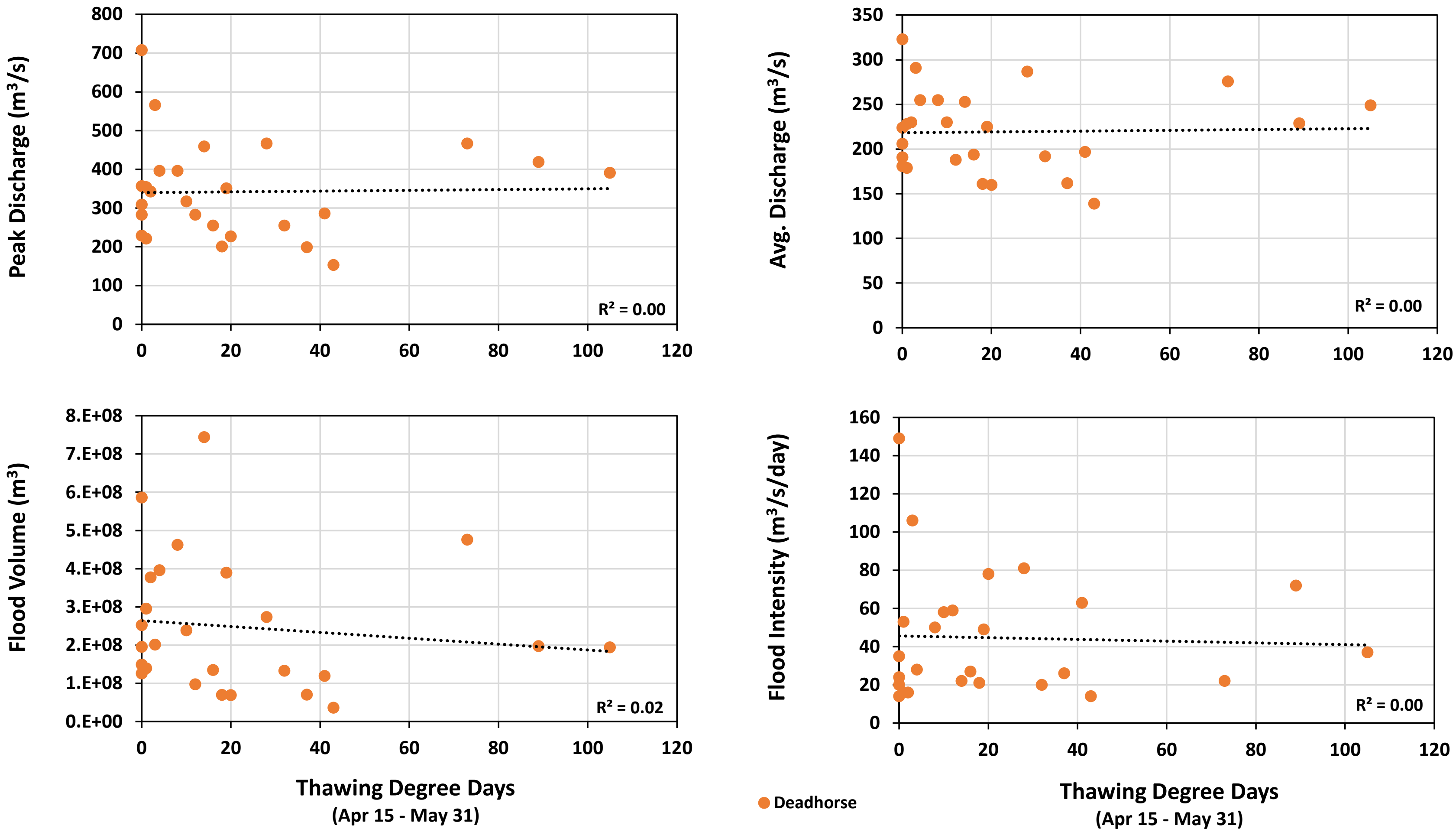

Figure 27. Correlation between TDD (Deadhorse) and streamflow (Sagavanirktok River)

1.4 Precipitation

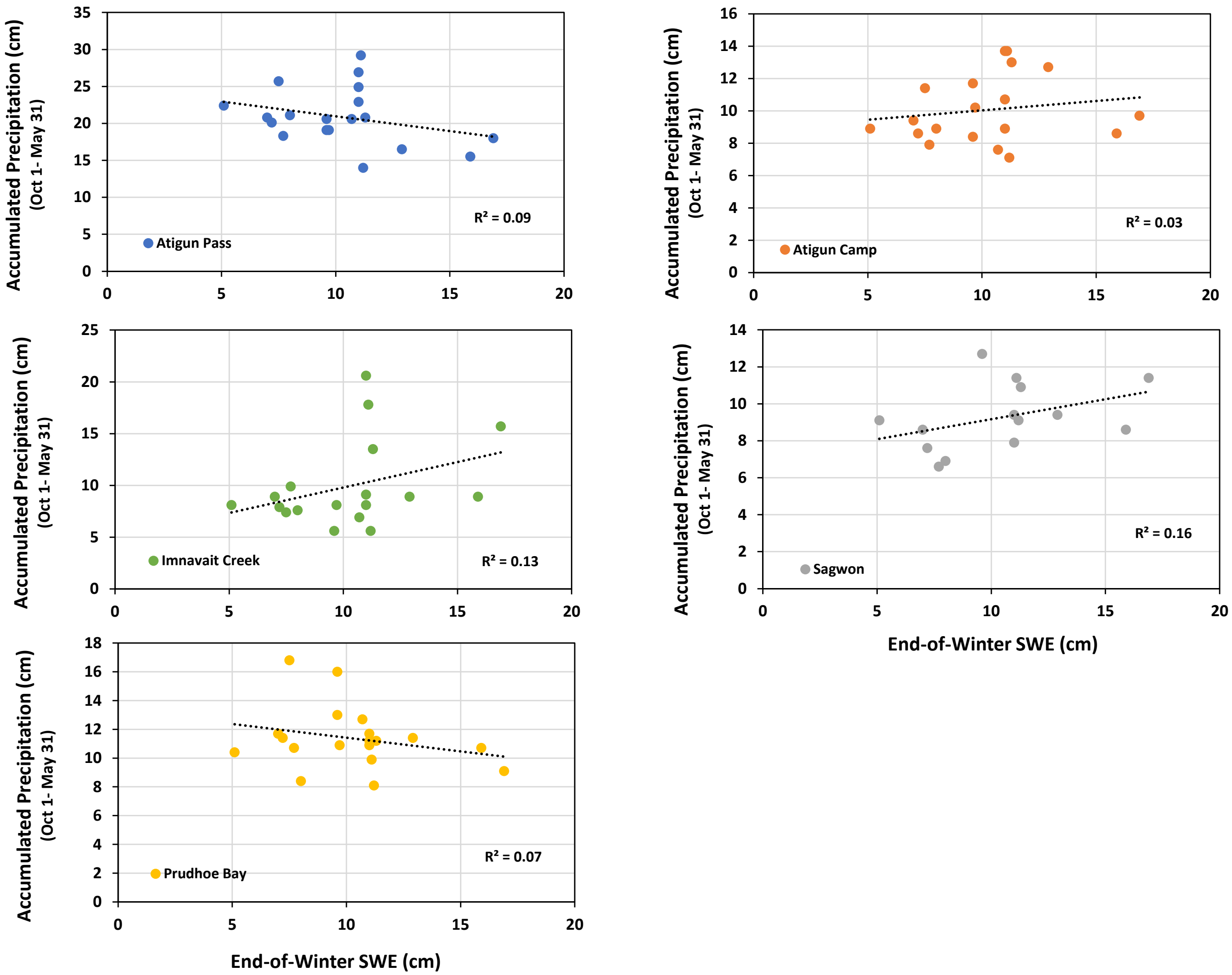

Figure 28. Correlation between precipitation and end-of-winter SWE (Upper Kuparuk River Watershed)

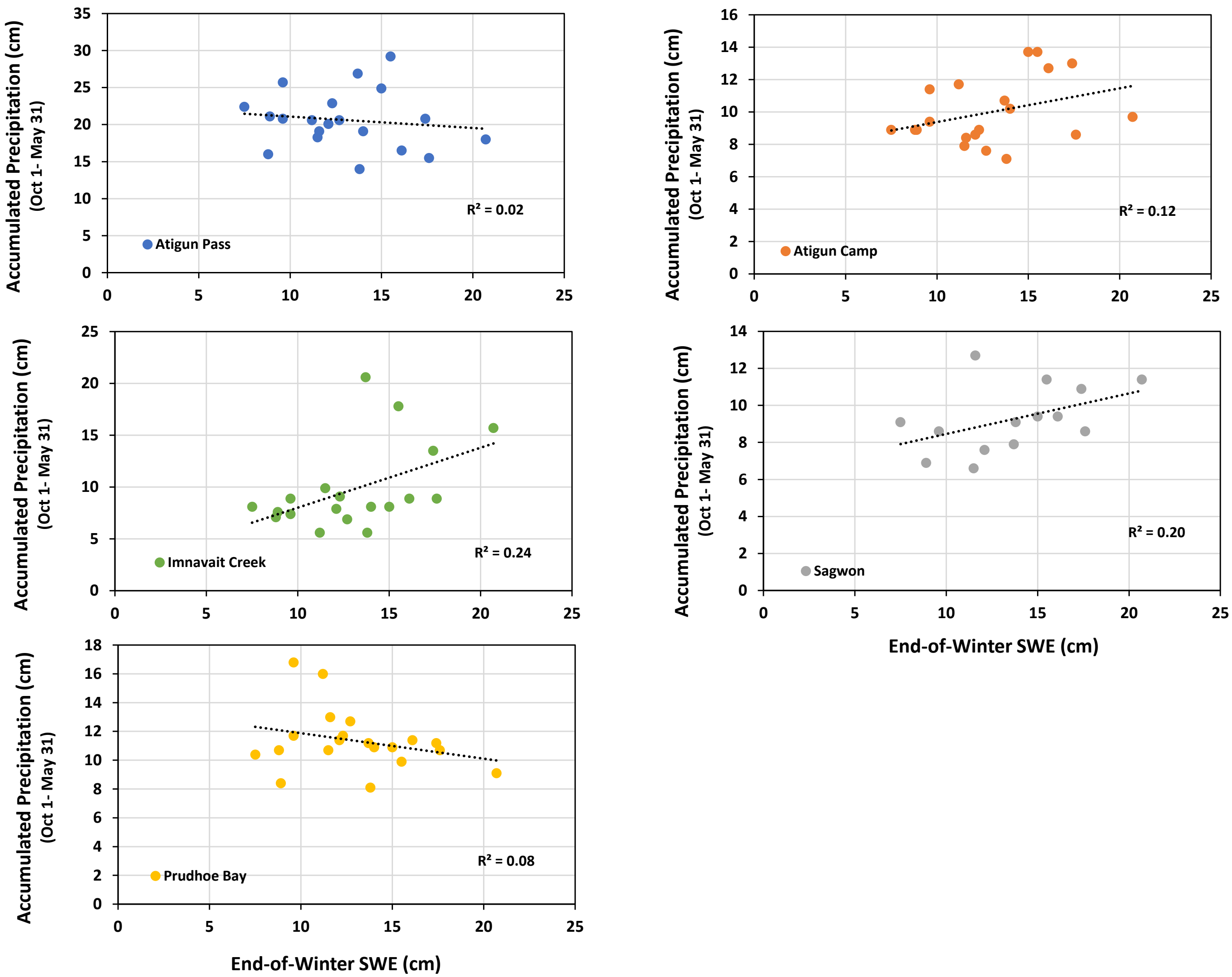

Figure 29. Correlation between precipitation and end-of-winter SWE (Imnavait Creek Watershed)

2 Correlation between Environmental Parameters and Overflood Area (by River)

2.1 Colville River

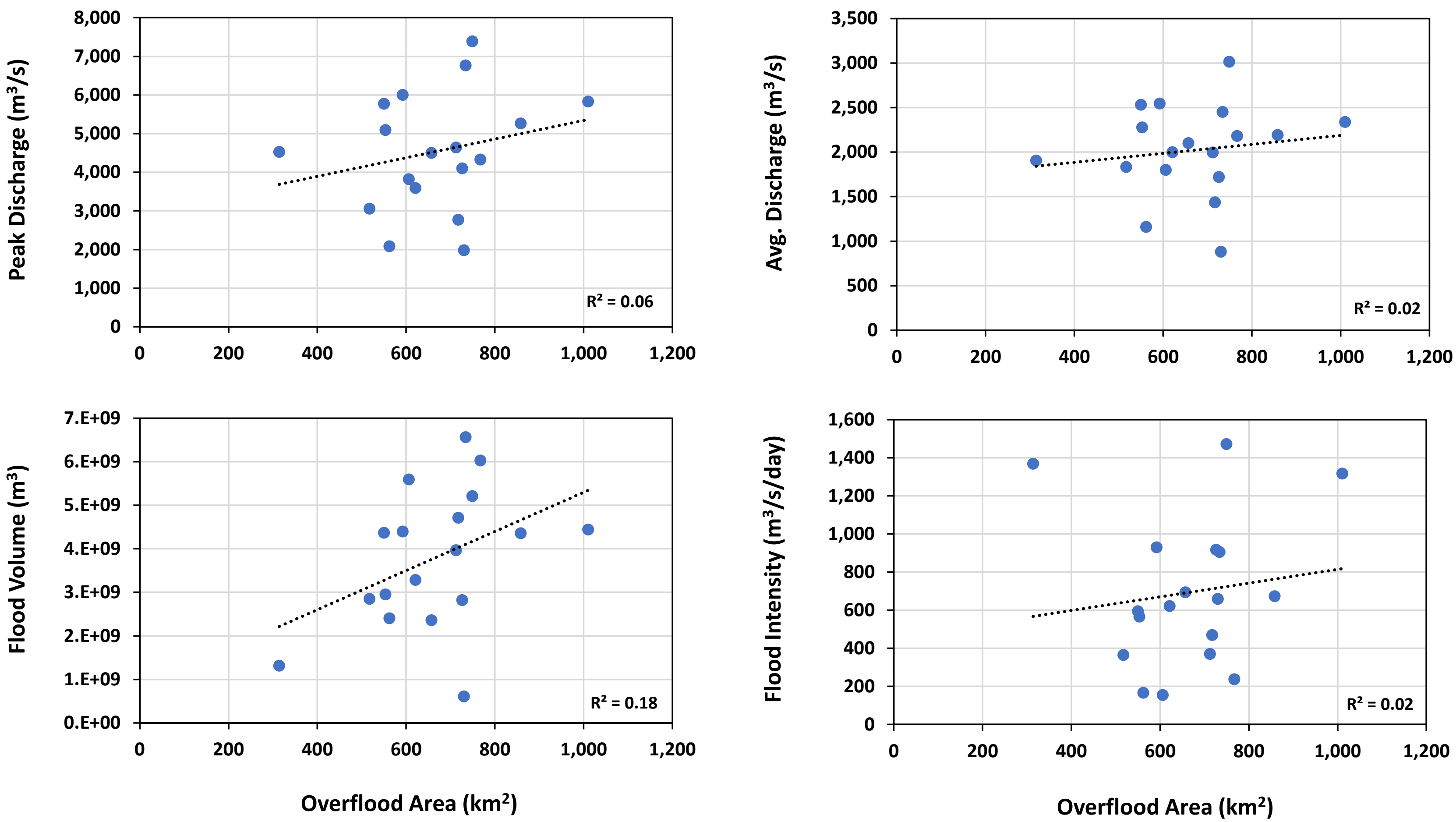

Figure 30. Correlation between streamflow (Colville River) and overflood area (Colville River)

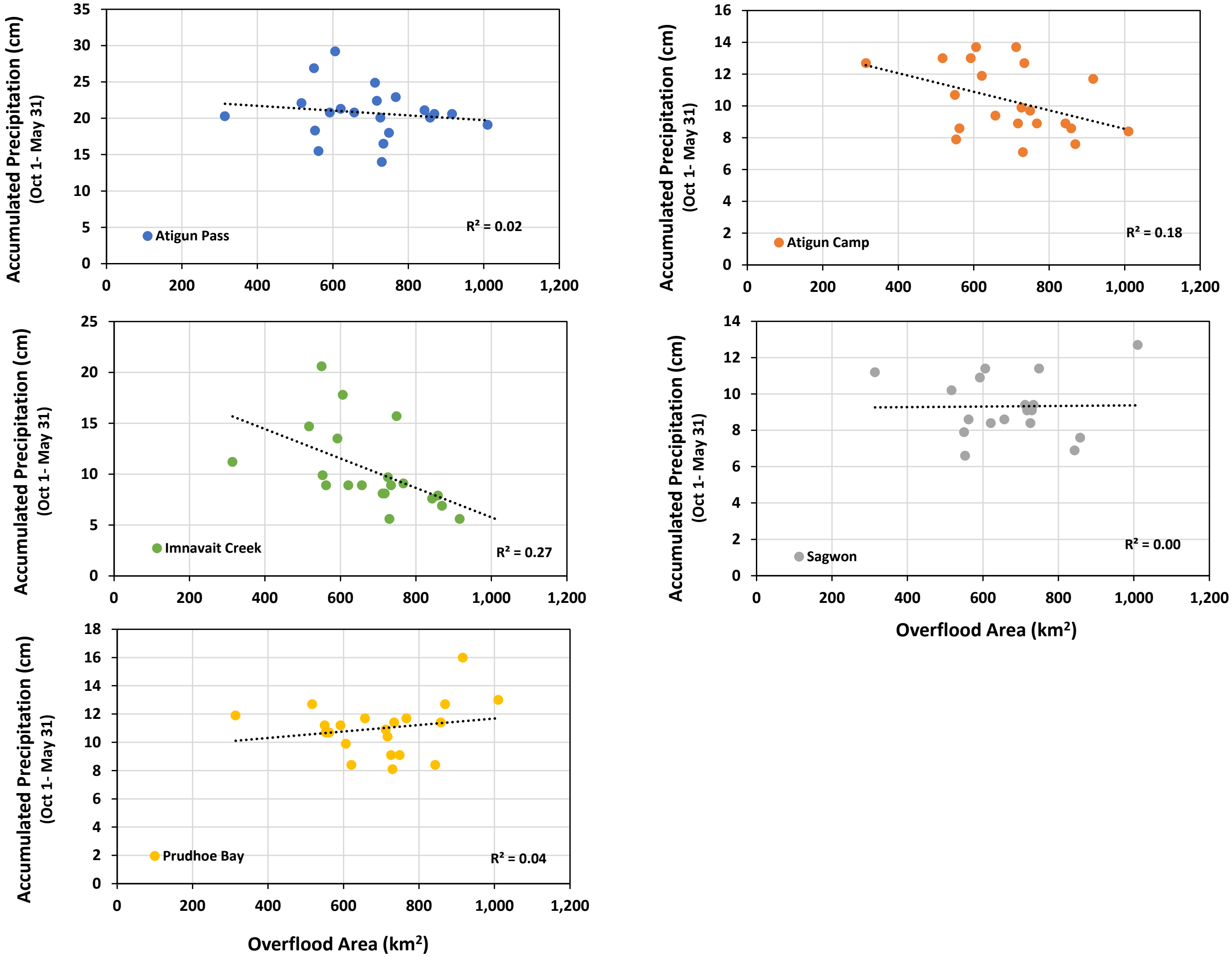

Figure 31. Correlation between precipitation and overflood area (Colville River)

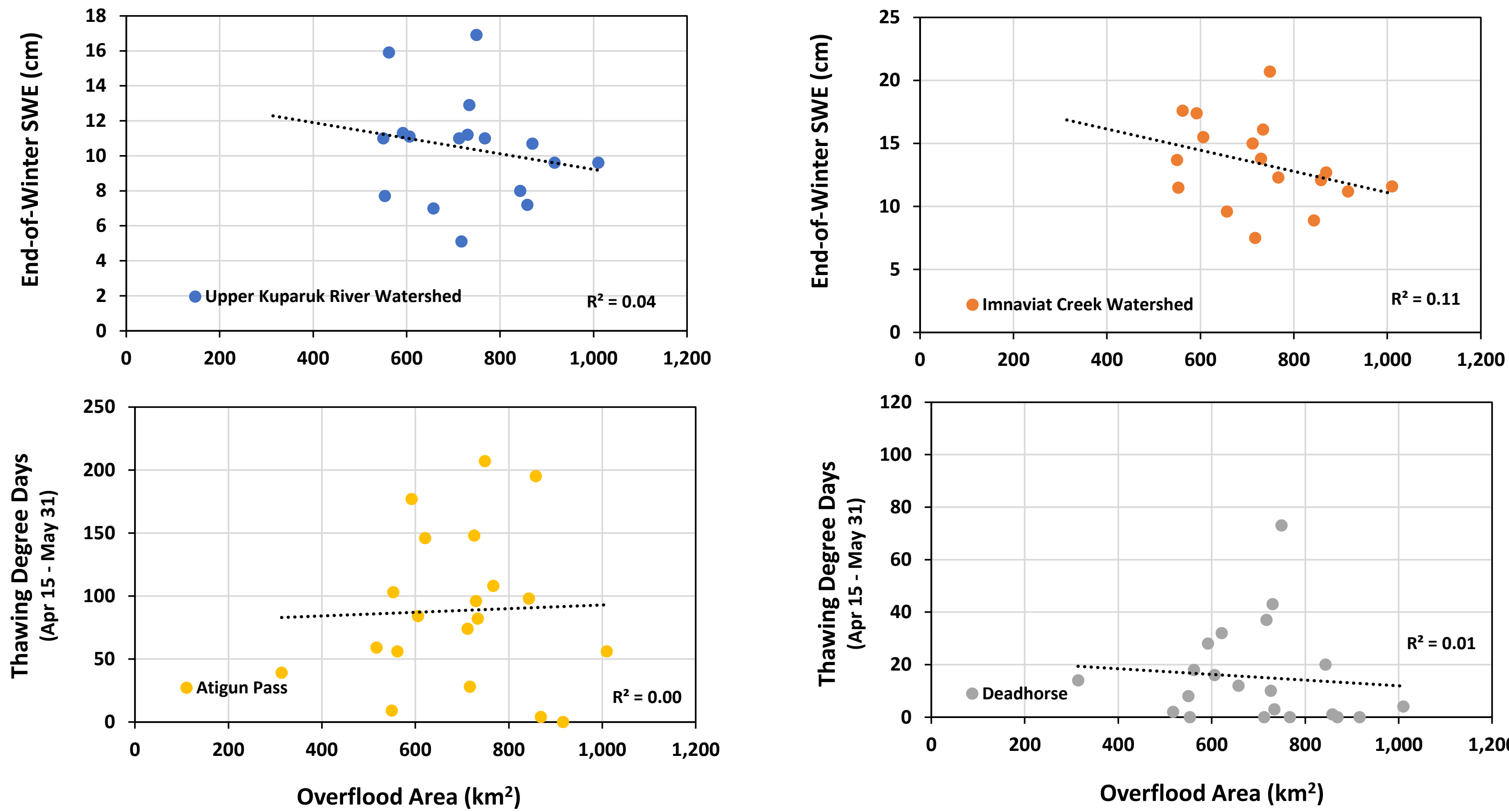

Figure 32. Correlation between end-of-winter SWE, TDD, and overflood area (Colville River)

2.2 Kuparuk River

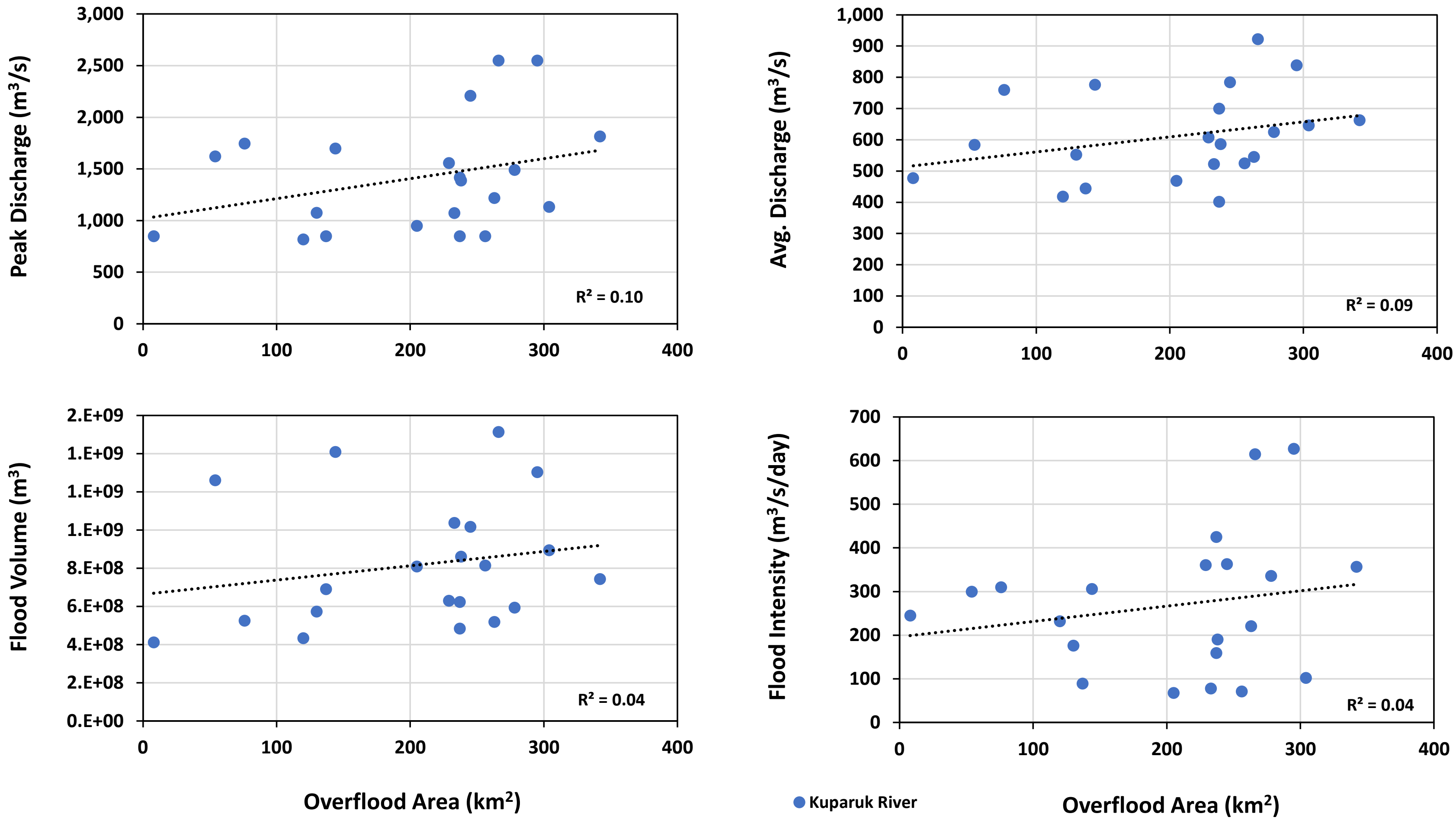

Figure 33. Correlation between streamflow (Kuparuk River) and overflood area (Kuparuk River)

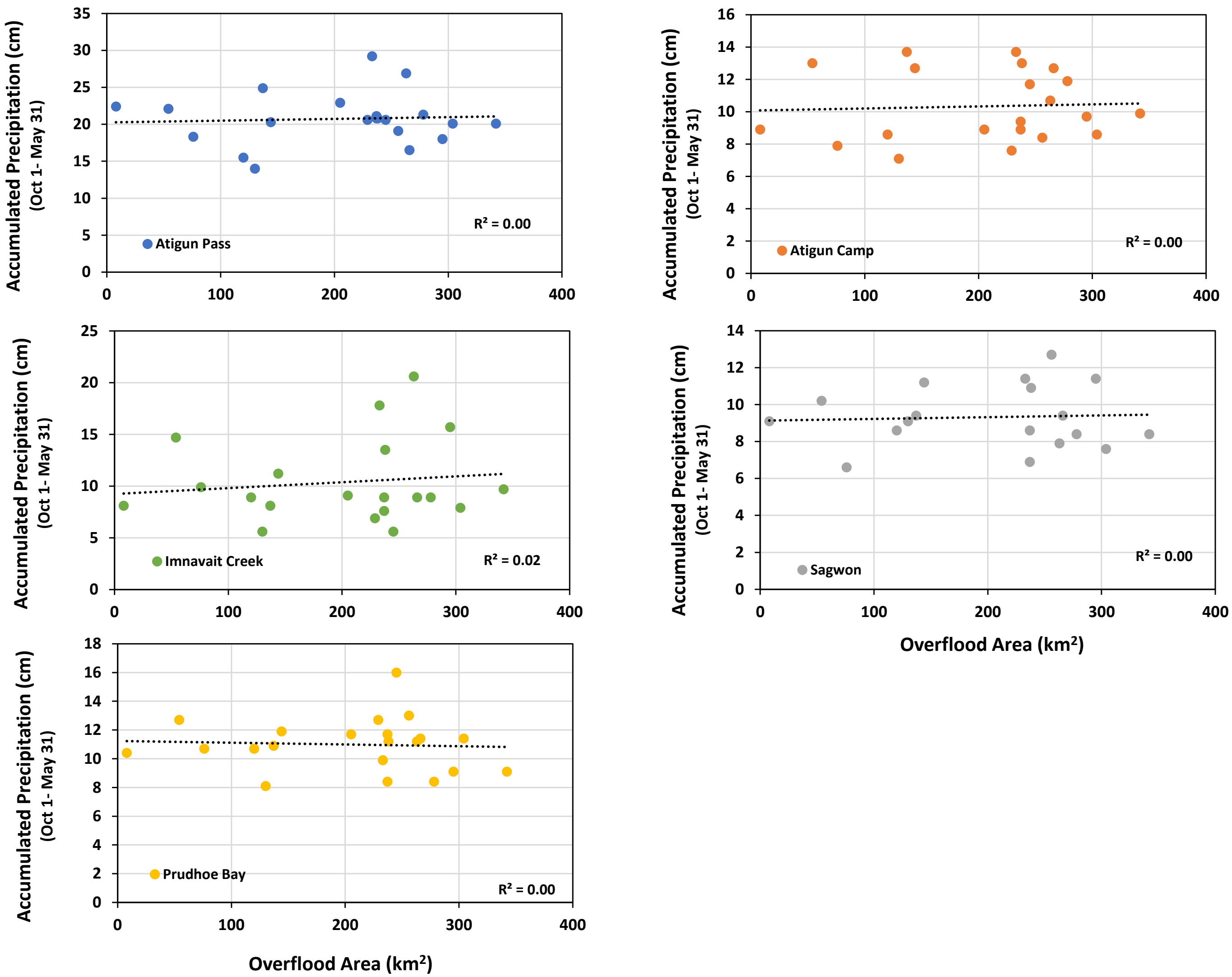

Figure 34. Correlation between precipitation and overflood area (Kuparuk River)

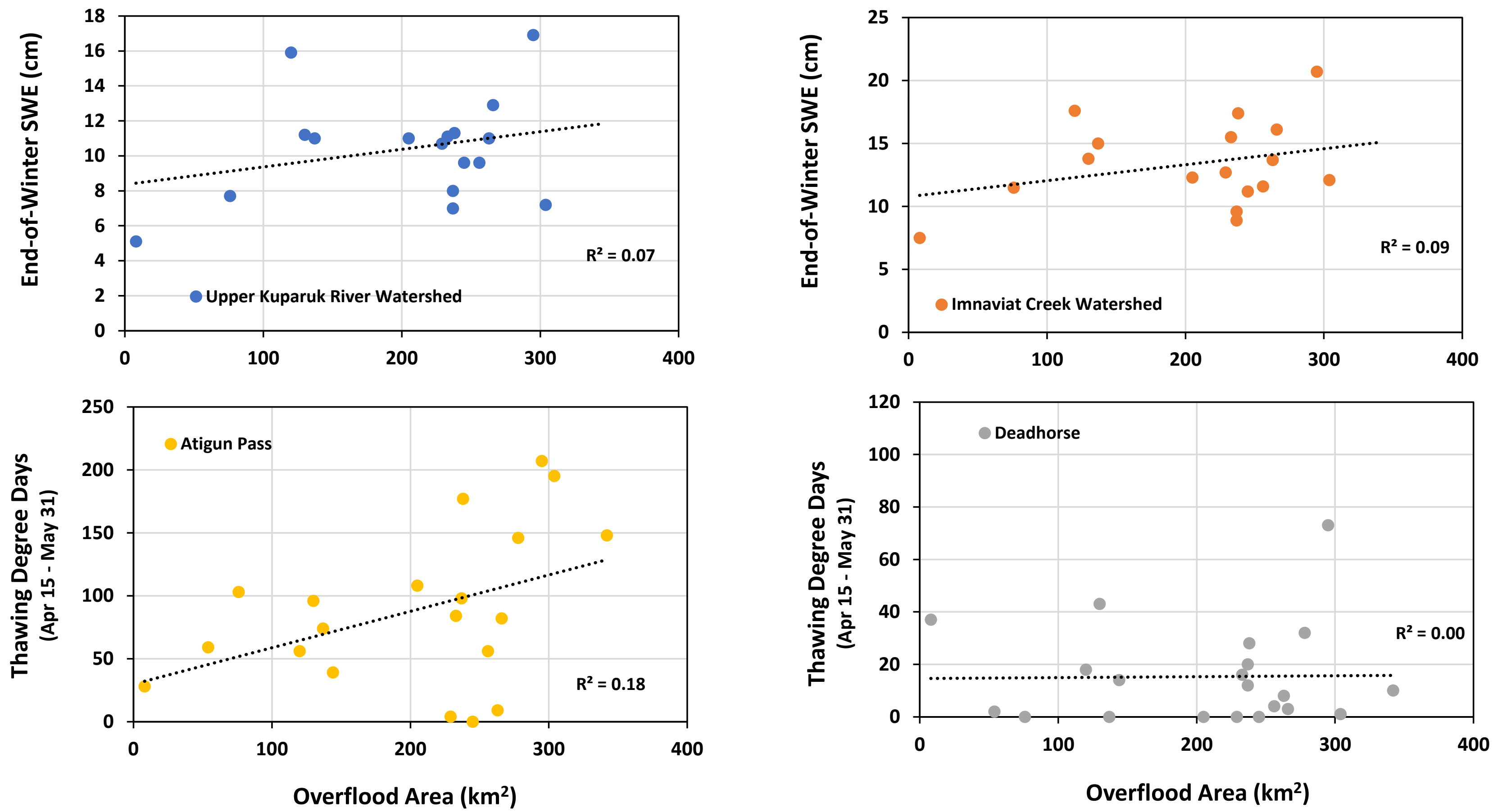

Figure 35. Correlation between end-of-winter SWE, TDD, and overflood area (Kuparuk River)

2.3 Sagavanirktok River

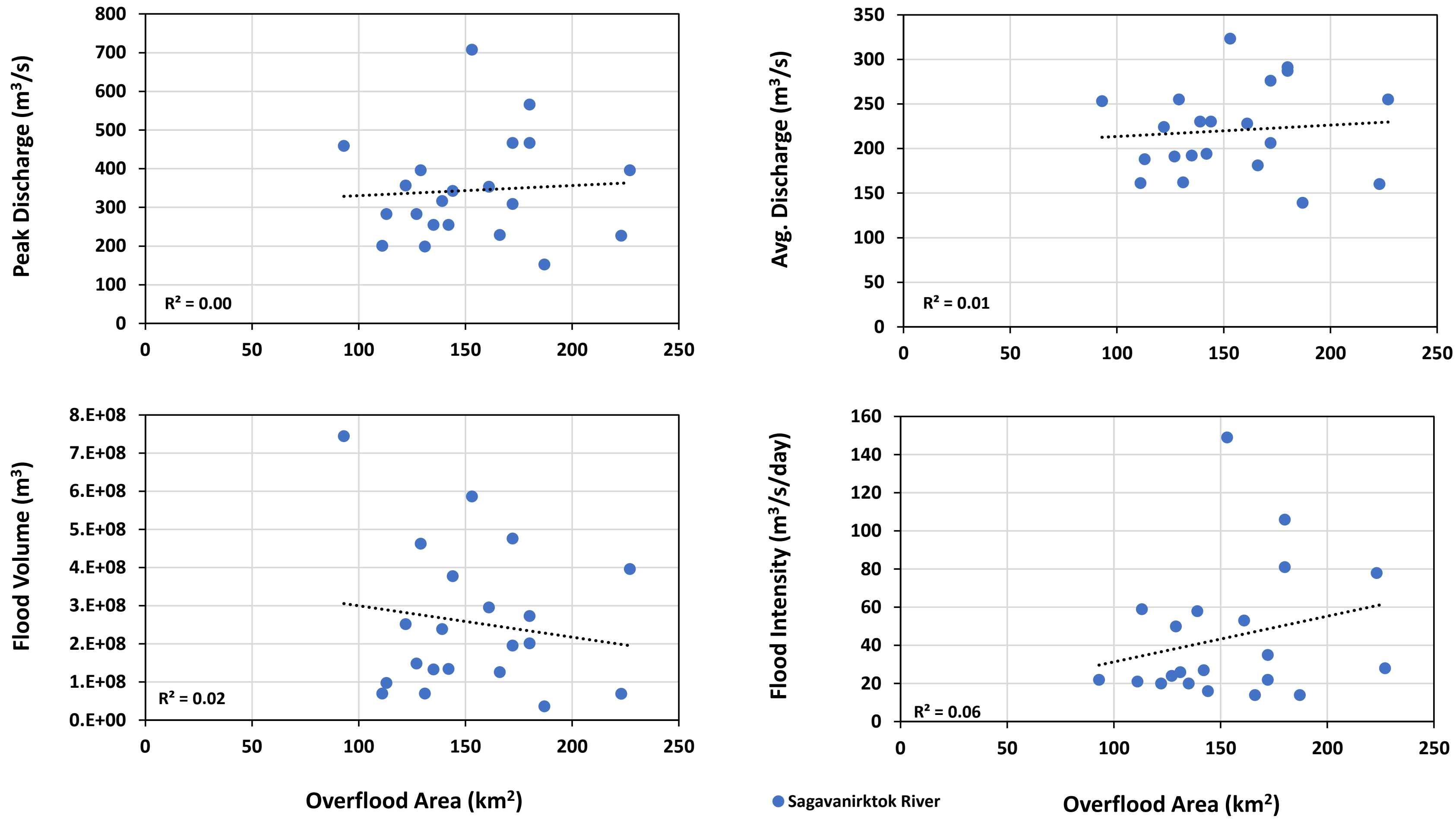

Figure 36. Correlation between streamflow (Sagavanirktok River) and overflood area (Sagavanirktok River)

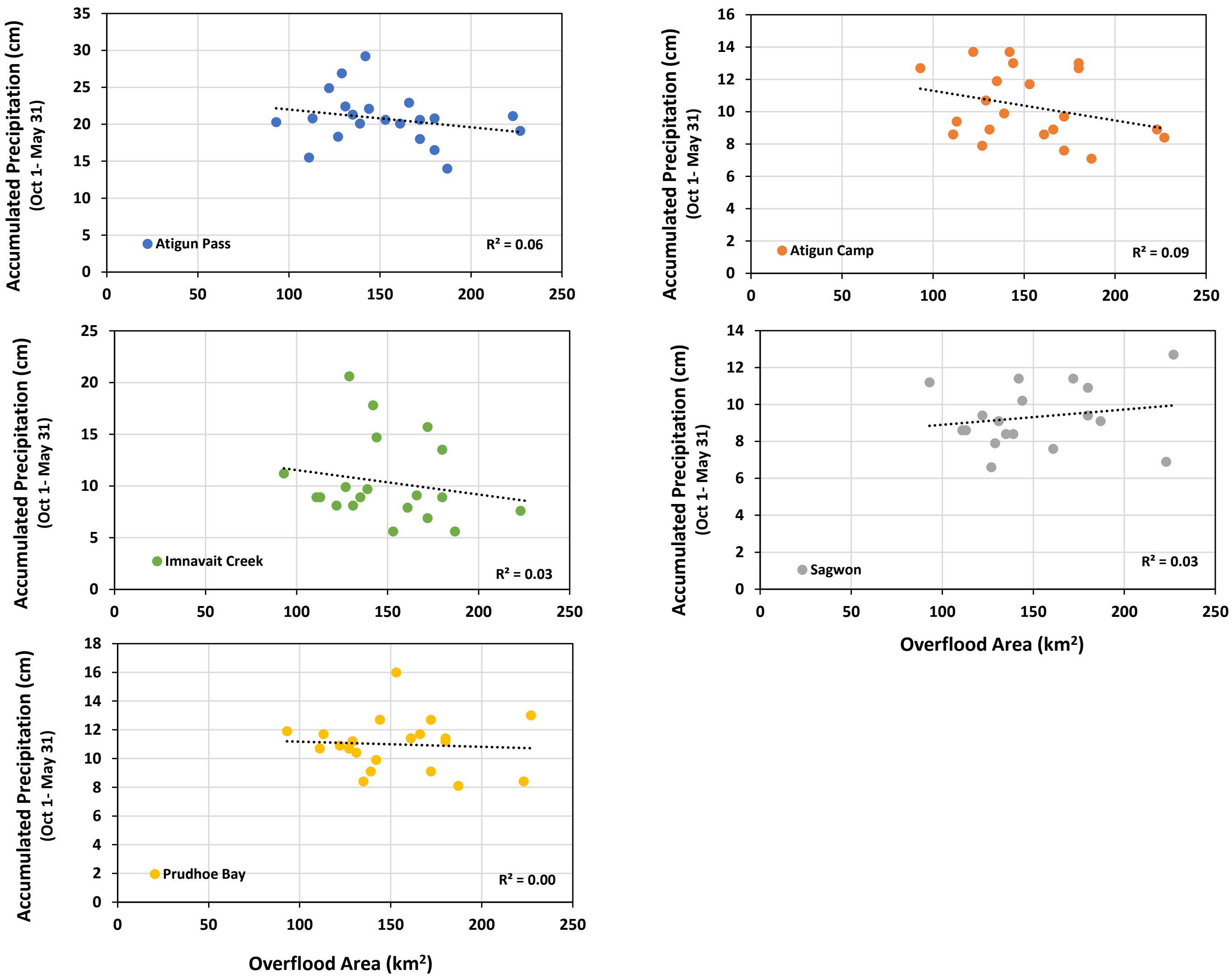

Figure 37. Correlation between precipitation and overflood area (Sagavanirktok River)

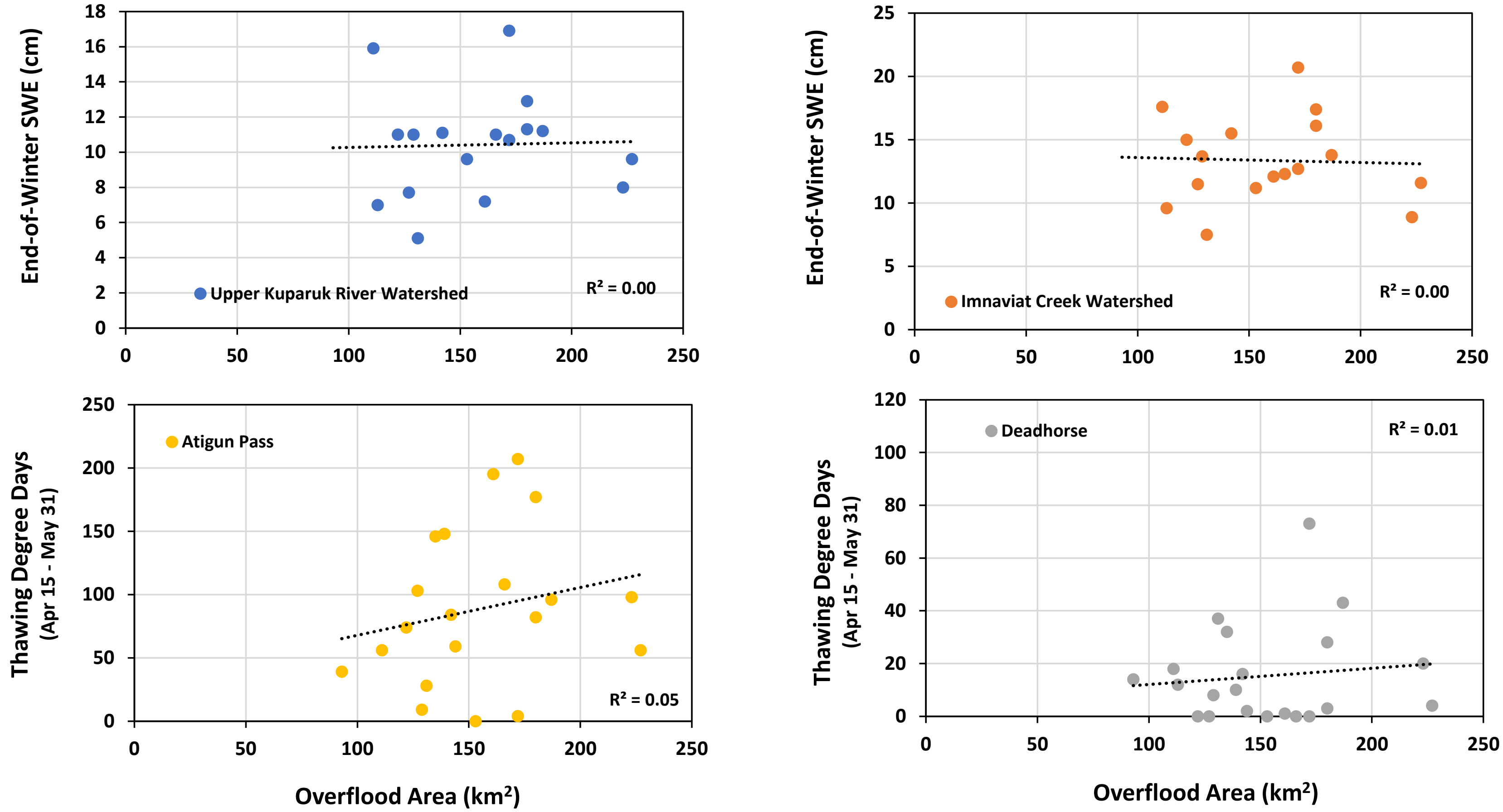

Figure 38. Correlation between end-of-winter SWE, TDD, and overflood area (Sagavanirktok River)

3 Correlation between Environmental Parameters and Overflood Area (by WBD)

3.1 Lower Colville River WBD

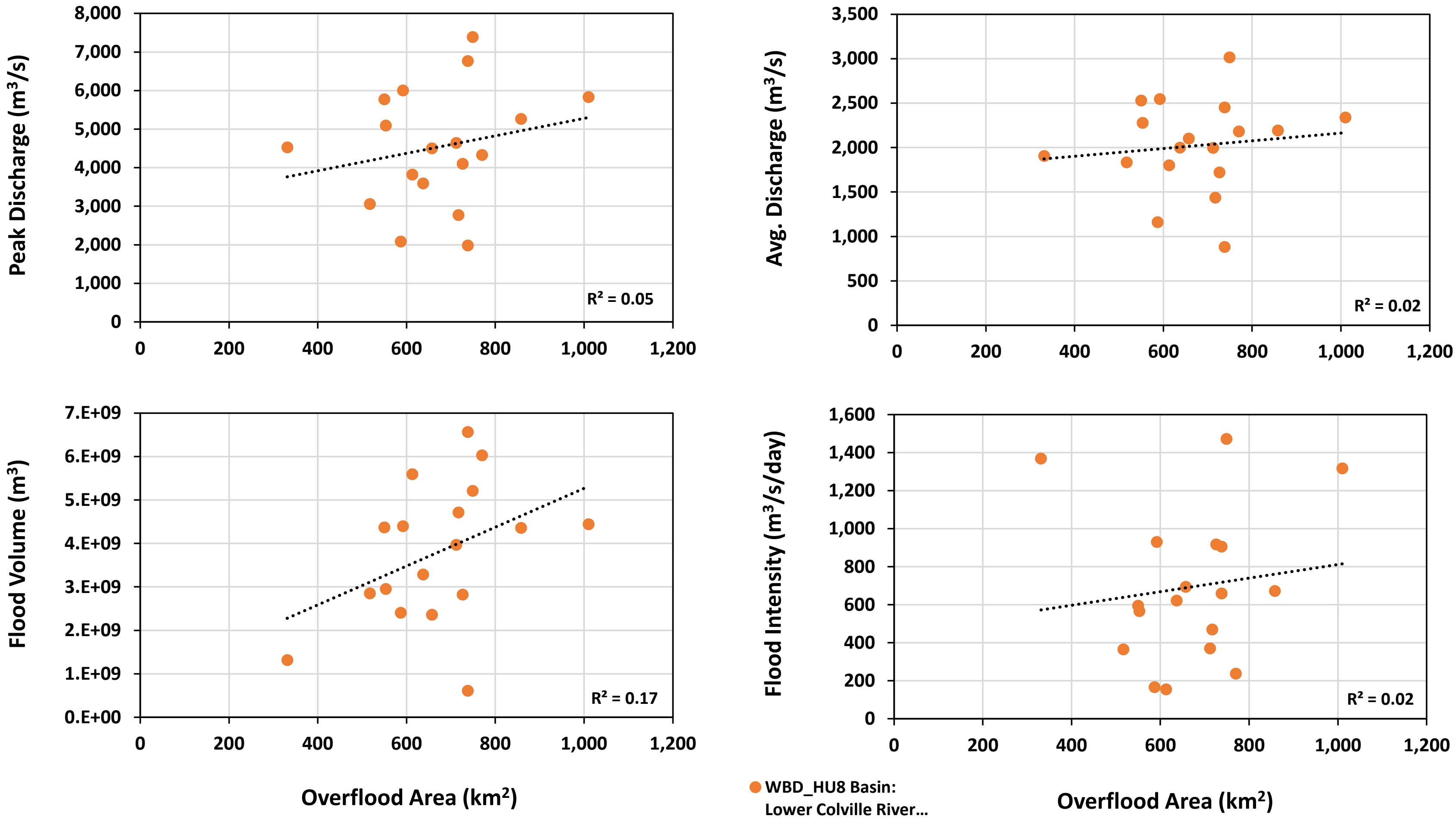

Figure 39. Correlation between streamflow (Colville River) and overflood area (Lower Colville River WBD)

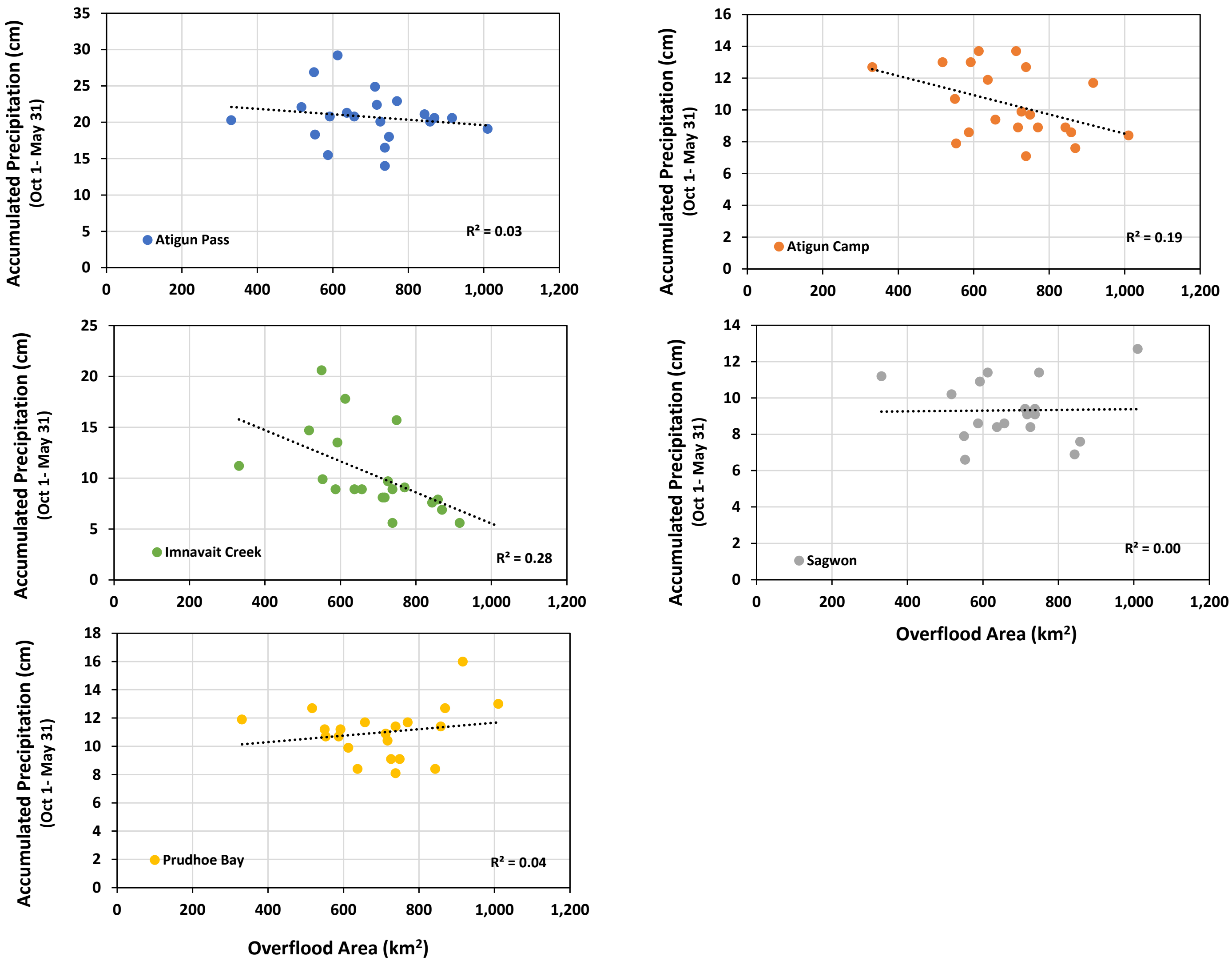

Figure 40. Correlation between precipitation and overflood area (Lower Colville River WBD)

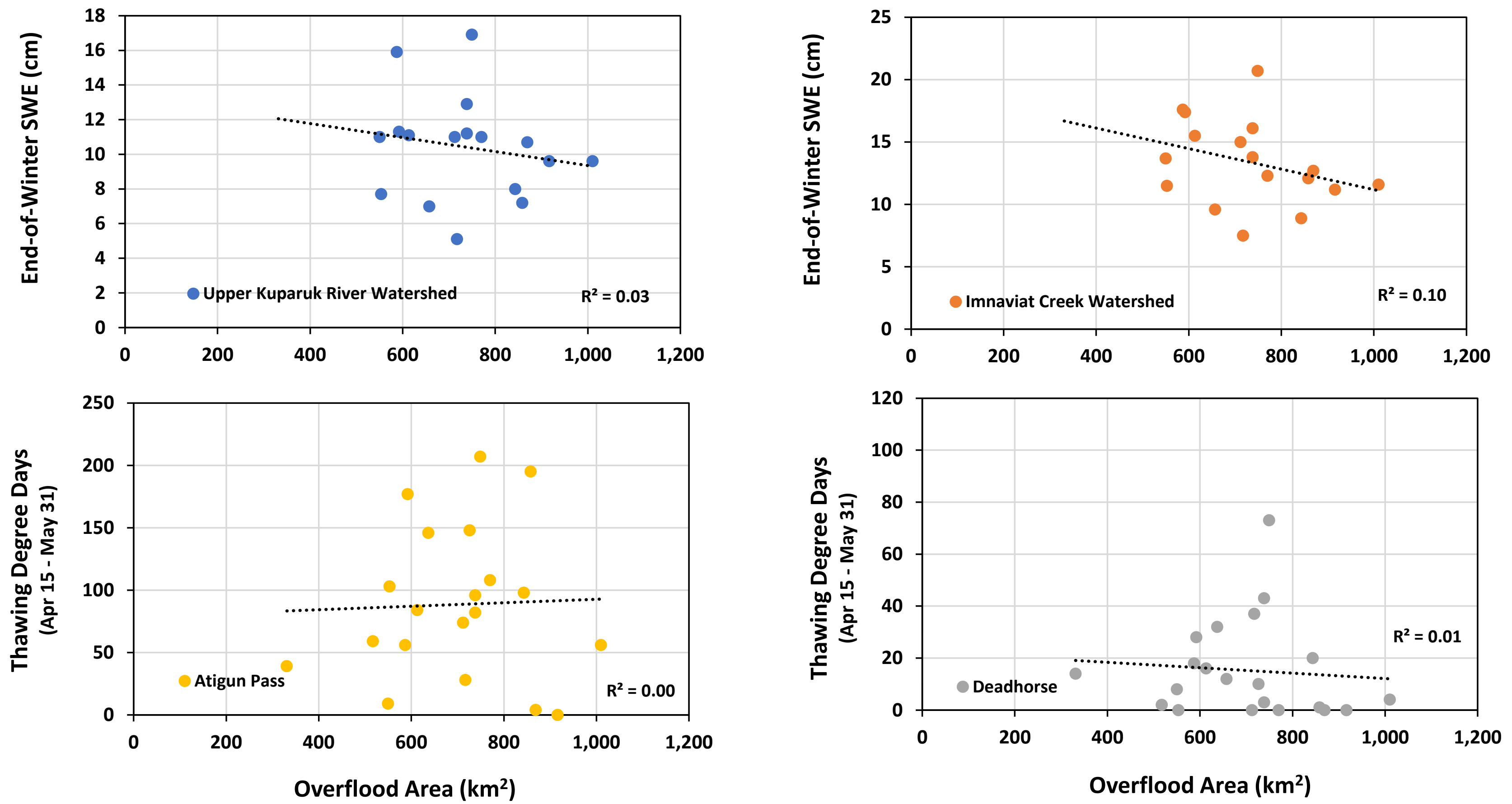

Figure 41. Correlation between end-of-winter SWE, TDD, and overflood area (Lower Colville River WBD)

3.2 Kuparuk River WBD

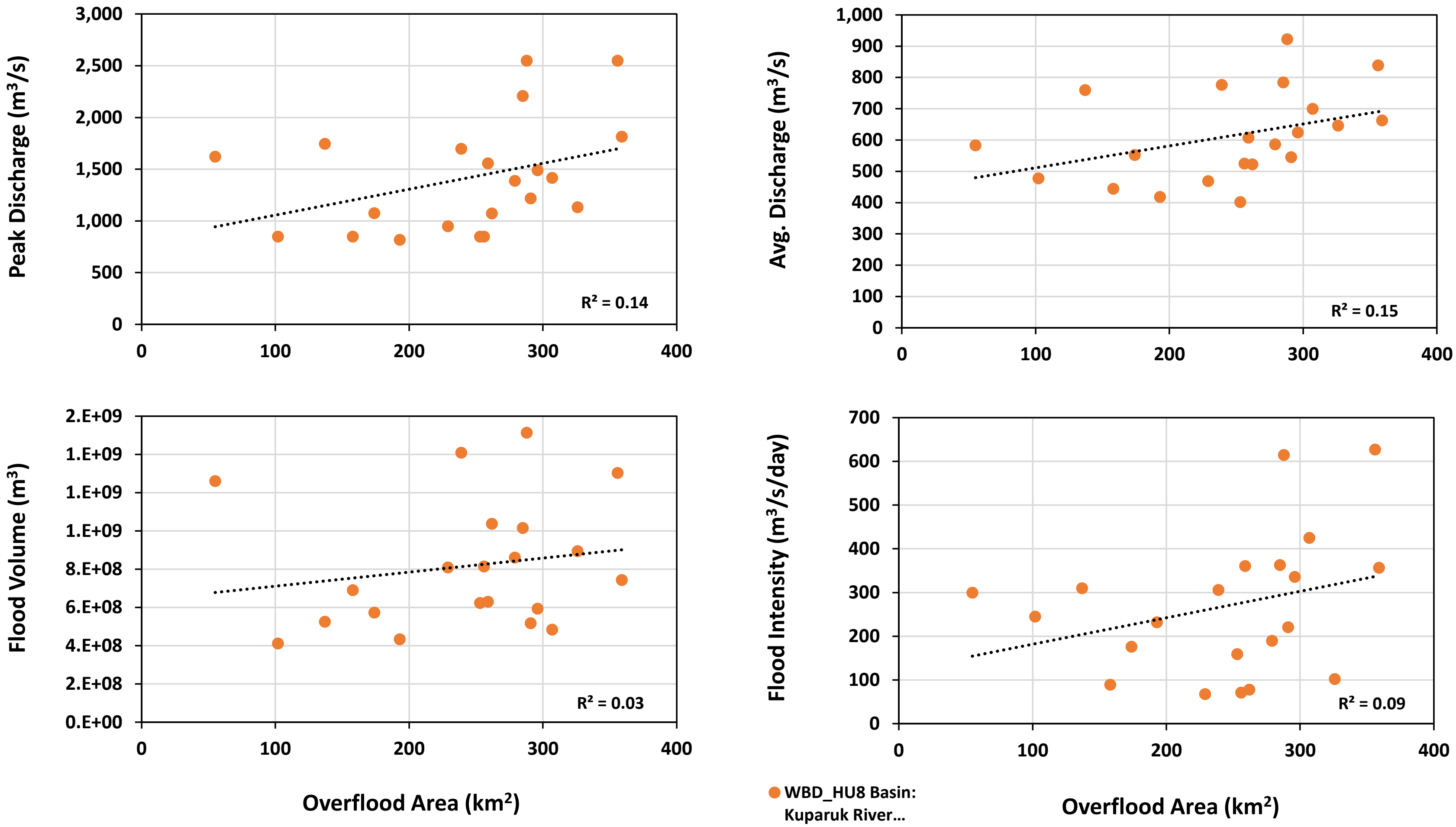

Figure 42. Correlation between streamflow (Kuparuk River) and overflood area (Kuparuk River WBD)

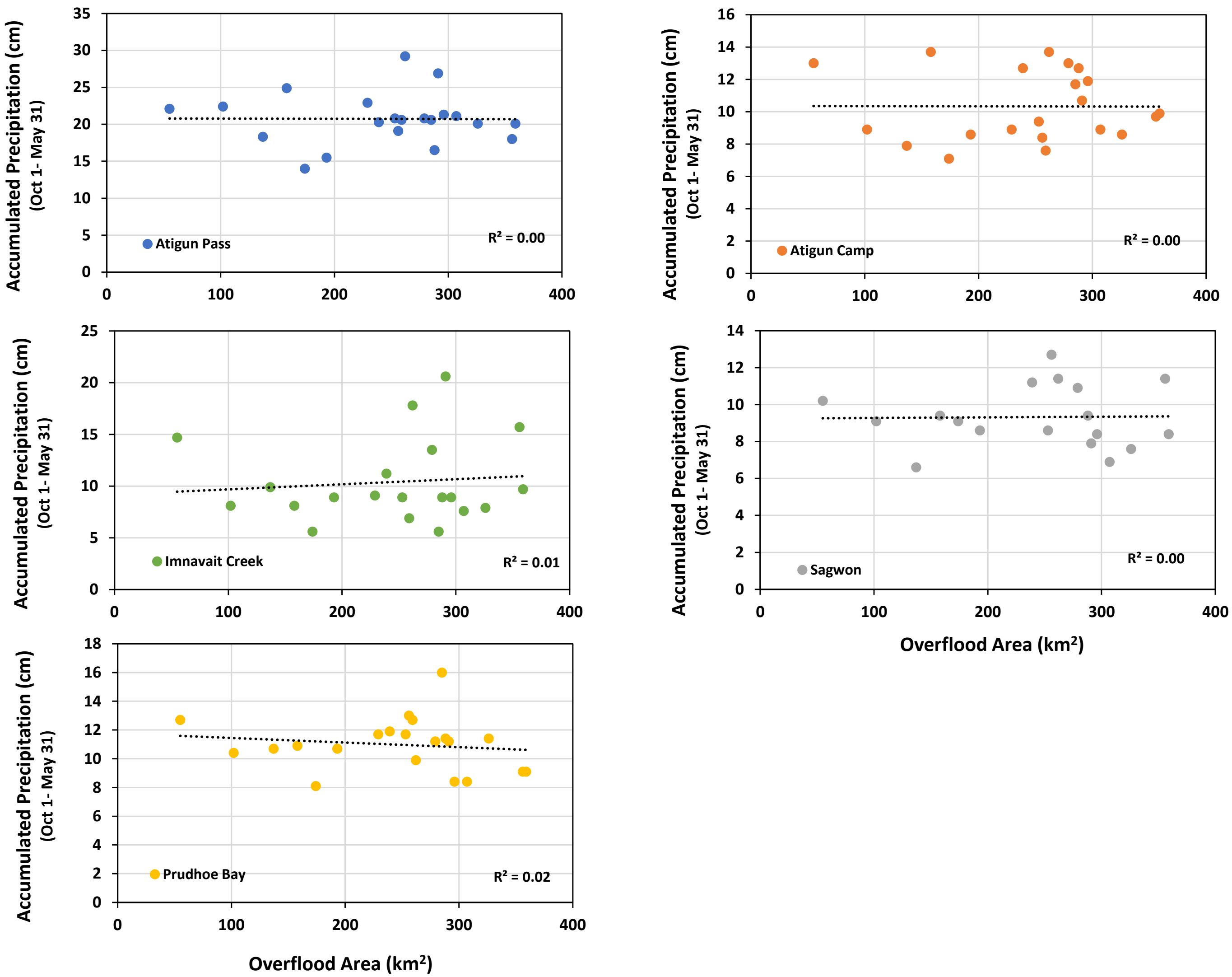

Figure 43. Correlation between precipitation and overflood area (Kuparuk River WBD)

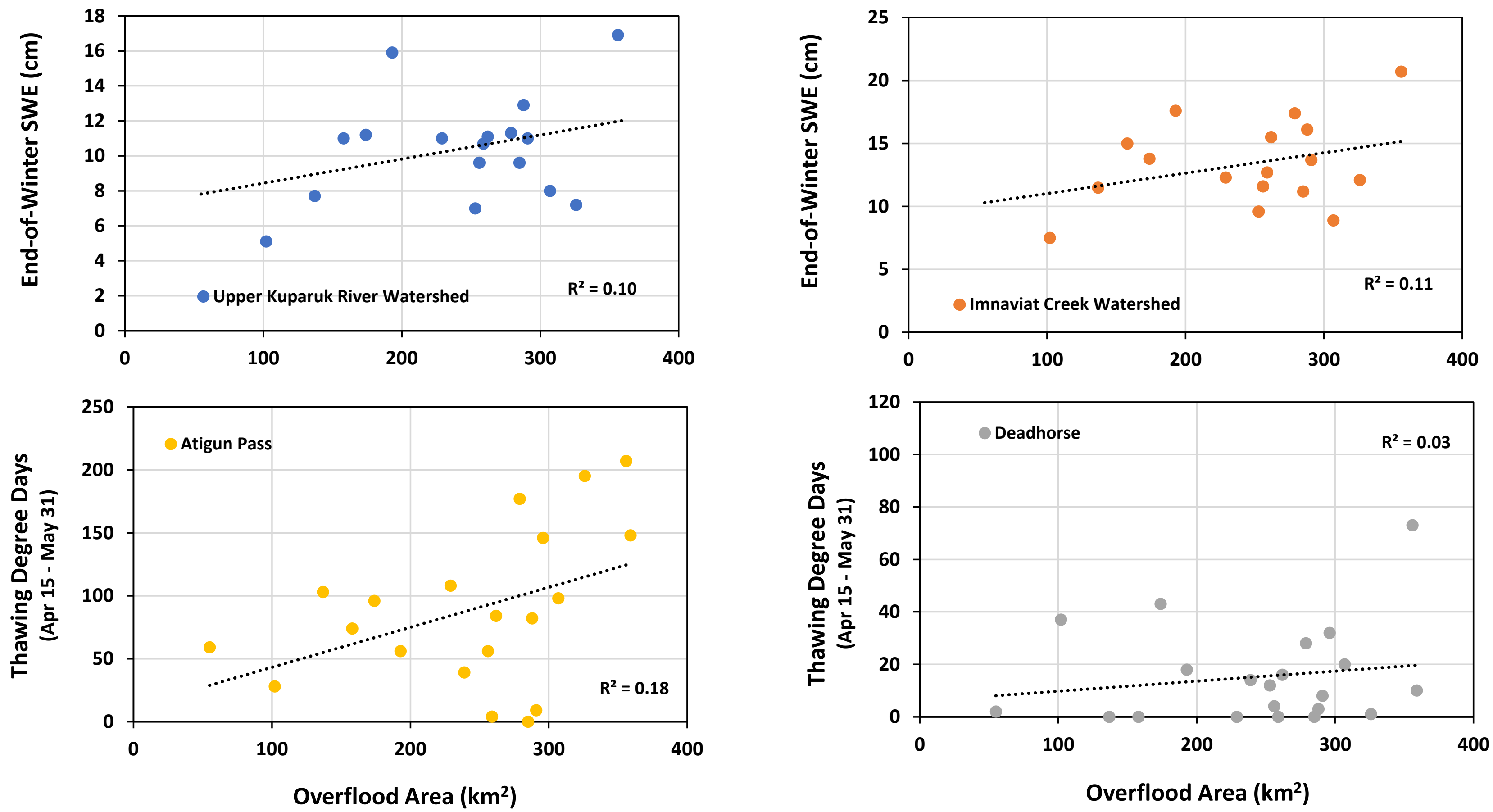

Figure 44. Correlation between end-of-winter SWE, TDD, and overflood area (Kuparuk River WBD)

3.3 Sagavanirktok River WBD

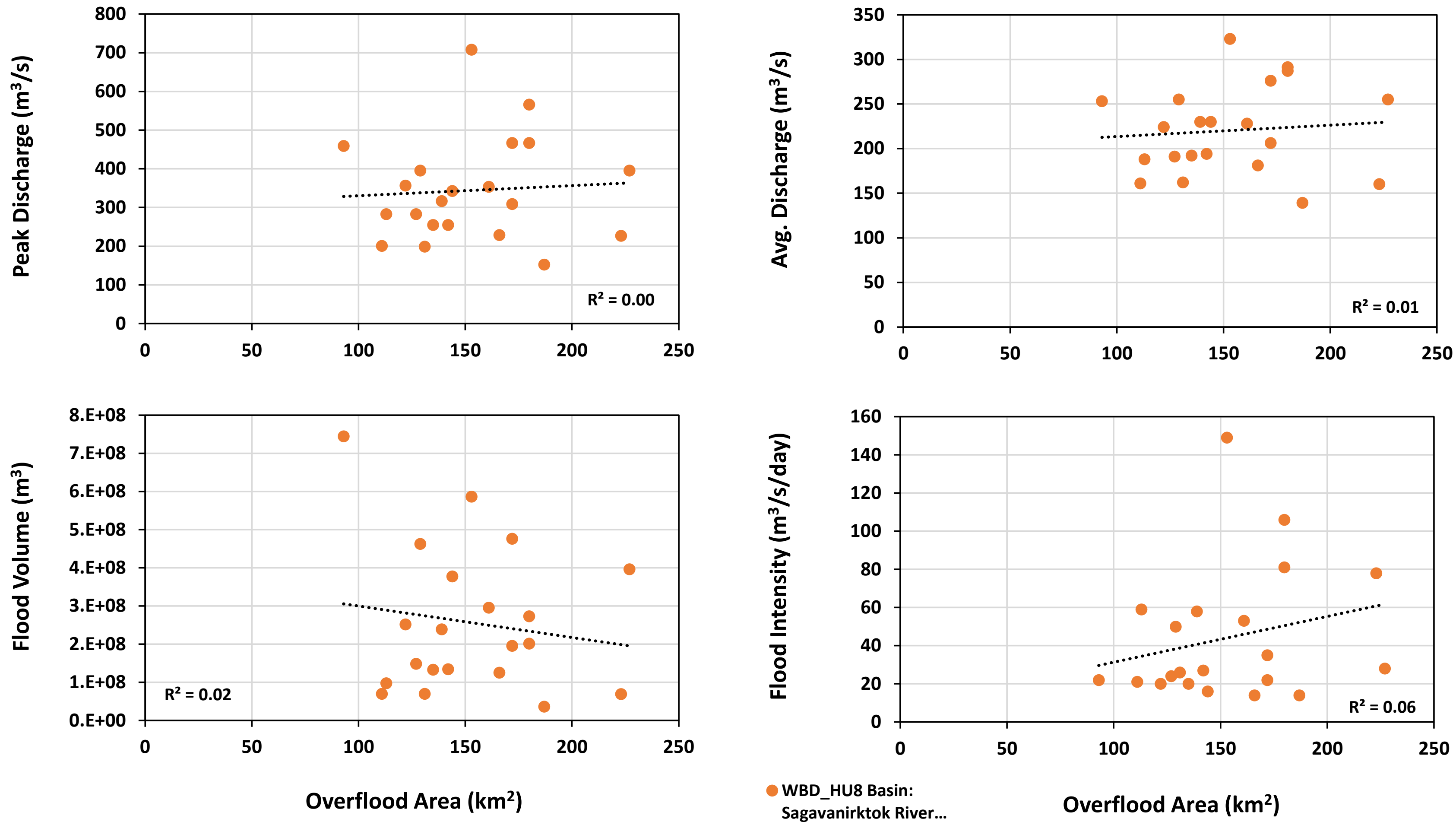

Figure 45. Correlation between streamflow (Sagavanirktok River) and overflood area (Sagavanirktok River WBD)

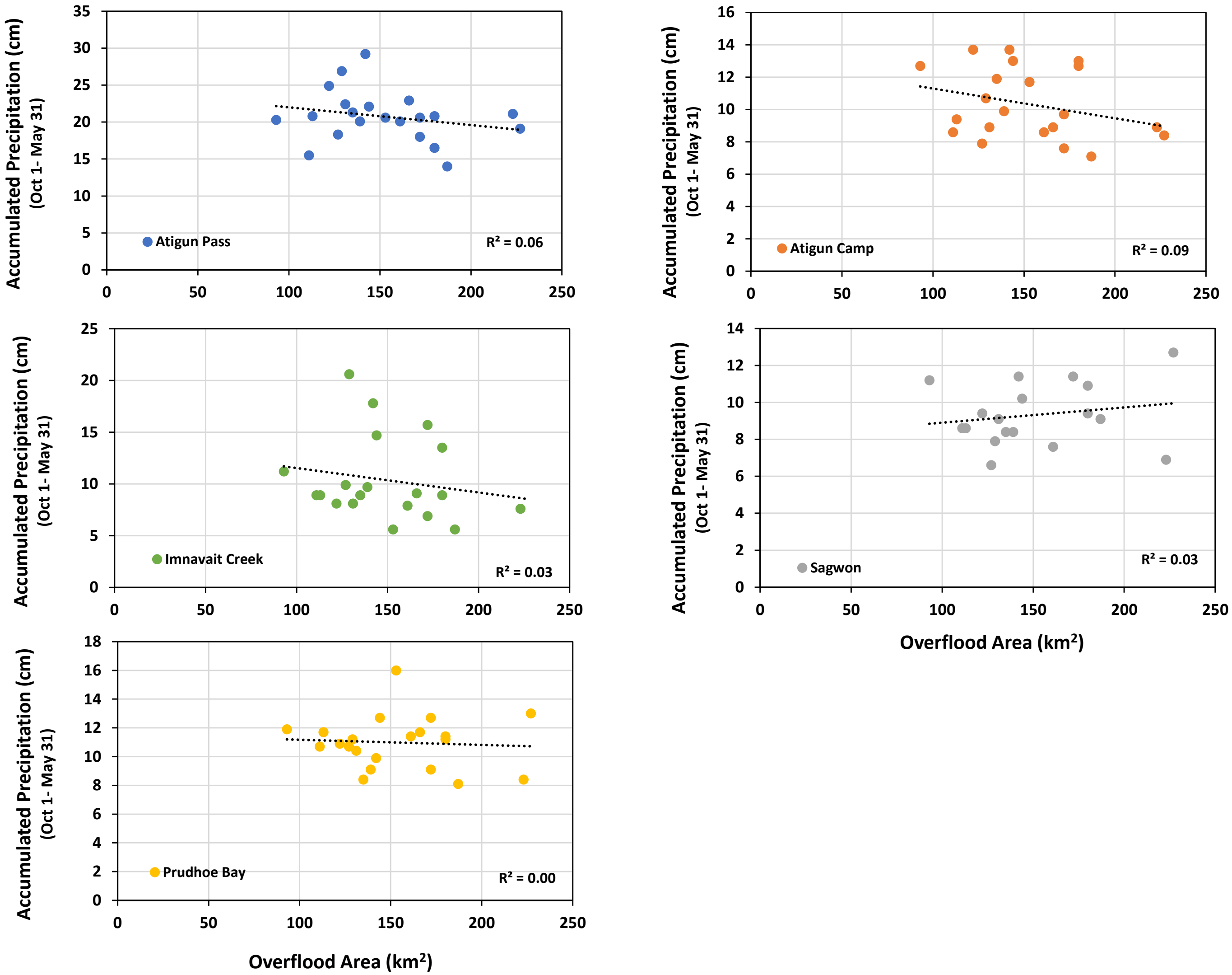

Figure 46. Correlation between precipitation and overflood area (Sagavanirktok River WBD)

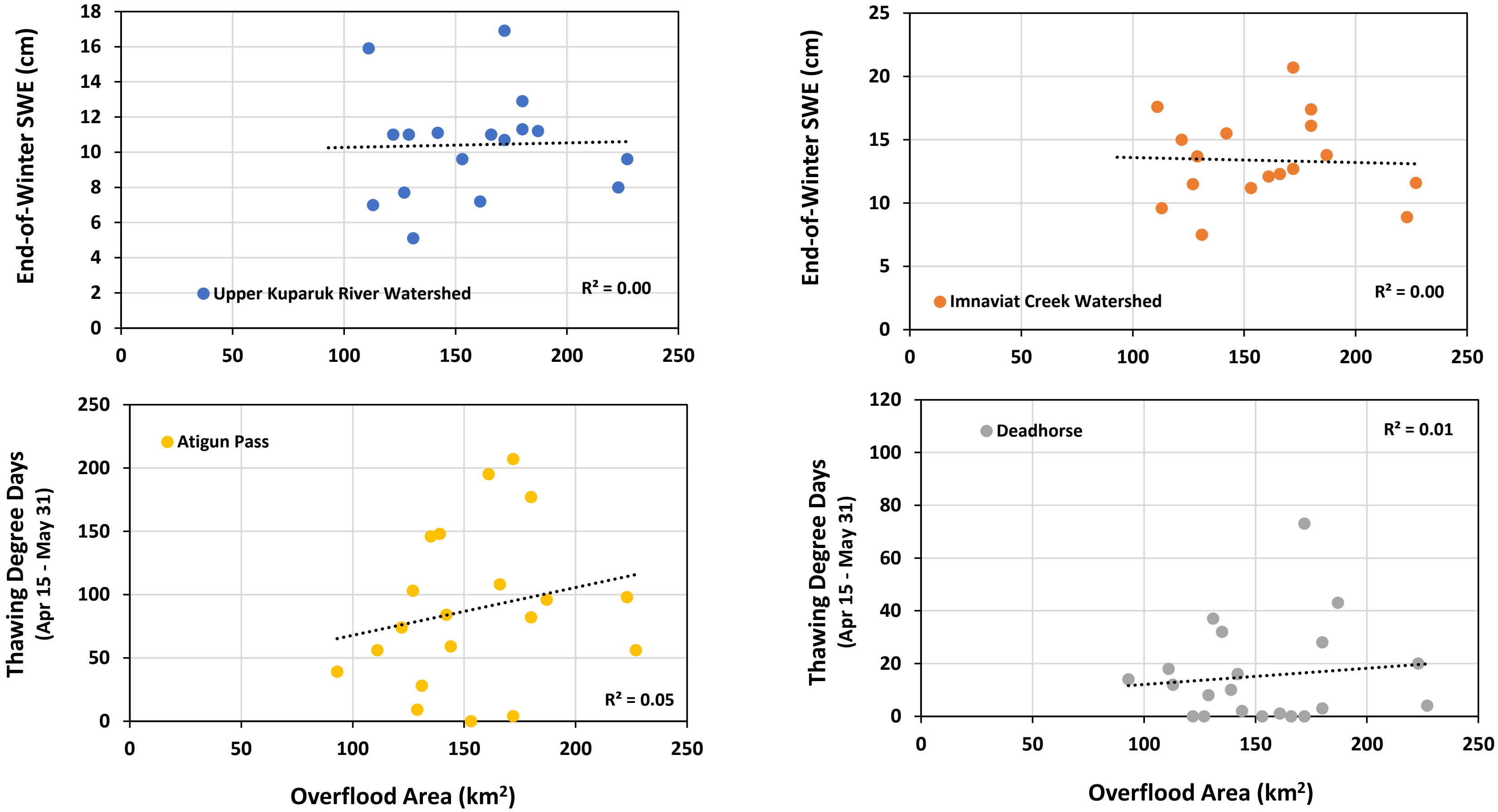

Figure 47. Correlation between end-of-winter SWE, TDD, and overflood area (Sagavanirktok River WBD)

4 Correlation between Environmental Parameters and Total Overflood Area

4.1 Streamflow

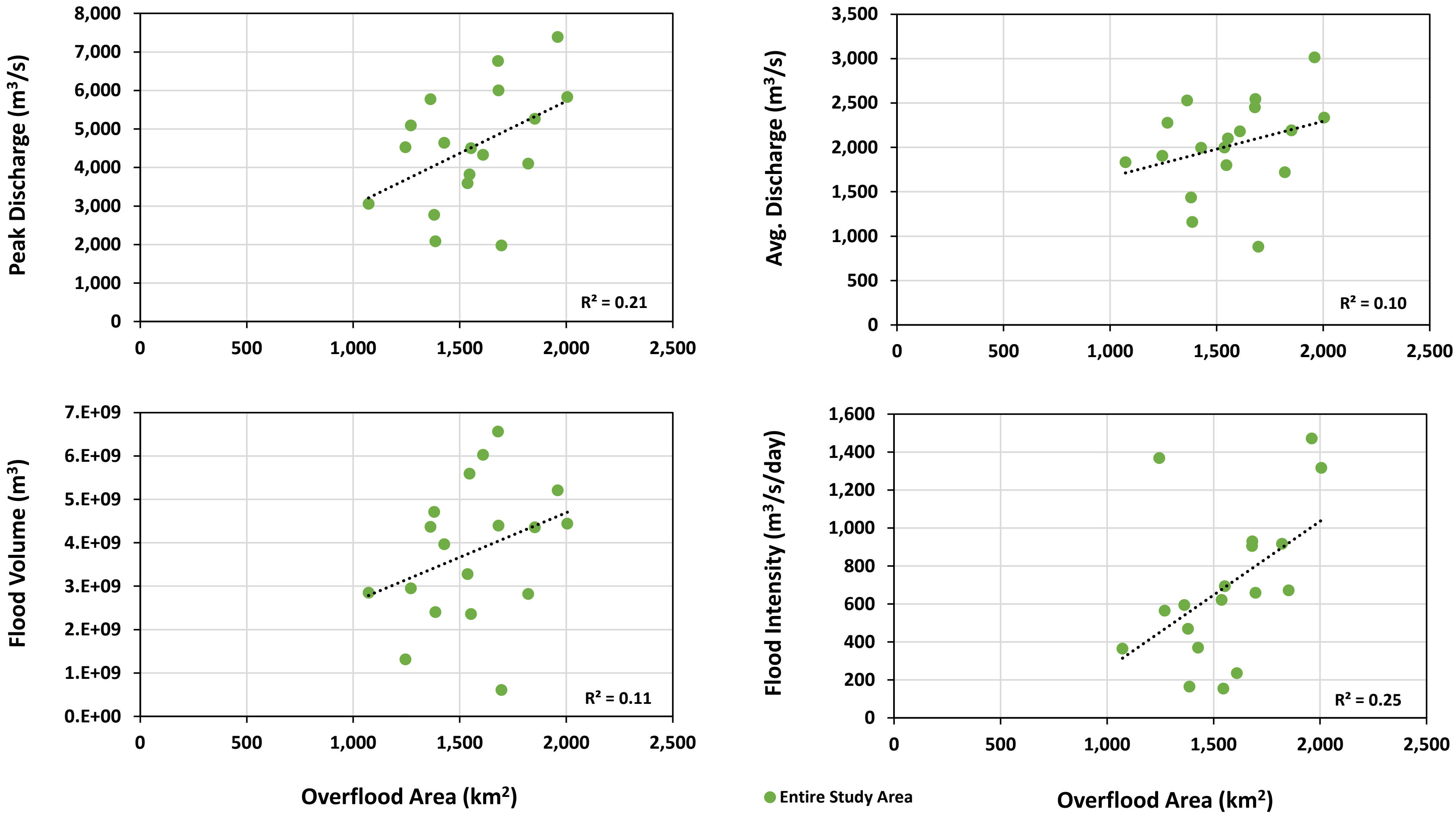

Figure 48. Correlation between streamflow (Colville River) and total overflood area

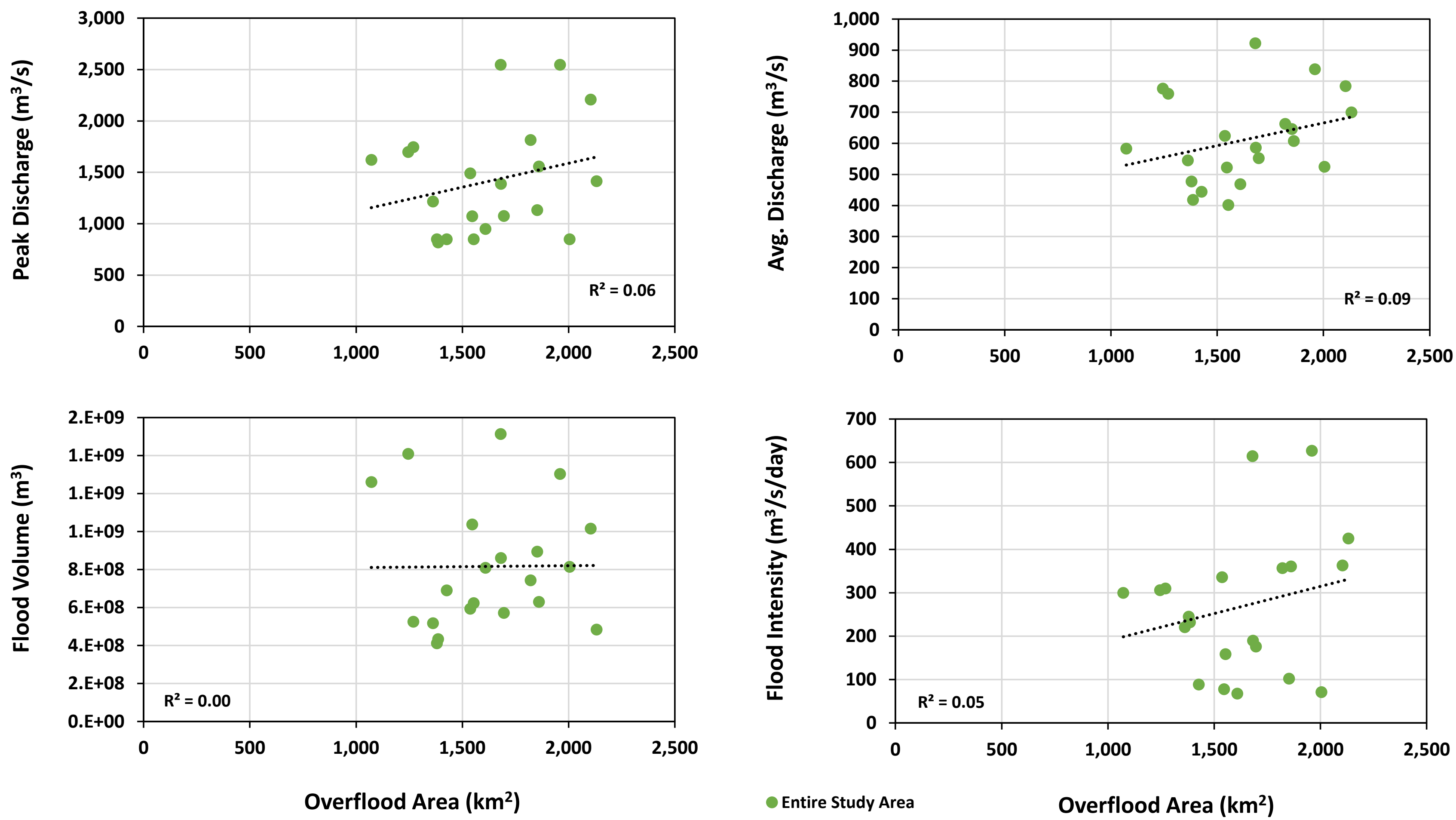

Figure 49. Correlation between streamflow (Kuparuk River) and total overflood area

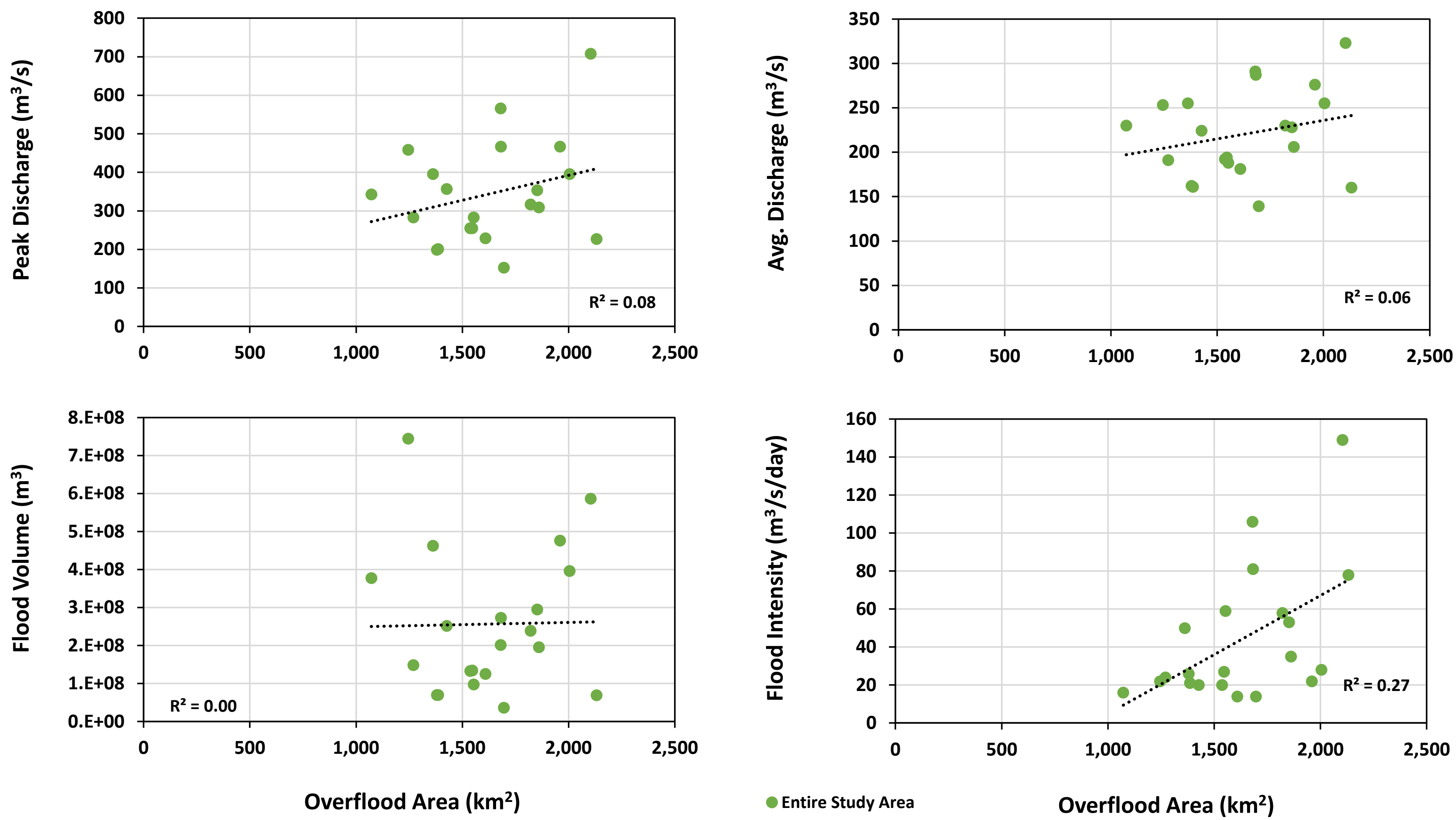

Figure 50. Correlation between streamflow (Sagavanirktok River) and total overflood area

4.2 Precipitation

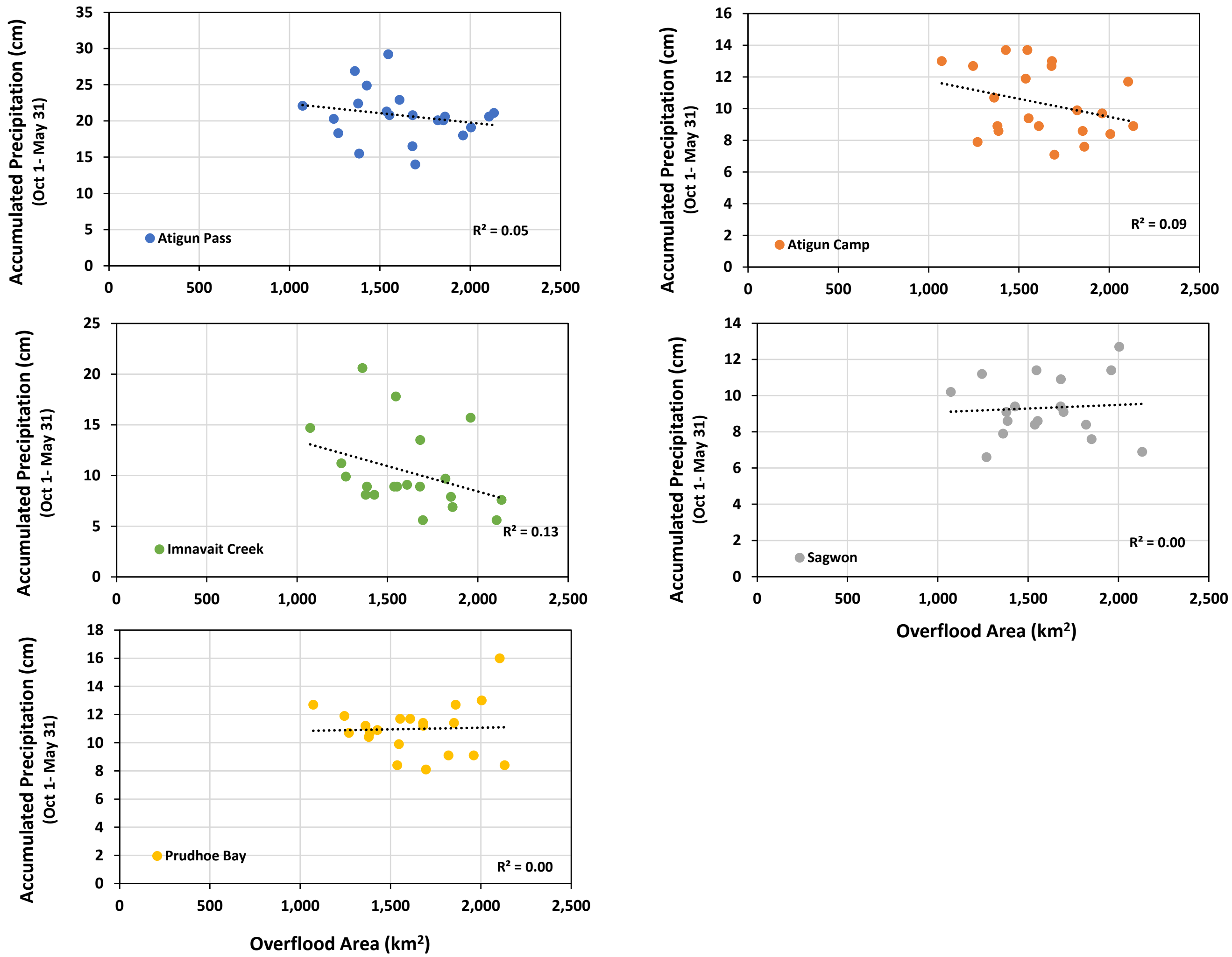

Figure 51. Correlation between precipitation and total overflood area

4.3 Snowpack and Air Temperature

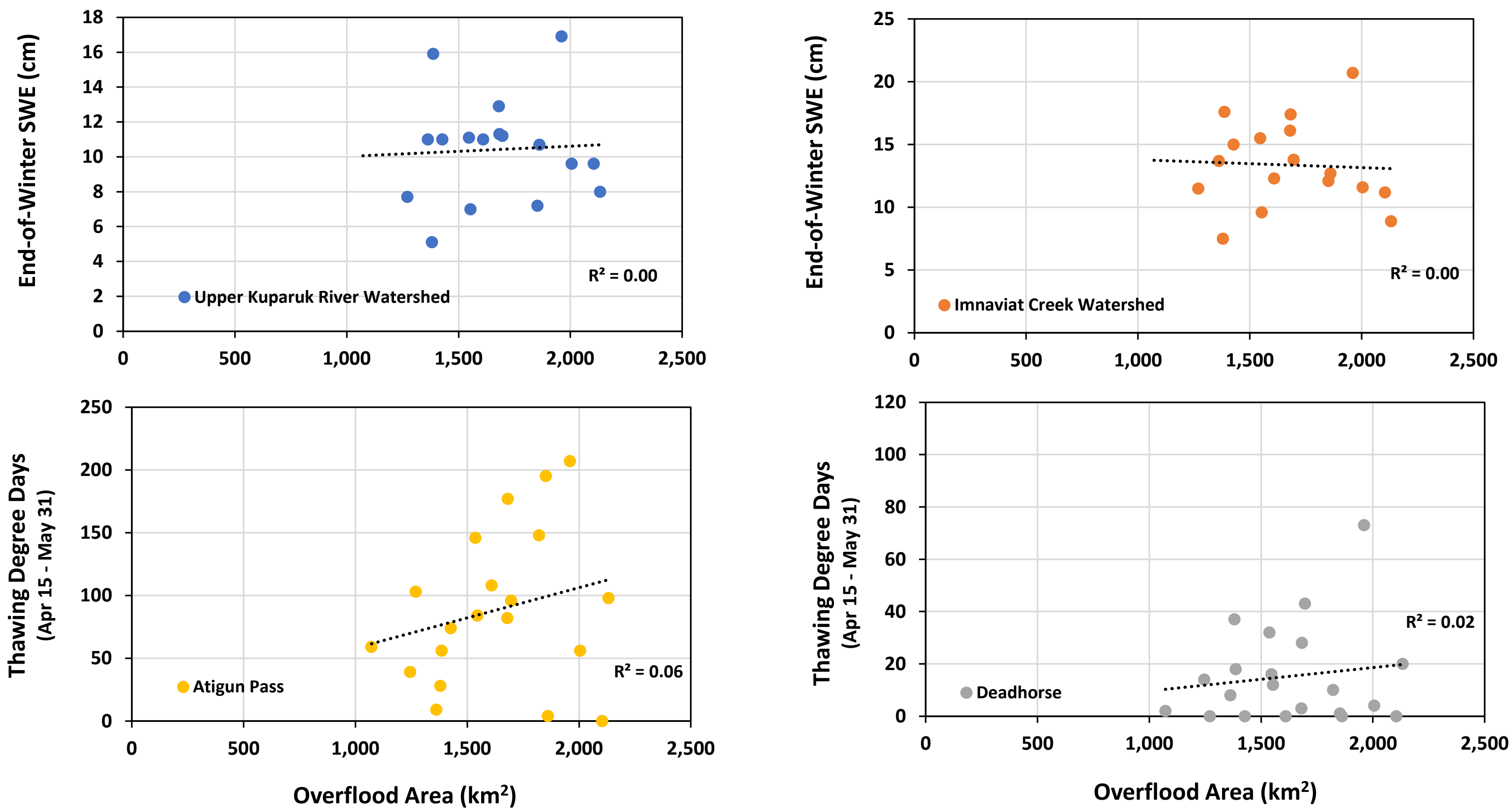

Figure 52. Correlation between end-of-winter SWE, TDD, and total overflood area

U.S. Department of the Interior (DOI)
The DOI protects and manages the Nation's natural resources and cultural heritage; provides scientific and other information about those resources; and honors the Nation's trust responsibilities or special commitments to American Indians, Alaska Natives, and affiliated island communities.

Bureau of Ocean Energy Management (BOEM)
BOEM's mission is to manage development of U.S. Outer Continental Shelf energy and mineral resources in an environmentally and economically responsible way.

BOEM Environmental Studies Program
The mission of the Environmental Studies Program is to provide the information needed to predict, assess, and manage impacts from offshore energy and marine mineral exploration, development, and production activities on human, marine, and coastal environments. The proposal, selection, research, review, collaboration, production, and dissemination of each of BOEM's Environmental Studies follows the DOI Code of Scientific and Scholarly Conduct, in support of a culture of scientific and professional integrity, as set out in the DOI Departmental Manual (305 DM 3).